January 2009

Phase Formation, Liquid Structure, and Physical Properties of Amorphous- and Quasicrystal-forming Alloys

Victor Wessels
Washington University in St. Louis

WASHINGTON UNIVERSITY IN ST. LOUIS

Department of Physics

Dissertation Examination Committee:
Kenneth F. Kelton, Chair
Richard L. Axelbaum
William E. Buhro
Patrick C. Gibbons
James G. Miller
Zohar Nussinov

PHASE FORMATION, LIQUID STRUCTURE, AND PHYSICAL PROPERTIES OF AMORPHOUS AND QUASICRYSTAL-FORMING ALLOYS

by

Victor Medgar Wessels

A dissertation presented to the
Graduate School of Arts and Sciences
of Washington University in
partial fulfillment of the
requirements for the degree
of Doctor of Philosophy

August 2009

Saint Louis, Missouri

ABSTRACT OF THE DISSERTATION

Phase Formation, Liquid Structure, and Physical Properties of Amorphous and Quasicrystal-forming Alloys

by

Victor Medgar Wessels

Doctor of Philosophy in Physics

Washington University in St. Louis, 2009

Professor Kenneth F. Kelton, Chairperson

Since the discovery of quasicrystals in 1985 and the development of commercially viable bulk metallic glasses (BMGs) in the mid 1990's a great deal of attention has been given to the characterization of new alloys with desirable properties, such as larger amorphous casting thickness, higher mechanical strength, or hydrogen storage capacity. Here, the results of a number of investigations into the structures and properties of some non-crystalline solid alloys will be presented and analyzed. Beamline electrostatic levitation (BESL), a method for determining supercooled liquid structure and phase formation *in-situ*, was used. Using BESL, the development of structural and chemical inhomogeneity was observed in supercooled liquid $Cu_{46}Zr_{54}$ (a BMG when cast) with an onset at 845 ± 5°C, providing experimental support for structural changes determined from molecular dynamics (MD) simulations of these liquids. Differing segregation of Hf and Zr atoms was observed in solidified $Ti_{45}Zr_{(38-x)}Hf_xNi_{17}$ using scanning electron microscopy (SEM), and correlated to a previously observed, sharp boundary in phase formation near x = 19 that was further investigated using BESL. In addition to the BESL studies, results will be

presented and discussed on changes in microstructure and devitrification mechanisms with the addition of Ag in $Mg_{65}Cu_{(25-x)}Ag_xGd_{10}$ BMGs, interesting for their light weight and resistance to oxygen during casting, using transmission electron microscopy (TEM), SEM, and differential scanning calorimetry (DSC). Previous, preliminary results on the hydrogen storage capacity of icosahedral quasicrystal $Ti_{45}Zr_{38}Ni_{17}$ were re-examined, using an improved apparatus and analysis method developed as part of this work, and the previous results found to be in error.

Acknowledgements

I would first like to thank my advisor, Prof. Ken Kelton for his great enthusiasm for science and his support for me and all his students, both intellectually and through his work to maintain funding. I especially want to thank him for his help as I prepared this thesis, over a short period, during an otherwise very busy time for him. I will try to reflect his dedication and work ethic in my future endeavors.

I would also like to thank Prof. Pat Gibbons for his help and good company during my time here. His expertise with microscopy and electronics was valuable. Dr. Anup Gangopadhyay was very helpful in discussions of my research and to keep me honest and precise. Dr. Kisor Kumar Sahu was, and still is, a good friend and an insightful scientist.

My fellow graduate students, Karyn Bondi, Tae Ho Kim, Nick Mauro, Youtao Shen, and Lydia Spoor were indispensable, both for scientific discussions (mostly "stupid questions" from me) and for listening to me vent occasional anger about grad school and research. I can't go without thanking all the other great friends I made during my time here. They are just too many to list and I would hate to leave anyone out. You know who you are and all the fun we had.

I would like to acknowledge the agencies that funded this research, the National Science Foundation, under grant DMR 06-06065, and NASA, under grant NNX07AK27G.

Finally, I would like to dedicate this thesis effort to my mom, Deborah, my sister, Emanuelle, and to the memory of my dad, Kenneth Wessels, who passed away during my time in grad school. I know you are all proud of me, but more than that I know you would be proud of me, and support me, no matter what.

Table of contents

List of Figures

After enlightenment, the laundry.
proverb

Chapter 1

Introduction

The processing of metals and alloys has been an important part of human development. It is closely tied to the rise of civilization through technological advancement, with applications to agriculture and hunting, defense, and the machinery of industry. It is so important, in fact, that a nearly 5000 year span of human history is categorized based on the materials mastered by humans during that time: the Bronze Age (alloying Copper and Tin derived from ores, from ~3000-600BCE), the Iron Age (development of higher temperature smelting techniques and the processing of some steel, but mostly wrought Iron, up to ~400CE), and, in the Modern Age, the mastery of steel processing that gave rise to the industrial revolution.

Some mysteries of ancient metalworking persisted until very recently, and required the use of modern science to explain. For example, the nature of Damascus steel, which was worked by people of the Middle East into swords of legendary sharpness and strength from unique, imported metal stock from India and Sri Lanka, was only recently characterized using high resolution transmission electron microscopy (HRTEM). It was found to contain carbon nanotubes and cementite nanowire structures, which gave the steel its unique appearance and desirable mechanical properties [1]. Somewhat similarly, a deep understanding of today's advanced materials may be lacking.

Over the last 60 years, using a variety of processing techniques, alloys have been discovered that form novel phases, which do not possess the long-range periodicity (or long-range order, LRO) associated with crystalline solid metals. Some alloys can be

prepared with a highly disordered, or amorphous, structure that gives them very desirable engineering properties, such as high strength and hardness and improved resistance to fracture and corrosion, due to a lack of grain boundaries or dislocations that are often a weakness in crystalline materials [2, 3]. Others can be produced with very well-ordered crystal structures that do not possess periodic translational symmetry. Such structures are called *quasicrystals*; certain alloys in this phase have shown promise for solid storage of hydrogen for renewable energy applications [4], to be discussed in Chapter 6. Expanded discussions of the amorphous and quasicrystal phases will be provided in later sections of this chapter.

Often these phases are formed by rapidly cooling the molten alloys, but the relationship between the physics of the liquid state and the formation of non-crystalline solid phases is not well understood. In this thesis, the physics of formation and properties of glasses, quasicrystals, and some related phases, are examined. The influence of liquid structural changes on formation of these phases will be discussed in detail. A variety of advanced techniques, including new experimental ones and a combination of experiments with computer modeling, for structural characterization and analysis, will be discussed. This introductory chapter will provide an overview of the basic properties of liquids, glasses, and quasicrystals, and introduce definitions and measurement techniques to probe their atomic structures. It also contains a discussion of supercooling in liquids, as well as current and historical theories of crystallization, which will be relevant to later discussions of solidification of liquids and devitrification (crystallization of a glass upon heating). Finally, §1.8 provides a summary of this chapter and an overview of the thesis.

1.1. Order in non-crystalline systems

Largely absent from the commonplace description of the states of matter (solid, liquid, and gas) is mention of *order* in their atomic arrangements. As already discussed, this dissertation work, in large part, explored the physics of the liquid phase in systems that can form non-crystalline solids. Schematic atomic arrangements for a crystal, networked glass (e.g. SiO_2), and a gas are shown in Figure 1.1. In the crystal there is periodic LRO (i.e. given the lattice and basis, the positions of all atoms are known, to within defects, grain boundaries, and other impurities) and the configuration of the gas is random. The glass, however, possesses a high degree of short-range order (SRO, i.e. order on the scale of first nearest-neighbors), with many individual atoms tetrahedrally coordinated; medium-range order (MRO, second or third nearest-neighbor distances) in glasses is still under investigation [5]. The local structures of glasses and liquids are similar; the glass can be thought of as having a "frozen-in" liquid structure. A further discussion of metallic glasses is given in §1.4. The full nature of the similarity of liquid and glass structures is still debated, and subtle changes in the liquid structure prior to glass formation are not well understood, which in part motivates this work.

The purpose of many of the experiments presented here was, in short, to determine the positions of atoms in non-crystalline systems. Several theoretical approaches have been developed to describe the order in non-crystalline systems (particularly liquids, but they can be applied to glasses). The Percus-Yevick and Hypernetted-Chain models attempt to produce the pair distribution function $g(r)$ (a quantity that is determined from experimental diffraction data, to be discussed in the ensuing section) from the pair-potential $\varphi(r)$.

(a) (b) (c)

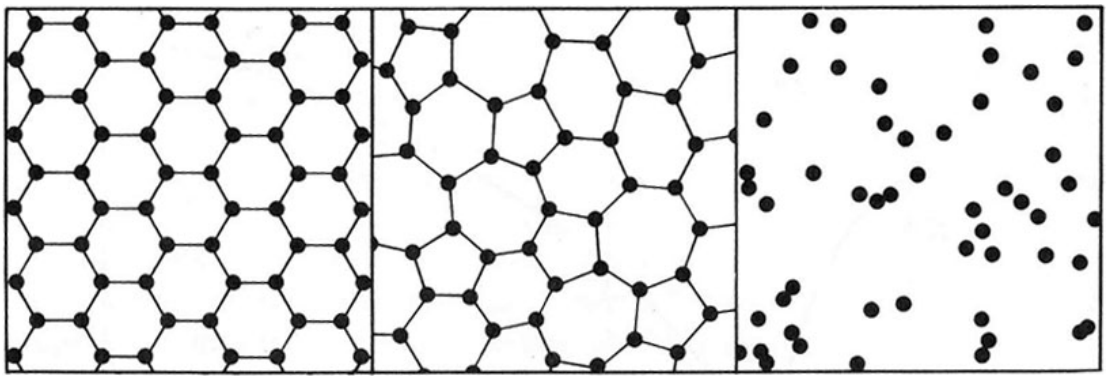

Figure 1.1 – A schematic representation of the atomic structures of (a) a crystal, (b) a network glass, and (c) a gas; image from [6].

These models produce equations relating the two functions, and have been extended with simple inter-atomic potentials, such as non-interacting hard spheres. A full description of these models is beyond the scope of this thesis; a good overview can be found in reference [7]. While instructive, these models break down for the complicated systems of interest here, and so simulation methods, such as the Reverse Monte Carlo method (discussed in §1.7) are used to model their atomic configurations.

1.2. Measuring order in non-crystalline systems

As already mentioned, the positions of atoms (ignoring structural defects) in most solid metals can be readily determined due to the long-range order of their crystal structures. In practice, crystal structures are determined from x-ray diffraction (XRD) experiments. A full review of the physics of XRD is beyond the scope of this thesis, but can be found elsewhere [8, 9]. The Bragg formula relates the separation, d, of planes of atoms to half the angular positions of peaks in the intensity of scattered x-rays, θ, due to constructive interference, i.e.

$$n\lambda = 2d\sin\theta,$$

where n is the order of reflection and λ is the wavelength of incident x-rays. The Bragg formula is a convenient formalism, derived from the more general theory of Laue diffraction, useful for studying crystals.

For disordered systems such as liquids and glasses well defined planes of atoms are not present so applying the Bragg law can be misleading; a different formalism is needed. These systems exhibit a distribution of short- and medium-range order, which is described in real (position) space by the pair distribution function (PDF), denoted as $g(r)$,

and in reciprocal (momentum) space by the liquid structure function, or structure factor, denoted as $S(q)$. $g(r)$ gives the probability of finding an atom at a radial position, r, from a defined center (a thorough discussion of the subtleties of PDF analysis can be found elsewhere [10]). $S(q)$ gives a normalized value of the scattered intensity as a function of wave-vector difference between the incident and scattered beams, a further description will be given later in this section. This section will provide an overview of the theoretical formulations for $S(q)$ and $g(r)$ for disordered systems, complete treatments can be found elsewhere [7, 11].

In XRD experiments, the measured quantity is the total scattered intensity, $I(q)$, where the wave vector, q, is related to θ by

$$q = \frac{4\pi \sin\theta}{\lambda}.$$

The coherent scattering intensity is given by

$$I^{coh}(q) = \left\langle \sum_j \sum_k f_j(q) f_k(q) \exp\{-iq(r_j - r_k)\} \right\rangle,$$

where $f_i(q)$ is an atomic scattering factor and r_i is an atom position. For a structure of N atoms of a single element, $S(q)$ is defined as

$$S(q) = N^{-1} \left\langle \sum_j \sum_k \exp\{-iq(r_j - r_k)\} \right\rangle = I^{coh}(q) \Big/ Nf^2(q).$$

Thus, $S(q)$ is a construct of the measured scattering intensity, normalized by the total number of atoms and the atomic scattering factors. The experimental determination of *S(q)* will be discussed in Chapter 2. For multicomponent systems, $S(q)$ is defined as a sum of *partial* structure functions, for which different equations have been proposed [7]. Partial functions refer to the correlations between the different species of atoms in the

system; thus, from combinatorics, for an n-component system there are $\frac{n(n-1)}{2}$ different partial pair functions. For this work, the Faber-Ziman (FZ) formulation was used to define the total $S(q)$ from the partials, i.e.

$$S_{FZ}(q) = \left[I^{coh}(q) - \left\{ \left\langle f^2(q) \right\rangle - \left\langle f(q) \right\rangle^2 \right\} \right] / \left\langle f(q) \right\rangle^2 = \sum_{\alpha} \sum_{\beta} \left[c_\alpha c_\beta \frac{f_\alpha(q) f_\beta(q)}{\left\langle f^2(q) \right\rangle} \right] * S_{\alpha\beta}(q) ,$$

(1.2.1)

where

$$\left\langle f^2(q) \right\rangle = \sum_n c_n f_n{}^2(q)$$
$$\left\langle f(q) \right\rangle = \sum_n c_n f_n(q) \quad .$$

Here, the important quantities are the FZ interaction coefficients, given by the leading term (inside the square brackets, []) on the right-hand side of Eq. 1.2.1. These are necessary for the RMC simulations described in §1.7.1. The structure factor and the pair distribution function are related by a Fourier transform, i.e.

$$\rho g(r) = \int dq \left[S(q) - 1 \right] e^{-iq \cdot r} \quad .$$

It is instructive to examine the typical behavior of these functions for non-crystalline systems. Figure 1.2 shows schematic drawings of the atomic configurations and the resulting $g(r)$ for a gas, liquid (with a region approximating an amorphous solid), and a crystal. From this figure, it is clear that in a gas the atomic arrangement is random, in a liquid there is some order up to length scales of a few atomic diameters, a glass is liquid-like, but is more ordered, and a crystal has well-defined LRO.

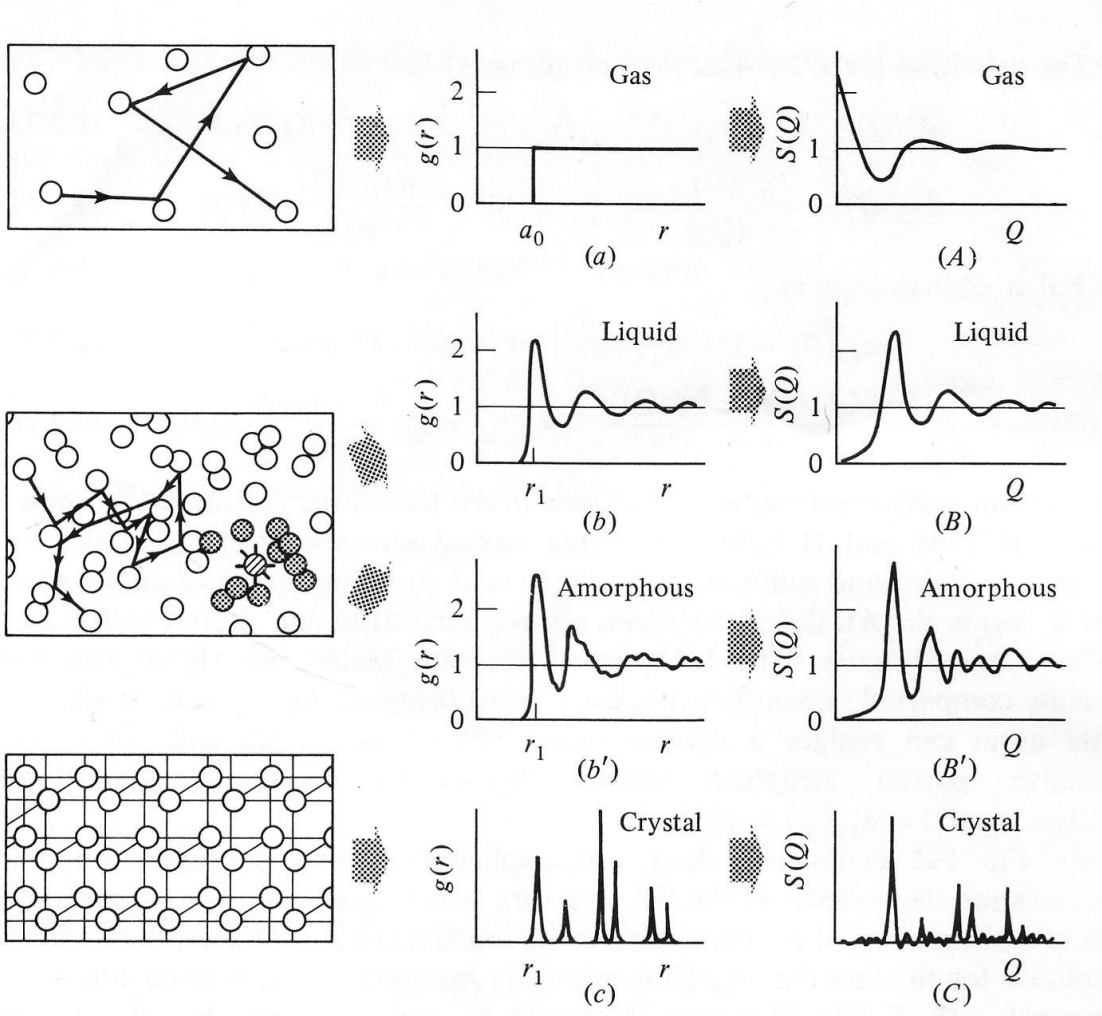

Figure 1.2 – The characteristic radial distribution functions, $g(r)$, and total structure functions, $S(q)$, for (a) a gas, (b) a liquid, (b') a glass, and (c) a crystal; image taken from [7].

It is important to note the broadening of peaks for the liquid and amorphous systems. In $g(r)$, this reflects the distribution of interatomic separation distances, with the position of maximum intensity of the broad peak corresponding to the most probable distance, and the onset of the first peak corresponding to the minimum distance allowed by atomic impingement. A further discussion of the relationship between liquid and glass structures will be given in §1.4. So far quasicrystals have not been discussed. These systems are well ordered, but unlike a crystal, this order is not periodic. Further explanation will be given in §1.5.

1.3. Liquid supercooling

Supercooled liquid water, i.e. water that remains liquid at a temperature below the equilibrium melting temperature (0°C at atmospheric pressure) was first described by Fahrenheit in 1724 [12]. In this state, the liquid is *metastable*; formation of the solid phase (ice) is energetically favorable, but due to inhibited kinetics arising from a large barrier to nucleation (see §1.6), and the absence of impurities to catalyze crystallization, it remains liquid. A further discussion of the kinetic and thermodynamic contributions to crystallization is given in §1.6. Small fluctuations in the local order of the supercooled liquid will eventually induce crystallization (the rapid solidification of a supercooled liquid, accompanied by the release of the enthalpy of fusion, is called *recalescence*). In 1950, Turnbull first described supercooling of a metallic liquid using dilatometric measurements made on Hg [13], shown in Figure 1.3. Since this discovery, levitation (or more generally, *containerless*) processing techniques have been developed to study supercooling and structure in liquid metals and alloys. These techniques are introduced in the following section.

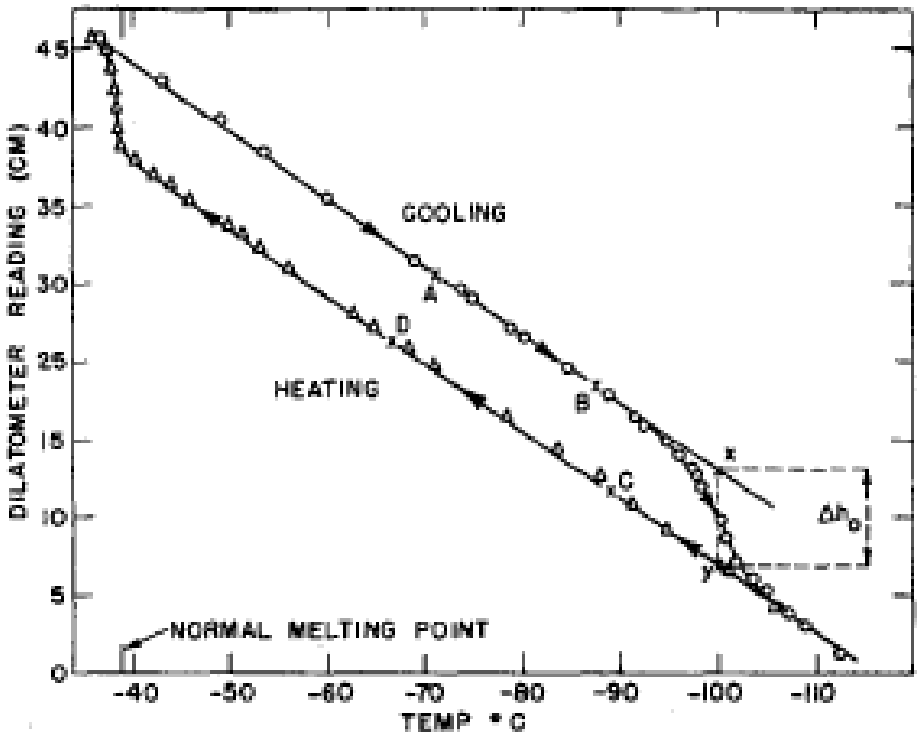

Figure 1.3 – Turnbull's classic result showing supercooling of liquid Hg; image taken from [13].

1.3.1. Levitation techniques for the study of liquids

Liquids will exhibit supercooling to lower temperatures in the absence of crucibles or containers, which can provide catalytic sites for the formation of crystal nuclei (a form of *heterogeneous nucleation*, to be contrasted with *homogeneous nucleation*; nucleation will be discussed in §1.6). In all of the techniques discussed below, metallic samples are melted and allowed to cool freely, in the absence of container walls, by radiation in a high vacuum (10^{-7} torr or less) or inert gas environment, while the temperature is measured by an optical pyrometer. Details of the experimental techniques relevant to this dissertation work will be provided in Chapter 2.

Early levitation experiments used gas jets (aerodynamic levitation), sound waves (acoustic levitation), or beams of laser light (optical levitation) [14]. Researchers at NASA used drop-tube and drop-tower facilities to utilize the microgravity of freefall for supercooling studies [15, 16]. More recently, electromagnetic levitation (EML), in which samples are levitated and heated by a radio frequency (RF) coil, was developed for the study of metallic liquids [17]. The electrostatic levitation (ESL) technique, wherein small samples are levitated in an electrostatic field controlled by a computerized feedback algorithm, was developed [18] to overcome some limitations of EML such as coupled heating and levitation, and the requirement that samples be electrical conductors. A detailed description of the ESL apparatus used for the experiments presented in this thesis is given in Chapter 2.

Modifications of the ESL technique to include in-situ high energy x-ray diffraction of levitated droplets from synchrotron radiation (beamline electrostatic

levitation, or BESL [19]) were made, and used to study the relationship between icosahedral short-range order (ISRO) in supercooled liquids and the nucleation barrier [20], confirming the long standing hypothesis of Frank [21], which supposed icosahedral packing of atoms in supercooled liquids. The ISRO was further studied by Kim using a cluster model, and found to agree with observed scattering data [22]. Functionalities for thermo-physical property measurements, such as density, viscosity, and surface tension, were also developed and combined with ESL. The specifics of these measurements relevant to this work will be described in detail in Chapter 2.

1.4. Metallic glasses

A glass forms when a liquid cools and solidifies without crystallization. The glass transition, reviewed later in §1.4.1, is not fully understood. Further, a description of the evolution of order in the supercooled liquid, both chemically and topologically, prior to the glass transition, is an open question. An exploration of this question is one of the main purposes of this dissertation work. Many glasses require cooling rates of 10^5-10^7 K/s, which produce samples that retain the amorphous structure up to a thickness of 20-50 μm. The maximum thickness for which the structure is fully amorphous is called the *critical thickness*. For engineering applications slower cooling rates, on the order of 10^1-10^2 K/s, and larger critical casting thicknesses are desirable. Research on such *bulk metallic glasses* (BMG's) is relevant to the study of Cu-Zr alloys presented in Chapter 4 and the Mg-based BMG's of Chapter 5.

When a glass forms from solidification of a supercooled liquid, the disordered structure of the liquid is "frozen in." The word *amorphous* (from the Greek, meaning "without form") implies that the atomic structure of a glass is random. This is actually an

inappropriate name since, as already discussed, glasses possess a certain degree of SRO and MRO. Glass can form naturally as Obsidian (a volcanic rock), but the most common glasses are man-made silicate glasses (the material used in windows, dishware, and other familiar items), which have a well-described structure consisting of randomly networked oxide tetrahedrons [23]. That structure is not present in metallic glasses; further study is needed to fully characterize them.

The first metallic glass was found in 1960 by Klement, Willens, and Duwez in $Au_{75}Si_{25}$ [24] when the liquid was cooled at an extremely rapid rate (10^5 to 10^6 K/s). Following this discovery, glasses were found in other alloys, using similarly fast cooling rates. The first BMG, formed at more moderate cooling rates similar to those used to prepare silicate glasses, was discovered in 1984 by Turnbull and others in $Pd_{40}Ni_{40}P_{20}$. The critical thickness was 10 mm and the cooling rates were on the order of 10^1 K/s [25], but the preparation technique (fluxing) was not desirable for application. The first commercially viable BMG was discovered in 1992 by Peker and Johnson in $Zr_{41.2}Ti_{13.8}Cu_{12.5}Ni_{10.0}Be_{22.5}$ (they named the alloy Vitreloy1) [26]. Glasses with composition similar to that of Vitreloy1 have been marketed for athletic equipment and small consumer goods, such as cell phone and flash drive casings. These alloys have critical casting thicknesses on the order of centimeters and cooling rates of 10^1 K/s.

1.4.1. The glass transition

As already mentioned, a glass forms when a liquid cools and solidifies without crystallization. The liquid-glass transition is marked by changes in the physical properties of the system that occur at the *glass transition temperature*, T_g. The transition is not first order, like crystallization, since it is marked by smooth changes in the volume

and entropy (first derivates of the free energy). A schematic drawing of the different volume changes during crystallization and glass formation is shown in Figure 1.4. The glass transition may, thus, be a higher order transition, since these functions vary continuously through T_g; others propose that the transition arises from percolation, or a dynamical slowing-down transition. A full discussion of this topic is beyond the scope of this thesis, but a good overview can be found elsewhere [27].

In this work, T_g was measured using differential scanning calorimetry (DSC, described in detail in Chapter 2). Briefly, DSC measures the differential power required to heat a sample and a reference material, while maintaining both at the same temperature. In an ideal scanning, or nonisothermal, (see Chapter 2) DSC experiment, the measured signal is the specific heat of the sample as a function of temperature. From DSC measurements during heating of a glass, a sudden, but smooth, rise in the specific heat begins at T_g. With increasing temperature, a sharp exothermic event corresponding to crystallization, with an onset at the *crystallization temperature*, T_x, is observed. A typical DSC trace of differential power vs. temperature is shown in Figure 1.5. The volume and viscosity show strong temperature dependence above T_g, which imply the ability of the liquid to access many different configurational states (a liquid able to access all states is called *ergodic*) [28]. In a glass, the liquid state is frozen in, and the system is non-ergodic.

The glass transition is influenced by both kinetic and thermodynamic factors. The kinetic aspect of the glass transition is reflected in a cooling-rate dependence of some properties of the glass.

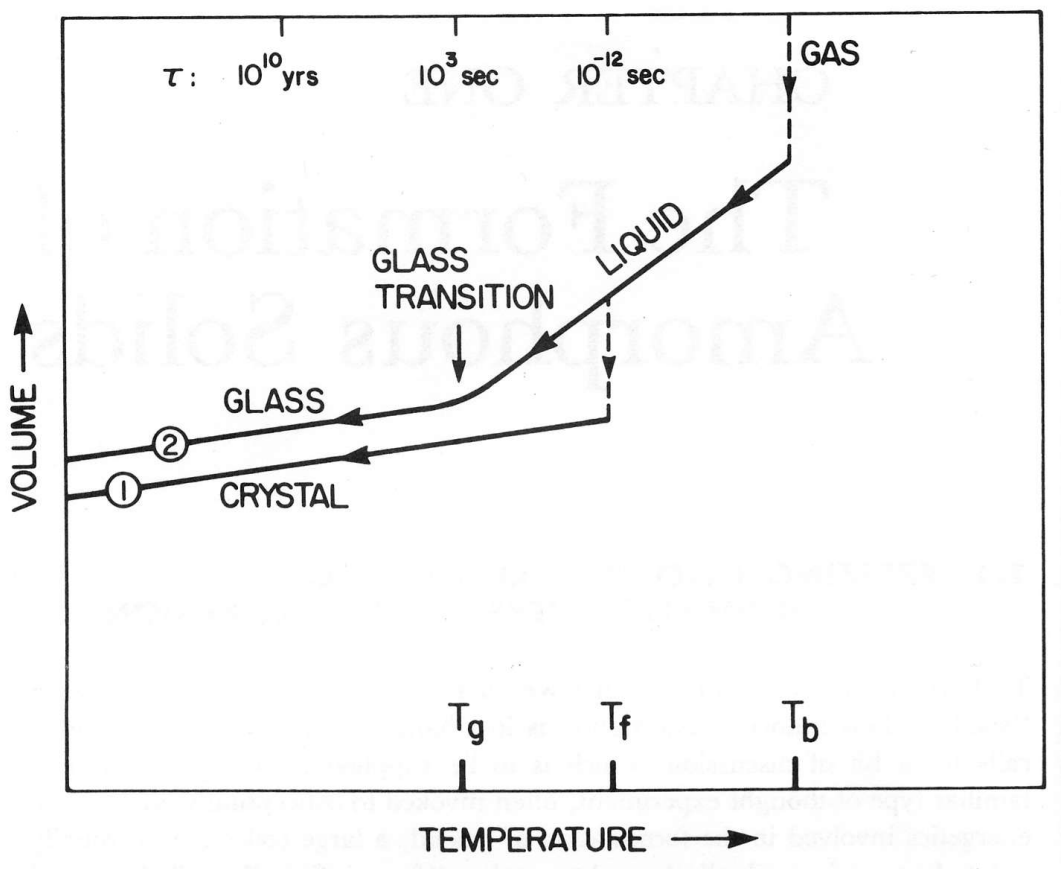

Figure 1.4 – A schematic representation of the volume of a liquid along different cooling paths; image from [6].

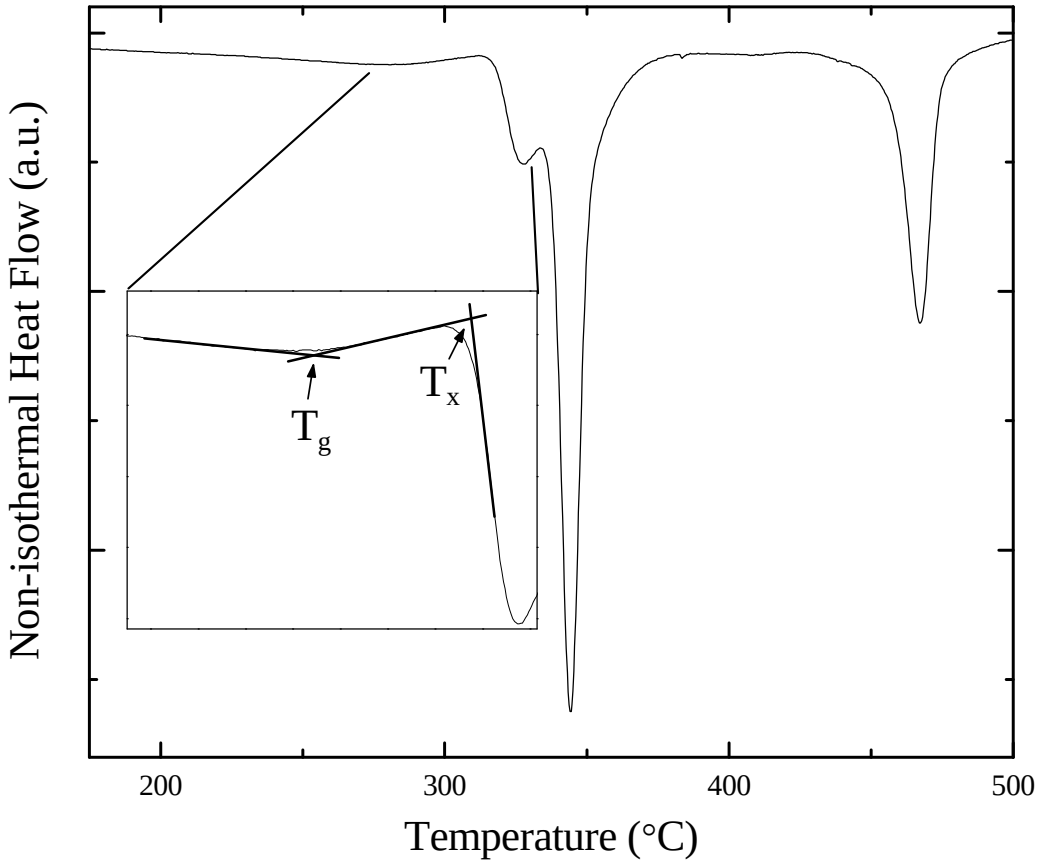

Figure 1.5 – The differential power measured from scanning (nonisothermal) DSC, showing the glass transition temperature, T_g, and the crystallization temperature T_x; image from [5].

Experimentally, T_g is lower for glasses prepared from the liquid with slower cooling rates, and higher for those with faster cooling rates, by a small amount (about 8°C for a factor of 5000 decrease in cooling rate [3]). For faster cooling rates, the timescale of the experiment is much less than the timescale of atomic rearrangement; a high-temperature liquid structure is frozen in. For slower cooling rates, the timescale of the experiment may approach the timescale of atomic rearrangement. A glass prepared with a slower cooling rate from the liquid will have higher density, ρ, and viscosity, η, and a lower T_g, than one with a faster cooling rate. This is evidenced by the phenomenon of *structural relaxtion*, where with annealing below T_g the atoms rearrange into the lowest energy state without crystallizing. Structural relaxation is characterized by a decrease in T_g, an increase in η, and an enhancement of the DSC signature of T_g [29].

The existence of a transition from a supercooled liquid to a glass was argued from thermodynamic grounds by Kauzmann in 1948 [30]. The entropy difference between the liquid and the crystal can be determined as a function of temperature from the enthalpy of fusion, measured at the melting temperature, and integrating the specific heat difference between the two phases; such data are shown schematically in Figure 1.6. The entropy difference can be described qualitatively as a difference in disorder. By extrapolating the specific heat of the liquid to lower temperature, a temperature is reached at which the excess entropy equals zero. This temperature is argued to define the ideal glass transition temperature, or Kauzmann temperature, T_k. A paradox becomes evident when considering glass formation. Below T_k, if no phase transformation has occurred in the liquid, the excess entropy will become negative, indicating the liquid has a lower entropy than the crystal. While appearing to be unphysical, this does not violate any of the laws

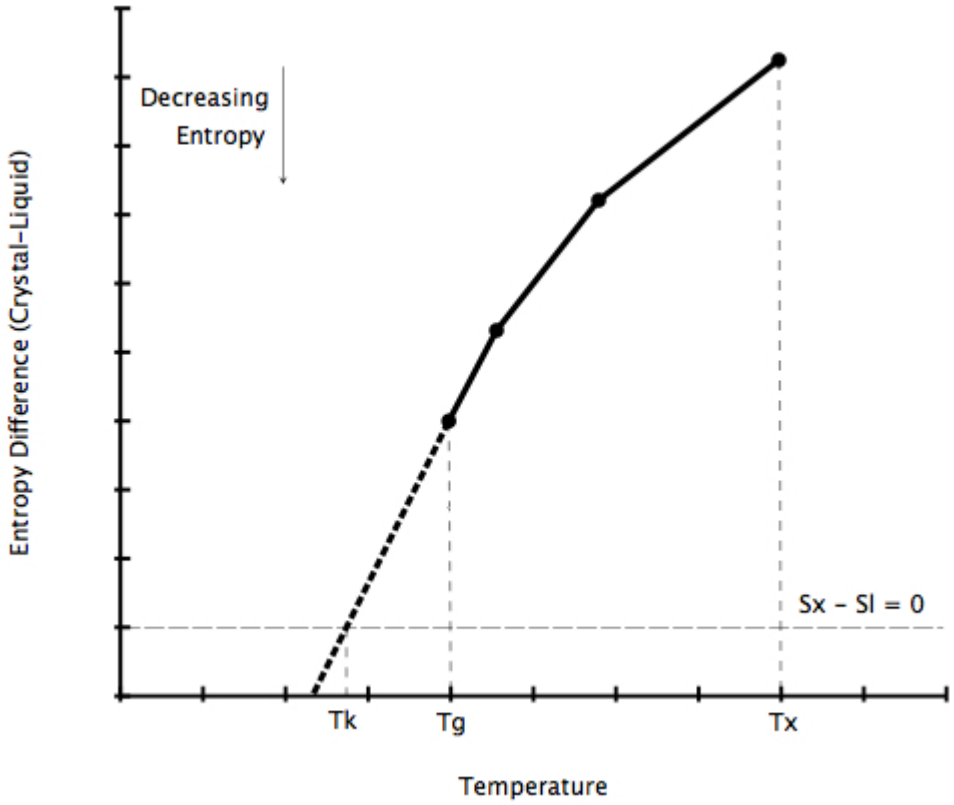

Figure 1.6 – A schematic drawing of the excess entropy between liquid and crystal phases, illustrating Kauzmann's paradox; the crystallization temperature is marked by T_x, the glass transition temperature T_g, and the Kauzmann temperature by T_k.

of thermodynamics. However, if the trend is continued to absolute zero, the liquid would have a negative entropy (since the entropy of a perfectly ordered crystal is zero), violating the Third Law. The Kauzmann paradox suggests that the glass transition is a true phase transition. In practice this ideal glass transition is inaccessible due to the kinetic effects already discussed.

1.5. Quasicrystals and rational approximants

As already discussed, crystals have long-range order (LRO) that is periodic and are *space-filling*, i.e. the unit cell will tile all space without gaps or overlaps. It can be shown that a crystal has periodic translational LRO if and only if it possesses 1-, 2-, 3-, 4-, or 6-fold rotational symmetry [31]. The diffraction pattern from a crystal contains sharp spots that exhibit the same symmetry as the crystal structure. In 1984 Schectman and others discovered a novel crystal phase in an Al-Mn alloy that showed a five-fold symmetry in its diffraction pattern [32]. These well-ordered solids without periodic translational symmetry challenged the long-standing definition of a crystal. This state was thus called a *quasicrystal* [33], and alloys have since been found that exhibit other "forbidden" symmetries, including 8-fold, 10-fold, and 12-fold symmetries. Following the initial discovery in Al-Mn, several stable icosahedral quasicrystal phases (i-phase) were discovered, including in a a ternary Ti-Zr-Ni alloy with 17 at.% Ni [34, 35]. Figure 1.7 shows a large i-phase grain with well developed pentagonal faces. These alloys showed promise for hydrogen storage applications (see Chapter 6). The i-phase and its rational approximants (RAs, to be defined later) are relevant to the work presented in Chapters 3 and 6, so the crystallography of quasicrystals will be reviewed briefly here.

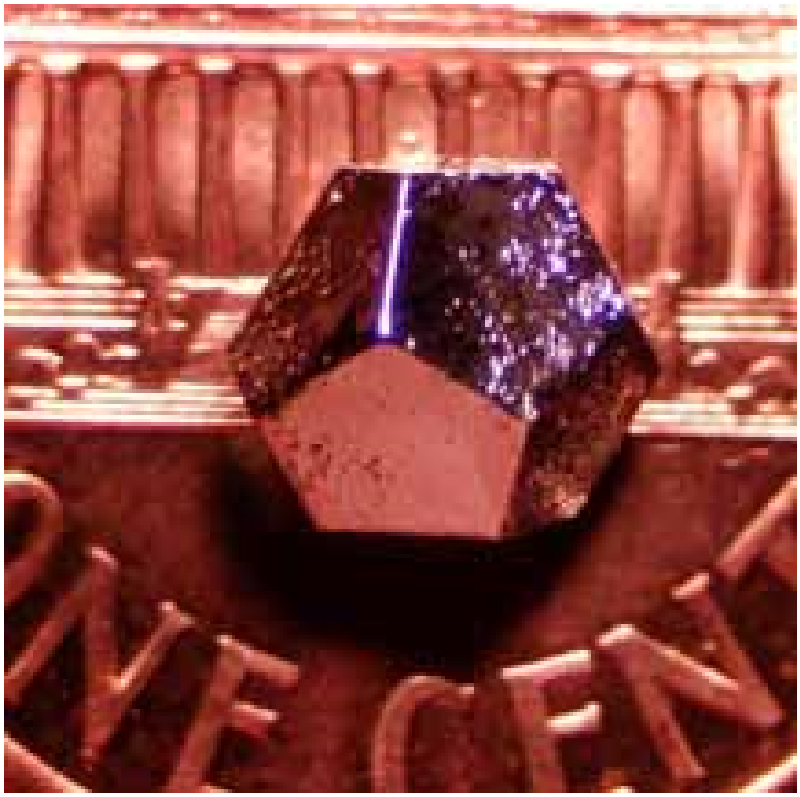

Figure 1.7 – A large quasicrystal grain showing well-developed pentagonal faces, placed on a penny for scale; image courtesy of Ames Laboratory.

The Fibbonaci sequence is an example of quasiperiodic order in one dimension. The familiar sequence gives the number n_i as a sum of the two previous numbers, i.e.

$$n_i = n_{i-2} + n_{i-1},$$

and the ratio of successive numbers in the sequence approaches the golden mean, i.e.

$$n_i / n_{i-1} \Rightarrow \tau = \frac{1+\sqrt{5}}{2} \approx 1.618\ldots.$$

Thus each point is well defined, but there is no periodic distribution. The Fibonacci sequence is also instructive in defining the golden mean, which is relevant to the study of the i-phase, since the number τ appears, e.g., in the scaling of its diffraction spots in TEM.

The method for indexing the diffraction peaks of a quasicrystal is different than for a crystal. A cut-and-project method is used to project a 6-dimensional cubic hyper-lattice onto 3 dimensions [36, 37]. It is impossible to visualize the hyper-lattice, so Figure 1.8 illustrates the projection of a 2-dimensional (2D) lattice onto 1 dimension. A line of arbitrary slope (marked $X_{\|}$) is placed over the 2D lattice, an acceptance window is defined (the two additional solid lines), and lattice points that fall within the acceptance window are projected onto $X_{\|}$. If $X_{\|}$ and the acceptance window have slope $1/\tau$, the resulting 1D quasilattice will have a Fibonacci sequence of repeating short and long distances. If the slope of the line is not exactly $1/\tau$, but rather a rational number approaching $1/\tau$, such as $(1/2)^{-1}$ or $(3/2)^{-1}$, the resulting structure is crystalline, and called a *rational approximant* (RA) to the quasicrystal. Such structures have been observed experimentally and shown to be distinct from quasicrystals [38, 39]. Selected area diffraction (SAD) patterns from a true i-phase and some crystal RA's are shown in Figure 1.9. Simulation methods can be used to distinguish a true i-phase from a RA [38].

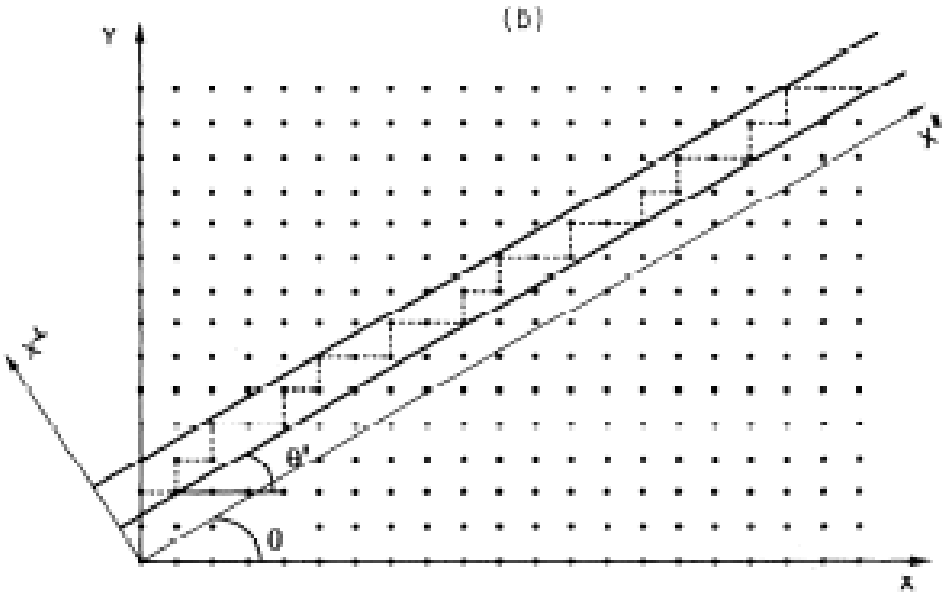

Figure 1.8 – The cut and projection method of a two-dimensional lattice onto a one-dimensional quasiperioid structure; image from [36].

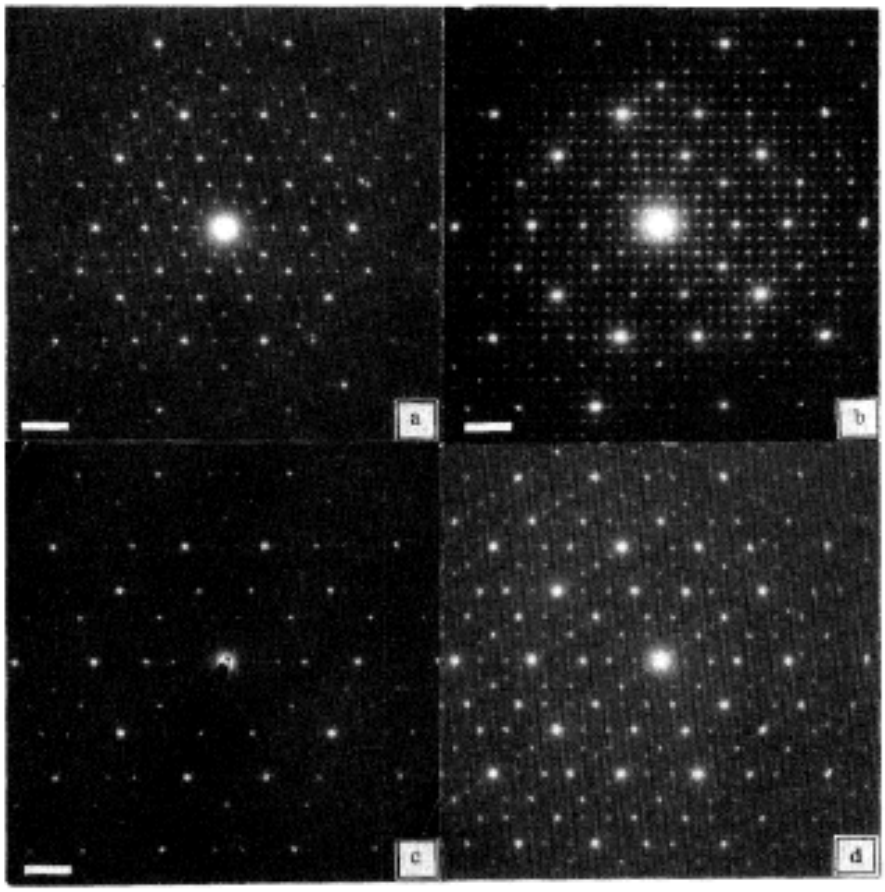

Figure 1.9 – The icosahedral fivefold and pseudo-fivefold patterns from selected area diffraction of a Ga-Mg-Zn alloy for (a) the i-phase, (b) the 3/2-2/1-2/1 side-centered orthorhombic phase along the [110] zone axis, (c) the 2/1 cubic phase along the [058] zone axis, and (d) the 2/1 rhombohedral phase along the [001] zone axis; the scale bar is $1Å^{-1}$; image from [36].

1.6. The classical theory of nucleation

Much of this dissertation work deals with an analysis of the solidification products of supercooled liquids (Chapters 3 and 4); the phenomenon of recalescence has already been introduced. In Chapter 5, the devitrification of Mg-based BMG's will be discussed. Therefore, it is instructive to review the theory of crystallization. This section presents the classical theory of nucleation (a complete review can be found elsewhere [40]).

In order for a crystal (daughter phase) to form from its parent phase (for the purposes of this thesis, either a liquid or glass), the first step is the creation of ordered regions that form the seeds of the crystal, from here on called *crystal nuclei*. The creation of these nuclei is thus called *nucleation*. The thermodynamic drive to nucleate the daughter phase is the difference in Gibbs free energy between the two phases, at the given temperature. The work required to form a daughter nucleus of *n* monomers from the parent phase is given by

$$W_n = n\delta\mu + \sigma A, \qquad (1.6.1.1)$$

where δμ is the free energy difference, σ is the interfacial free energy (the free energy of formation of the interface between the parent and daughter phases) per unit area, and *A* is the area of the interface. This expression illustrates the competing forces for nucleation. For example, in a supercooled liquid δμ equals zero at the melting temperature, and becomes negative with supercooling. The interfacial term is always positive, and thus competes with the δμ term.

For spherical clusters, Equation 1.6.1.1 becomes

$$W_n = n\delta\mu + (36\pi)^{1/3}\bar{v}^{2/3}n^{2/3}\sigma\,, \qquad (1.6.1.2)$$

where $\bar{v}$ is the molecular volume. The competition between the free energy (volume) and the interfacial (surface) terms as a function of cluster size (n) is illustrated schematically in Figure 1.10. From Figure 1.10, a maximum in the work of cluster formation can be found for a value of $n = n^*$, called the *critical cluster size*. Clusters smaller than the critical size are on averaging dissolving, and clusters larger than the critical size are on average growing. Calculating this maximum,

$$n^* = \frac{32\pi}{3\bar{v}}\frac{\sigma^3}{|\delta\mu_v|^3},$$

where $\delta\mu_v$ is the free energy difference per unit volume. By substituting this value into Equation 1.6.1.2, the work to form a critical cluster (the maximum work of cluster formation) is

$$W_{n^*} = \frac{16\pi}{3}\frac{\sigma^3}{\delta\mu_v{}^2}\,.$$

Cluster development is a stochastic process and, in a system such as a supercooled liquid at the beginning of recalescence or a glass near the crystallization temperature, clusters are dissolving and growing probabilistically. The probability of forming a nucleus of size n is proportional to a Boltzmann-type factor, i.e.

$$P_n \propto \exp(-\frac{W_n}{k_B T})\,,$$

where k_B is Boltzmann's constant.

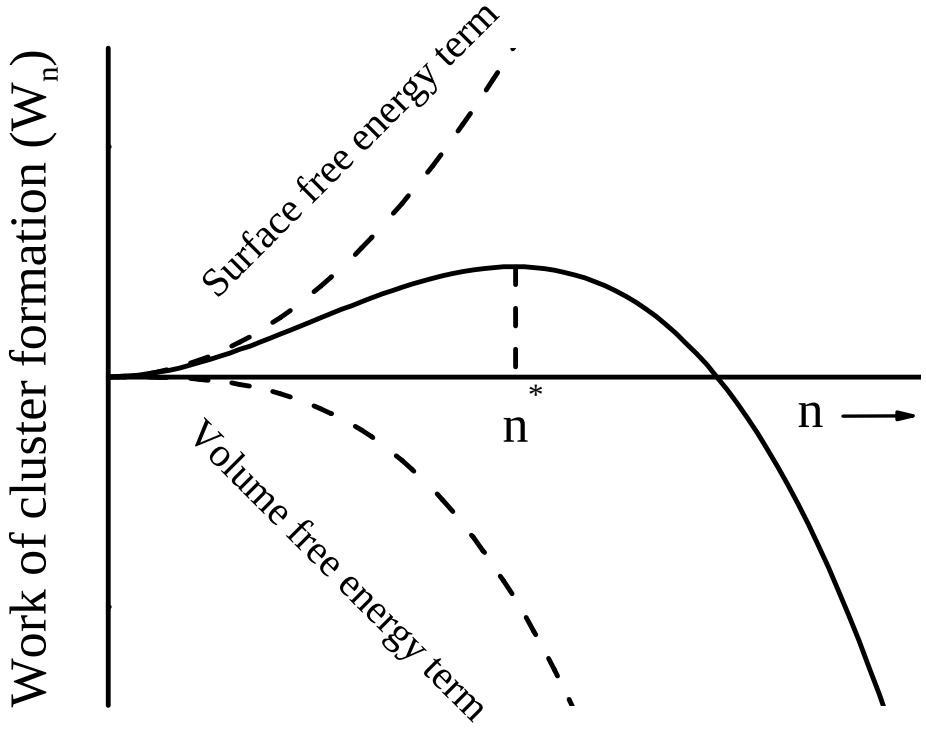

Figure 1.10 – A schematic illustration of the competing volume and surface free energy terms in the work of cluster formation; image from [5].

Volmer and Weber developed a kinetic theory of nucleation in 1926, wherein clusters grow or shrink by the addition or loss of monomers. This stochastic cluster development is expressed by a series of coupled differential equations, i.e.

$$\frac{dN_{n,t}}{dt} = N_{n-1,t}k_{n-1}^{+} - [N_{n,t}k_{n}^{-} + N_{n,t}k_{n}^{+}] + N_{n+1,t}k_{n+1}^{-},$$

where $N_{n,t}$ is the time- and size-dependent cluster density, and k_n^+ and k_n^- are the rates of monomer addition or loss, respectively. Figure 1.11 shows the evolving cluster density as a function of cluster size, based on the theory of Volmer and Weber. This method yields a time- and size-dependent nucleation rate, given by

$$I_{n,t} = N_{n,t}k_{n}^{+} - N_{n+1,t}k_{n+1}^{-}.$$

Volmer and Weber assumed the back-flux to be zero for clusters larger than the critical size. Becker and Döring argued for a steady-state distribution of clusters, giving, after some assumptions, a constant nucleation rate I^S of the form

$$I^S = A^* \exp\left[-\frac{W^*}{k_B T}\right],$$

where W^* is the barrier to nucleation of a critical cluster, and A^* is a dynamical factor describing the rate at which the cluster grows. An expression for A^* was determined by Becker and Döring, but its value in real systems is still debated.

The classical theory presented here is interface-limited; it cannot properly describe processes in which the concentrations of the initial and final phases are different. To include these effects, a model for time-dependent homogeneous nucleation that took into account the coupled fluxes of interfacial attachment and long-range diffusion was

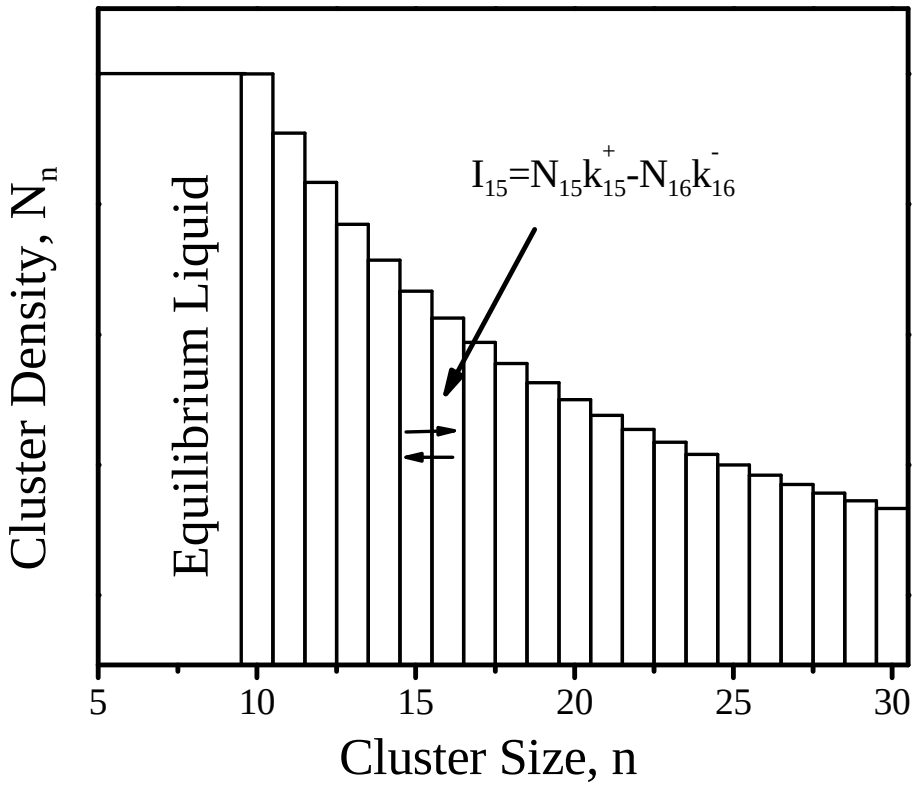

Figure 1.11 – A schematic histogram of cluster development from the kinetic theory Volmer and Weber; image from [40].

developed by Kelton [41]. This model may provide new insight into mechanisms for nanocrystal formation upon devitrification of metallic glasses, such as those discussed in Chapter 5.

Also important is the development of crystal nuclei following nucleation. The development can proceed as *growth*, which requires an increase in the total volume-fraction of crystalline material, or a *coarsening* process, in which larger grains grow at the expense of smaller grains, with no net volume-fraction transformed. A simple method using DSC has been proposed by Chen and Spaepen to discriminate between these processes [42], but the validity of their method is debated. A further, brief, discussion of growth mechanisms will be given in Chapter 5.

1.7. Structural modeling and characterization

As mentioned in §1.1, the goal of a diffraction experiment is to determine the atomic configuration of the system. This can be accomplished from theory, i.e. a model potential is developed and used to generate an atomic configuration, usually by approximating the fast-cooling needed to prepare a glass from a liquid, and a comparison is made between the simulated and experimental $g(r)$ or $S(q)$. Alternatively, the atomic configuration can be deduced by solving an inverse problem, i.e. given the experimental data, a configuration is generated to match. The former method describes a molecular dynamics (MD) simulation, with *ab-initio* potentials, the latter a Monte Carlo (MC) method. A detailed comparison of the two methods can be found elsewhere [11]. MD simulations with *ab-initio* potentials have been used in the study of liquids and glasses with some success [43], but limitations on computing power restrict the size of the system to perhaps a hundred atoms, and the time-scale for cooling to picoseconds. Here

a Reverse Monte Carlo (RMC) method was used. The atomic configurations generated by RMC were analyzed using two methods to quantify the order of the configuration. These techniques will be described in the following subsections.

1.7.1. Reverse Monte Carlo simulation for structural modeling

This section gives an overview of the RMC method developed by McGreevy and others; a full description is beyond the scope of this thesis and can be found elsewhere [44, 45]. A detailed description of the determination and optimization of the input parameters is provided in Chapter 2. RMC requires an initial configuration (here a random configuration was used) and the experimental data (either $S(q)$ or $g(r)$), along with some physical properties of the system and the FZ interaction coefficients (see §1.2). RMC implements a *rejection sampling algorithm*, using the goodness-of-fit, χ^2, as an analog to the energy in Metropolis Monte Carlo (MMC). In other words, a random move of an atom is made, and either accepted or rejected subject to the following conditions (where n corresponds to the nth move):

If $\chi_n^2 < \chi_{n-1}^2$, accept.

If $\chi_n^2 > \chi_{n-1}^2$, accept with probability $e^{\left[-\left(\chi_n^2-\chi_{n-1}^2\right)/2\right]}$,

Else, reject

The acceptance of some moves that increase χ^2 prevents the system from becoming "trapped" in a local minimum. An example RMC simulation fitting $g(r)$ for an amorphous system, along with schematic drawings of the corresponding configurations, is shown in Figure 1.12.

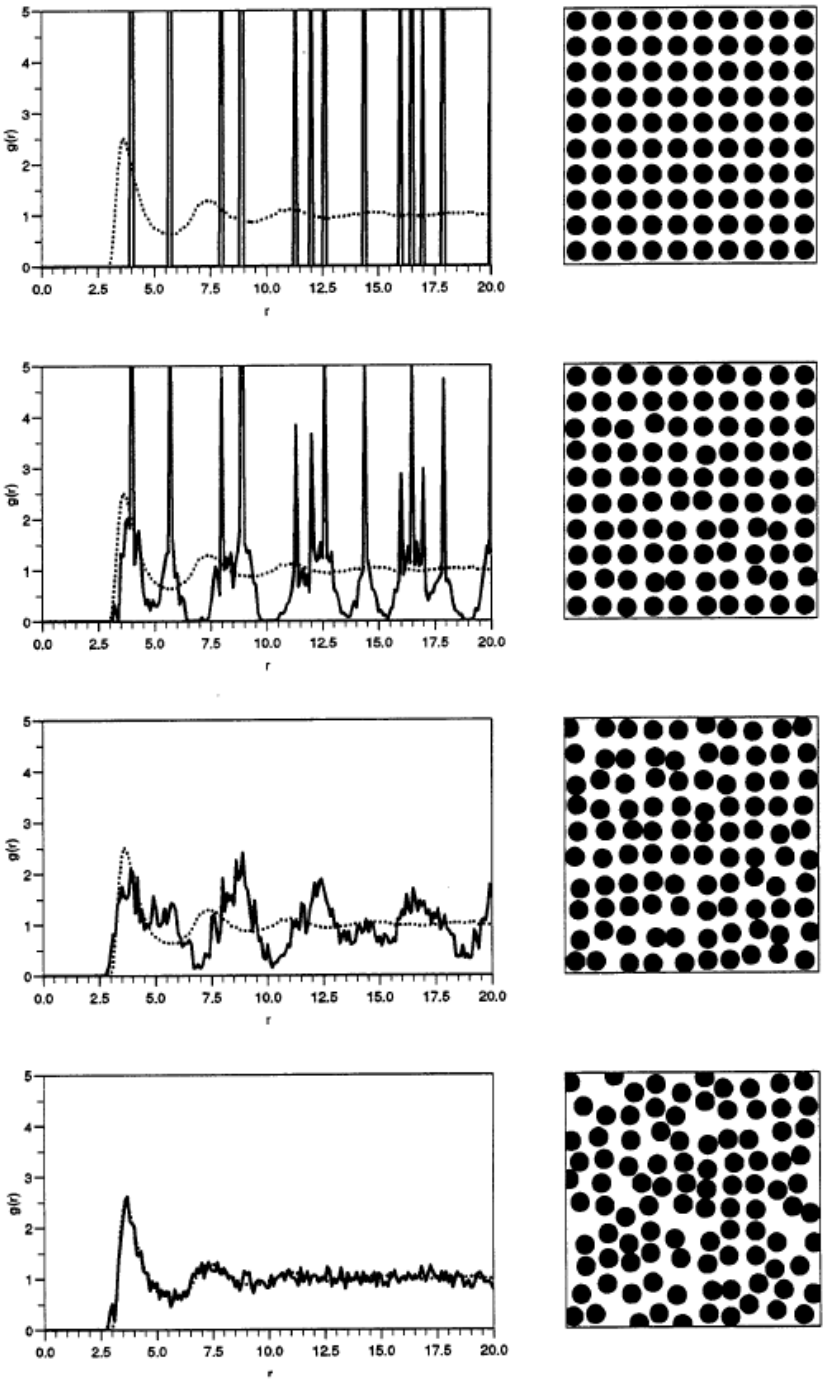

Figure 1.12 – An example of RMC fitting g(r) for an amorphous system, beginning from an initial configuration of a cubic lattice; image from [44].

From this method, RMC simulations determine a maximum entropy state of the system. RMC has received some criticism since, as already mentioned, a glass is a frozen-in state of the high temperature liquid, which is not necessarily a unique state. Thus, the configuration from RMC may not represent the exact configuration from experiment. This concern is lessened for liquids, where the measured liquid state is in fact a time-average of many possible states, since the system is ergodic. Despite this criticism, RMC is a useful tool in the study of non-crystalline systems, and in fact, as will be shown in Chapter 4, is able to capture subtle changes in the chemical order of supercooled liquids.

1.7.2. Characterization of modeled structures

The output of the RMC simulation is a model atomic configuration that produces a diffraction pattern matching the experimental data. To gather quantitative information on atomic ordering from the positions of thousands of atoms, further analysis techniques are needed. This section presents two similar, but complimentary methods used to characterize the model structures. These were the indexing scheme of Honeycutt and Andersen (HA index analysis, [46]) and the bond orientational order parameter (BOO) analysis of Steinhardt, Nelson, and Ronchetti [47]. For this work, both methods were implemented using software developed by Kim [22]. One additional method not discussed is the Voronoi polyhedral analysis, which has been applied to supercooled liquids, yielding some interesting results [43].

The HA index method analyzes the local configuration of a pair of atoms, called a *root pair*, and categorizes order of the group of atoms using a 4-digit indexing scheme. The first index represents the distance between atoms in the root pair, i.e. the

corresponding peak number in $g(r)$ (1 – nearest neighbors, 2 – next nearest neighbors, and so on). The second index is the number of atoms counted as neighbors to the root pair, the third index is the number of bonds between those neighbors, and the fourth index differentiates unique structures having the same first three indices. A visualization of the 1551 cluster (an icosahedral cluster) is shown in Figure 1.13.i. From this analysis, distorted or partially-formed clusters are measured. The analysis produces histograms of cluster frequency.

In the BOO parameter analysis, quadratic and third-order invariants are constructed from bond spherical harmonics for quantitative analysis. The quadratic invariant, Q_l is defined as

$$Q_l \equiv \left[\frac{4\pi}{2l+1} \sum_{m=-l}^{l} \left| \bar{Q}_{lm} \right|^2 \right]^{1/2},$$

where

$$Q_{lm}\left(\vec{r}\right) \equiv Y_{lm}\left(\theta\left(\vec{r}\right), \phi\left(\vec{r}\right)\right),$$

and

$$\overline{Q_{lm}} = \frac{1}{N_b} \sum_{bonds} Q_{lm}\left(\vec{r}\right).$$

The Y_{lm}'s are spherical harmonics; θ and φ are the polar angles of the bonds measured with respect to a reference coordinate system. Figure 1.13.ii shows the distributions of Q_l for five simple clusters. From that figure, it is evident that the icosahedral cluster is defined by the presence of $l = 6$ and $l = 10$.

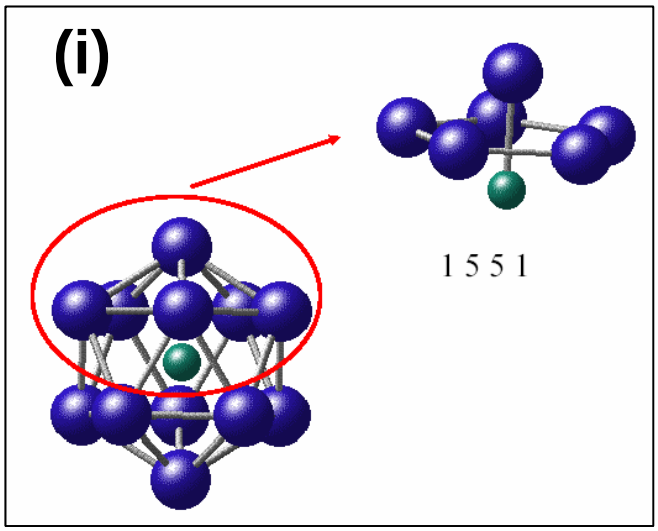

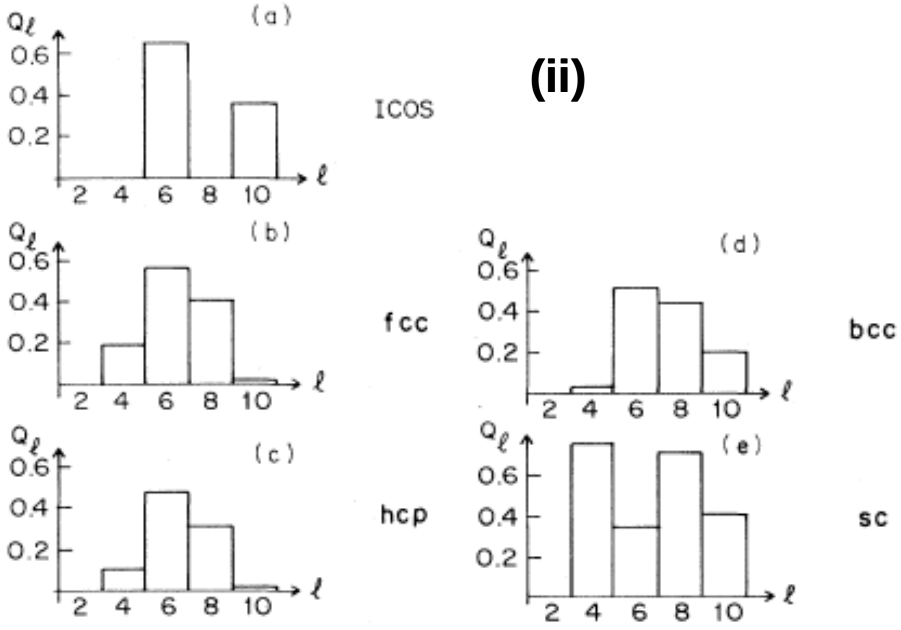

Figure 1.13 – The two analysis methods used for quantifying atomic configurations modeled by RMC: (i) a schematic drawing of an icosahedral cluster and the corresponding 1551-coordinated root pair, and (ii) the distributions of Q_l for five common fully-formed clusters detected by the BOO analysis.

As previously mentioned, icosahedral short-range order (ISRO) is common in glasses and supercooled liquids. The analysis for those phases is complicated somewhat by the presence of $l = 6$ and $l = 10$ in clusters other than the 13-atom icosahedral cluster.

These two methods are different in that the HA index analysis detects partially-formed or distorted clusters, while the BOO analysis is sensitive to more fully-formed clusters. The BOO method is comparable to the Voronoi polyhedral analysis used by Kramer and others to analyze the results of MD simulations [43], and the HA index method provides distinct and complimentary information about the configuration.

1.8. Summary and thesis overview

This introductory chapter presented an overview of the history, theoretical background, and methods for the study of liquids and glasses, in part to motivate this dissertation work and inform the following chapters. Specifically, the history, definitions, and phenomenology of liquids, metallic glasses, and quasicrystals were presented. The formalism of atomic order in non-crystalline systems was discussed, and the classical theory of nucleation was reviewed for its relevance to solidification of supercooled liquids and devitrification. Experimental techniques and simulation methods used throughout the rest of the thesis were also introduced.

A complete description of methods will be provided in Chapter 2, including detailed step-by-step procedures for running the computer simulations, supplemented by Appendices 1 and 2, which contain, in part, text of all software code and macros used to analyze diffraction data. Chapter 3 will present an analysis of phase formation and liquid structure with changing Hf concentration in $Ti_{45}Zr_{(38-x)}Hf_xNi_{17}$ alloys, and a previously measured phase formation boundary is explained using data from BESL and microscopy

methods. Chapter 4 will present and discuss measurements, also using BESL, of structural and chemical ordering in supercooled liquid Cu-Zr alloys, interesting for their ability to form binary BMGs when cast. These results represent possible experimental confirmation of cluster predictions from MD simulations of these liquids and glasses, which may influence the GFA. Chapter 5 will present a study on the devitrification mechanisms and a structure of some Mg-based BMG's, using TEM, high energy XRD, and DSC techniques. Chapter 6 will present results of hydrogen storage experiments in i-phase $Ti_{45}Zr_{38}Ni_{17}$, including descriptions of modifications to an existing apparatus and analysis techniques used to overcome some long-standing experimental difficulties. (The texts of computer codes/macros and detailed hardware specifications are given in Appendix 3.) Finally, Chapter 7 summarizes and concludes the thesis.

References

1. M. Reibold, P. Paufler, A. A. Levin, W. Kochmann, N. Patzke, and D. C. Meyer, Nature, 2006. **444**(7117): p. 286-286.
2. A. L. Greer, Science, 1995. **267**(5206): p. 1947-1953.
3. S. Schneider, J. Phys. Condensed Matter, 2001. **13**: p. 7723-7736.
4. A. M. Viano, E. H. Majzoub, R. M. Stroud, M. J. Kramer, S. T. Misture, P. C. Gibbons, and K. F. Kelton, Philosophical Magazine A, 1998. **78**(1): p. 131-142.
5. K. S. Bondi, *Analysis of the effects of microalloying on glass formation in Al-Y-Fe alloys by fluctuation electron microscopy*. 2009, Washington University.
6. R. Zallen, *The Physics of Amorphous Solids*. 1983, New York: John Wiley & Sons.
7. Y. Waseda, *The structure of non-crystalline materials*. 1980: McGraw-Hill.
8. C. Kittel, *Introduction to Solid State Physics*. 1995: Wiley.
9. B. E. Warren, *X-ray diffraction*. 1969: Addison-Wesley.
10. T. Egami and S. J. L. Billinge, *Underneath the Bragg peaks*. 2003: Pergamon.
11. D. Chandler, *Introduction to modern statistical mechanics*. 1987: Oxford.
12. D. G. Fahrenheit, Philosophical Transactions, 1724. **33**(381-391): p. 1-3.
13. D. Turnbull, The Journal of Chemical Physics, 1952. **20**(3): p. 411-424.
14. E. H. Brandt, Science, 1989. **243**(4889): p. 349-355.
15. L. L. Lacy, M. B. Robinson, and T. J. Rathz, Journal of Crystal Growth, 1981. **51**(1): p. 47-60.
16. M. B. Robinson, R. J. Bayuzickf, and W. H. Hofmeister, *Review of Drop Tube and Drop Tower Facilities and Research*, in *Space Commercialization*, F. Shahrokhi, G.A. Hazelrigg, and R.J. Bayuzick, Editors. 1990.
17. D. M. Herlach, Annual Review of Materials Science, 1991. **21**(1): p. 23.
18. W.-K. Rhim, S. K. Chung, D. Barber, K. F. Man, G. Gutt, A. Rulison, and R. E. Spjut, Review of Scientific Instruments, 1993. **64**(10): p. 2961-2970.
19. A. K. Gangopadhyay, G. W. Lee, K. F. Kelton, J. R. Rogers, A. I. Goldman, D. S. Robinson, T. J. Rathz, and R. W. Hyers, Review of Scientific Instruments, 2005. **76**(7): p. 073901.
20. K. F. Kelton, G. W. Lee, A. K. Gangopadhyay, R. W. Hyers, T. J. Rathz, J. R. Rogers, M. B. Robinson, and D. S. Robinson, Physical Review Letters, 2003. **90**(19).
21. F. Frank, Proceedings of the Royal Society of London Series A, 1952. **215**(43).
22. T. H. Kim, *Structural Study of Liquids*. 2007, Washington University: St. Louis.
23. W. H. Zachariasen, Journal of the American Chemical Society, 1932. **54**(10): p. 3841-3851.
24. W. Klement, R. H. Willens, and P. O. L. Duwez, Nature, 1960. **187**(4740): p. 869-870.
25. H. W. Kui, A. L. Greer, and D. Turnbull, Appl. Phys. Lett., 1984. **45**(6): p. 615-616.
26. A. Peker and W. L. Johnson, Appl. Phys. Lett., 1993. **63**(17): p. 2342-2344.

27. P. G. Debenedetti and F. H. Stillinger, Nature, 2001. **410**(6825): p. 259-267.
28. R. W. Cahn and A. L. Greer, *Metastable states of alloys*, in *Physical Metallurgy*, R.W. Cahn and P. Haasen, Editors. 1996, Elsevier Science: North Holland. p. 1723-1830.
29. A. L. Greer, *Amorphous Phases*, in *Intermetallic Compounds - Principles and Practice*, J.H. Westbrook and R.L. Fleischer, Editors. 1995, John Wiley and Sons: Chichester. p. 731-754.
30. W. Kauzmann, Chem. Rev., 1948. **43**: p. 219.
31. C. Kittel, *Introduction to Solid State Physics*. 1996: John Wiley and Sons.
32. D. Shechtman, I. Blech, D. Gratias, and J. W. Cahn, Physical Review Letters, 1984. **53**(20): p. 1951.
33. D. Levine and P. J. Steinhardt, Physical Review B, 1986. **34**(2): p. 596.
34. K. F. Kelton, W. J. Kim, and R. M. Stroud, Applied Physics Letters, 1997. **70**(24): p. 3230-3232.
35. K. F. Kelton, A. K. Gangopadhyay, G. W. Lee, L. Hannet, R. W. Hyers, S. Krishnan, M. B. Robinson, J. Rogers, and T. J. Rathz, Journal of Non-Crystalline Solids, 2002. **312-314**: p. 305-308.
36. A. I. Goldman and R. F. Kelton, Reviews of Modern Physics, 1993. **65**(1): p. 213.
37. V. Elser, Physical Review B, 1985. **32**(8): p. 4892.
38. V. T. Huett, *The Formation, Structure, and Hydrogen Storage Properties of Ti/Zr/Hf Based Quasicrystals and Related Phases*. 2004, Washington University: St. Louis, Missouri.
39. F. Spaepen, in *Quasicrystals*, M.V. Jaric and S. Lundqvist, Editors. 1990, World Scientific.
40. K. F. Kelton, Solid State Physics - Advances in Research and Applications, 1991. **45**: p. 75-177.
41. K. F. Kelton, Journal of Non-Crystalline Solids, 2000. **274**(1-3): p. 147-154.
42. L. C. Chen and F. Spaepen, Journal of Applied Physics, 1991. **69**(2): p. 679-688.
43. S. G. Hao, M. J. Kramer, C. Z. Wang, K. M. Ho, S. Nandi, A. Kreyssig, A. I. Goldman, V. Wessels, K. K. Sahu, K. F. Kelton, R. W. Hyers, S. M. Canepari, and J. R. Rogers, Physical Review B (Condensed Matter and Materials Physics), 2009. **79**(10): p. 104206-7.
44. R. L. McGreevy, Journal of Physics: Condensed Matter, 2001. **13**: p. R877-R913.
45. R. L. McGreevy and L. Pusztai, Molecular Simulation, 1988. **1**(6): p. 359-367.
46. J. D. Honeycutt and H. C. Andersen, Journal of Physical Chemistry, 1987. **91**: p. 4950-4963.
47. P. J. Steinhardt, D. R. Nelson, and M. Ronchetti, Physical Review B, 1983. **28**(2): p. 784.

Chapter 2

Experimental and analysis methods

The experiments performed for this work required reproducible preparation of alloy samples and careful use of characterization techniques for thermal properties and microstructures of alloys. High energy x-ray diffraction was used to probe the structures of liquids and glasses at the atomic scale, and simulation and modeling methods were used to characterize the resulting atomic structures. In this chapter, the experimental methods for most of the work discussed in later chapters will be presented. Methods that are specific to only one study will be discussed in the respective chapters. This chapter also provides instructions for analysis of the high energy x-ray diffraction data, with supporting information and the text of scripts and macros used for automated analysis provided in Appendices 1 and 2.

2.1. General sample preparation

Reproducible sample preparation is necessary for study of the physics of materials. For this work, metastable solid phases, such as glasses and quasicrystals (see definitions in Chapter 1) were often prepared. The procedure, processing environment, and cooling rates were controlled as much as possible.

2.1.1. Preparation of alloy ingots by arc-melting

High purity (99.99% or greater, unless specified) metals were purchased from Alfa Aesar. The primary impurities were typically other transition metals. The purity of

the Hf or Zr used was 99.7%, with nominal 0.3% Zr in Hf and nominal 0.3% Hf in Zr. All elements were stored in vacuum (~30 mtorr) until the time of use, and the exposure time to the atmosphere was minimized. Commercial stock and lot numbers for all of the source elements used were recorded. (The particular source material can affect properties of the sample, as will be discussed later for the oxygen content of Zr.)

A target total mass of 0.5-1.0g was used in alloy preparation. The mass of one constituent was fixed, and the others determined from it. Constituent alloy elements were massed using a Mettler Toledo AB54-S/FACT balance with +/- 0.05mg accuracy. In this dissertation, all alloy compositions are given in atomic percent (at.%), as opposed to weight percent (wt.%), unless indicated.

Alloy ingots were prepared by arc-melting the constituent elements on a water-cooled Cu hearth in an evacuated chamber. The arc-melting apparatus, depicted in Figure 2.1, consists of the Cu hearth and a water-cooled wand with a tip made from a Tungsten rod, which was cut and ground to a sharp point. The wand was electrically connected to a Miller Syncrowave 250 constant current AC/DC arc welding power source. To initiate the arc, the circuit between the tip and the generator was closed using a foot pedal, and the arc formed between the tip and the hearth. The arc was directed above the sample to heat and achieve melting. In this setup, the tip could be removed and was occasionally re-ground to a point if the arc became diffuse or erratic.

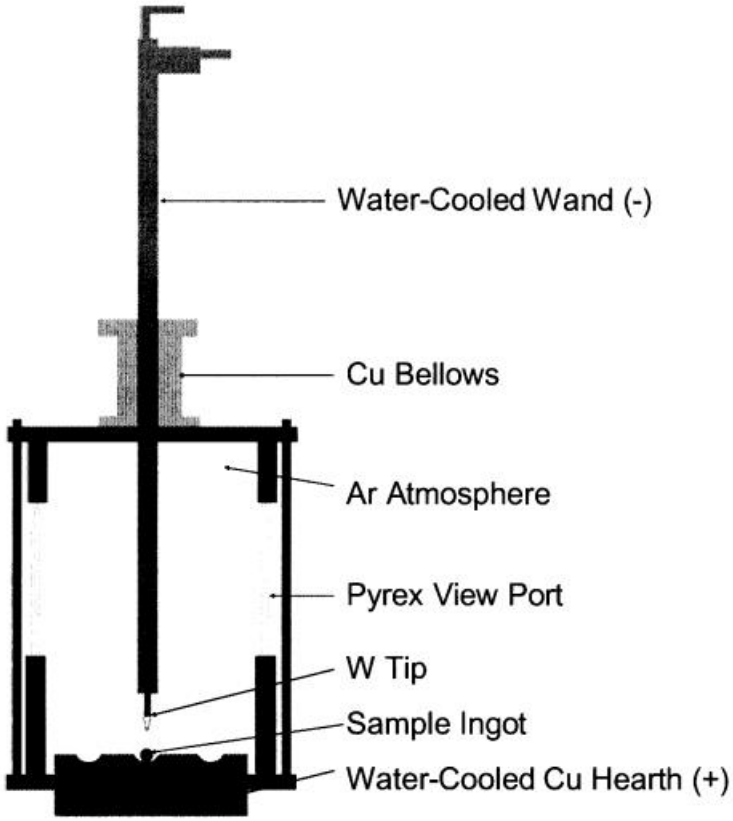

Figure 2.1 – The arc-melting apparatus (image from [2]).

To limit oxygen contamination during arc-melting, the chamber was first evacuated using a mechanical pump, and back-filled with high purity (99.998%) Argon gas. The evacuation/back-filling cycle was repeated a minimum of 3 times until the final pressure was 10-20mtorr. To further purify the chamber atmosphere, a 1g ingot of $Ti_{50}Zr_{50}$ (a getter) was melted first to remove any remaining oxygen. Initially the arc was struck on the Cu hearth and then moved onto the getter for a minimum of 30 seconds, until it was completely melted. Whenever the arc was initiated, the getter was first melted before melting any sample. If the getter turned black or multicolored, this indicated poor vacuum or an excess of oxygen, and processing was stopped. Elements were stacked, with those with the highest melting temperature at the top to encourage complete mixing. Sometimes alloys were prepared in stages if they contained elements with a wide range of melting temperatures.

The typical current used for melting was 40-60 amps depending on the highest melting temperature element, and the arc was typically held on the sample for 10-30 seconds; the wand was moved while holding the arc on the sample to improve mixing. Cooled ingots were flipped using the wand and re-melted; to ensure complete mixing this was repeated 3 times. The final mass of the ingot was recorded after arc-melting and compared against the initial sum the constituent masses. Throughout this dissertation there will be references to samples "as-cast" by arc-melting. This refers to samples prepared by the above procedure and allowed to cool on the Cu hearth, which provided cooling rates on the order of 100K/s.

2.1.2. Quenching by melt-spinning

For many alloys, the desired metastable phases will only form from the liquid with cooling rates of order 10^5-10^6 K/s. Such rapid cooling is called quenching, and precludes the use of simple casting methods (cooling rates of 10-100 K/s), including from the water cooled hearth used in arc-melting, to prepare samples in these phases. For this work, the melt-spinning process was used for quenching samples.

After arc-melting, ingots were transferred to a graphite crucible prepared from a 1cm diameter graphite rod (R.W. Elliot & Sons, Inc.), which had been hollowed, using a lathe, to a wall thickness of 1mm and had a 1mm opening drilled into the bottom. The crucibles were cleaned by sonication in ethanol and heated for 5 minutes under vacuum by an oxy-acetylene torch, to remove contamination, before the sample was loaded. The crucible containing the sample was then loaded into a quartz tube, which was placed in the quenching chamber, depicted in Figure 2.2.

When in place in the quenching chamber, one end of the quartz tube was connected to a tank of high purity (99.998%) Argon gas at 16PSI, isolated by a solenoid valve. The other end of the quartz tube, containing the crucible, was in a radio frequency (RF) induction heating coil powered by a Lepel T-10-3-KC-HW RF generator. The quenching chamber contained an 8” Cu wheel that was rotated by an AC motor, which was powered by a Variac. The chamber atmosphere was purified by repeated evacuation and back-filling cycles. After evacuating/back-filling for at least 3 cycles, the chamber was filled with argon to approximately 10mmHg vacuum; the gas was necessary to allow cooling of the motor.

An IRCON UX-10 optical pyrometer was mounted above the quartz viewing window and used to measure the temperature of the sample. An RF power near 60% of full scale was sufficient to achieve complete melting of the samples discussed in this thesis. Once samples were completely melted, the wheel speed was increased to the desired value by adjusting the Variac; the wheel speed was measured in RPM by an optical detector inside the chamber. The sample melt was ejected onto the spinning wheel by opening the solenoid valve. To minimize exposure of the melt to oxygen or other atmospheric contaminants, this procedure was followed as quickly after melting as possible. The melt cooled rapidly during contact with the spinning wheel and the solidified sample was ejected, either into the long trunk or onto the bottom of the chamber. Long, thin ribbons of the quenched alloy were produced.

2.2. Basic characterization methods

As-prepared (quenched or cast) samples were analyzed by various methods to determine microstructure and thermal properties. These techniques were most often used to confirm the presence or purity of a desired phase, rather than for detailed analysis. In some cases experiments were performed using these methods to determine properties of the sample, such as the specific heat by using differential scanning calorimetry (DSC, for the Mg-glasses discussed in Chapter 5). Those methods will be discussed in their respective chapters, but the basic operation methods detailed here were the same.

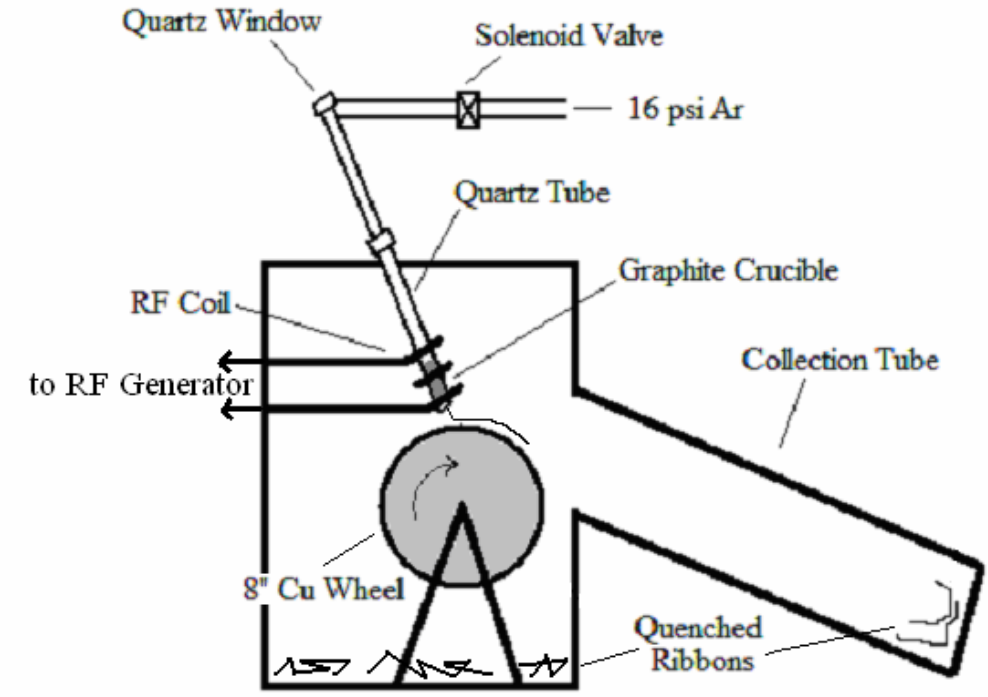

Figure 2.2 – A Schematic diagram of the apparatus used for quenching by melt-spinning.

2.2.1. Differential scanning calorimetry and differential thermal analysis

Differential scanning calorimetry (DSC) measurements were made on the as-prepared samples, using a Perkin Elmer DSC7, to determine transformation enthalpies and phase transition temperatures. In DSC, the differential power between the sample and a reference is measured while a computer-controlled furnace maintains a set heating rate (for a scanning, or *nonisothermal*, measurement), or temperature (for an isothermal measurement), as a function of temperature or time, respectively. During a phase transition in DSC, the integrated differential power is equal to the enthalpy of transformation. Unless otherwise noted, the heating rate used for nonisothermal scans was 20K/s. Representative plots of the differential power measured for these two types of measurement are shown in Figure 2.3.a-b. As discussed in Chapter 1, a nonisothermal scan provides the glass transition temperature, T_g, and the crystallization temperature, T_x, while data from an isothermal scan provide information on the nature of the transformation process. In this work, 6-12 mg sample was found to yield a good signal in this instrument.

For samples with high vapor pressures (such as those discussed in Chapter 5), special Al sample pans (Perkin Elmer part #02190062) were used, which were hermetically sealed by a crimping anvil (Perkin Elmer part #02190061) to avoid deposition of harmful vapor on the DSC sample holder assembly.

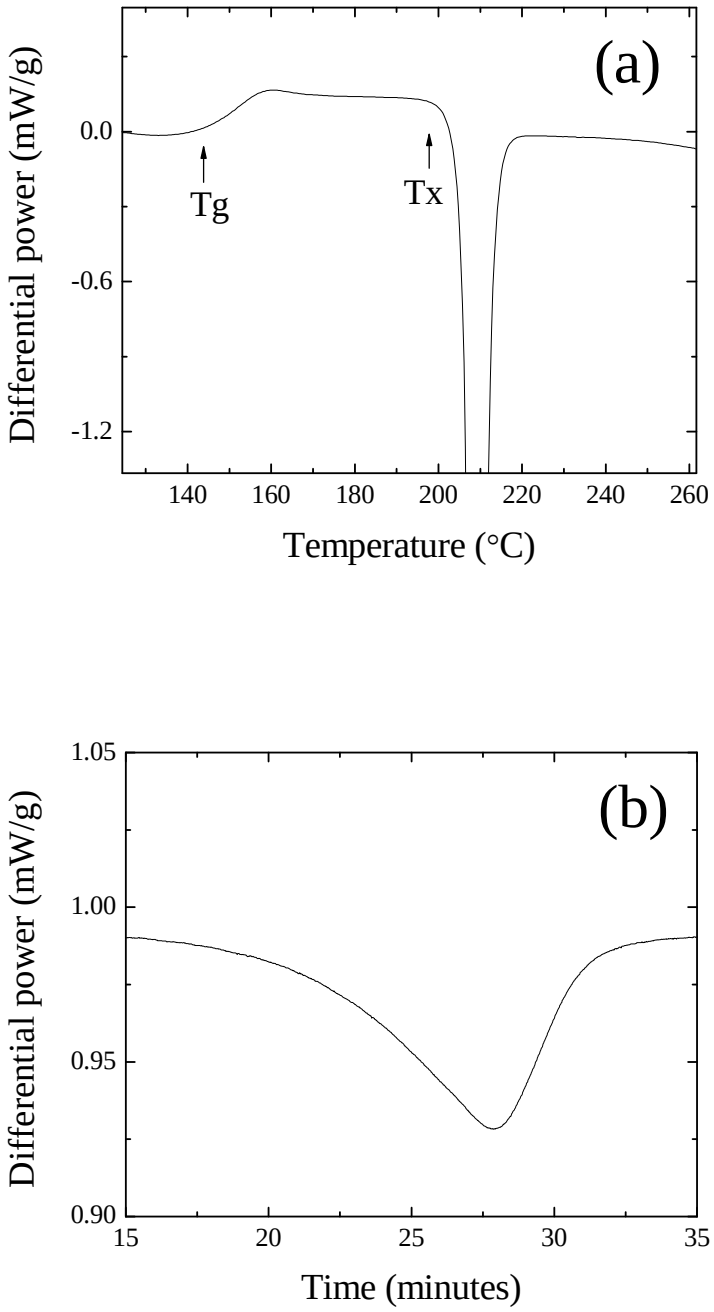

Figure 2.3 – The differential power from DSC in (a) a typical nonisothermal scan, with the glass transition and crystallization temperatures labeled by T_g and T_x, respectively, and (b) a typical isothermal DSC scan showing crystallization of a glass with a well resolved peak in the measured signal.

Differential thermal analysis (DTA) was used to determine the liquidus temperature (the temperature of complete melting) of alloys using a Setaram Labsys DTA/DSC. DTA is similar to DSC, but in DTA the sample and reference pans are heated/cooled identically by a common external furnace and the temperature difference between the sample and reference is measured. Samples for the DTA measurements were prepared by first filling a small ceramic crucible to about 1/3 of capacity with alumina (Al_2O_3) powder. The sample was then pressed into the powder and the crucible filled completely. The sample was completely surrounded by the powder and did not touch the walls of the crucible, or the liquid sample would adhere to the crucible wall. A reference was prepared by filling an identical ceramic crucible with alumina powder. During operation, the DTA furnace was purged with high purity (99.998%) Ar gas at 36PSI and cooled with room-temperature water at 40 PSI. The Setaram DTA used did not have programmable calibration, but rather instrument offset was determined by measuring standards, and the offset recorded and used to correct measured data. Thus, it was important to routinely measure the differential temperature signal for Ag (melting point 1235K) and Ni (melting point 1726K) to determine these offsets over a wide range of temperature.

2.2.2. Low energy x-ray diffraction

Sample structures were analyzed from x-ray diffraction (XRD), with a Rigaku Geigerflex diffractometer in a reflection geometry with a Cu K-α x-ray source (λ = 1.5418 Å). Whenever possible, samples were powdered and the powder adhered to a glass slide using a small amount of petroleum jelly. Samples that could not be powdered

were either adhered to a glass slide with a small amount of petroleum jelly, or were taped to an open aluminum slide to minimize the background contribution from the glass slide. Care was taken to arrange the ribbon sample such that the same side of each ribbon was facing up. The sides of the ribbon are unique; those that were in contact with the wheel had a matte finish, while those that were away from the wheel were more lustrous. The side touching the wheel was studied by XRD, because the cooling rates there would be fastest.

2.2.3. Microscopy methods

Microstructural characterization beyond that obtained from XRD was performed using scanning electron microscopy (SEM) and transmission electron microscopy (TEM). SEM recreates the surface topography of the sample from scattered or emitted electrons to generate an image with a large (on the order of micrometers) depth of field. TEM is performed in transmission geometry on thin samples, and the resulting micrographs provide 2-dimensional projections of 3-dimensional structures. Both techniques allow for spectroscopy and diffraction experiments. Complete technical details and discussions of advanced techniques in SEM and TEM are beyond the scope of this thesis, but may be found elsewhere [1, 2].

2.2.3.1. Scanning electron microscopy

Micrographs of as-prepared or heat-treated (annealed) sample surfaces were made with scanning electron microscopy (SEM), with a resolution on the order of 10nm, using a JEOL JSM-7001LVF FE-SEM. Experiments discussed in this thesis were performed in either secondary electron imaging (SEI) or backscattered electron (BSE) mode. In SEI

mode the microscope raster-scans the area of interest with the electron beam and measures the intensity of low energy (<50eV) electrons emitted after inelastic scattering of the incident beam, to recreate an image of the sample topography. In BSE mode, electrons backscattered from the sample surface by elastic scattering are measured at the detector. SEI mode is useful for measuring topology, BSE composition (BSECOMPO) mode detects regions of differing composition.

Energy dispersive spectroscopy (EDS) was performed using an Oxford EDS apparatus coupled to the SEM. In EDS, electrons in the atoms of the sample are excited by the incident beam out of the ground state into higher energy levels, creating holes in the lower energy levels, which are then filled by outer electrons that "fall" into the lower energy state. This results in the emission of characteristic x-rays that vary for different elements, which are measured by an x-ray detector to create a spectrum for the sample.

2.2.3.1.1. Sample preparation

Samples for SEM were prepared by a combination of grinding and etching in an acid solution. Spherical samples from levitation studies (discussed in §2.3.2) were first attached to an aluminum post using Crystalbond 509 mounting adhesive. Crystalbond 509 has a softening temperature around 70°C, which makes it ideal for mounting and un-mounting alloy samples without substantially heating them. The post was first heated to the desired temperature on a hot plate, and a small amount of adhesive applied to the post until it flowed. The sample was then placed in the adhesive, allowed to thermally equilibrate, and a small amount of adhesive applied around the edge of the sample for added stability. The sample was then ground flat on one end by a sequence of grinding papers of 180, 400, 600 and 1000 grit, respectively. Grinding was finished on a powered

grinding wheel using 1 micrometer alumina slurry followed by 0.3 micrometer alumina slurry. Samples were then etched for 2 minutes in a solution of 10% Hydrofluoric acid, 30% Nitric acid, and 60% distilled water.

2.2.3.2. Transmission electron microscopy

Micrographs and diffraction measurements were made using transmission electron microscopy (TEM) on a JEOL 2000FX and a JEOL JEM-2100F. The former was used for basic characterization and diffraction studies; it has an image resolution limit of 3.1 Å, which allows Fourier transform (FT) determination of diffraction patterns with a limit of wave vectors less than 1 $Å^{-1}$, which is not suitable to capture the dominant order in the diffraction pattern. The latter was used for high resolution microscopy, having a resolution limit of 2 Å, which enables FT diffraction patterns to be calculated with wave vectors up to about 3 $Å^{-1}$, which is suitable to observe the dominant order. Both microscopes were operated in TEM imaging mode, and aligned and calibrated following the standard guidelines for the instrument. During imaging studies on the JEOL 2000FX, the CCD was routinely calibrated to correct for burn-in of previously measured, intense features. For the diffraction studies, images were obtained on film from selected area diffraction (SAD) using a range of exposure times above and below that suggested automatically by the instrument control computer based on the maximum intensity. In SAD measurements, the aperture that covered the region of interest with the least contribution from other areas was chosen.

2.2.3.2.1. Sample preparation

For TEM it is necessary to prepare thin samples that are electron transparent typically on the order of 100nm thick or less. All samples for TEM discussed in this dissertation were prepared from ribbons produced by the melt-spinning process discussed in §2.1.2. Samples were prepared in either of two ways: milling by a focused ion beam, or powder preparation. All samples were placed on Cu TEM grids purchased from Structure Probe Incorporated (SPI).

The ion-milling was performed on either a Gatan model 600 dual ion mill or a Gatan model 691 precision ion polishing system. The model 600 mill had a liquid nitrogen cooling system, which cooled the sample during milling and reduced the effects of sample heating from the ion beam. The model 691 mill used a lower energy and a more focused beam for shorter periods of time. For some samples the former provided better thinning, for some the latter, and for some a combination of the two was used. The specific thinning sequence for a particular sample will be noted in the respective chapters. Both milling systems operated under high vacuum (10^{-6} torr). Milling on either system was performed in two steps, a longer-time milling step at 20 degrees until a visible hole was produced, and a shorter polishing step at 12 degrees to smooth and further thin the edges of the milled section. Milled ribbon samples were mounted on 3mm Cu 50/50 folding double TEM grids (SPI part #2510C).

A powder method was used for brittle samples, for which ion-milling was not possible. Samples were powdered using a mortar and pestle and the powder deposited onto a holey carbon grid, i.e. a 100 mesh Cu grid that was treated to contain a thin, perforated coating of C (SPI Inc.). The holey carbon grid was shaken in the sample powder to achieve a good coating. Sufficiently small sample pieces that adhered near a

perforation on the C coating were examined using TEM. This method may not capture the bulk structure, as only the small grains that adhere to the grid are imaged.

2.3. Electrostatic levitation (ESL)

A major portion of this dissertation work is focused on determination of liquid structures and physical properties. As discussed in Chapter 1, levitation methods were developed to measure the properties of liquid samples in a high vacuum environment in the absence of crucibles or container walls. For this dissertation work, electrostatic levitation (ESL) was used to make these measurements on deeply supercooled liquids. In §2.4.3, modifications to the ESL method that facilitated high energy x-ray diffraction of levitated liquids *in-situ* will be discussed. That method is called Beamline Electrostatic Levitation (BESL), and comprises much of the work presented in this thesis.

2.3.1. Apparatus

The ESL apparatus is a high vacuum chamber (10^{-8} torr, generally achieved using a turbomolecular pump) containing an electrode assembly for levitation of charged samples in an electrostatic field (0-2 MV/m), and access ports that facilitate experiments for measurements of temperature, density, surface tension, and viscosity of the liquid. The original apparatus design was by Rhim and others at the Jet Propulsion Laboratory at the California institute of technology [3], and further improvements were made by Rulison, Watkins, and Zambrano at Space Systems/LORAL [4]. The latter design was adopted and applied by Rogers and others at NASA Marshall Space Flight Center (MSFC), Huntsville, AL [5]. Very recently an ESL apparatus has been built in the Laboratory for Materials Physics Research at Washington University in St. Louis.

However, all of the experiments discussed in this dissertation were performed in 2007 using the ESL apparatus of Rogers at NASA MSFC.

A diagram of a typical ESL is shown in Figure 2.4, and a picture of the facility at Washington University is shown in Figure 2.5. Levitation is achieved by a pair of z-axis electrodes and four x-y positioning electrodes, all computer-controlled using a fast, active feedback control system with input from position-sensitive detectors (PSDs), which detect the sample position by measuring the shadow cast by low-power positioning lasers. In the NASA MSFC facility used for this work, the levitated sample was stable to within 50μm. Charge was maintained on the sample via the photoelectric effect from a UV lamp, which did not significantly heat the sample. Controlled heating was achieved from a laser; for the NASA MSFC facility a 50W Nd:YAG laser was used. More complete discussions of the hardware and software principles and design are given elsewhere [3, 4].

2.3.2. Sample preparation for levitation studies

Samples for levitation studies were prepared by arc-melting as described in §2.1.1. Approximately 0.5g ingots were made and broken into smaller pieces, which were then re-melted, at a lower current setting, to produce 1-2mm diameter spheres with masses between 20-60mg depending on the sample density. Each sample used in ESL was preserved and cataloged for further study. The source material after preparation of the small ingots for levitation studies was also preserved. Samples were cataloged using the naming/numbering system shown in Figure 2.6. In the experiments performed in collaboration with NASA MSFC, samples were also assigned a designation of the form STL###. For example, the sample BESL074203 of Figure 2.6 was also designated STL913.

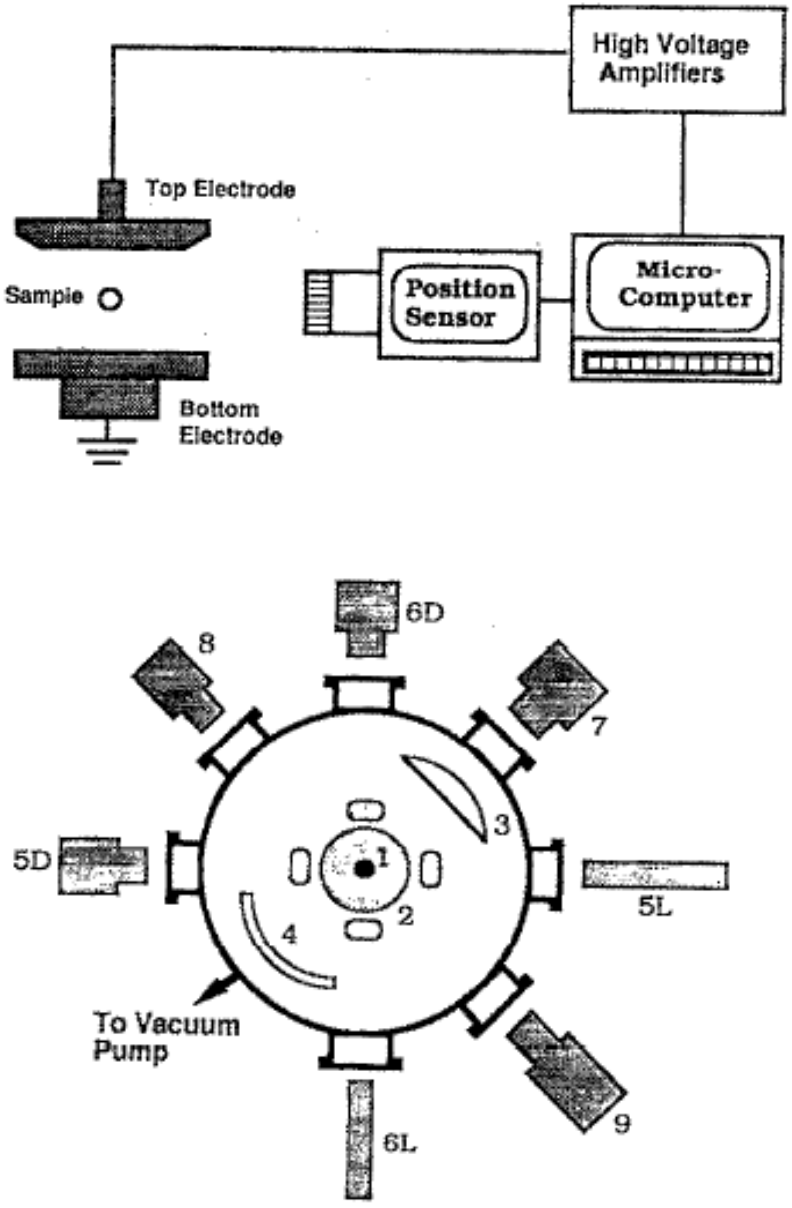

Figure 2.4 – A schematic diagram of the z-axis levitation electrodes and sample positioning system (top) and a top-view schematic diagram of the viewports and x-y positioning electrodes for a typical ESL setup (bottom); images taken from [3].

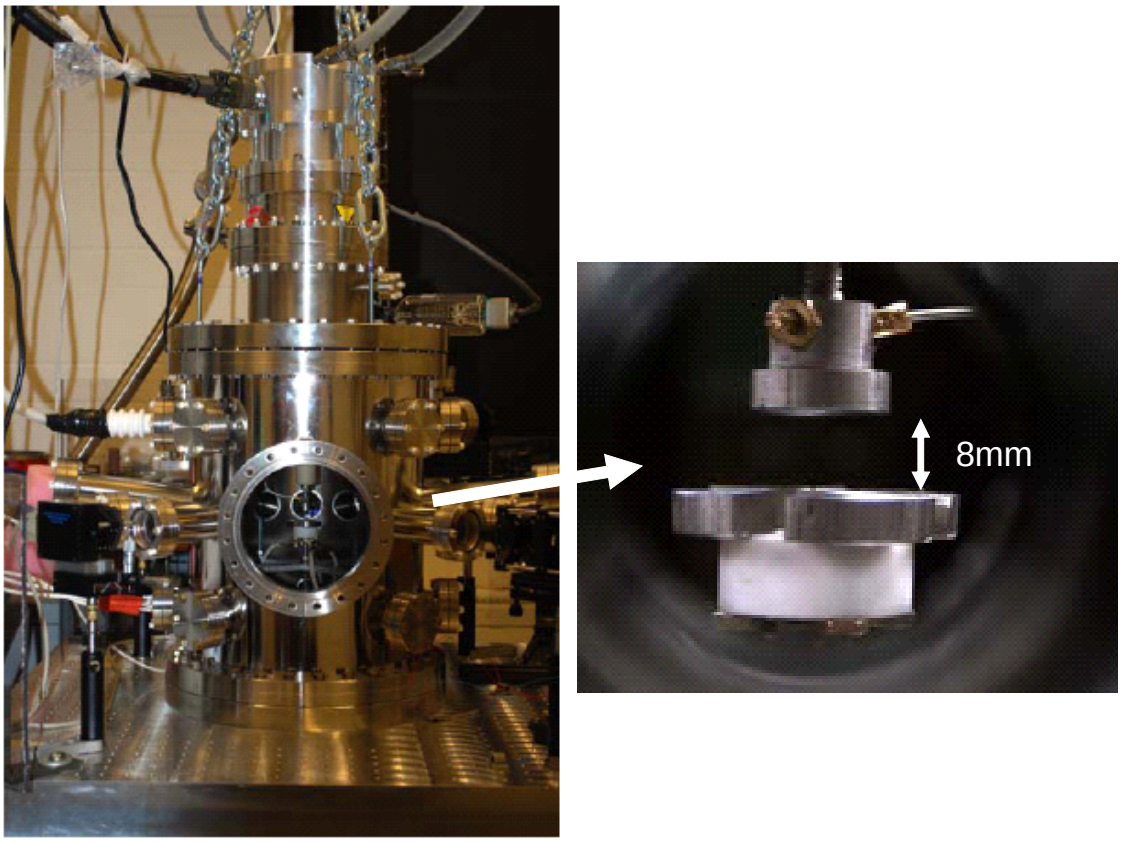

Figure 2.5 – An image of the ESL chamber at Washington University and a magnified image of the levitation electrode assembly; images courtesy of N.A. Mauro.

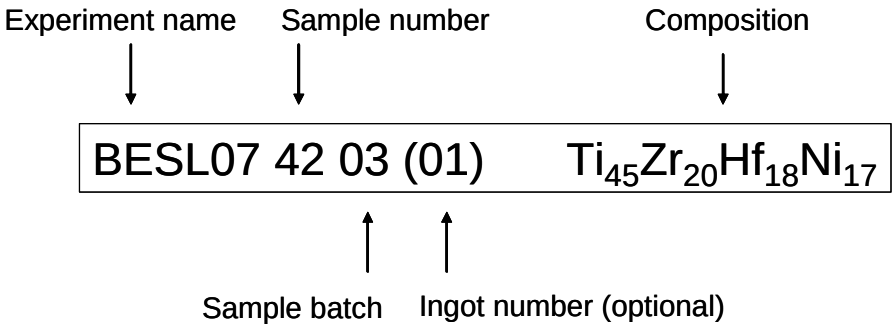

Figure 2.6 – The cataloging scheme used for May 2007 and August 2007 levitation experiments.

2.3.2.3. Oxygen and impurity content in starting materials

Oxygen analysis was performed on a number of samples as-cast and after processing in the ESL/BESL. The analysis was performed by Dr. Matthew J. Kramer at Ames Laboratory, Ames, Iowa, USDOE using a Leco TC400C inert gas fusion analyzer. ESL experiments performed in 2003 by T.H. Kim revealed a dependence of supercooling and formation of the quasicrystal phase on the elemental Zr used in sample preparation. Oxygen analysis was performed on some alloys studied here, and on the elements used in their preparation. The results of the oxygen analysis for the Zr used in preparation of Ti-Zr-Ni alloys by Kim in 2003 (Alfa Aesar lot # D10N23, stock# 42558) and the new stock used for this work (lot 826 prepared by Ames Lab in 2007) showed an increased oxygen content (304ppm) for the Zr used in 2003 over that used in 2007 (202ppm). Thus, an increase in oxygen for the Zr that facilitates icosahedral phase formation was observed, which suggests that oxygen concentration plays a role in formation of the quasicrystal phase; this should be considered in future ESL/BESL sample preparation.

2.3.3. Data collection and analysis

Thermo-physical property data were collected on liquid alloy samples using ESL. Temperature measurements were made as a function of time using an optical pyrometer during heating and cooling of the sample. Such measurements from pyrometers require the total hemispherical emissivity, ε_t, which is, in principle, a temperature dependent quantity $\varepsilon_t(T)$. Ideally, $\varepsilon_t(T)$ can be measured by a technique based on laser reflectivity using rotating analyzer ellipsometry [6]. For this work, such a measurement was not

possible, and $\varepsilon_t(T)$ was assumed to be a constant, which is a reasonable approximation [7]. The particular values of the constant varied for each metal or alloy, and were determined where possible by comparison of the measured melting temperature to a previously measured or published value.

Bulk density measurements were made using the improved photographic edge-fitting and integration technique developed by Bradshaw and Hyers, described in detail elsewhere [8, 9], by R.W. Hyers and S. Canepari using a high resolution video camera, which captured a continuous image of the liquid sample during cooling. The data were analyzed at the University of Massachusetts, Amherst. The known mass measured before processing was divided by the volume, determined from the edge-fitting and integration procedure, to give the density of the liquid. Mass losses due to evaporation affected the density measurements. If the sample was processed multiple times at a high enough temperature, a uniform shift in the observed density-temperature curve was observed for each processing cycle. For most experiments performed here, mass losses were negligible, and were ignored unless otherwise noted in the text.

2.4. High energy x-ray diffraction of liquids and glasses

Diffraction experiments were made on alloy liquids and amorphous solids using high energy x-rays from a synchrotron light source at the 6ID-D beamline of the Advanced Photon Source (APS) at Argonne National Laboratory (ANL). The APS is a third-generation synchrotron source providing high energy, high brilliance x-rays from a storage ring of greater than 350 meter diameter.

Storage rings like this one at the APS maximize flux (number of photons per second passing through a defined area) and brilliance (a measure of the intensity and directionality of an x-ray beam). Higher flux is beneficial for experiments that use the entire, unfocused beam and higher brilliance is beneficial for experiments requiring a focused beam, such as diffraction in BESL. As of this writing, the APS provides the most brilliant x-rays available for research in the western hemisphere.

Two types of diffraction experiments using synchrotron x-rays are described here: diffraction studies from fixed-position solid samples, such as metallic glasses prepared by the melt-spinning technique (described in §2.1.2) or slices of bulk metallic glasses, which will be referred to as 'stationary' diffraction studies, and studies of liquids and the resulting solids using the BESL.

2.4.1. General data collection and reduction methods

The methods for data reduction for both stationary diffraction studies and studies in BESL have some commonality, and this section presents the methods that apply to both. The intensity of the diffracted beam was measured on a flat-plate detector. For the stationary studies a MAR3450 image plate was used; for the BESL studies a GE Revolution 41-RT amorphous Si flat panel detector was used. The basic procedure in either configuration, after the desired alignment of the sample was achieved, was to open the x-ray shutter to allow diffraction from the sample, then expose the detector for a specified amount of time and retrieve the intensity data from the detector in ASCII format. Experiments of either type were performed in a transmission geometery, i.e. the incident beam impinged on one side of the sample and the Laue diffraction cone was measured on the other. Stoppage of the transmitted beam is an important technical consideration.

Details of the beam-stop mechanism for each configuration will be discussed later in this chapter.

The integrated intensity measured at the detector face as a function of scattered wave vector, $I^{meas}(q)$, was determined using the program Fit2D (Figure 2.7), a general purpose, freeware data analysis program [10]. More details of this step, including macros used for data processing, are given in Appendix 1. The total liquid structure function $S(q)$ was generated from $I^{meas}(q)$ by first correcting for the scattering intensity from the sample chamber background,

$$I^{corr}(q) = I^{meas}(q) - I^{BG}(q)$$

The background subtraction for BESL 2007 data was performed as part of a pre-processing step using batch processing scripts, details of which are also provided in Appendix 1. *S(q)* was generated from the corrected intensity as

$$S(q) = \frac{\beta I^{corr}(q) - I_{eu}^{in}(q) - f(q)^2}{f(q)^2},$$

where the scale factor β is defined by

$$\beta = \frac{\xi(1-\gamma)}{PA},$$

where ξ is a detector-specific scaling to convert to electron units, γ is a multiple-scattering term, P is the polarization factor, and A is an absorption correction given by

$$A = (t/\cos(\theta))\exp(-\mu t/\cos(\theta)),$$

where t is the thickness, μ is the mass-absorption coefficient (obtained from standard tables), and θ is half the scattering angle. The incoherent Compton scattering is given by

$I_{eu}^{in}(q)$ [11], and *f(q)* is an atomic form factor [12]. *g*(*r*) was calculated by Fourier transform (see Chapter 1).

The analysis program PDFgetX2 [13] was used to generate *S*(*q*) and *G*(*r*). The software IDL Virtual Machine (VM) is necessary to run PDFgetX2, and was installed alongside it. PDFgetX2 has many adjustable parameters, and some degree of empirical optimization of variables was needed for the particular experiments. The values of these parameters used, and the method for optimization of *S*(*q*) and *G*(*r*) using PDFgetX2, for all analyses discussed in this work, are provided in Appendix 1. One important note is the possibility of error introduced by applying the oblique incidence and x-ray polarization corrections in both Fit2D and PDFgetx2; it is important to make these corrections in only one of the programs, not both. This was found to be a major source of error when applied improperly. In this work, the correction was made in Fit2D (see macros of Appendix 1).

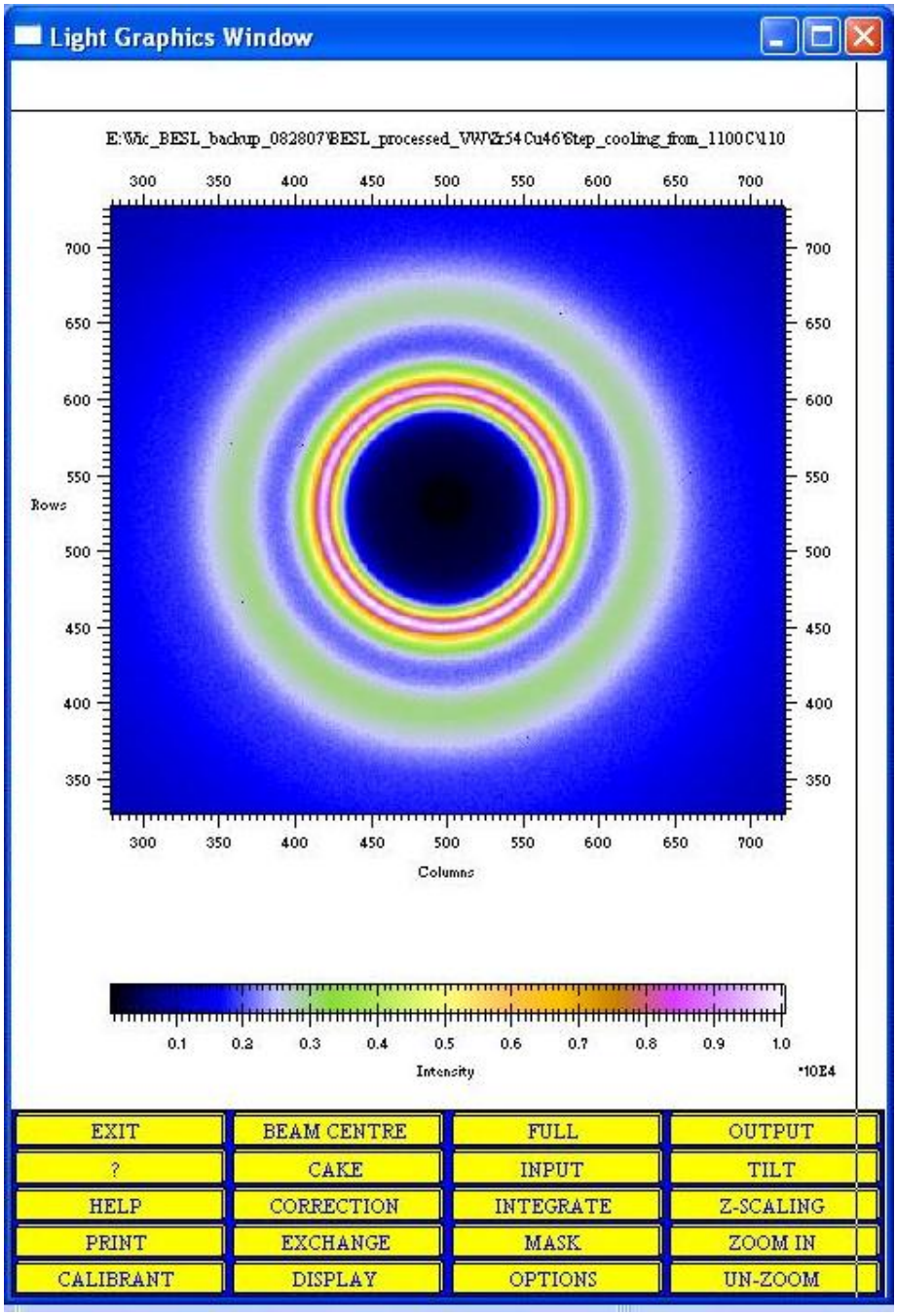

Figure 2.7 – A Fit2D data processing window with an image of the measured intensity at the detector face for representative liquid scattering data.

2.4.2. Stationary diffraction methods

This section provides an overview of the method for stationary diffraction; details for particular samples will be presented in the respective chapters. Ribbon samples produced from the melt-spinning technique discussed in §2.1.2 were prepared on 1" x 1" x 1/16" aluminum slides with half-inch circular openings by stacking (for brittle ribbons) or wrapping the sample (for ductile ribbons). A total thickness of 1-2 mm was desired. For some samples a powder technique was used, in which a thicker (1/8") slide with a small (3mm) opening was filled with the sample powder and sealed on either end with Kapton tape. Samples of bulk metallic glasses (BMGs) were prepared by first slicing the ingots on a diamond saw (South Bay Technologies model 650), polished with 600 grit sandpaper to achieve a smooth surface, and then mounted on an Al slide similar to that used for ribbons.

To reduce the contribution to the background intensity due to x-ray scattering from air molecules, a beam flight path was designed and built to provide an evacuated path for the incident and diffracted beam, as shown in Figure 2.8. It consisted of a sample chamber, outfitted with a small goniometer on a moveable sled for optimal positioning of the sample, and a large cylindrical chamber for the diffracted cone. The output end was closed with a 1/8" thick polycarbonate exit window with an 8mm cylindrical Tungsten beam-stop, placed outside the chamber at the center of the window, which was machined with a cupped end to trap the stopped beam and prevent edge-effect scattering. The entire chamber was evacuated using a scroll pump to roughly 100mtorr.

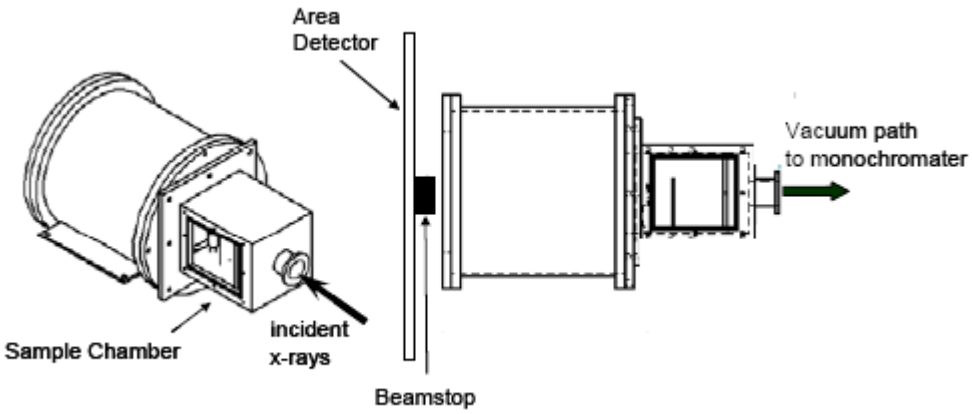

Figure 2.8 – A schematic drawing of the flight path used in the stationary diffraction studies.

The geometry of the cylinder and entrance and exit openings was designed to achieve scattering in the range from 0.8 to 18 $Å^{-1}$ for 100keV beam energy. This was calculated from the relation

$$q = \frac{4\pi \sin\theta}{\lambda}, \tag{2.5.1}$$

where q is the scattered wave vector and θ is half the scattering angle. In the example, depicted schematically in Figure 2.9.a, the incident beam travels through the flight path and scatters off the sample at **A**, the Laue diffraction cone emerges along with the transmitted beam, which are stopped by the container wall at **B**, and the finite thickness beam-stop at **C**, respectively. The angle formed between the rays **AC** and **AB** is defined as twice the angle θ, which was used with Eq. (2.5.1) to determine the maximum available q-range. The position of the sample (i.e. the length of the ray **AC**) could be adjusted somewhat using the sled built into the sample holder assembly (not shown). This provided an adjustable parameter when aligning the sample to empirically achieve a better signal at the detector. The minimum q accessible was similarly calculated using Equation 2.5.1, with respect to the finite thickness of the beam-stop, which blocked part of the low-q portion of the scattered beam, as shown in Figure 2.9.b.

The flight path is equipped with adjustable legs to achieve alignment on all axes, i.e. pitch, roll, and yaw. It is important to align the flight path, in part so that the x-ray beam is centered on the beam-stop. Edge effects and scattering from the beam-stop can contribute to the background intensity measured on the detector for lower values of q.

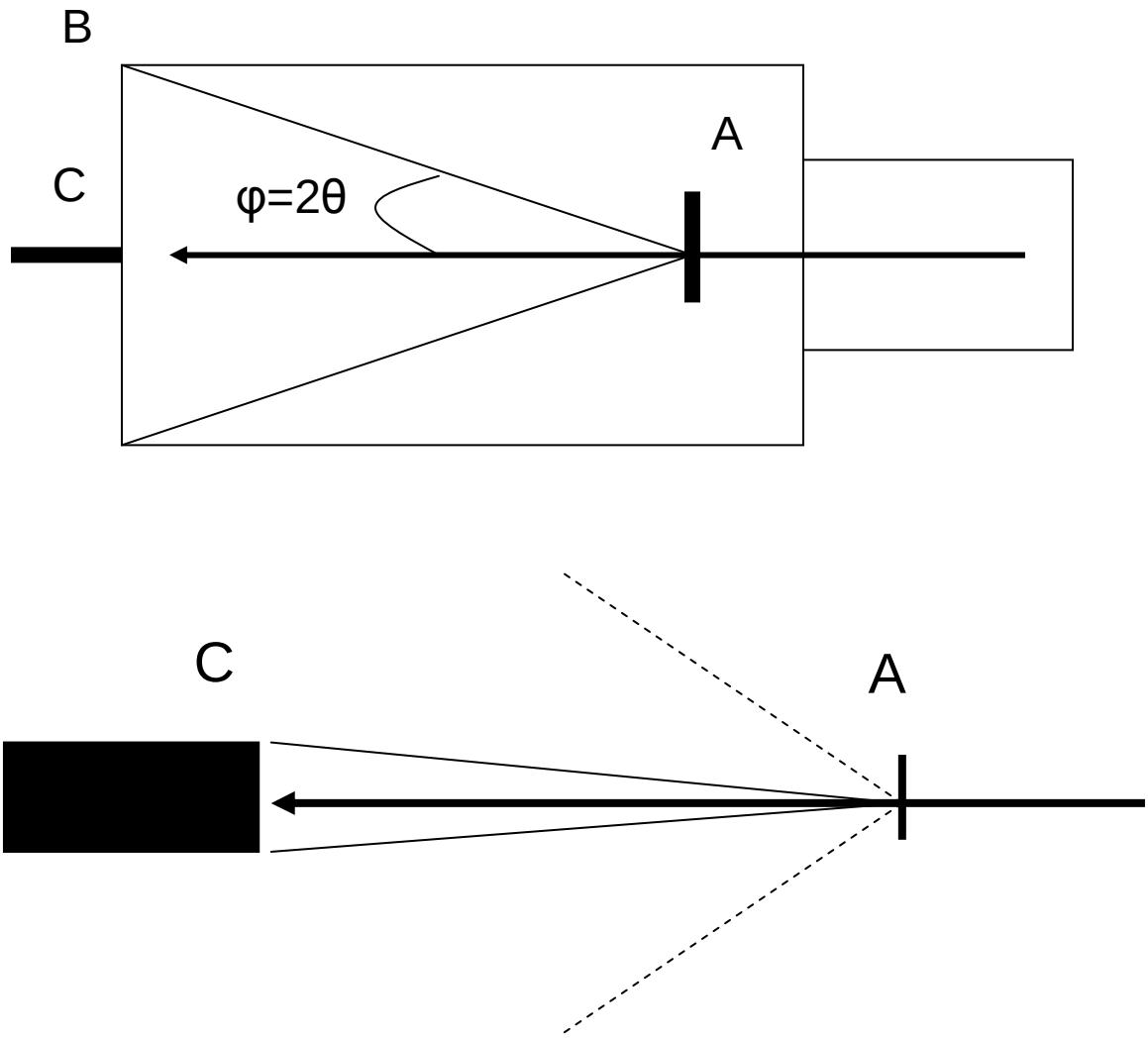

Figure 2.9 – Schematic diagrams of the scattering of the incident beam from the sample mounted inside the beam flight path, used for the calculation of maximum and minimum q-range; the top figure (figure a) shows the rays used to calculate the maximum *q*, the bottom figure (figure b) shows the rays used to calculate the minimum *q*.

Very short (1 second) exposures were made to determine beam-stop centering and alignment of the flight path, adjustments were made, and then the aligned configuration was locked into place. Diffraction from a Si-standard was also important for calibration, and was collected throughout the experiment. The standard used was a NIST SRM 640C powdered Si.

For all samples, a short (10 second) exposure was made to determine the approximate counts per second incident on the detector, and then the total exposure time was programmed. The MAR3450 detector saturated at around 65000 counts, so the target exposure time produced around 50000 counts. These exposures were repeated up to ten times to produce a total intensity near 500000 counts.

2.4.2.4. Data reduction and background correction

A correction for the background is very important for weak scattering materials, such as metallic glasses, and the full nature of reproducibility and background correction at the point of data collection in the stationary diffraction experiments discussed here is still being explored. The total counts per second incident on the detector, and the signal to noise ratio with respect to the background are influenced by subtle changes in the sample mounting, as well as sample and detector alignment, and changes in the incident beam between exposures, all of which are difficult parameters to control, as reflected in a somewhat erratic quality of the scattering data. The general procedure for collecting a background file was to unload the sample slide from the flight path, load and center an empty slide of similar type, evacuate the flight path, and take an exposure of the same time as that used for the data run.

Raw data collected from the MAR3450 detector were processed using the Fit2D software to generate the integrated intensity for each repetition of exposure. A macro was used to streamline the data analysis. The macro was modified to include the calibration and beam centering information that was performed as close to the time of the data collection as available, and in the same configuration. A sample macro is *Aug08_noGEOcorr_080508_1031.mac,* where the date/time information included in the filename is that of the Si calibration used to determine the distance and center. The text of the macro is provided in Appendix 1.

An average intensity was determined for both the sample and background. If the background data were not collected using equal exposure time to that of the sample data, the file with the longer exposure time was scaled to match that with the shorter exposure time. This was accomplished using information contained in the experiment log file *setup.spec*. The last line of each entry gives the monitor value, which represents the total intensity of exposure. Thus, the intensity could be scaled as

$$I_1^{'} = I_1 * \left(\frac{m_2}{m_1} \right),$$

where m_2 ($m_2 < m_1$) is the monitor value for the shorter exposure, and I_1 is the intensity to be downscaled. In principle this procedure could be implemented for all exposures, but it remains to be demonstrated if this is needed. After the sample data and associated background were processed, the background was subtracted from the data to give the corrected intensity. The .chi file containing the corrected intensity was supplied to PDFgetX2 along with the physical parameters, as described in §2.4.1, to generate the total structure factor $S(q)$ and the reduced pair correlation function $G(r)$.

Filtering of the scattered x-ray beam with aluminum shielding was also tested to determine the effect on background correction and improved signal to noise ratio. Al has no absorption edge near the energy of x-rays used in this experiment (100keV), so filtering in this manner could absorb low energy radiation from fluorescence while allowing the diffracted cone from the sample to pass through almost unaffected. A sequence of increasingly thick Al sheets was placed between the end of the flight path and the detector. Complete details of this experiment and its use in data correction are provided in Appendix 2.

2.4.3. Beamline Electrostatic Levitation

High energy x-ray diffraction studies of levitated liquid metals and alloys were made *in situ* using the previously described ESL apparatus from NASA MSFC, which was modified to include Be entrance and exit windows for through transmission of an x-ray beam. The modified chamber was then located in the beam path at the 6ID-D high energy station of the APS beamline at ANL This technique is called Beamline Electrostatic Levitation, or BESL. A schematic of the modified setup is shown in Figure 2.10. As already mentioned, a GE 41-RT Revolution detector was used in BESL. A complete technical description this detector in x-ray diffraction measurements using a synchrotron source can be found elsewhere [14]. The BESL method has been described elsewhere [15], but two important modifications were made in August 2007.

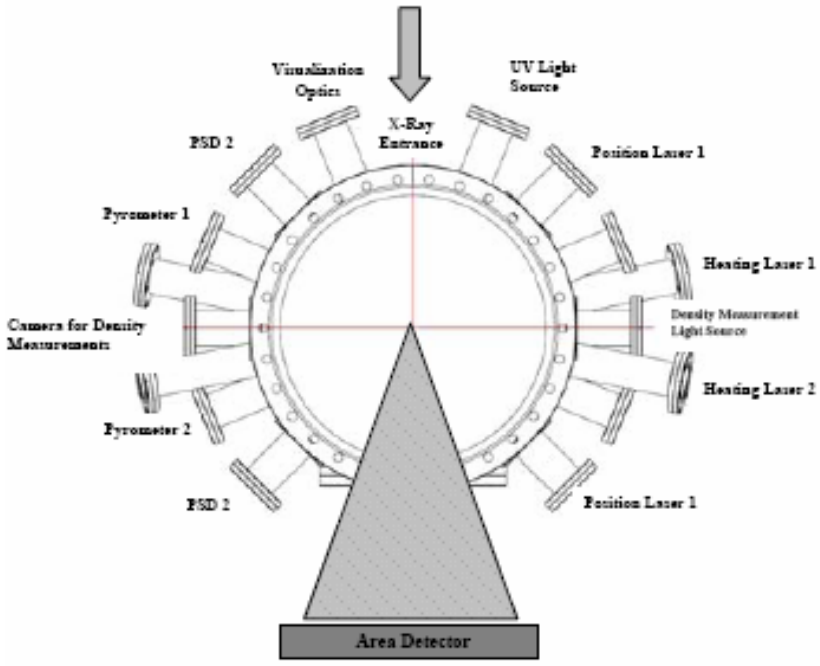

Figure 2.10 – A schematic of the ESL chamber modified for diffraction experiments (the schematic shown is for the WU-BESL).

First, a 3.4mm diameter Pb beam stop was placed just beyond the Be exit window, rather than at the detector face, which reduced forward beam air scattering and minimized the contribution to the background from scattering of the polycrystalline Be window; second, to reduce stray radiation entering the chamber, an evacuated beam flight path was placed between the x-ray source and the Be entrance window, and an aperture made from machinable tungsten was placed just upstream of the entrance window. These modifications gave improved data quality over that collected in previously using BESL.

In BESL, the diffraction measurement is coupled in real time to the previously described thermo-physical properties measurements of ESL. High energy (125keV) x-ray diffraction was performed for all samples studied using free cooling and step-cooling temperature-time profiles. For free cooling, the heating laser power was turned off when the desired temperature was reached, typically around 100°C above the melting temperature, and the sample allowed to cool by radiative emission in high vacuum with a nominal 1hz sampling rate of the detector during cooling. For step-cooling, the heating laser power was turned down in steps that corresponded to 50-100°C increments in the measured sample temperature, and 15-second detector exposures were taken at each step at a nominal 1Hz sampling rate, with each step followed by a 15-second exposure with the shutter closed to clear the detector elements of residual intensity.

Examples of free cooling and step-cooling temperature-time curves are shown in Figure 2.11, with the time between the x-ray shutter opening and closing indicated by red boxes. The shutter was coupled to the pyrometer readout to produce a binary voltage signal, recorded in the data file, at the time when the shutter was opened or closed. This was used to determine the temperature of each frame from free cooling data.

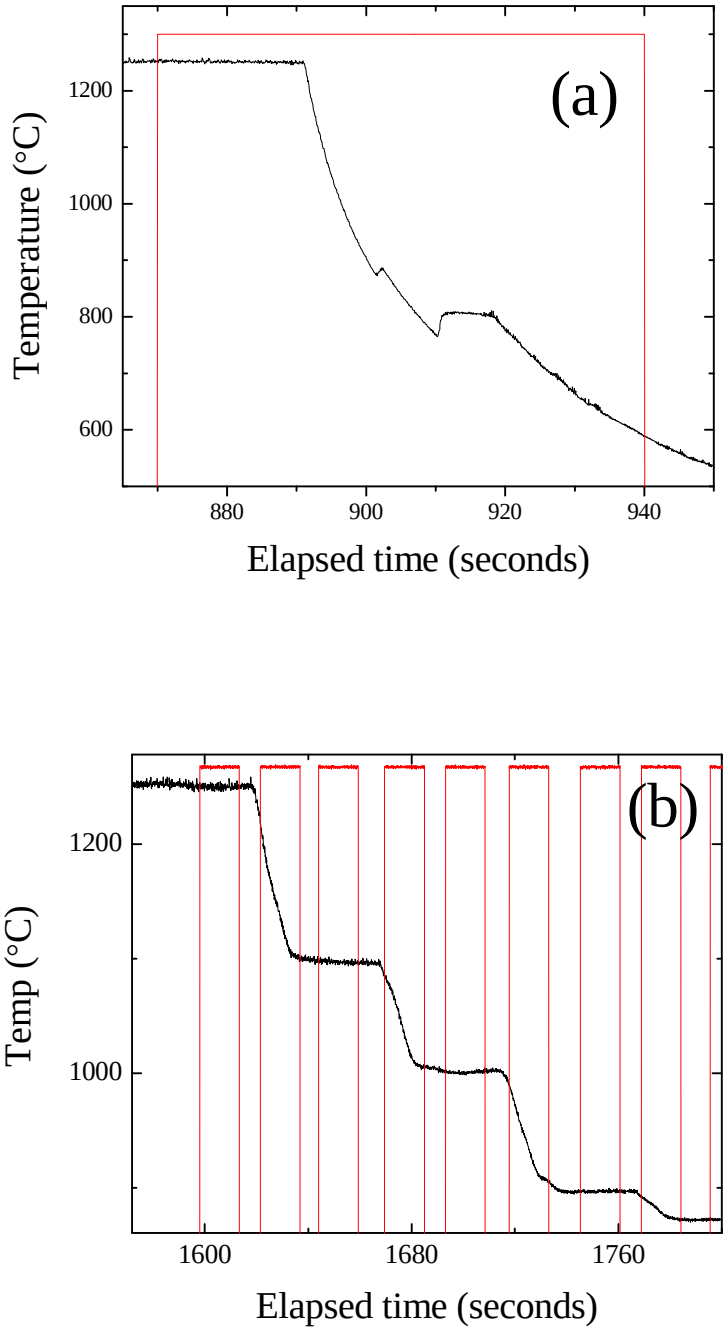

Figure 2.11 – (a) A representative free cooling and (b) step-cooling measurement in BESL; the black line is the pyrometer temperature reading, the red boxes indicate the intervals when the detector was sampling.

2.5. Simulation and analysis methods

Atomic positions were determined from the scattering data using a Reverse Monte Carlo (RMC) simulation. Configurations generated from RMC were characterized using two distinct but complimentary analysis methods: the index scheme of Honeycutt and Anderson (HA index) [16] and the Bond Orientational Order parameter (BOO) analysis developed by Steinhardt, Nelson, and Ronchetti [17]. The theoretical basis for each is provided in Chapter 1. All simulation and analysis programs were run on either a 2.66GHz Intel Pentium D dual-core processor with 1.0Gb RAM or a 2.40GHz Intel Core 2 Quad quad-core processor with 2.0Gb RAM, both in an Ubuntu Linux 8.04 environment, using the Wine Windows environment when needed.

2.5.1. Reverse Monte Carlo simulation

As described in Chapter 1 and elsewhere [18], RMC uses a rejection sampling algorithm with Monte Carlo moves of atoms to generate atomic configurations that best match input experimental data. A random starting configuration was used for all simulations discussed in this thesis unless otherwise noted. Input parameters to the simulation were the number density, inter-atomic cutoff distances, maximum atomic move distances, interaction coefficients, and the input scattering data. Number densities were determined from measured densities at the appropriate temperature. Inter-atomic cutoff distances were determined from an optimization method described later in this section. Maximum move distances could be optimized empirically, but the quality of fit was not strongly dependent on this value; a value of 0.3 was used in all cases considered.

Interaction coefficients were determined from the Faber-Ziman formulation described in Chapter 1.

Input scattering data provided were either $S(q)$ or $g(r)$. When using $g(r)$ as input data, it is important to note that PDFgetX2 outputs the function $G(r)$, the two of which are related as

$$g(r) = \left[\frac{G(r)}{4\pi r \rho_0} + 1 \right],$$

where ρ_0 is the number density. When optimizing the RMC simulation, it was sometimes the case that $g(r)$ or $S(q)$ would provide a better fit, although there was no generally preferred method. In later chapters, when a difference was observed it will be noted in the text. A sample RMC input file used in this work is provided in Figure 2.12.

2.5.1.5. Method for optimizing atomic cutoff distances

Cutoff distances were initially estimated by the atomic diameter of each element and the appropriate permutations for the interaction terms, taken from atomic radii provided by a standard periodic table of the elements [19]. Distances were refined by repeatedly running the simulation and modifying the cutoff distances to produce the smoothest possible partial $g(r)$ curves, following the procedure of Kim [20]. Figure 2.13 shows a comparison of non-smooth partial $g(r)$ curves and smooth curves after refinement of the inter-atomic cutoff distances.

```
STL907 Zr54Cu46 at 1100C run4
0.0530                          ! number density
2.25 2.20 2.10                  ! cut offs
0.3 0.3 0.3                     ! maximum moves
0.05552                         ! r spacing
.false.                         ! moveout option
0                               ! number of configurations to collect
1000                            ! step for printing
1000 20                         ! time limit (total time), time for saving
0 1 0 0                         ! sets of experiments
STL907_Zr54Cu46_1100C_Sq.dat
3 884                           ! points to use
1.0                             ! const. to subtract
0.3822 0.2360 0.1458            ! coeff.
0.005                           ! sigma
.false.                         ! renormalise
.true.                          ! offset
0                               ! no of coord. constr.
0                               ! no of av. coord. contsr.
.false.                         ! potential
```

Figure 2.12 – An RMC input file for a Zr-Cu liquid at 1100°C**.**

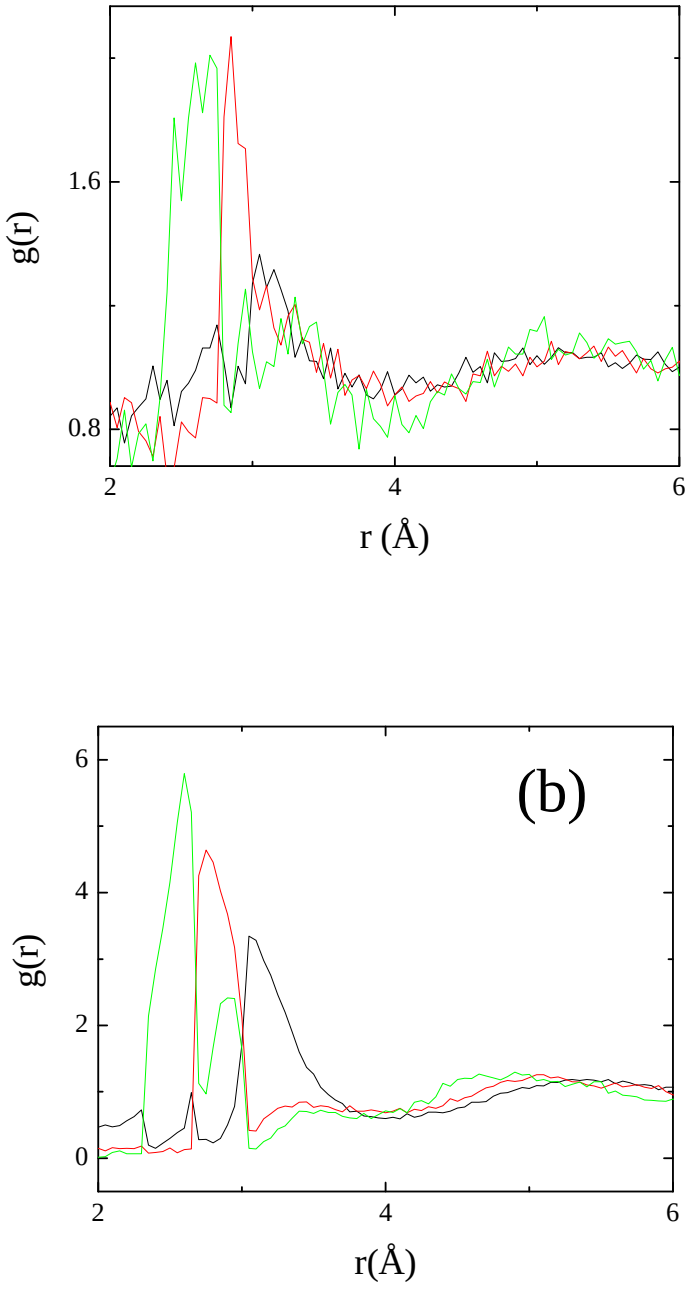

Figure 2.13 – The partial g(r)'s generated by RMC for a Zr-Cu liquid (a) before optimization of cutoff distances and (b) after optimization.

2.5.2. Methods for characterization of liquid structures

As already mentioned, HA index and BOO analyses were used to characterize the structures from RMC. Briefly, the HA analysis indexes a root pair of atoms based on the number of neighbors and the number of bonds connecting those neighbors. In this way the frequencies of both fully formed and partially formed clusters are detected. The BOO parameter analysis uses the bond angles between an atom at the center of a cluster and vertex atoms to form an average order parameter, Q_l, which is expressed in terms of bond spherical harmonics. The BOO analysis measures the frequency of more fully formed clusters. Thus the two measures provide somewhat different, but complimentary information.

The bond cutoff distance is an important input parameter in both analysis methods. This was calculated from the *r*-position of the first minimum in the radial distribution function, defined as

$$RDF = 4\pi r^2 \rho_0 g(r),$$

divided by the edge length of the 'box' containing the atoms (a quantity determined when the input density of atoms is mapped into a cube of equal density, such that all atom coordinates have values between 0 and 1), which is printed in the .log file generated by RMC. The HA analysis was implemented by running the program *HAindexfinal.out* in the Linux command line with the final configuration from RMC as input. The resultant collection of HA indices was sorted by running the program *HAsortfinal.out.* The BOO analysis was implemented by running the program *BOO0803.exe*, in a Linux command line using the Wine Windows environment, with the final configuration from RMC as input. The results were sorted by running the program *Ql0803.exe*.

2.6. Summary

In this chapter experimental and analysis methods for many of the experiments performed for this dissertation work were presented. This comprised sample preparation and reproducibility, basic characterization of thermo-physical properties and microstructure, and advanced techniques for high energy x-ray diffraction. The methods of simulation and modeling of diffraction data to determine atomic positions and local order in liquids and amorphous solids were also presented. Instructions on data analysis methods were provided, with further information in Appendices 1 and 2.

References

1. J. I. Goldstein, *Scanning electron microscopy and X-ray microanalysis : a text for biologists, materials scientists, and geologists*. 2 ed. 1992, New York: Plenum Press.
2. D. B. Williams and C. B. Carter, *Transmission electron microscopy : a textbook for materials science*. 1996, New York: Plenum Press.
3. W.-K. Rhim, S. K. Chung, D. Barber, K. F. Man, G. Gutt, A. Rulison, and R. E. Spjut, Review of Scientific Instruments, 1993. **64**(10): p. 2961-2970.
4. A. J. Rulison, J. L. Watkins, and B. Zambrano, Review of Scientific Instruments, 1997. **68**(7): p. 2856-2863.
5. J. R. Rogers, R. W. Hyers, T. Rathz, L. Savage, and M. B. Robinson, *Thermophysical property measurement and materials research in the NASA/MSFC electrostatic levitator*, in *AIP Conference Proceedings*. 2001, American Institute of Physics. p. 332.
6. G. Hansen, S. Krishnan, R. Hauge, and J. Margrave, Metallurgical and Materials Transactions A, 1988. **19**(8): p. 1889-1894.
7. S. Krishnan and P. C. Nordine, Journal of Applied Physics, 1996. **80**(3): p. 1735-1742.
8. R. W. Hyers, Measurement Science and Technology, 2005. **16**: p. 394-401.
9. R. C. Bradshaw, D. P. Schmidt, J. R. Rogers, K. F. Kelton, and R. W. Hyers, Review of Scientific Instruments, 2005. **76**(12): p. 125108-8.
10. A. Hammersley, http://www.esrf.eu/computing/scientific/FIT2D/index.html.
11. H. H. M. Balyuzi, Acta Crystallographica, 1975. **A31**.
12. D. Waasmaier and A. Kirfel, Acta Crystallographica, 1995. **A51**: p. 416-431.
13. X. Qiu, J. W. Thompson, and S. J. L. Billinge, Journal of Applied Crystallography, 2004. **37**: p. 678.
14. J. H. Lee, J. Almer, C. Aydıner, J. Bernier, K. Chapman, P. Chupas, D. Haeffner, K. Kump, P. L. Lee, U. Lienert, A. Micelia, and G. Vera, Nuclear Instruments and Methods in Physics Research A, 2007. **582**(1): p. 182-184.
15. A. K. Gangopadhyay, G. W. Lee, K. F. Kelton, J. R. Rogers, A. I. Goldman, D. S. Robinson, T. J. Rathz, and R. W. Hyers, Review of Scientific Instruments, 2005. **76**(7): p. 073901.
16. J. D. Honeycutt and H. C. Andersen, Journal of Physical Chemistry, 1987. **91**: p. 4950-4963.
17. P. J. Steinhardt, D. R. Nelson, and M. Ronchetti, Physical Review B, 1983. **28**(2): p. 784.
18. R. L. McGreevy, Journal of Physics: Condensed Matter, 2001. **13**: p. R877-R913.
19. *CRC Handbook of Chemistry and Physics, 89th Edition (Internet Version 2009)*, ed. D.R. Lide, Boca Raton, FL: CRC Press/Taylor and Francis.
20. T. H. Kim, *Structural Study of Liquids*. 2007, Washington University: St. Louis.

Chapter 3

Phase Formation and Supercooled Liquid Structure in $Ti_{45}Zr_{(38-x)}Hf_xNi_{17}$ Alloys

3.1. Introduction and background

Since the discovery of quasicrystalline and amorphous phases in Ti- and Zr-based alloys, there has been interest in studying the effects of composition on phase formation in these systems. This chapter presents the results of a study of the structures, physical properties, and phase transitions in $Ti_{45}Zr_{(38-x)}Hf_xNi_{17}$ liquids. Before discussing these results, it is useful to review the previous studies by this group and others.

Huett [1], from this group, discovered a rather sharp phase formation boundary when Hf was substituted for Zr in $Ti_{45}Zr_{38}Ni_{17}$ (thus $Ti_{45}Zr_{(38-x)}Hf_xNi_{17}$) in 3% increments. A transition in the phases formed was observed for samples prepared both by rapid quenching using the melt-spinning technique and for cast samples prepared by arc-melting on a water-cooled Cu hearth, although the Hf-concentration associated with the phase formation boundary varied slightly between the two methods (see Chapter 2 for a detailed discussion of these techniques for sample preparation). The atomic structures were determined using the X-ray diffraction (XRD) method discussed in chapter 2, which revealed the phase formation boundary for both rapidly quenched and cast samples. Figure 3.1 and Figure 3.2 show the intensity measured from XRD as a function of scattering angle, $I(2\theta)$, with changing Hf concentration for the quenched and cast samples, respectively.

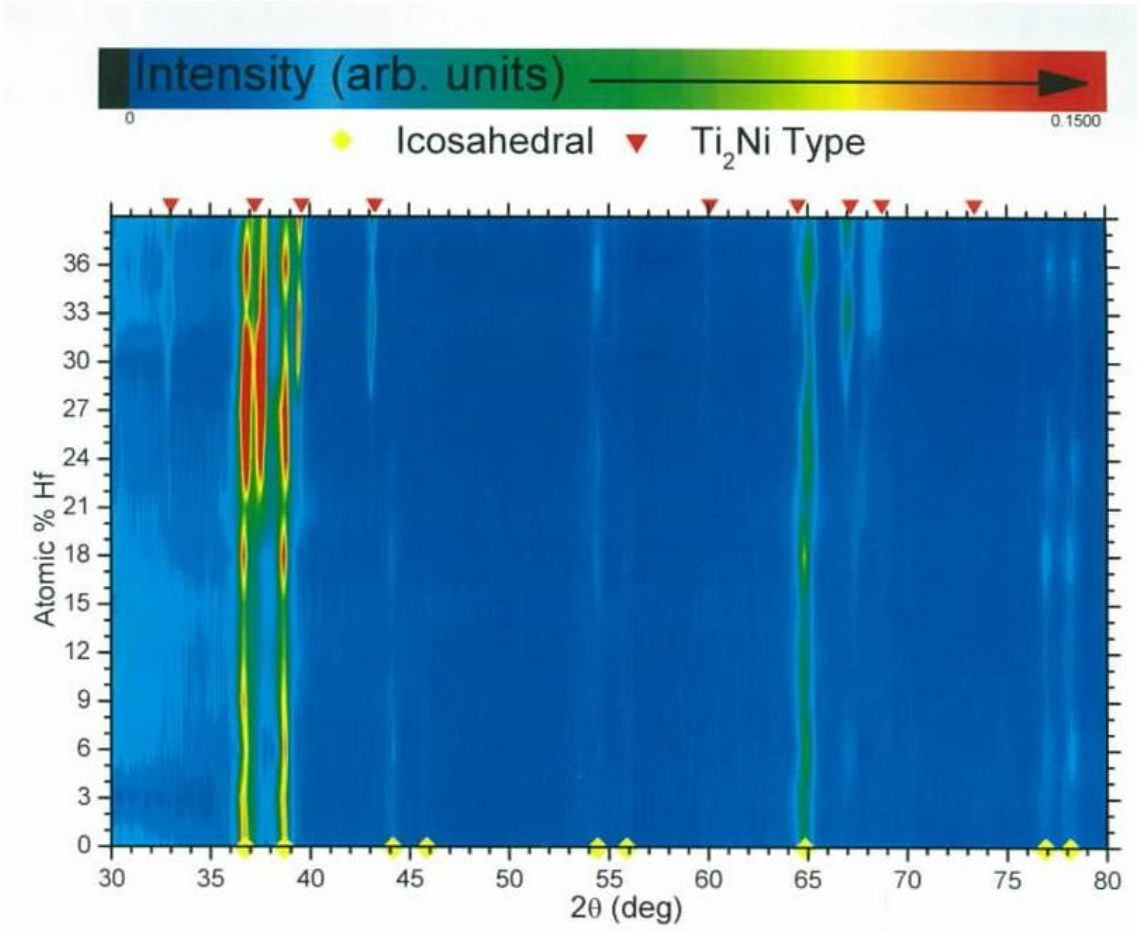

Figure 3.1 – The X-ray diffraction peaks for as-quenched samples of $Ti_{45}Zr_{(38-x)}Hf_xNi_{17}$ as a function of Hf content, x, obtained from low energy XRD measurements; the intensity is represented by the color scale, with 2θ on the abscissa and Hf concentration on the ordinate; image from [1].

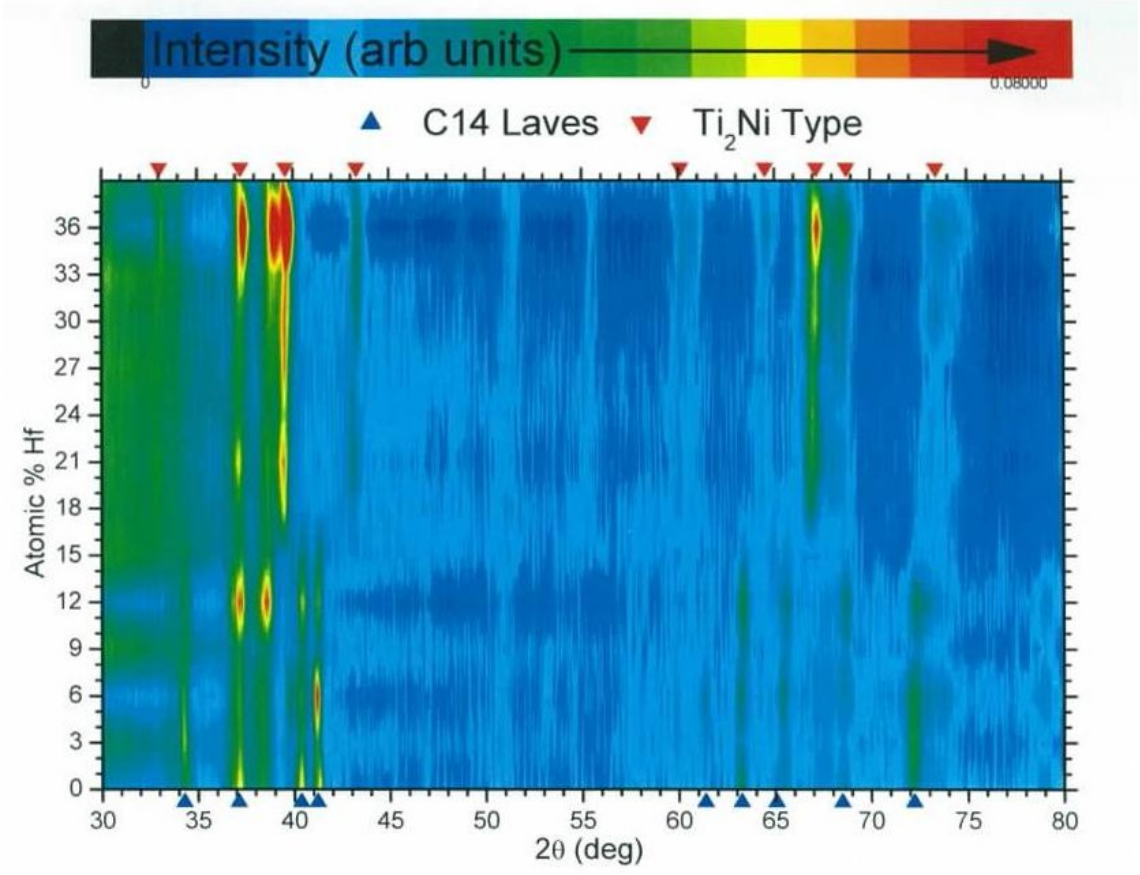

Figure 3.2 – The X-ray diffraction peaks for as-cast samples of $Ti_{45}Zr_{(38-x)}Hf_xNi_{17}$ as a function of Hf content, x, obtained from low energy XRD measurements; the intensity is represented by the color scale, with 2θ on the abscissa and Hf concentration on the ordinate; image from [1].

In the cast samples, the phase formation boundary was observed near 15-18% Hf. Below this Hf concentration the C14 Laves phase (space group P63/mmc; prototype $MgZn_2$) forms, while for higher Hf concentrations a Ti_2Ni-type phase (a large unit cell fcc phase, space group Fd3m, Pearson symbol cF96) forms. The structures of the C14 and Ti_2Ni phases are shown in Figure 3.3. The phase formation boundary for quenched samples is near 18-21% Hf. On the Zr-rich side of this boundary composition, the icosahedral quasicrystal phase (i-phase) forms as the dominant phase (see Chapter 1 and [2] for a discussion of quasicrystals and rational approximants (RAs) to the quasicrystal). On the Hf-rich side, samples contain a phase mixture of the i-phase and a Ti_2Ni-type phase. For all samples, regardless of Hf concentration, small amounts of the hexagonally close-packed (hcp) α(Ti/Zr/Hf/Ni) solid solution phase were also present. This phase forms by a solid state transition from the β(Ti/Zr/Hf/Ni) body-centered cubic (bcc) phase, which will be discussed in detail later in this chapter.

Huett also showed that rapidly quenched $Ti_{100-(x+y)}Hf_xNi_y$ alloys can form metallic glasses and RAs, phases not found in the Ti-Zr-Ni alloys. The i-phase, 3/2 RA, and the C14 and Ti_2Ni phases, as well as the glass, all contain local polytetrahedral order, though to different degrees. In Ti-Zr-Ni, the development of icosahedral short-range order (ISRO) in the supercooled liquid has been shown to dramatically lower the nucleation barrier for the i-phase [3]. ISRO has been demonstrated as the cause of the geometrical frustration underlying the glass transition and argued as important for improved glass formation [4, 5]. Changes in ISRO in the liquid with changing composition are thus important to phase formation. The (Ti/Zr)-Ni phase diagram has been studied using BESL [6, 7], and the phases formed were found to be sensitive to the Ni concentration.

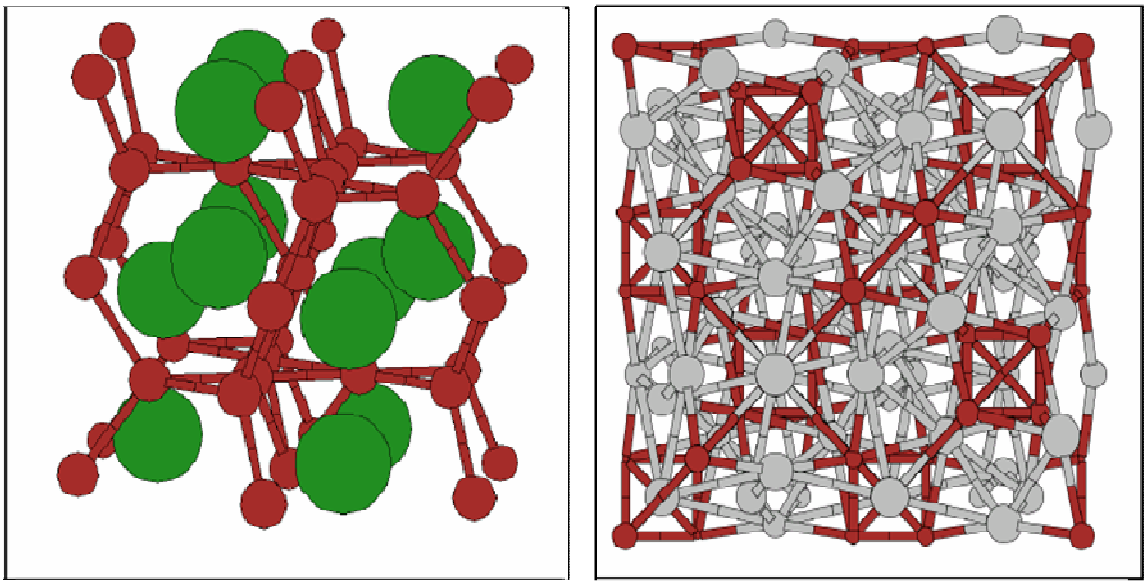

Figure 3.3 – A representation of the C14 (left) and Ti_2Ni (right) structures; from [8].

Other Ti-Zr-Hf-Ni alloys with 17 at.% have been studied, including by Basu and Ranganathan [9], who studied changes in phase formation in rapidly quenched $Ti_{41.5}(Zr/Hf)_{41.5}Ni_{17}$ as a function of Zr/Hf composition. In that study both alloys (i.e. containing Zr or Hf) could be quenched to form an amorphous phase, but changes were observed in the crystallization behavior during devitrification. The alloy containing Zr had a complex crystallization sequence, beginning with the low temperature precipitation of a nanoquasicrystalline phase from the amorphous phase; this transformed to a cF96 phase when fully crystallized. The alloy with Hf exhibited only one transition, directly to a cF96 phase; this occurred more slowly than the transformations in the alloy with Zr. While these reports indicated changes in phase formation and microstructural evolution on transformation in these alloys, which is correlated with the substitution of Hf for Zr, the underlying causes of this are not well understood.

That substitution of Hf for Zr can have a dramatic effect on phase formation and physical properties is surprising given that Zr and Hf are almost chemically identical, with properties summarized in Table 3.1. The similarity in atomic size can be attributed to the Lanthanide contraction (poor shielding of the nuclear charge by 4f electrons), affecting the transition metals following the Lanthanides; in this case Hf. Zr and Hf also typically exhibit similar chemistry, due to similar outer shell electrons (4d and 5d, respectively). Zr and Hf are thus difficult to separate in the production of pure metals.

Table 3.1 – A Comparison of the Properties of Zr and Hf.

	Zr	**Hf**
Atomic radius (Å)	2.16	2.16
Ionic radius (Å)	0.72	0.71
Covalent radius (Å)	1.45	1.44
Room temperature crystal structure	Hexagonal	Hexagonal
Melting point (K)	2128	2504
Electron configuration	$[Kr]5s^2 4d^2$	$[Xe]4f^{14} 6s^2 5d^2$

The purpose of the study presented in this chapter was to examine the role of Hf on phase formation in Ti-Zr-Hf-Ni alloys. The structures of equilibrium and supercooled liquid $Ti_{45}Zr_{(38-x)}Hf_xNi_{17}$ alloys and the products of their solidification were determined for a range of compositions from *in situ* diffraction studies using the BESL technique. The density and other thermo-physical properties of the liquid were also measured directly, and scanning electron microscope (SEM) studies were used to determine the solidification microstructures. From these measurements, chemical and topological changes in the liquids and solidification products were determined, providing new insight into the relationship between the liquid structure and phase formation. These results were combined with simulation and modeling studies to determine the influence of Hf on the liquids and solids and on the physical properties of these phases. These results are presented and discussed, paying particular attention to correlations with the solid phase formation boundary discovered by Huett.

3.2. Experimental methods

3.2.1. Sample preparation

Samples for the BESL experiment were prepared by arc-melting as described in Chapter 2. Variations in the oxygen impurity concentration of the Zr used in sample preparation cause variations in the supercooling limit and phase formation in other Ti-Zr-Ni alloys. Thus samples were prepared in different batches using different sources for the Zr. The stock and lot numbers, purity, and oxygen concentration of the source elements (measured as described in Chapter 2) are listed in Table 3.2. Table 3.3 lists the catalog numbers, source materials, and the oxygen concentrations of the samples studied.

Table 3.2 – The cataloging information for elements used in sample preparation.

Element	**Batch**	**Company**	**Purity (%)**	**Lot#**	**Stock#**	**Oxygen (ppm)**
Zr	01	Alfa Aesar	99.97	D10N23	42558	304
Zr	03	AML	n/a	826	n/a	202
Hf	01	Aldrich	99.97	03072842	n/a	183
Hf	02	Alfa Aesar	99.97	A19K06	39711	135
Ni	01	Alfa Aesar	99.999	D18M33	42333	87
Ti	01	Alfa Aesar	99.999	C18Q29	42394	448

Table 3.3 – The sample ID numbers, elements used, and alloy oxygen concentrations.

Sample ID #	**Composition**	**Zr batch**	**Hf batch**	**Oxygen (ppm)**
BESL-073801	$Ti_{45}Zr_{38}Ni_{17}$	01	n/a	483
BESL-073901	$Ti_{45}Zr_{26}Hf_{12}Ni_{17}$	01	01	351
BESL-074203	$Ti_{45}Zr_{20}Hf_{18}Ni_{17}$	03	01	370
BESL-074003	$Ti_{45}Zr_{17}Hf_{21}Ni_{17}$	03	01	296
BESL-074301	$Ti_{45}Hf_{38}Ni_{17}$	n/a	01	307
BESL-074001	$Ti_{45}Zr_{17}Hf_{21}Ni_{17}$	01	01	296
BESL-073803	$Ti_{45}Zr_{38}Ni_{17}$	03	n/a	378
BESL-074103	$Ti_{45}Zr_{11}Hf_{27}Ni_{17}$	03	01	289

3.2.2. Liquid structure determination

The liquid structure factor, $S(q)$, and its Fourier transform, the pair correlation function, $g(r)$, were determined from the corrected scattered intensity data as described in Chapter 1. Diffraction measurements were made using the BESL technique, and data were analyzed using the PDFgetX2 software [10], using the methods described in Chapter 2. Hf has an absorption edge near 125keV, the energy of x-rays used in this study, causing it to fluoresce. The uniform background in the measured intensity due to the fluorescence was removed by adjusting a subtracted value until the oscillations in $S(q)$ decayed asymptotically to unity. A plot of the fluorescence correction with increasing Hf concentration is shown in Figure 3.4.

3.2.3. Determination of liquidus temperatures by differential thermal analysis

The liquidus temperature, or temperature of complete melting of the alloy, is an important quantity in supercooling studies. It can, in principle, be measured by differential thermal analysis (DTA, described in Chapter 2). Determination of the liquidus temperature using DTA can be difficult, since the measured differential temperature signal upon crossing the liquidus is very weak. In the present study, the differential temperature was measured while the furnace temperature was ramped up and down, as depicted in Figure 3.5. For all DTA experiments, data were adjusted for instrument offset using measurements of Ni and Ag standards, and error bars were estimated from the scatter in the data. A further discussion of the liquidus determination will be given in §3.3.1.

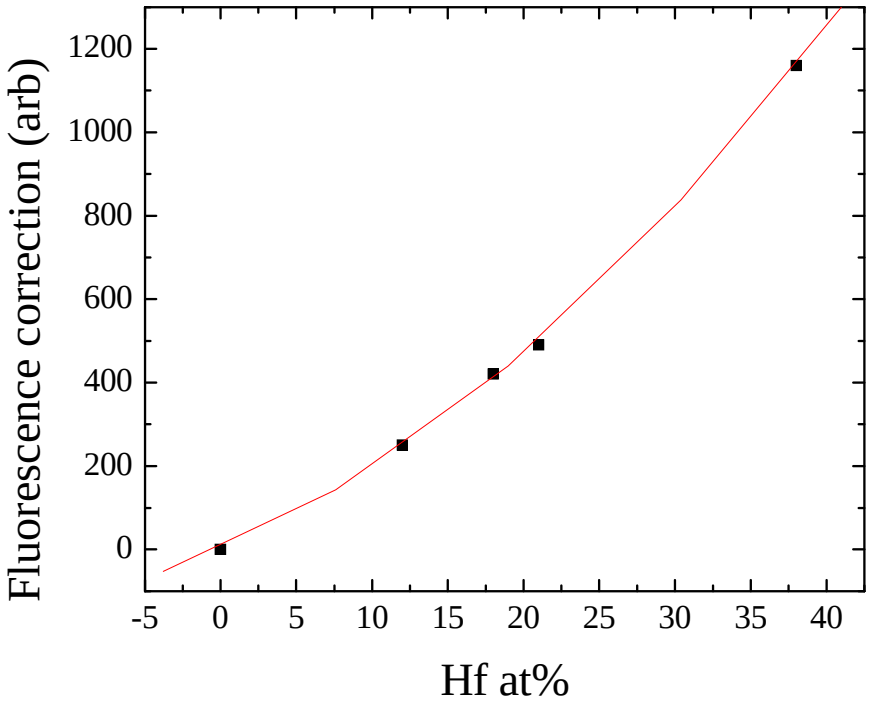

Figure 3.4 – The fluorescence correction applied to the scattered intensity as a function of Hf content (black points) and quadratic fit (red line), that indicates a $<Z>^2$ type dependence, as expected from the quantum mechanical treatment of fluorescence, with R^2=0.9993.

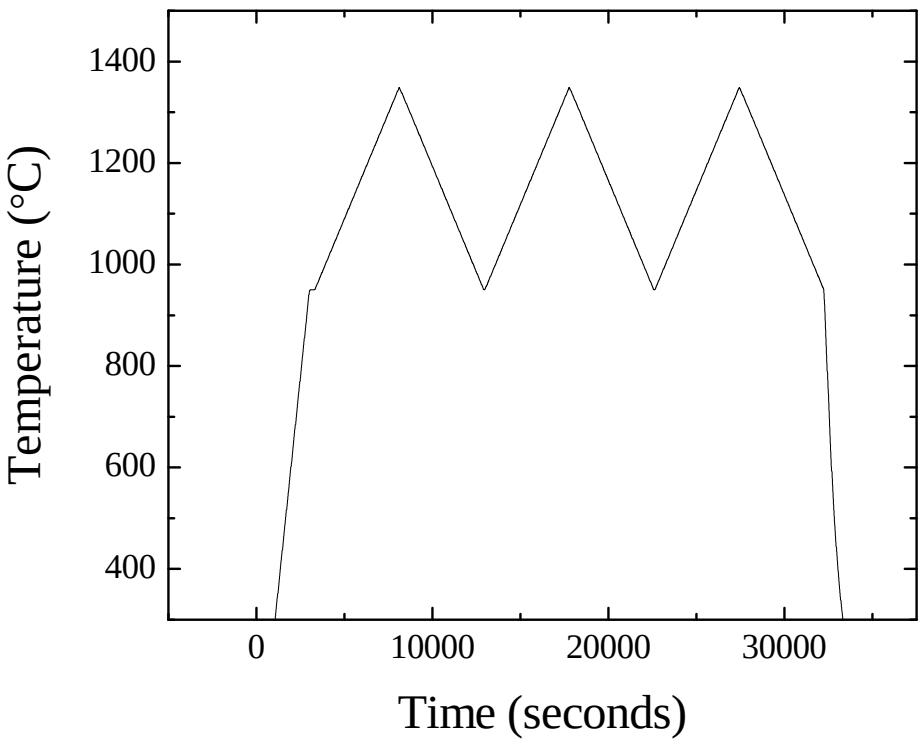

Figure 3.5 – A typical temperature-time sequence used in the DTA liquidus temperature measurements.

3.3. Results

3.3.1. Liquid supercooling and liquidus determination

Using ESL (with the method described in Chapter 2) the temperature of the levitated liquid during free-cooling in vacuum was measured as a function of time. These measurements were made for $Ti_{45}Zr_{(38-x)}Hf_xNi_{17}$ alloys for a range of Hf concentrations above and below the value corresponding to the phase formation boundary (x = 0, 12, 18, 21, 38). The cooling rates were approximately 20K/s in the temperature range studied. The phase formation sequence in BESL was similar to that of quenched and cast samples (§3.1). Primary crystallization produced the β(Ti/Zr/Hf/Ni) BCC solid solution phase for all compositions studied. Secondary crystallization produced either the C14 or the Ti_2Ni-type phase, depending on composition, and the β(Ti/Zr/Hf/Ni) transformed at lower temperatures to the α(Ti/Zr/Hf/Ni) HCP phase, completing the crystallization sequence.

The temperatures as a function of time during free-cooling for all alloy compositions studied are shown in Figure 3.6. Figure 3.7 shows a plot of the onset of primary recalescence to the β(Ti/Zr/Hf/Ni) phase (also the lowest liquid temperature), the highest temperature achieved during primary recalescence (here called the offset temperature), the onset of secondary recalescence, and the offset of secondary recalescence for all samples. The peaks in the temperature-time plot associated with recalescence of the β(Ti/Zr/Hf/Ni) were integrated to estimate the relative volume fractions of the liquid that crystallized to β; the areas and heights as a function of Hf concentration are shown in Figure 3.8. Both the area and the height are maximal at a composition near that of the phase formation boundary.

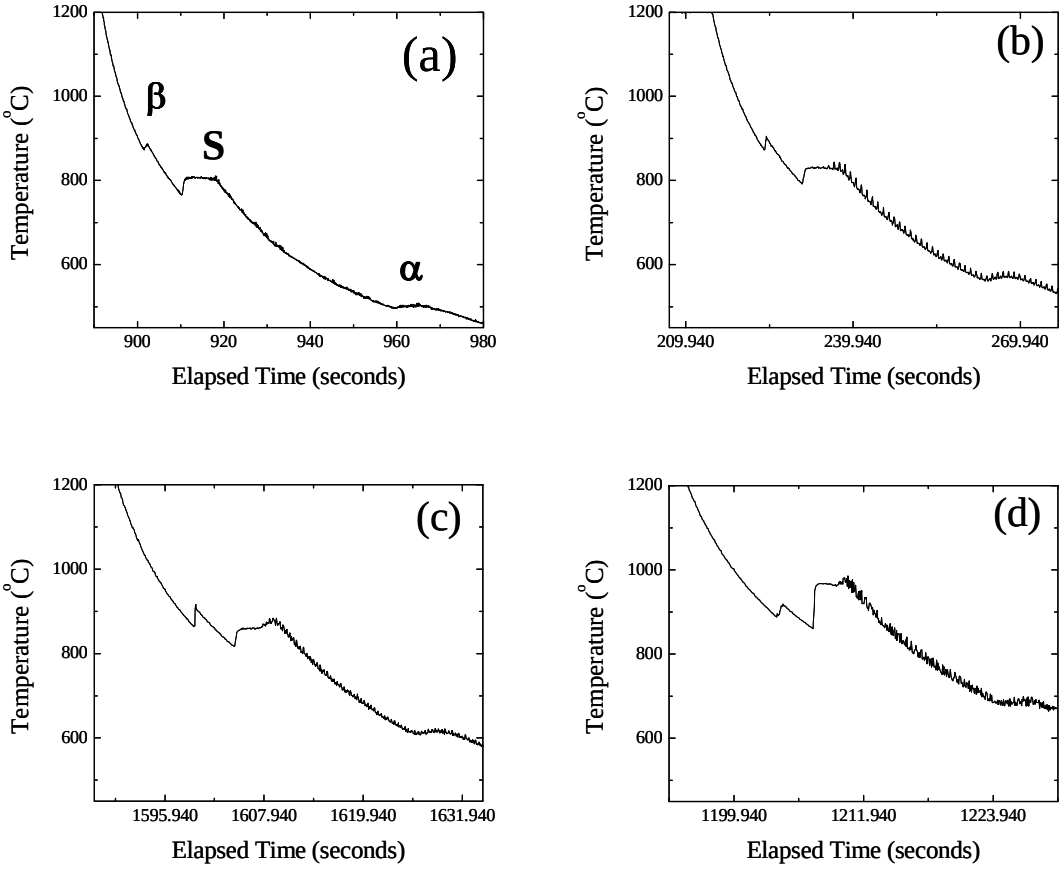

Figure 3.6 – The temperature measured as a function of time using ESL, for Ti45Zr(38-x)HfxNi17 liquids for (a) x = 0, (b) x = 12, (c) x = 21, and (d) x = 38 (the curve for x = 18 is not shown); the formation of the high temperature β(Ti/Zr/Hf/Ni) solid solution phase from the liquid is indicated by β, the formation of the secondary phase (C14 or Ti2Ni) is indicated by S, and the low temperature α-β transition is indicated by α.

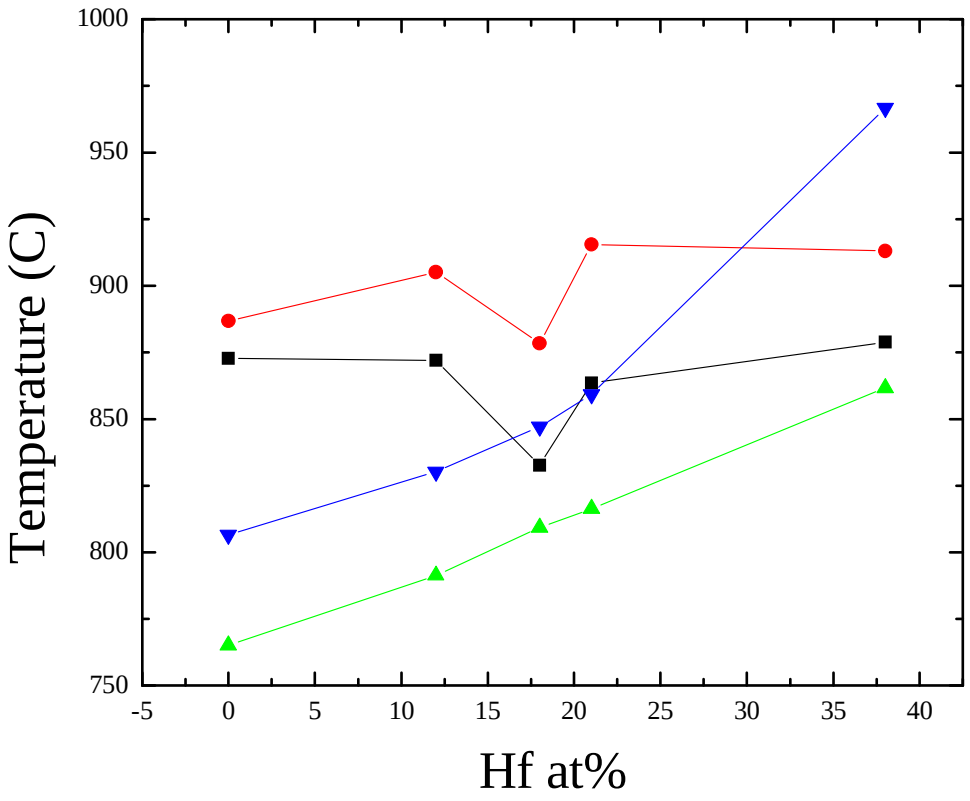

Figure 3.7 – The onset and offset temperatures of primary and secondary recalescence as a function of Hf concentration: (black) – onset of primary recalescence to β(Ti/Zr/Hf/Ni); (red) – offset of primary recalescence; (green) – onset of recalescence to secondary phases; (blue) – offset of secondary recalescence.

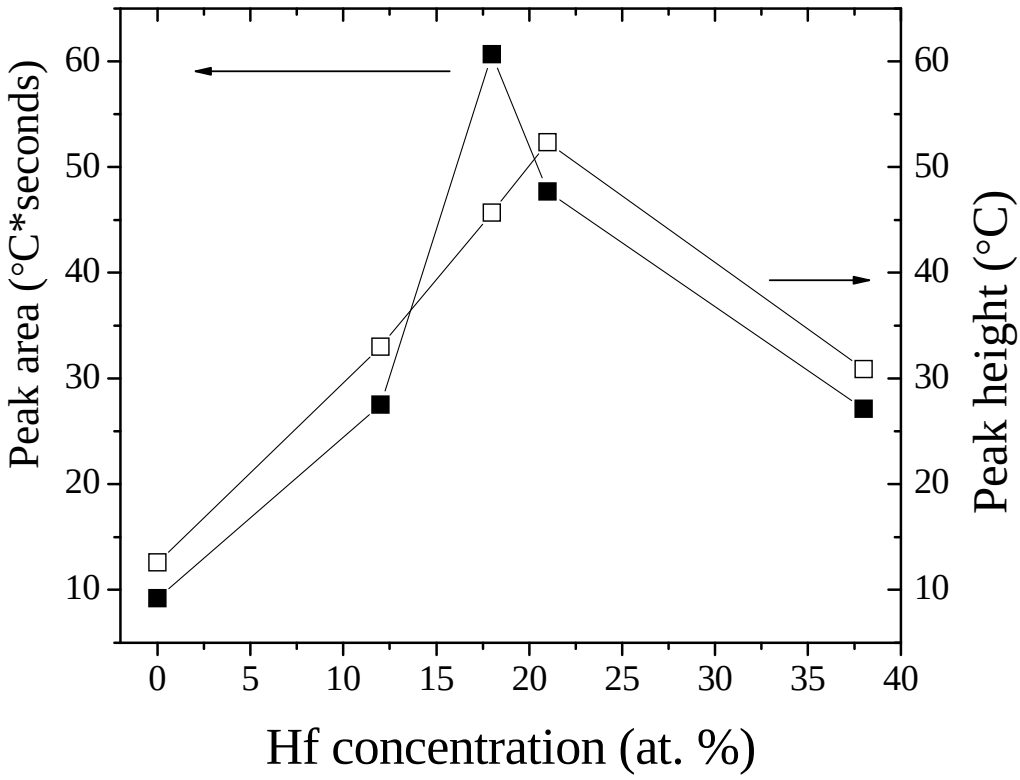

Figure 3.8 – The areas (closed symbols) and heights (open symbols) of the peaks in the temperature-time curves associated with recalescence of the β(Ti/Zr/Hf/Ni) phase; both plots are maximal near the phase formation boundary composition (18-21 at.% Hf).

The temperature of a plateau following primary recalescence is a good measure of the liquidus temperature; if no plateau is observed, however, the offset cannot be assumed to equal the liquidus temperature. The latter was the case for all compositions studied, which indicates that there was insufficient heat released during solidification to compensate for sample cooling. Thus, the liquidus temperatures were estimated using two methods other than the temperature-time curve. The first was DTA using the ramped heating/cooling described in §3.2.3. The other was based on an empirical method using diffraction data. (The diffraction data will be discussed in detail with regard to liquid structure in §3.3.2.1, here they are used only for estimating the liquidus.)

Figure 3.9 shows the measured differential temperature from DTA, ΔT_{DTA}, as a function of furnace temperature, T, in the range between 1000 and 1200°C, for the alloy containing no Hf. A subtle inflection between 1030 and 1060°C was observed during cooling, but varied in temperature depending on the cycle. Features of this type were associated with the liquidus temperatures for all compositions. For comparison, the liquidus temperature for the alloy with 0 at.% Hf has been measured to be 1060°C using ESL [6]. For all alloys the liquidus was determined on cooling; the lowest value of the temperature inflection observed from all 3 cycles was recorded as the liquidus temperature.

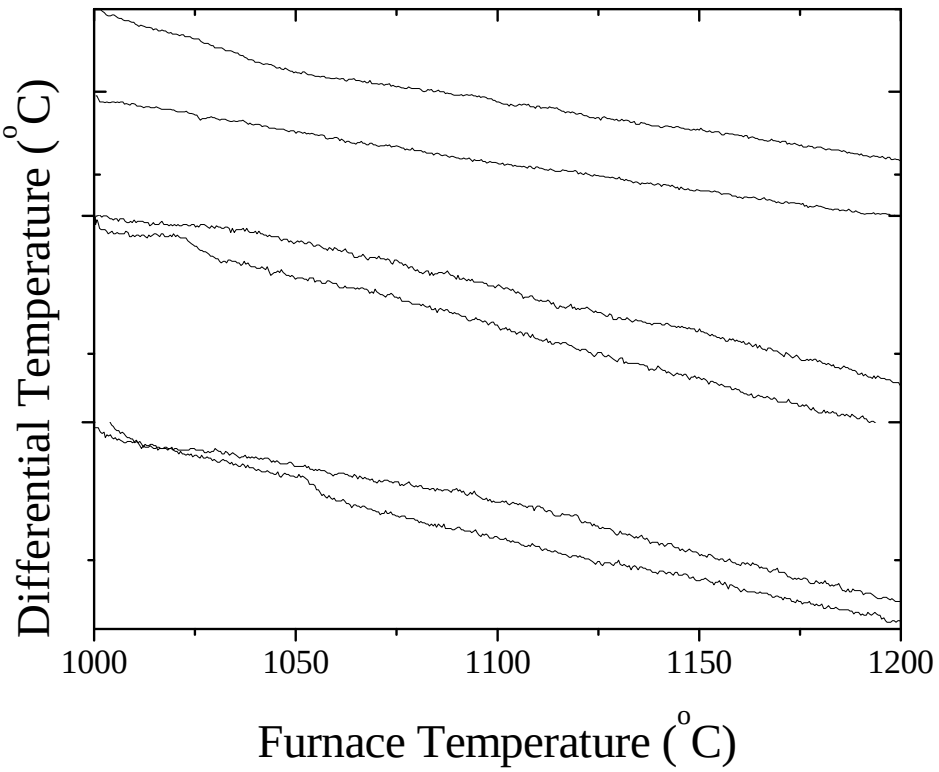

Figure 3.9 – The measured differential temperature in the alloy with 0 at.% Hf, showing a subtle inflection when crossing the liquidus temperature.

The Hansen-Verlet freezing criterion [11] states that, for a pure element, $S(q_0)$, the value of the first peak in the structure factor of the liquid, where q_0 is the wave vector corresponding to the center of the peak, has a particular value at the melting temperature, i.e.

$$S(q_0) \approx 2.8.$$

A full interpretation of this criterion and its application are given elsewhere [12]. It was applied here as another method for determining the liquidus temperatures, although further examination of its validity for alloys is warranted. At 1060°C, the previously measured value of the liquidus temperature for $Ti_{45}Zr_{38}Ni_{17}$, the diffraction results gave $S(q_0) = 2.9$, close to the value predicted for pure elements. Estimates for the liquidus temperatures for the other alloy compositions were therefore made by plotting the intensity of the first peak as a function of temperature and interpolating to find the temperature where $S(q_0) = 2.9$. A comparison of the liquidus temperatures determined by this method and by the DTA method is shown in Figure 3.10.

The results of these two methods were averaged and, using the average liquidus values, the reduced supercooling, T_{rl}, was computed as a function of Hf concentration.

$$T_{rl} = \left(T_l - T_r\right) / T_l ,$$

where the temperature is measured in Kelvin. As discussed in Chapter 1, this quantity provides a useful measure of the nucleation barrier and is used to estimate the driving free energy of solidification of the melt at the recalescence temperature. Larger values of the reduced supercooling indicate that the nucleation and growth of the crystal phase are more difficult than for liquids with smaller values of T_{rl}. The reduced supercooling as a function of Hf concentration is shown in Figure 3.11.

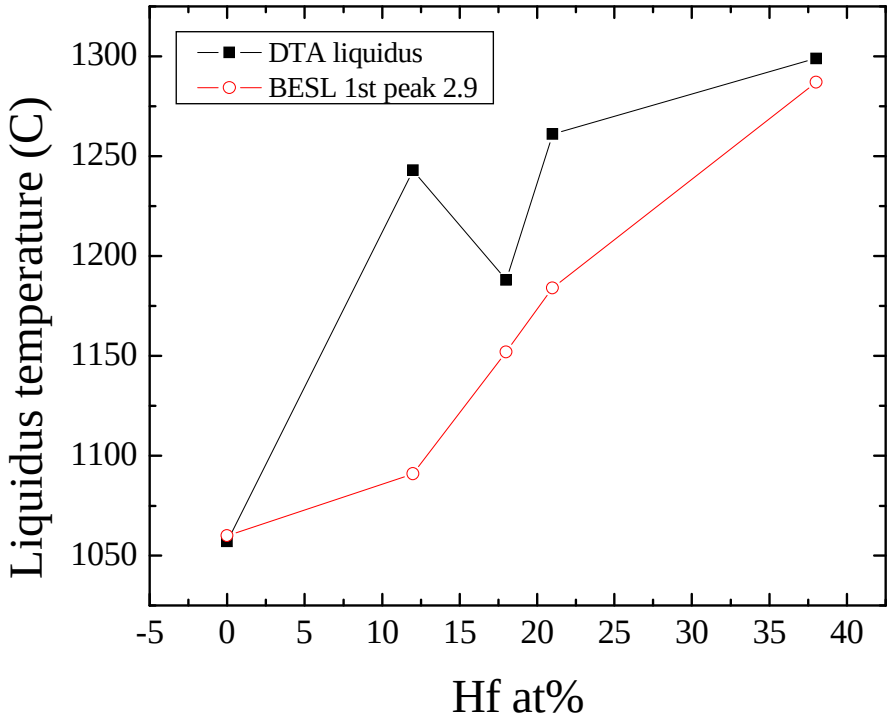

Figure 3.10 – A comparison of the liquidus temperatures determined by DTA (solid black squares) and by the Hansen-Verlet criterion (hollow red circles).

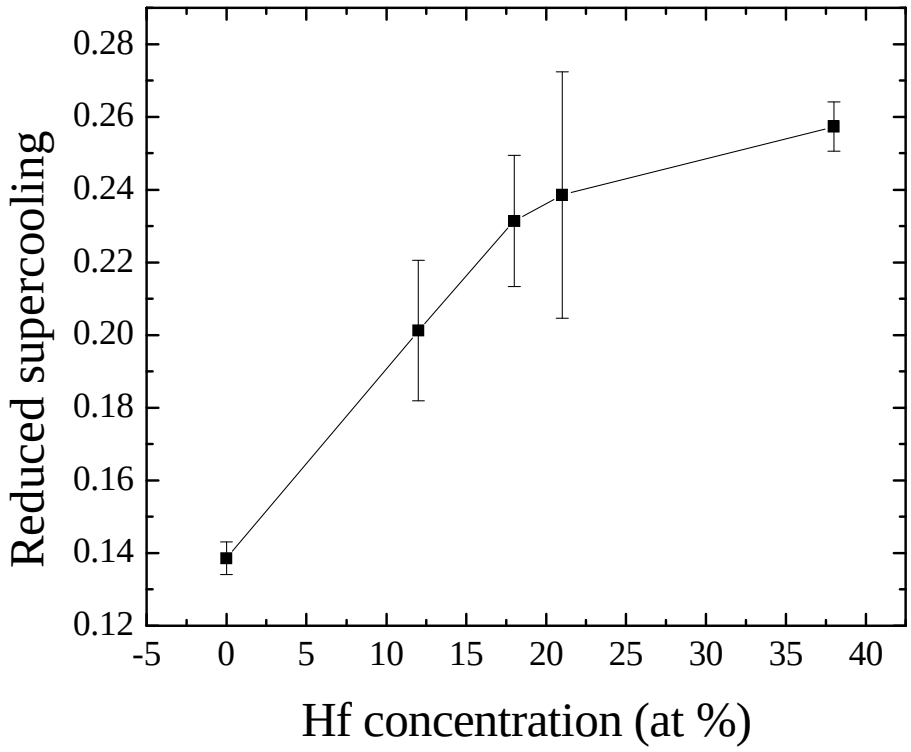

Figure 3.11 – The calculated reduced supercooling, T_{rl}, using the average liquidus temperature.

The $Ti_{45}Zr_{(38-x)}Hf_xNi_{17}$ alloys showed a high reduced supercooling, achieving a value for T_{rl} that is greater than 0.25 for x = 38. This is larger than previously observed in other Ti- Zr-Ni alloys studied using ESL [6]. These values were determined with respect to the primary crystallizing phase, β(Ti/Zr/Hf/Ni). Much of the sample remained as a metastable liquid after primary recalescence, and that liquid crystallized to the secondary phase (either C14 or the Ti2Ni-type). Thus, it was also useful to estimate the reduced supercooling of the secondary phase relative to the solidus temperature (T_s, the temperature of partial melting of a phase mixture). This constructed quantity was defined as

$$T_{rs} = (T_s - T_r) \Big/ T_s ,$$

where T_r is the recalescence temperature of the secondary phase. A plot of T_{rs} as a function of Hf concentration is shown in Figure 3.12. A dramatic increase in reduced supercooling is observed between the endpoint compositions (x = 0 and x = 38), with a shallow minimum near the phase formation boundary. These data suggest that the local structures of the liquid and crystal phases become slightly more compatible with increasing Hf up to the phase formation boundary composition, and quickly become incompatible for greater Hf concentrations. It is important to note that the reduced supercooling for the primary crystallizing phase is a smooth function of Hf concentration, showing little change on crossing the phase formation boundary. In contrast, the secondary recalescence of the residual liquid remaining after primary crystallization does reflect the presence of the phase formation boundary. This result will be discussed further in §3.5.

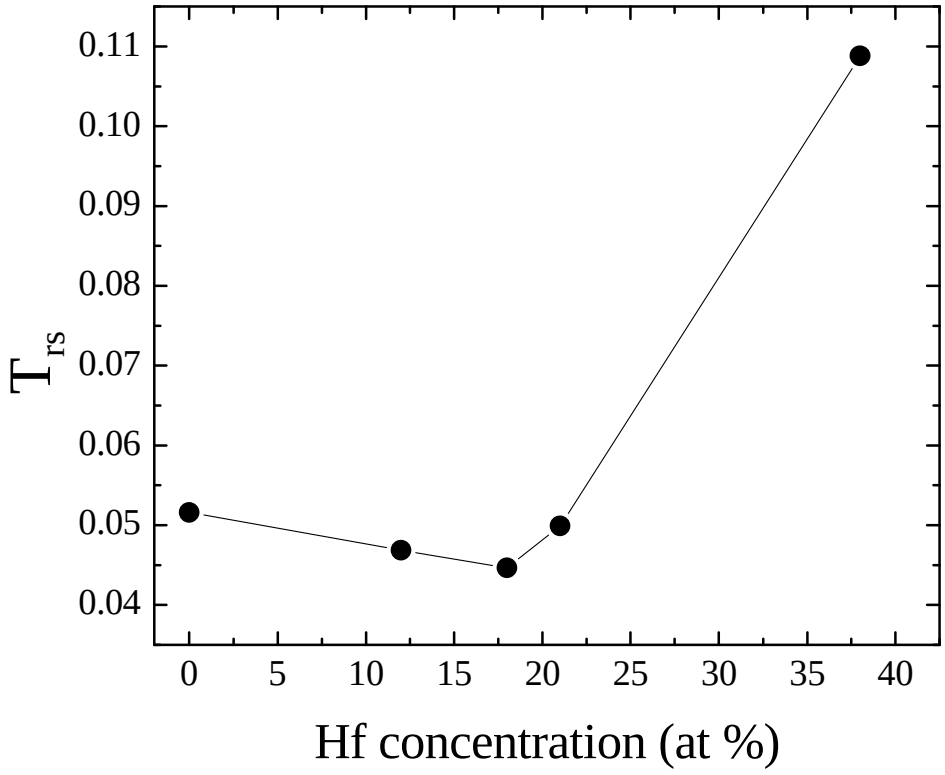

Figure 3.12 – The reduced supercooling relative to the solidus temperature for secondary recalescence.

Another important consideration is the solubility of Ni in β(Ti/Zr/Hf/Ni). From the binary phase diagrams [13], there is no solubility of Ni in β(Hf), some limited solubility (2%) of Ni in β(Zr) and about 10% solubility in β(Ti). This implies that, with increasing Hf concentration in β, the remaining liquid after primary recalescence will be richer in Ni than in the homogeneous alloy liquid. These effects will be illustrated in the following sections, and discussed further in §3.5.

3.3.2. Structural studies

3.3.2.1. Liquid structure

Representative $S(q)$ results from the step-cooling experiments, and magnifications of the first and second peaks, for the alloy with 21 at.% Hf are shown in Figure 3.13.a-c. From Figure 3.13.c, the intensity on the low-q side of the second peak increases with supercooling; this has been argued to indicate increased icosahedral short-range order (ISRO) in the liquid [7]. Figure 3.14.a-b show the measured $S(q)$ and calculated $g(r)$, respectively, for the alloys with x = 12, 18, 21, and 38 at approximately the same fraction of the melting temperature. Figure 3.15.a-b show the first and second peak positions, respectively, in $g(r)$ for all Hf concentrations at the liquidus temperature. An approximately monotonic increase in the first peak position, up to about 1%, was observed with increasing Hf concentration, indicating an increase in the average separation distance between the first neighbor atoms. The evolution of the second peak position is greatest near the phase formation boundary composition, between x = 18 and x = 21, reflecting an expansion then a contraction of the average second neighbor atom separation in the liquid.

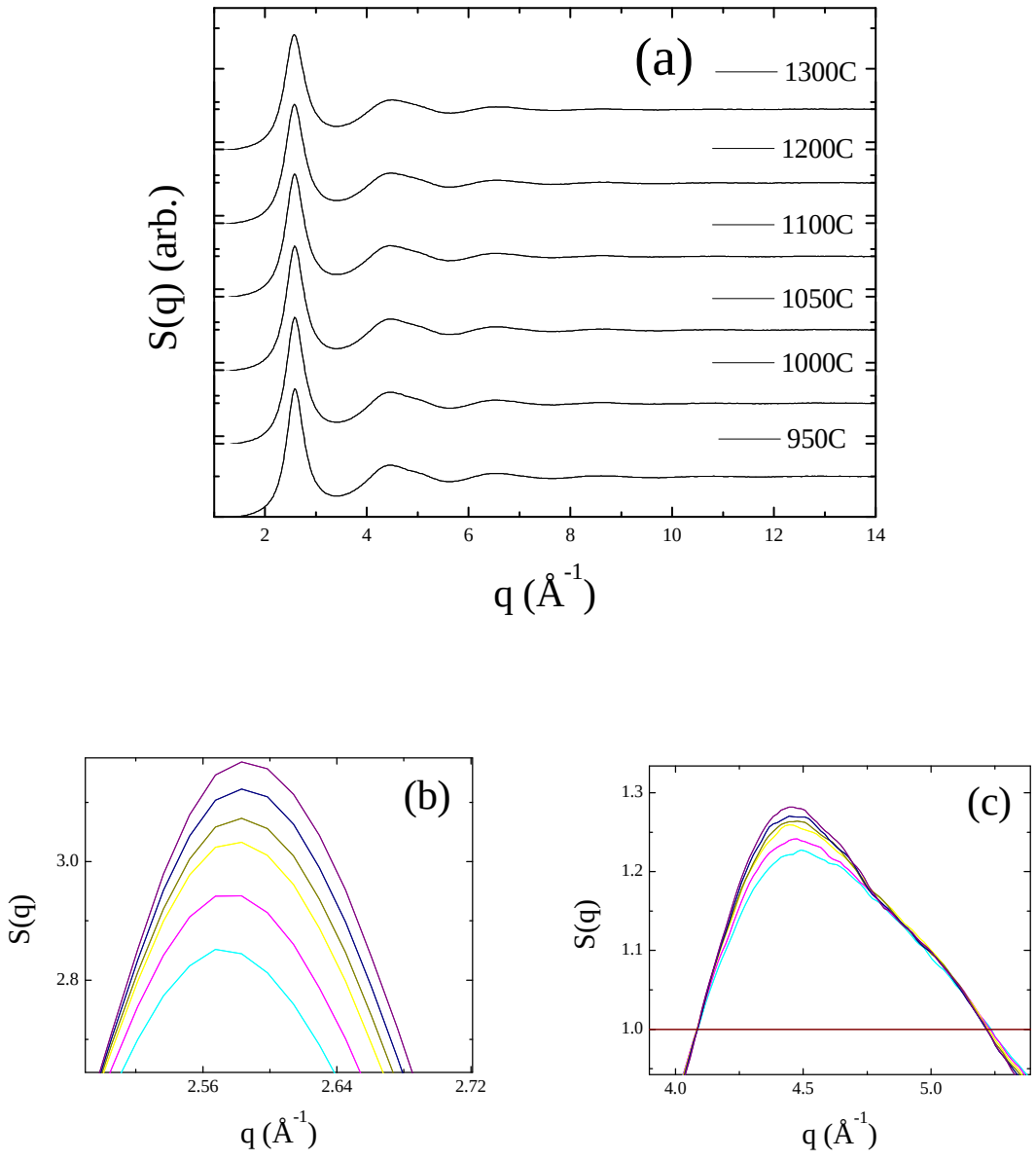

Figure 3.13 – (a) The $S(q)$ data for liquid $Ti_{45}Zr_{17}Hf_{21}Ni_{17}$ taken at several temperatures during step-cooling; magnified images of (b) the first peak in $S(q)$ and (c) the second peak, showing development of the low-q shoulder.

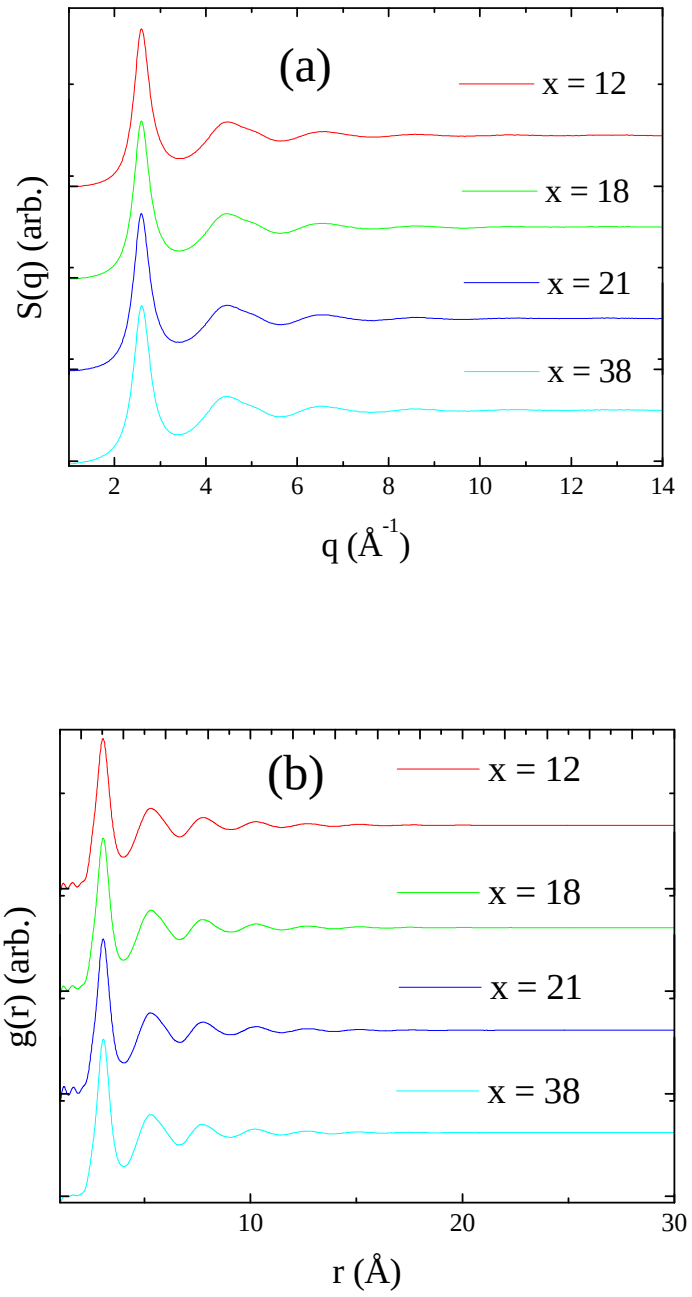

Figure 3.14 – The total structure factors, $S(q)$, (a) and pair distribution functions, $g(r)$, (b) for liquid $Ti_{45}Zr_{(38-x)}Hf_xNi_{17}$ for several Hf concentrations at approximately the same reduced temperature.

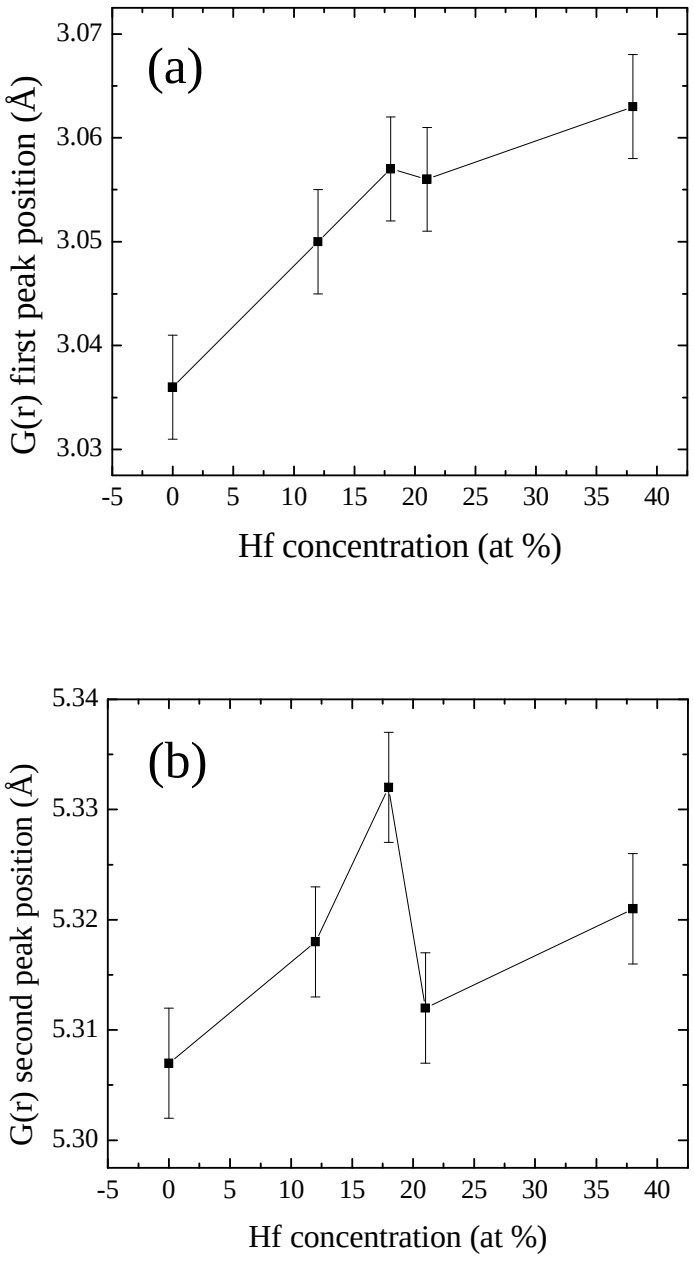

Figure 3.15 – The position of the first (a) and second (b) peaks in $G(r)$ at the liquidus temperature for liquid $Ti_{45}Zr_{(38-x)}Hf_xNi_{17}$ for all Hf concentrations studied.

Thus, it is the second nearest neighbor distance that correlates with the crystal phase selection, not the nearest neighbor distance. Figure 3.16 gives the position of the first peak in $S(q)$ with changing Hf concentration, at the liquidus temperature, showing a shallow minimum near the phase formation boundary composition.

The coordination number for the nearest neighbors was determined by integration of the radial distribution function, obtained from $g(r)$ as

$$RDF = 4\pi r^2 g(r).$$

The coordination number, Z, is then given by

$$Z = \int_0^{r_0} 4\pi r^2 g(r) dr,$$

since integration of this function up to r_0 will yield the total number of atoms at that distance. A decrease was observed in the coordination number calculated for the nearest neighbors (Figure 3.17), obtained from integration of *RDF* up to the first minimum. The coordination number decreases from 14.25 to 13.32 with the addition of 12 at.% Hf. With further addition of Hf, it decreases slightly then increases, forming a shallow minimum near the phase formation boundary composition. It should be noted, however, that this minimum is largely within the experimental error.

3.3.2.2. Crystal structures in BESL

Diffraction studies of the primary and secondary crystallizing phases for all compositions were also made using BESL with free-cooling. Fluorescence effects were negligible due to the strong scattering of the crystal phases. As already discussed, the primary crystallizing phase is the high temperature β(Ti/Zr/Hf/Ni) solid solution.

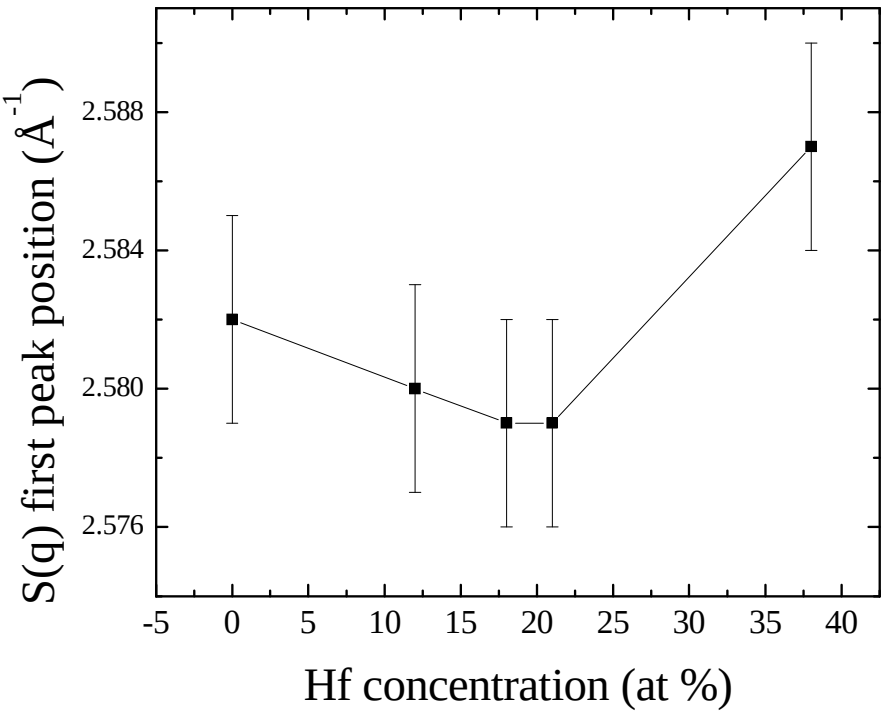

Figure 3.16 – The position of the first peak in $S(q)$ at the liquidus temperature for liquid $Ti_{45}Zr_{(38-x)}Hf_xNi_{17}$ for all Hf concentrations studied.

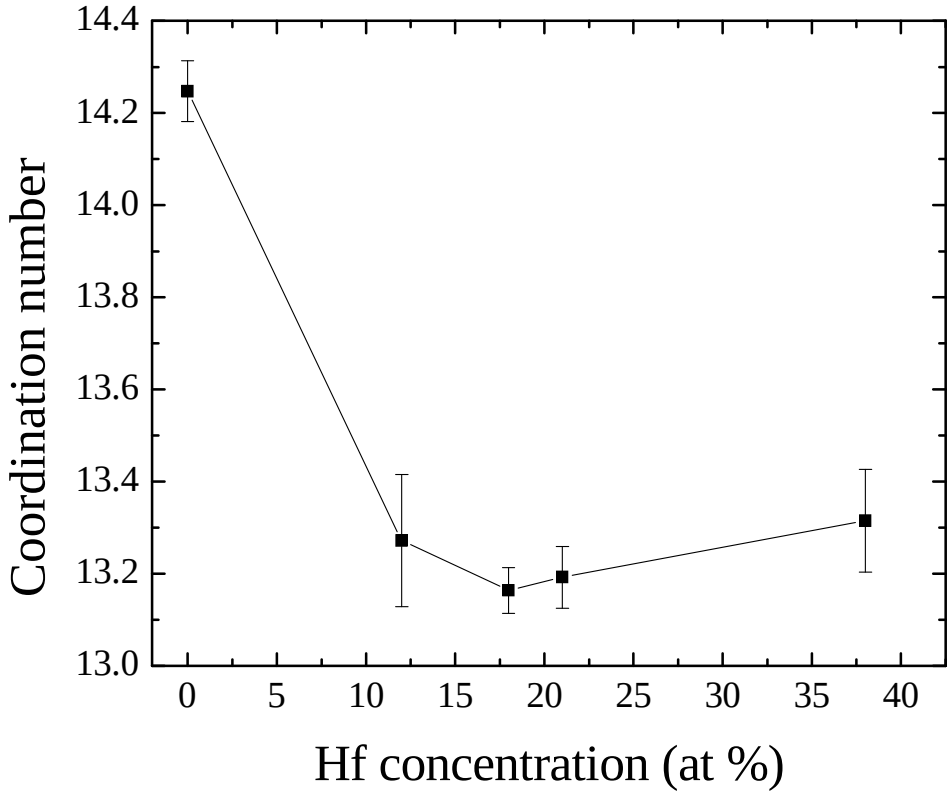

Figure 3.17 – The coordination number at the liquidus temperature for liquid $Ti_{45}Zr_{(38-x)}Hf_xNi_{17}$ for all Hf concentrations studied.

Representative plots of the diffracted intensities for β for x=0, 12 and 18 are shown in Figure 3.18. Interestingly, the bcc lattice constant, *a*, decreases with increasing Hf concentration (Figure 3.19). The cause of the contraction is an increasing number of Ni-Ti bonds, which will be explained in §3.3.2.3.

As previously mentioned, which phases are formed during secondary crystallization depends on the Hf concentration of the alloy. A Rietveld refinement, using the GSAS software with the EXPGUI graphical frontend [14], was made on the diffracted intensity measurements following the second recalescence and before the low temperature α-β transition. The results of the refinement confirm the formation of the C14 (P63/mmc) phase during the second recalescence from the $Ti_{45}Zr_{(38-x)}Hf_xNi_{17}$ liquid for x = 0, 12, and 18 and a Ti_2Ni-type structure (cF96) for x = 21 and 38. For all compositions the primary β(Ti/Zr/Hf/Ni) phase was included in the refinement. The best convergence was obtained assuming only the C14 or the Ti_2Ni-type secondary phase; no case of a mixed secondary phase was observed. Results of the refinement for $Ti_{45}Zr_{20}Hf_{18}Ni_{17}$ after secondary recalescence with the first four β reflections marked, and with all reflections for both phases marked are shown in Figure 3.20. The results for $Ti_{45}Hf_{38}Ni_{17}$ are shown in Figure 3.21. From these figures it is evident that there is a high degree of overlap between the β diffraction peaks and the peaks from the secondary crystallization for all Hf concentrations.

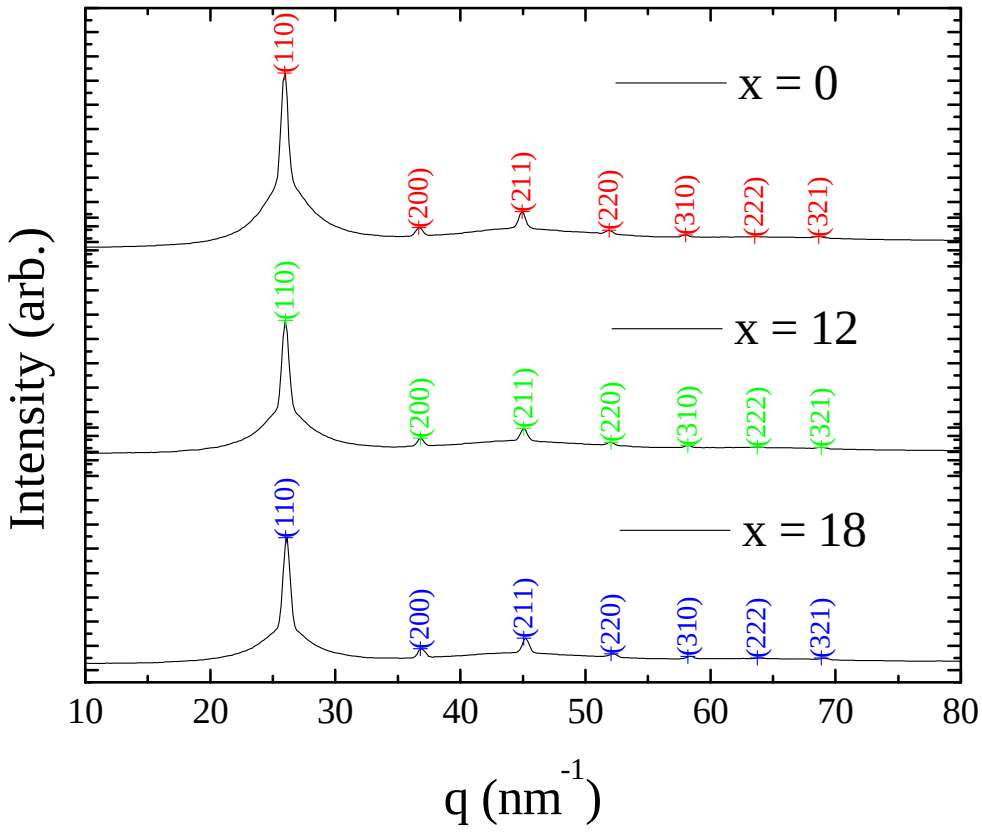

Figure 3.18 – The x-ray diffraction data for β(Ti/Zr/Hf/Ni) for several Hf concentrations showing characteristic BCC diffraction peaks.

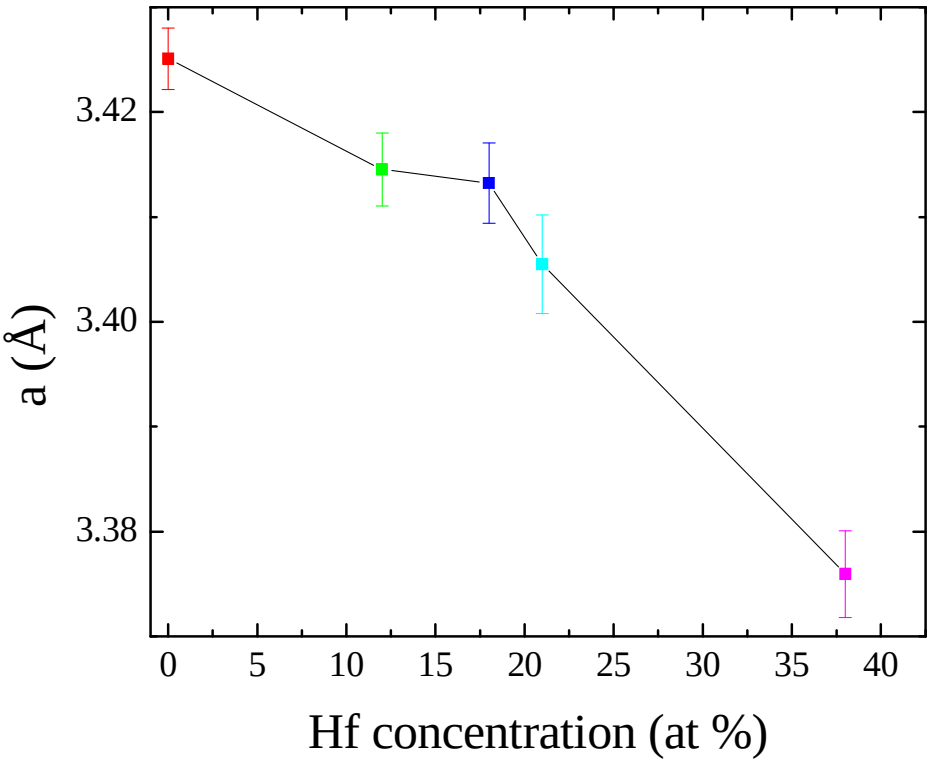

Figure 3.19 – The measured lattice parameter, a, for β(Ti/Zr/Hf/Ni) at 863 ± 3 °C as a function of Hf concentration (*x*) in the $Ti_{45}Zr_{(38-x)}Hf_xNi_{17}$ alloy, showing a decrease with increasing Hf.

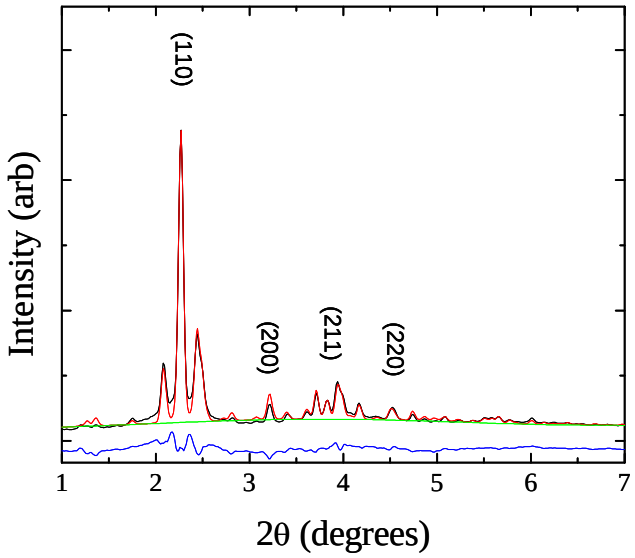

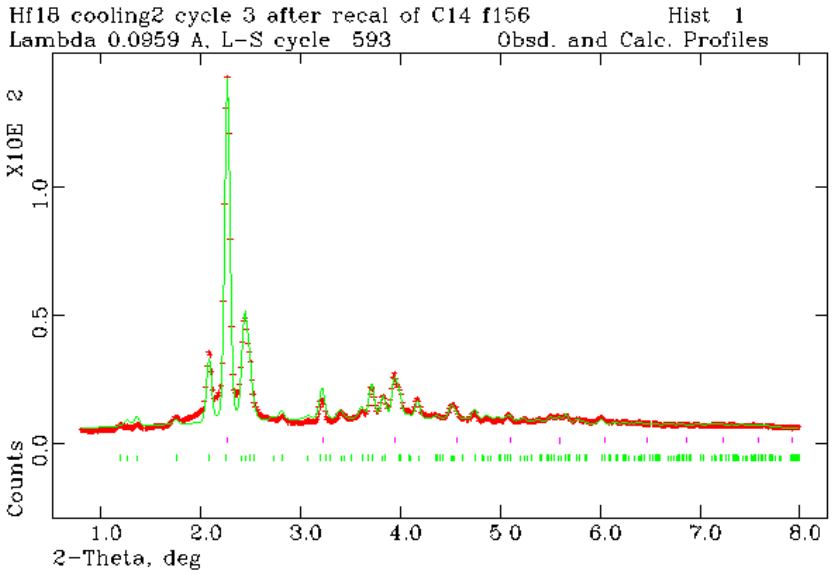

Figure 3.20 – The results of a Rietveld refinement for a $Ti_{45}Zr_{20}Hf_{18}Ni_{17}$ liquid after secondary recalescence showing (a) the data and fit using the C14 and β-phase, with the first four β peaks indicated, and (b) the same data, with the ideal positions for reflections from the C14 and β-phase phases indicated by the tick marks.

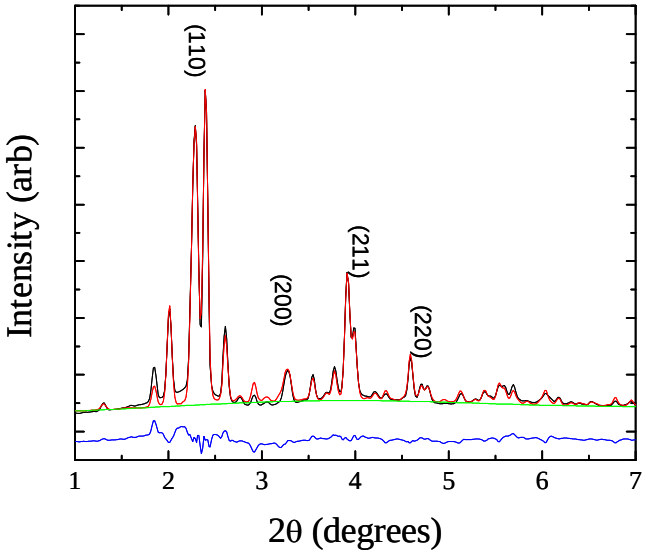

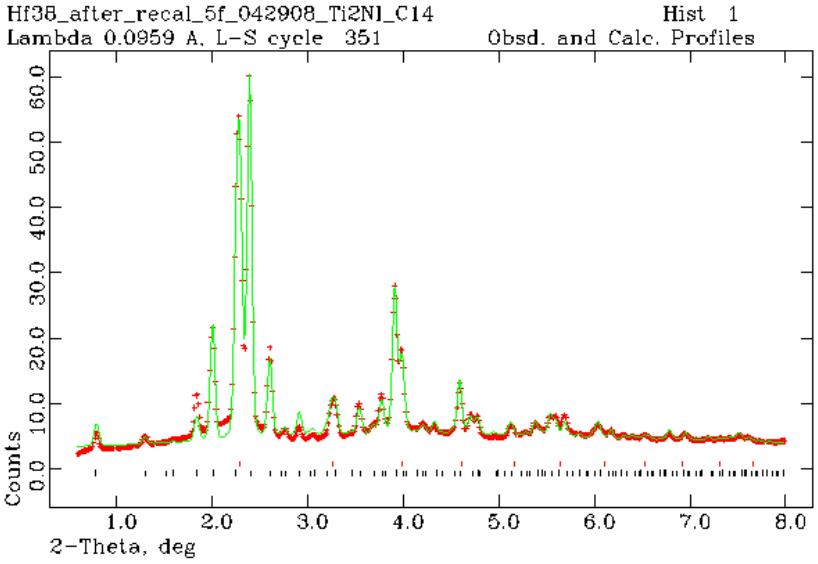

Figure 3.21 – The results of a Rietveld refinement for a $Ti_{45}Hf_{38}Ni_{17}$ liquid after secondary recalescence showing (a) the data and fit using the cF96 and β-phase, with the first four β peaks indicated, and (b) the same data, with the ideal positions for reflections from the cF96 and β-phase phases indicated by the tick marks.

3.3.2.3. SEM studies of solidification microstructures

Micrographs from scanning electron microscopy (SEM, as described in Chapter 2) were made in secondary electron imaging (SEI) mode for ESL-processed $Ti_{45}Zr_{(38-x)}Hf_xNi_{17}$ samples. These results show that the microstructures and phase formation are a function of the Hf concentration of the liquids, in agreement with the results already discussed. A micrograph of the $Ti_{45}Zr_{38}Ni_{17}$ sample is shown in Figure 3.22. It is evident that two qualitatively different regions formed during solidification. There are dark, circular (likely spherical) grains of one phase, and a lightly colored phase that fills the intermediate spaces between the circular grains. Figure 3.23 shows micrographs from $Ti_{45}Zr_{(38-x)}Hf_xNi_{17}$ samples for x = 0, 18, 21, and 38. The average size of the dark grains decreased with increasing Hf concentration of the liquids. For x = 0, the average grain diameter was about 10μm, for x = 18 it was about 5μm. For x = 21 the grains became less circular and were often elongated or more irregular. For x = 38 the dark grains were again irregular and the average diameters of either the dark or light grains was about 1μm.

Energy dispersive x-ray spectroscopy (EDS) measurements, as described in Chapter 2, confirmed the expected partitioning of Ni in all samples. Results of the EDS measurements are shown in Figure 3.24 through Figure 3.27. With increasing Hf concentration in the alloys, the remaining liquid after primary recalescence was richer in Ni than the β-phase, as already discussed. These results, then, suggest that the lightly colored regions correspond to the secondary phase and the dark colored regions to the α(Ti/Zr/Hf/Ni) that forms from the α-β transition.

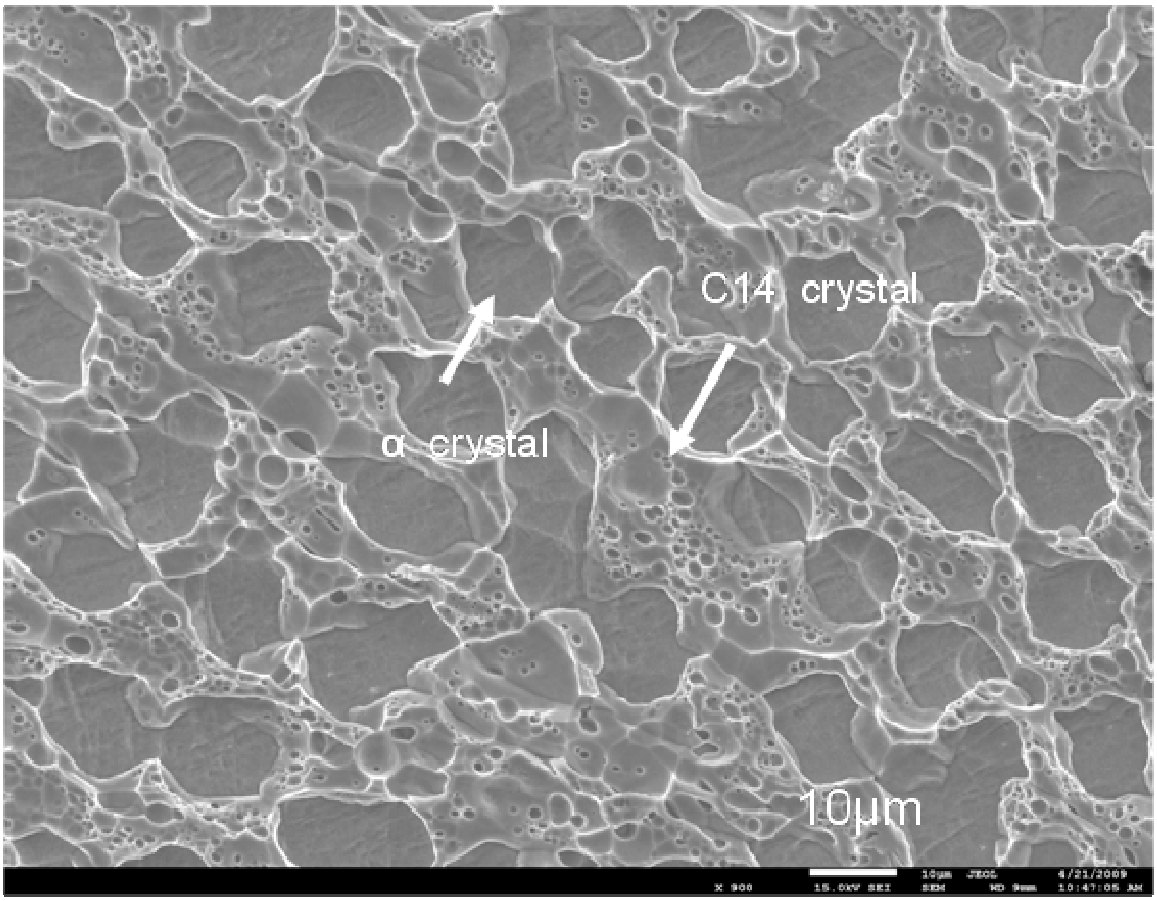

Figure 3.22 – A SEM micrograph of a $Ti_{45}Zr_{38}Ni_{17}$ sample after solidification of the liquid in BESL showing two distinct phase regions; phase identification was inferred from EDS data.

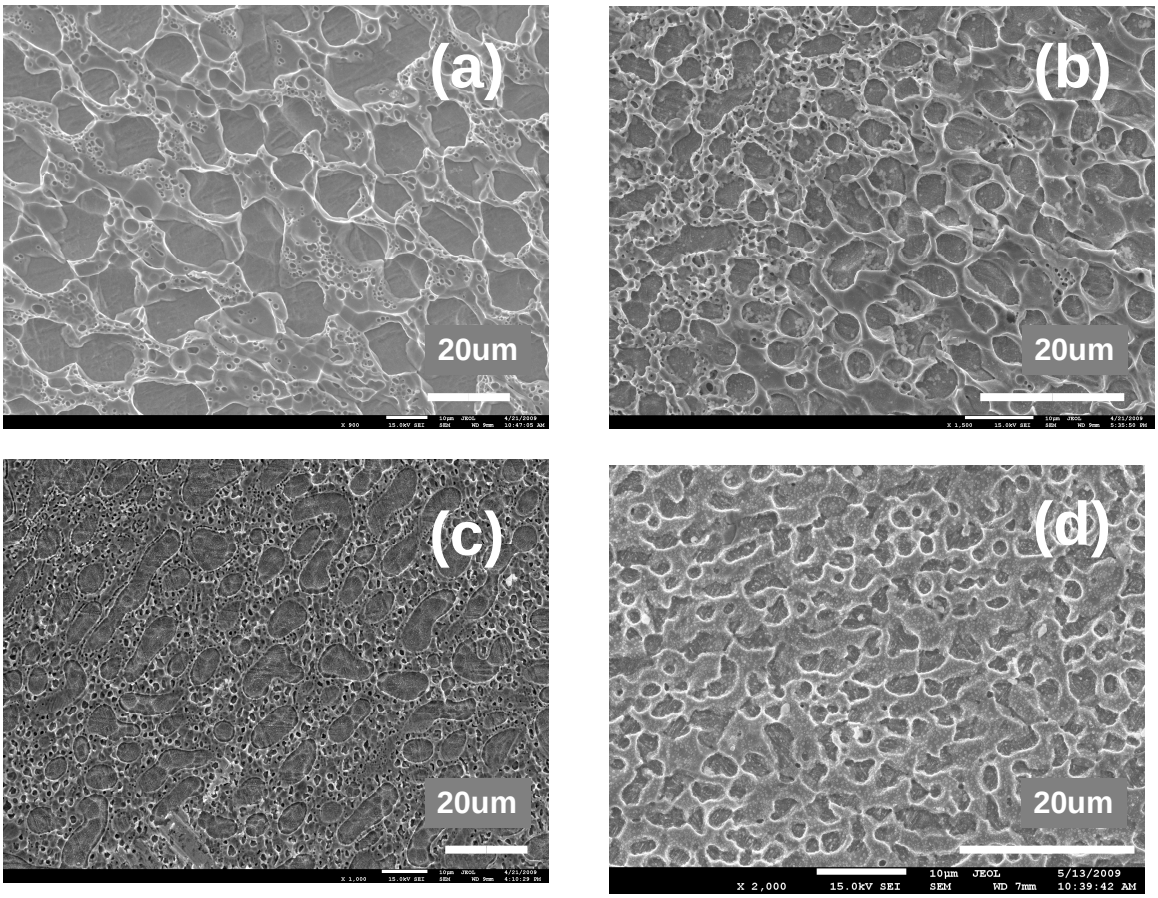

Figure 3.23 – SEM micrographs of $Ti_{45}Zr_{(38-x)}Hf_xNi_{17}$ samples solidified from the liquid in BESL for (a) x = 0, (b) x = 18, (c) x = 21, and (d) x = 38.

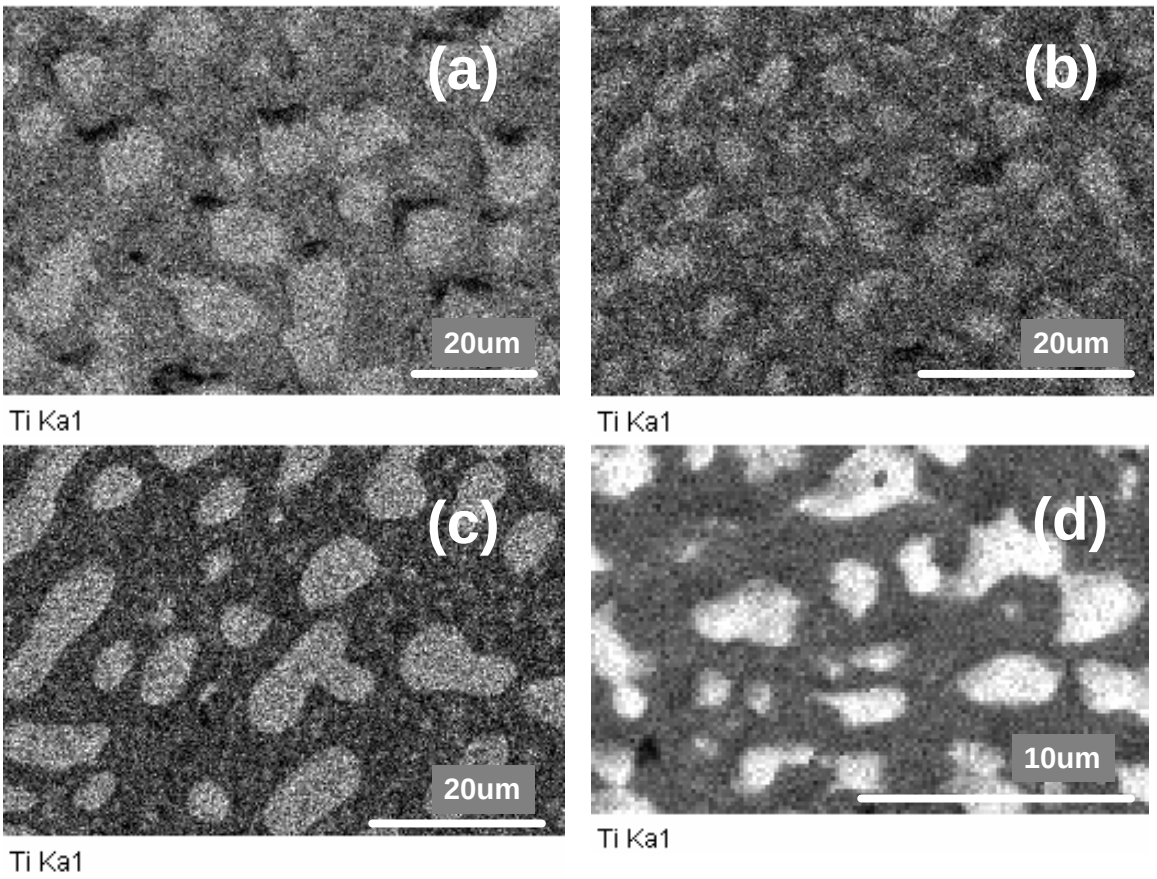

Figure 3.24 – Elemental maps for Ti, from EDS data, for $Ti_{45}Zr_{(38-x)}Hf_xNi_{17}$ samples solidified from the liquid in BESL for (a) x = 0, (b) x = 18, (c) x = 21, and (d) x = 38.

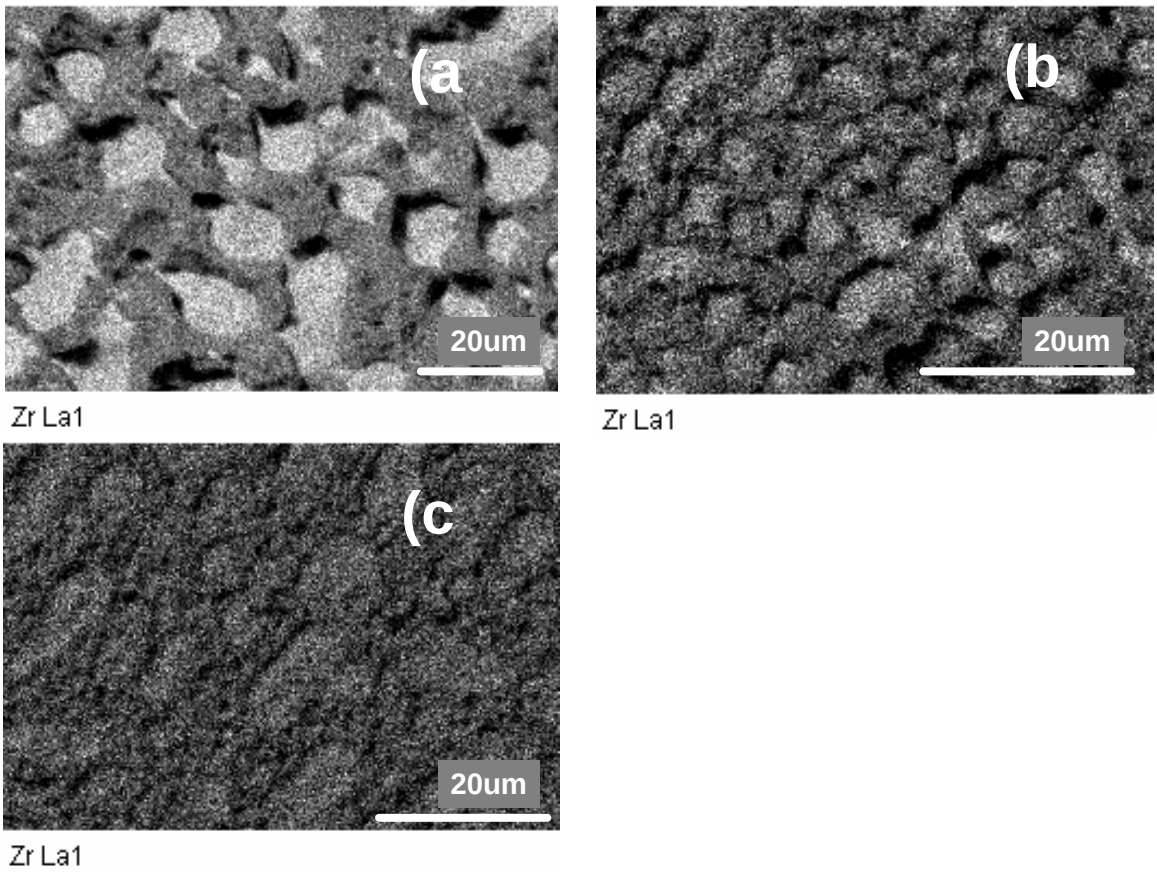

Figure 3.25 – Elemental maps for Zr, from EDS data, for $Ti_{45}Zr_{(38-x)}Hf_xNi_{17}$ samples solidified from the liquid in BESL for (a) x = 0, (b) x = 18, and (c) x = 21.

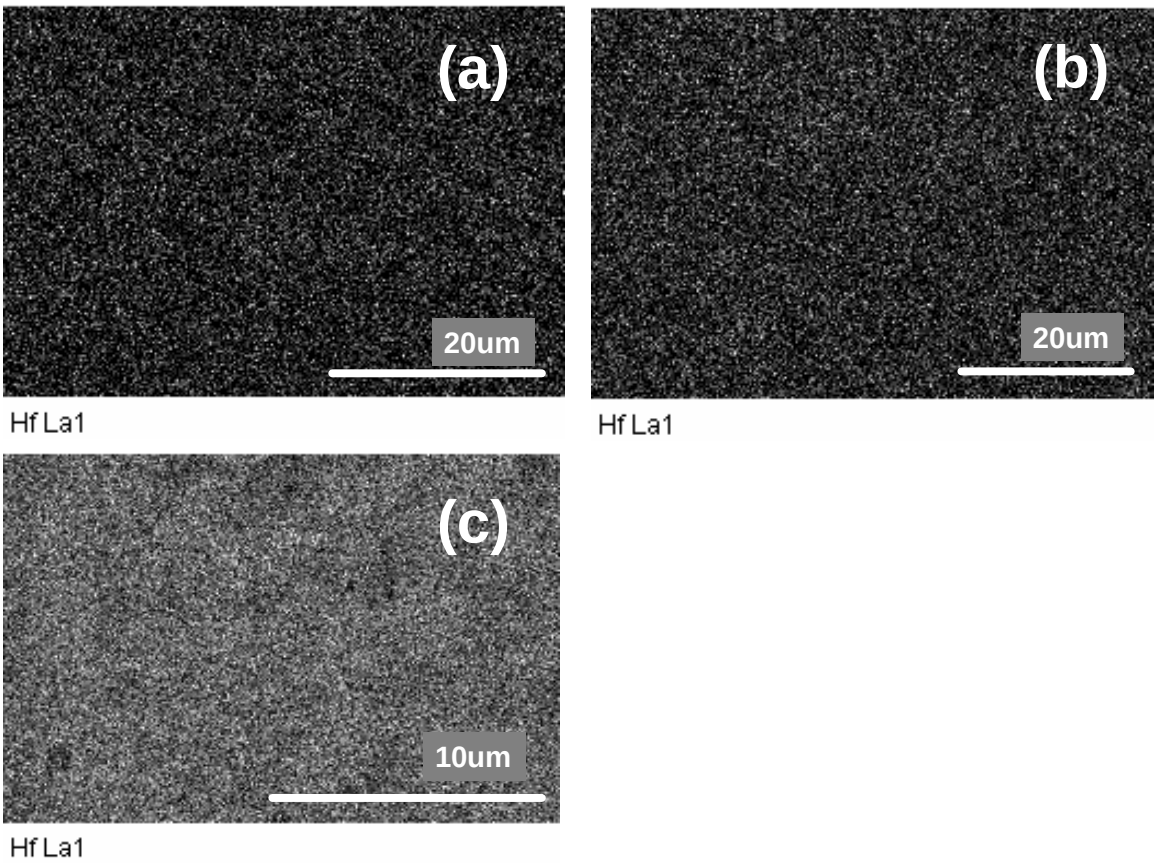

Figure 3.26 – Elemental maps for Hf, from EDS data, for $Ti_{45}Zr_{(38-x)}Hf_xNi_{17}$ samples solidified from the liquid in BESL for (a) x = 18, (b) x = 21, and (c) x = 38.

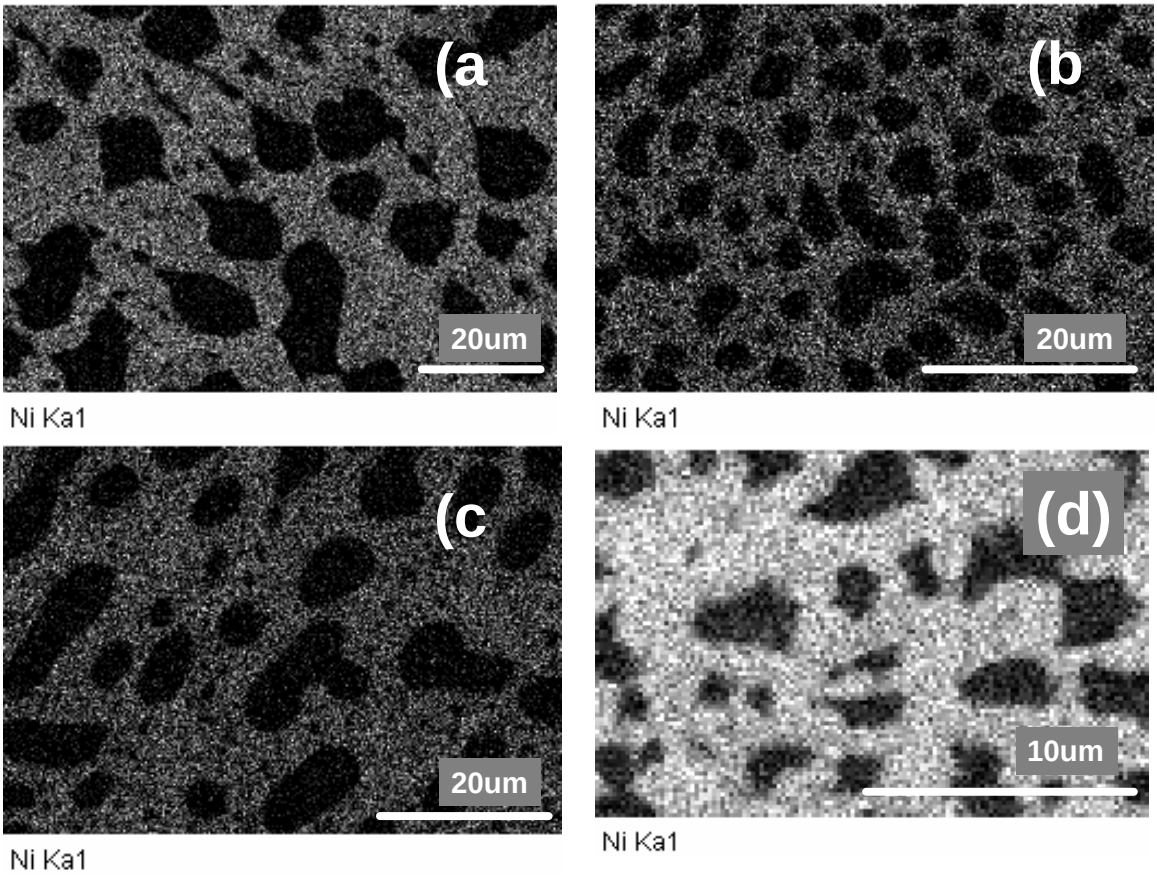

Figure 3.27 – Elemental maps for Ni, from EDS data, for $Ti_{45}Zr_{(38-x)}Hf_xNi_{17}$ samples solidified from the liquid in BESL for (a) x = 0, (b) x = 18, (c) x = 21, and (d) x = 38.

From Figure 3.24 and Figure 3.27, respectively, Ti and Ni were partitioned in all samples studied. From Figure 3.25 and Figure 3.26, respectively, an interesting decrease in the partitioning of Zr, and little or no partitioning of Hf were seen with increasing Hf. Further, EDS measurements were made on grains of the α-phase for x = 0, 18, and 38; the results are given in Table 3.4. These results show that the α-phase is, in fact, becoming slightly richer in Ni as the Hf concentration of the starting alloy is increased, although it is still depleted with respect to the composition of the homogeneous liquid before solidification. This result explains the shrinking grain size and the decrease in the BCC lattice parameter. The grain size is determined in part by diffusion of Ni into the β-phase regions and, based on the relative solubilities of Ni in Hf and Zr, an increase in Hf and decrease in Zr would slow the diffusion of Ni. Also, with increasing Ni in the β-phase, there will be more of the shorter Ni-Ti bonds, leading to the decreased lattice parameter with increasing Hf concentration. Further implications of these results will be discussed in §3.5.

3.3.3. Liquid density and physical properties

The density was measured for $Ti_{45}Zr_{(38-x)}Hf_xNi_{17}$ liquids for all values of *x* by Dr. Robert Hyers at the University of Massachusetts, Amherst, MA (see Chapter 2). The number density, or atomic volume (atoms/$Å^3$), was calculated from the bulk density by normalization using the atomic weight of the alloy. A plot of the number density for all samples, as a function of temperature, is shown in Figure 3.28. The number density at the liquidus temperature was determined as a function of Hf concentration, and shows a maximum near the phase formation boundary composition (Figure 3.29).

Table 3.4 – The compositions of the β-phase grains, and composition ratios, for Ti45Zr(38-x)HfxNi17 samples for various values of *x*, measured by EDS.

x	**Ti (at %)**	**Zr (at %)**	**Hf (at %)**	**Ni (at %)**	**Ti:(Zr/Hf) ratio**	**Ti:Ni ratio**
0	51.25	46.27	-	2.48	1.11	20.67
18	53.48	23.26	18.76	4.50	1.27	11.88
38	60.20	-	32.76	7.03	1.84	8.56

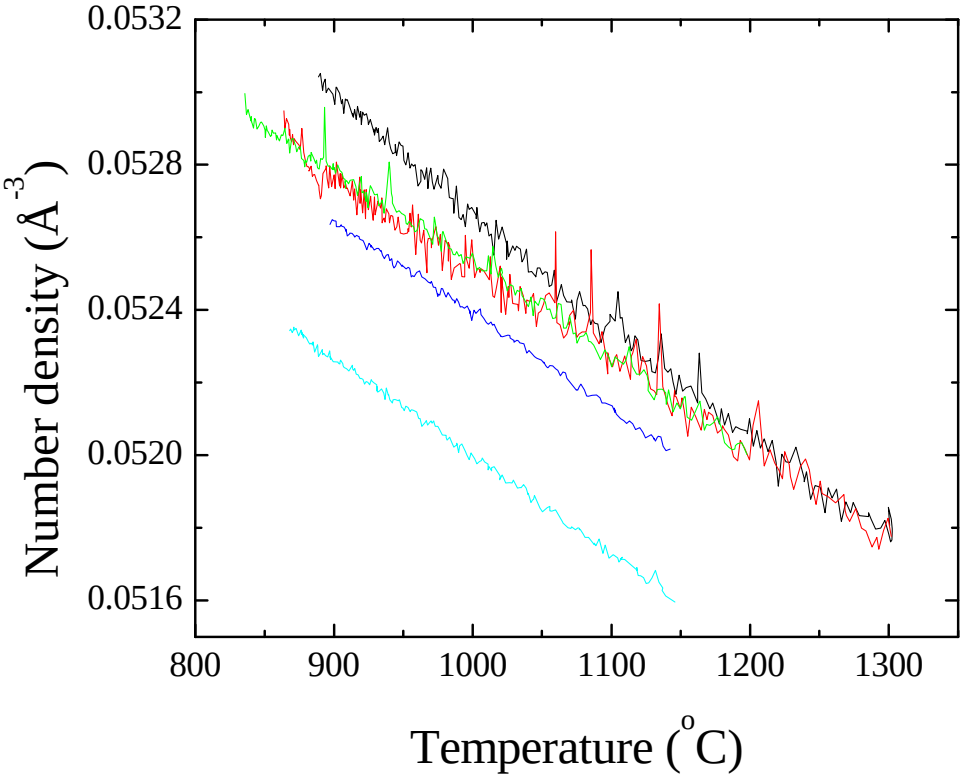

Figure 3.28 – The measured number density as a function of temperature for $Ti_{45}Zr_{(38-x)}Hf_xNi_{17}$ liquids with x = 38 (black line), x = 21 (red), x = 18 (green), x = 12 (dark blue), and x = 0 (light blue).

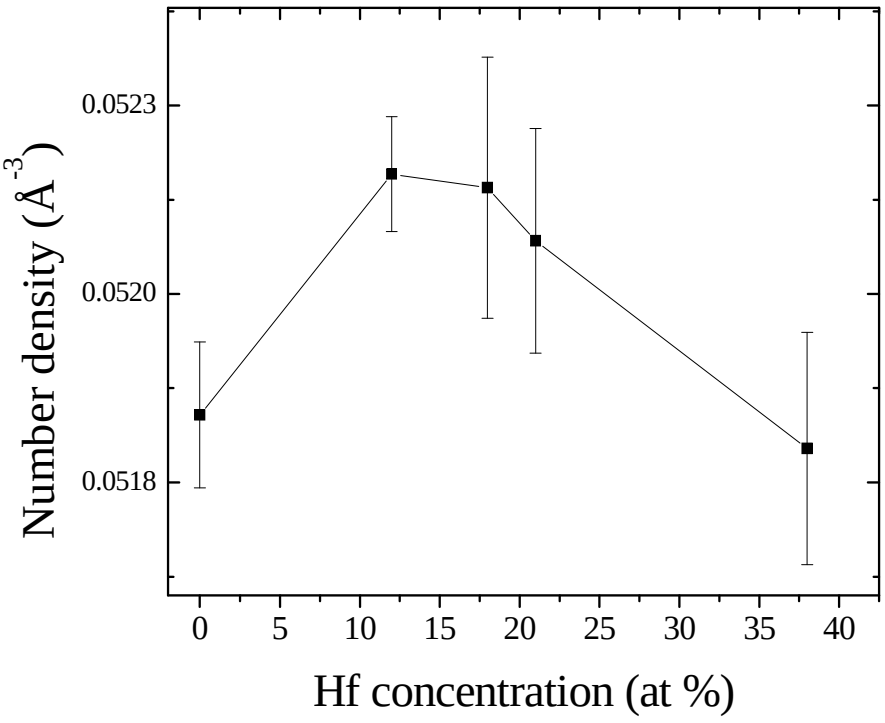

Figure 3.29 – The number density for $Ti_{45}Zr_{(38-x)}Hf_xNi_{17}$ liquids at the liquidus temperature as a function of Hf concentration, *x*.

The volume thermal expansion coefficient, κ, given by

$$\kappa = -\frac{1}{\rho(T)}\frac{\partial \rho}{\partial T},$$

was calculated at the liquidus temperature, and results are shown in Figure 3.30. There is a minimum near the phase formation boundary composition, and a large increase from there to x = 38. The peak in Figure 3.29 indicates a contraction then expansion of the liquid structure. The minimum in Figure 3.30 suggests strengthening atomic bonds as the Hf concentration increases up to that of the phase formation boundary, and weakening bonds with further increases in the Hf concentration. These results are internally consistent, but there is some conflict with the $G(r)$ data of Figure 3.15, which show an expansion of the nearest neighbor interatomic separation, and an expansion then contraction of the second nearest neighbor separation. It should be noted that the density measured is the bulk density of the liquid sample, while the scattering data indicate changes on the atomic scale.

3.4. Analysis by simulation and modeling

Atomic configurations were modeled using a Reverse Monte Carlo (RMC) simulation, and the interatomic cutoff distances were optimized using the methods described in Chapter 2. All RMC fits were performed using $S(q)$ as the input data, and no improvement was seen by fitting to $g(r)$. Figure 3.31 shows a typical RMC fit to input data with good agreement.

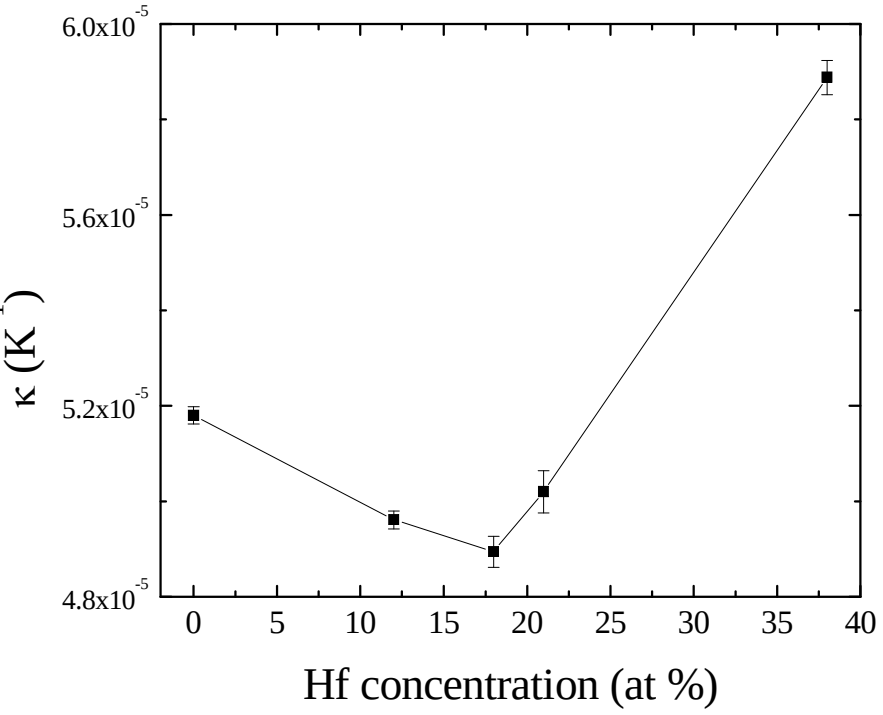

Figure 3.30 – The volume thermal expansion coefficient, κ, calculated for $Ti_{45}Zr_{(38-x)}Hf_xNi_{17}$ liquids at the liquidus temperature as a function of Hf concentration, *x*.

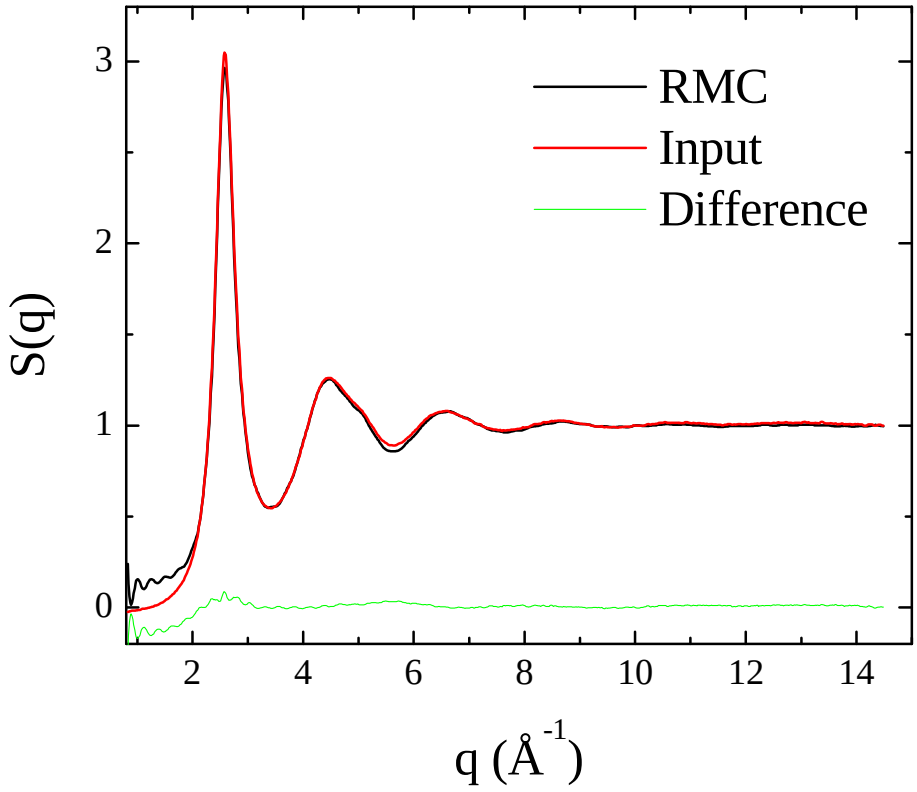

Figure 3.31 – RMC fit (black line) to input *S*(*q*) data (red line) and the difference (green line) for a $Ti_{45}Zr_{20}Hf_{18}Ni_{17}$ liquid at 1000 °C, showing good agreement.

Atomic configurations from RMC were characterized using the Honeycutt-Andersen (HA) index and Bond Orientational Order (BOO) parameter analyses discussed in Chapter 1. Figure 3.32 shows the HA index calculations for the $Ti_{45}Zr_{(38-x)}Hf_xNi_{17}$ liquids with changing temperature for x = 0, 18, 21, and 38. The icosahedral and distorted icosahedral indices are most frequent for all temperatures, and in the liquids with Hf concentration below 21 at.% the icosahedral order increases with supercooling, while in the liquids with Hf concentration above 21 at.%, the icosahedral order does not change with supercooling (Figure 3.33). Figure 3.34 shows the results of a BOO parameter calculation for the $Ti_{45}Zr_{20}Hf_{18}Ni_{17}$ liquid with changing temperature. Those data are representative of the BOO calculation for all Hf concentrations studied; the results did not show a strong dependence on composition or temperature. This analysis confirmed icosahedral order in the liquids, due to the prominence of Q6 and Q10, along with other cubic or hcp symmetries, consistent with the HA index result.

Atomic bonding in the alloy liquid was examined by analysis of the enthalpy of mixing between constituents. A model for the enthalpy of mixing in the $Ti_{45}Zr_{(38-x)}Hf_xNi_{17}$ liquids was constructed using a modified Bergman cluster, following the work of Hennig on Ti-Zr-Ni [15]. In this cluster, a central Ni atom is surrounded by 12 Ti atoms in the first shell, 20 Zr and 12 Ni atoms in the second shell, and the remaining atoms in the intra-cluster, or “glue” sites. By substituting Hf at the Zr sites, binary heats of mixing were obtained as a function of Hf concentration for the outer two layers. The binary heats of mixing for equilibrium liquids, calculated by Miedema and presented in reference [16], were plotted and fit by a third-order polynomial, and values interpolated for the concentrations studied.

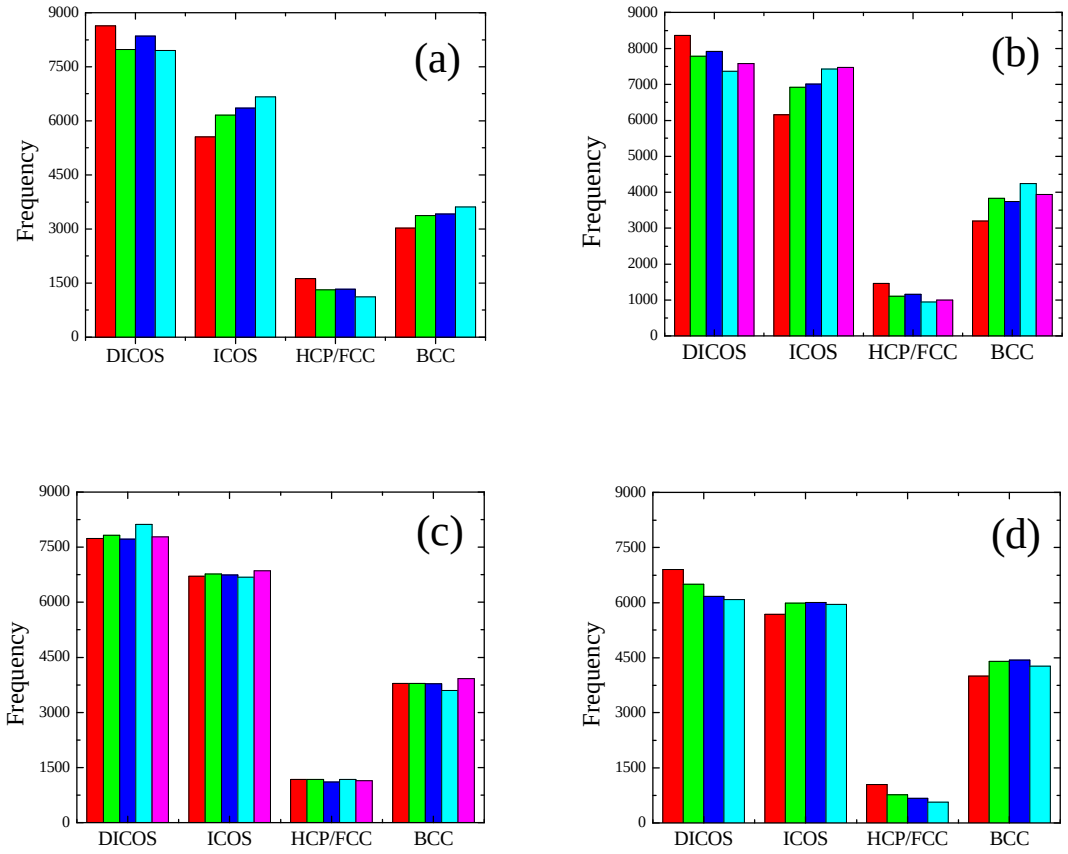

Figure 3.32 – The HA index analysis for the $Ti_{45}Zr_{(38-x)}Hf_xNi_{17}$ liquids for (a) x = 0, (b) x = 18, (c) x = 21, and (d) x = 38 at various temperatures (the highest temperature on the color scales is in red); the analysis for x = 12 is not shown.

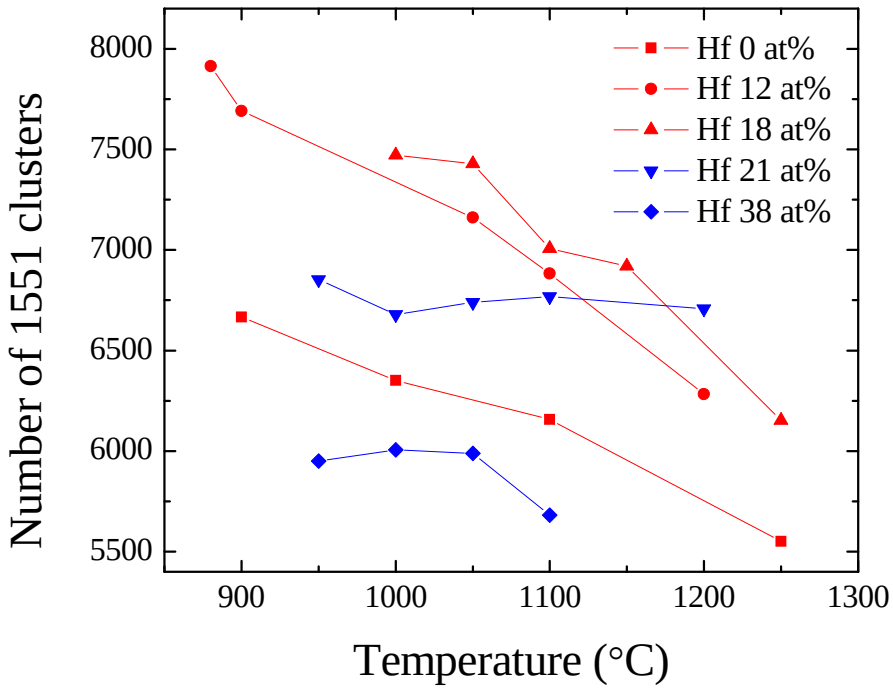

Figure 3.33 – The number of 1551 (icosahedral) clusters, determined from the HA index analysis, for the $Ti_{45}Zr_{(38-x)}Hf_xNi_{17}$ liquids for all values of *x* with changing temperature.

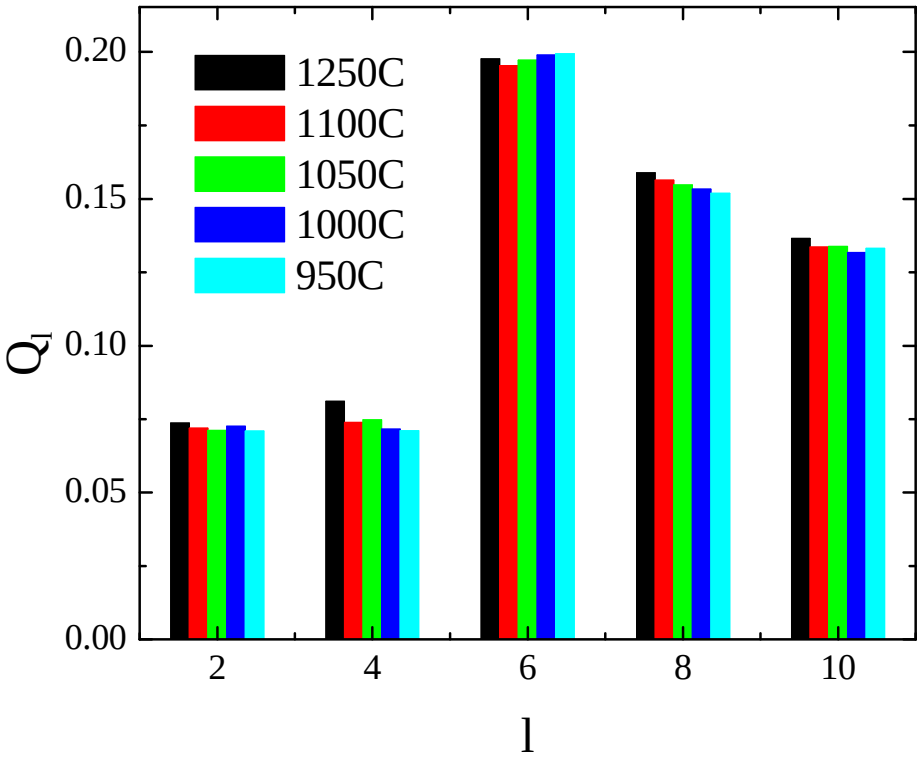

Figure 3.34 – The BOO parameter analysis for the $Ti_{45}Zr_{20}Hf_{18}Ni_{17}$ liquid at various temperatures, showing Q_6 and Q_{10}, indicating icosahedral order in the liquid; little or no temperature dependence is observed, and the presence of other values of Q_l indicates other symmetries in the liquid structure.

To calculate the total heat of mixing for Ni-(Zr, Hf), an admixture of the two components in the appropriate proportion, given for the second shell by

$$H^{2}_{Ni-(Zr,Hf)} = \left(1 - \frac{x}{38}\right) * H^{2}_{Ni-Zr} + \left(\frac{x}{38}\right) * H^{2}_{Ni-Hf}\ , \quad (4.4.1)$$

where H^2 indicates the enthalpy of mixing at the second shell, and x is the Hf concentration in at.%, was constructed. The values for the individual pairs were given by

$$H^{2}_{Ni-Zr} = H_{Ni-Zr}\left(20 * \left(1 - x/38\right) \Big/ 12 + 20 * \left(1 - x/38\right)\right), \text{ and} \quad (4.4.2)$$

$$H^{2}_{Ni-Hf} = H_{Ni-Hf}\left(20 * \left(x/38\right) \Big/ 12 + 20 * \left(x/38\right)\right), \quad (4.4.3)$$

where H represents the value interpolated from the polynomial fit, and the argument of H provides the concentration of Zr or Hf atoms in the second shell. Results of the calculation are shown in Figure 3.35.a for the second shell and Figure 3.35.b for the intra-cluster atoms.

From these, a minimum in the enthalpies of mixing at the 2nd shell and the intra-cluster atoms for Ni-(Zr, Hf), and a crossing of the individual enthalpies of mixing for Ni-Zr and Ni-Hf in the intra-cluster atoms near the phase formation boundary composition, were observed. The figure is consistent with the results for the density and thermal expansion already discussed, which suggest strongest bonding of the Ni-(Zr, Hf) atoms near the phase formation boundary composition.

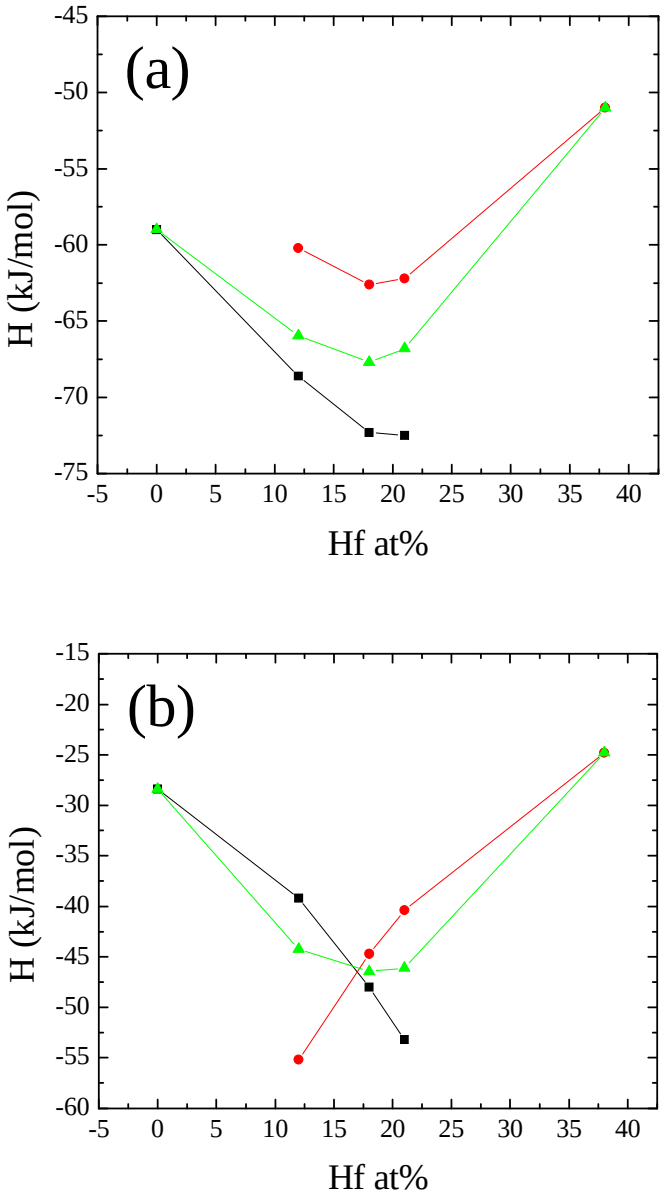

Figure 3.35 – The enthalpies of mixing for Ni-Zr (black), Ni-Hf (red), and total Ni-(Zr, Hf) (green) with increasing Hf concentration, calculated from equation (4.4.1) for (a) the second shell, and (b) the remaining intra cluster atoms in the Bergman cluster model; the enthalpy of mixing for Ni-Ti was constant.

3.5. Summary and conclusions

In this chapter results and analysis of a study using BESL to measure the structures and physical properties of $Ti_{45}Zr_{(38-x)}Hf_xNi_{17}$ alloys with changing Hf concentration, were presented. A sharp phase formation boundary near x = 18-21, previously measured by this group, was confirmed and examined in further detail. The liquid structures were determined over a wide range of temperatures, including in the supercooled state, and characterized by simulation and modeling methods. Crystal structures were determined using Rietveld refinement, and the morphologies and chemical segregation in the solidification microstructures examined using SEM and EDS. Thermo-physical properties, such as liquid supercooling, density, and thermal expansion were determined from experimental data. Bond enthalpies were calculated using a modified Bergman cluster model.

The reduced supercooling of the liquid prior to β-phase formation, T_{rl}, increased from about 0.1 to 0.25 with increasing Hf. The maximum value observed is much larger than for Ti-Zr-Ni alloys, indicating that the addition of Hf makes the liquid and the β-phase increasingly incompatible. The measured T_{rl} does not, however, correlate with the phase formation boundary. A constructed quantity to estimate the reduced supercooling for the remaining liquid after β-phase formation, T_{rs} (and by extension the incompatibility of the liquid and secondary phases), was minimal at the phase formation boundary composition and increased sharply with additional Hf. This suggests that changes in β-phase formation affect the secondary phase formation boundary by altering the

composition of the liquid remaining after primary recalescence. This conclusion is supported by the results for the solidification structures.

For the solidified $Ti_{45}Zr_{(38-x)}Hf_xNi_{17}$ samples for all values of *x*, SEM and EDS studies showed enriched Ni in the secondary phase, enriched Ti in the β-phase, and very little or no partitioning of Hf between the two phases. Zr was partitioned in the alloy with no Hf, showing enrichment in the β-phase. With increasing Hf, the distribution of Zr became more homogeneous, thus lowering the Zr concentration in the β-phase; the Ni concentration in the β-phase increased from about 2.5 at.% to 7 at.% and the Ti concentration in the β-phase increased from about 51 at.% to 60 at.% for the range of Hf concentrations studied. The result for Ni is surprising considering the lack of solubility of Ni in β-Hf, but the increase in the Ti concentration of the β-phase would have encouraged the formation of more Ti-Ni bonds. This in turn explains the observed contraction of the β BCC lattice with increasing Hf, since Ti-Ni bonds are shorter than Ti-(Zr/Hf) bonds.

From a previous study of the Ti-Zr-Ni phase diagram by Lee [17], a mixture of the C14 and α-phases, similar to that observed in this study for Hf concentrations below the phase formation boundary concentration, was found for many alloys with Ni concentrations between 0.1 and 0.25 at.% and (Ti/Zr) ratios in the range from about 1 to 3, including $Ti_{45}Zr_{38}Ni_{17}$. Different phases were found as the (Ti/Zr) ratio was decreased below 1. An FCC Zr_2Ni phase has been found as a metastable product of devitrification of a Zr-based metallic glass, and argued as a crystal approximant for the Zr-based i-phase due to local icosahedral symmetry [18]. In the present study, based on the results of EDS

and crystal structure determination, a similar FCC $(Ti/Zr/Hf)_2Ni$ phase was found as the product of secondary recalescence for $Ti_{45}Zr_{(38-x)}Hf_xNi_{17}$ liquids with $x \geq 21$.

From the above mentioned results, the sharp phase formation boundary measured here can be explained. In the alloy made without Hf, the (Ti/Zr) ratio in the liquid after the recalescence of β is higher than, or close to 1, based on the EDS results showing Zr and Ti enrichment in β. As Hf is added for Zr, the Hf does not partition much, if at all, and thus, if a relatively constant Ti-(Zr/Hf)-Ni composition is favored in β nuclei, the Zr will partition less, which was measured from EDS. Thus, the [Ti/(Zr, Hf)] ratio of the liquid remaining after primary recalescence will decrease until the liquid has left the phase field of C14 and forms the $(Ti/Zr/Hf)_2Ni$, as observed.

Some of the observations in this work warrant additional study. In particular, an examination of alloys with Hf concentration, *x*, in the range $21 \leq x \leq 38$ would be useful to confirm the non-partitioning of Zr with increasing Hf. A physical explanation for the differing behavior of Hf and Zr is still lacking, but may be due to bonding effects that could be explored through simulations. The results of the supercooled liquid structures, and their relationship to secondary phase formation, remain somewhat ambiguous. For liquids with $x \leq 18$ the icosahedral order increases with supercooling, while, for higher Hf-concentrations, the icosahedral order remains constant with supercooling. This result is interesting when compared to the reduced supercooling of Figure 3.11. In this system the icosahedral order is lowest in the liquid with the highest Hf concentration, where supercooling is highest. This could suggest that the Ti2Ni structure is less compatible with order present in the supercooled liquid, possibly helping to explain the sharp nature of the boundary, with no mixing of the secondary phases.

References

1. V. T. Huett, *The Formation, Structure, and Hydrogen Storage Properties of Ti/Zr/Hf Based Quasicrystals and Related Phases*. 2004, Washington University: St. Louis, Missouri.
2. K. F. Kelton and A. I. Goldman, Reviews of Modern Physics, **1993**. **65**: p. 213-230.
3. K. F. Kelton, G. W. Lee, A. K. Gangopadhyay, R. W. Hyers, T. J. Rathz, J. R. Rogers, M. B. Robinson, and D. S. Robinson, Physical Review Letters, 2003. **90**(19).
4. H. W. Sheng, W. K. Luo, F. M. Alamgir, J. M. Bai, and E. Ma, Nature, 2006. **439**(7075): p. 419-425.
5. Y. T. Shen, T. H. Kim, A. K. Gangopadhyay, and K. F. Kelton, Physical Review Letters, 2009. **102**(5): p. 057801-4.
6. G. W. Lee, A. K. Gangopadhyay, T. K. Croat, T. J. Rathz, R. W. Hyers, J. R. Rogers, and K. F. Kelton, Physical Review B, 2005. **72**: p. 174107.
7. G. W. Lee, A. K. Gangopadhyay, K. F. Kelton, R. W. Hyers, T. J. Rathz, J. R. Rogers, and D. S. Robinson, Physical Review Letters, 2004. **93**(3): p. 037802.
8. Center for Computational Materials Science of the United States Naval Research Laboratory. *http://cst-www.nrl.navy.mil/lattice/*. Crystal Lattice Structures Web page 2008.
9. J. Basu and S. Ranganathan, Acta Materialia, 2006. **54**: p. **3637-3646**.
10. X. Qiu, J. W. Thompson, and S. J. L. Billinge, Journal of Applied Crystallography, 2004. **37**: p. 678.
11. J.-P. Hansen and L. Verlet, Physical Review, 1969. **184**(1): p. 151.
12. N. H. March and M. P. Tosi, *Introduction to Liquid State Physics*. 2002: World Scientific.
13. *Smithell's Metals Reference Book*. 7th ed, ed. E.A. Brandes and G.B. Brook. 1992: Butterworth Heinemann.
14. B. Toby, Journal of Applied Crystallography, 2001. **34**(2): p. 210-213.
15. R. G. Hennig, K. F. Kelton, A. E. Carlsson, and C. L. Henley, Physical Review B, 2003. **67**(13): p. 134202.
16. F. R. deBoer, R. Boom, and W. C. M. Mattens, *Cohesion in Metals: Transition Metal Alloys*. 1988: North-Holland.
17. G. W. Lee, *Undercooling, local structure and phase transitions in icosahedral quasicrystal forming Ti-Zr-Ni alloy liquids*. 2004, Washington University.
18. C. Li and A. Inoue, Physical Review B, 2001. **63**(17): p. 172201.

Chapter 4

The Structure and Physical Properties of Supercooled Liquid Bulk Metallic Glass-forming $Cu_{(100-x)}Zr_x$ Alloys

4.1. Introduction and background

As discussed in Chapter 1, bulk metallic glasses (BMGs) have been explored as engineering materials because of their desirable mechanical properties, their disordered microstructure, and their ability to be worked during plastic deformation [1-4]. Most BMG alloys developed thus far are multi-component, often requiring micro-additions; many require costly materials such as Pd and Pt [2, 5]. The discovery of BMGs in binary transition metal alloys is thus quite interesting for engineering applications. Binary BMGs are also more tractable for computer modeling studies, such as those using molecular dynamics (MD) simulations with *ab initio* potentials. At this time, bulk glass formation, with fully amorphous rods of up to 2mm critical casting thickness, has been reported in Cu-Zr alloys for a range of compositions using a simple mold-casting technique [6-9]. The $Cu_{46}Zr_{54}$ alloy, studied here, was used as the basis for ternary and quaternary alloys with up to 1cm critical casting thickness [10]. Recently, those alloys, including the binary, were modeled by Cheng, Ma, and Sheng using MD simulations. They observed the development of icosahedral, Cu-centered clusters in the supercooled liquid region, which stabilize the amorphous structure [11]. Those results will be discussed further in later sections.

In his early work, Turnbull proposed the reduced glass transition temperature, T_{rg} ($T_{rg} = T_g/T_l$, where T_g is the glass transition temperature and T_l is the liquidus temperature) as an indicator of high glass-forming ability (GFA) [12]. This suggests that the best glass-formers should lie at eutectic compositions. The work by Wang at Al. [6] showed the best glass-forming composition in Cu-Zr binary to be at a slightly off-eutectic composition, qualitatively consistent with results for other ternary and quaternary systems [13, 14]. The improved GFA was suggested to be caused by inhibited crystal development related to a skewed eutectic coupled zone [14, 15]. Following this technique, binary BMGs were found in Ni-Nb [16] and Pd-Si [17] at off-eutectic compositions.. Highmore and Greer posited improved glass-forming ability at the so-called metastable eutectic point [18], constructed by extending steep liquidus lines of the equilibrium diagram to intersection.

The frustration model that motivates the empirical “rules” of multiple components and atomic size mismatches for BMG alloy development does not hold in binary systems. This suggests a different mechanism for glass formation in these alloys than in multi-component glasses. Structural changes in the liquid that make it incompatible with the equilibrium crystal structure would promote glass formation. One such change would be separation of the liquid into regions of distinct chemical and/or topological order. Such structural changes due to cluster development have been predicted from MD simulations of these alloys [11, 19, 20].

In the present study, the structure and physical properties of liquid $Cu_{(100-x)}Zr_x$ alloys were investigated over a range of temperatures, including the supercooled liquid, for x = 36, 40, 54, 60, and 70 using the Beamline Electrostatic Levitation (BESL) method.

BESL allows *in-situ,* containerless processing and diffraction measurements of levitated liquids, and is described in detail in Chapter 2 and elsewhere [21]. Results from studies of the maximum supercooling and structures of the supercooled liquids will be discussed. Diffraction measurements of the supercooled liquid, changes in the physical properties, and analysis of simulation and modeling studies reveal a transition to chemically and structurally inhomogeneous state at a temperature near 845°C. The correlation to improved GFA relative to an off-metastable eutectic composition will be discussed. The following sections present those results in detail, with a complete discussion in §4.5.

4.2. Experimental methods

All of the $Cu_{(100-x)}$ Zr_x samples were prepared using the method of arc-melting on a water-cooled Cu hearth, as described in Chapter 2. The sample with x = 54 was prepared at Washington University by the author, and the remaining compositions were prepared at Ames Laboratory (AML), Ames, IA by Dr. Matthew J. Kramer. Temperature measurements were made as a function of time for all samples during free cooling and step-cooling of the liquid using the ESL methods described in Chapter 2. Studies of the liquid structure were made using BESL, and measurements were made of the bulk density by Dr. Robert Hyers, University of Massachusetts, Amherst, MA. All analyses for the sample with x = 54 were performed at Washington University by the author; the analysis of $I(q)$ and calculations of $S(q)$ and $g(r)$ for the remaining compositions were performed by Kramer; all subsequent analyses presented in this dissertation for those compositions were performed by the author.

For the study of amorphous solid $Cu_{46}Zr_{54}$, samples were prepared by the melt-spinning technique and diffraction measurements were made using the method for

stationary diffraction studies, both described in Chapter 2. For the crystal structures, diffraction measurements were made of the $Cu_{46}Zr_{54}$ sample after recalescence of the radiation-cooled liquid using BESL. Melt-spun samples, devitrified by heating the as-quenched ribbons in a furnace filled with Ar gas, at 370°C for 400 minutes, were studied using the low energy XRD method described in Chapter 2.

4.3. Results

4.3.1. Metastable eutectic diagram and liquid supercooling

From the Cu-Zr binary phase diagram, shown in Figure 4.1 (taken from reference [22]) the composition range between 30 and 80 at. % Zr has many intermetallic phases bordered by steep liquidus lines. Highmore and Greer posited improved glass-forming ability for alloys with compositions prepared near a metastable eutectic point, determined by extending the liquidus curves in such a region [18]. Following their method, a metastable eutectic diagram, shown in Figure 4.2, was constructed for $Cu_{(100-x)}Zr_x$ by plotting points determined from the binary diagram of Figure 4.1 and fitting curves to extend the liquidus lines. The five compositions studied are marked by the vertical lines in Figure 4.2; two compositions were studied below the metastable eutectic point (near 49 at.%, or 58 wt.%, Zr), one very near it, and two above it. The temperatures measured as a function of time during free cooling of $Cu_{(100-x)}Zr_x$ liquids for x = 36, 54, 60, and 70 are shown in Figure 4.3.

The reduced supercooling, defined as

$$T_{rl} = \frac{\left(T_l - T_r\right)}{T_l},$$

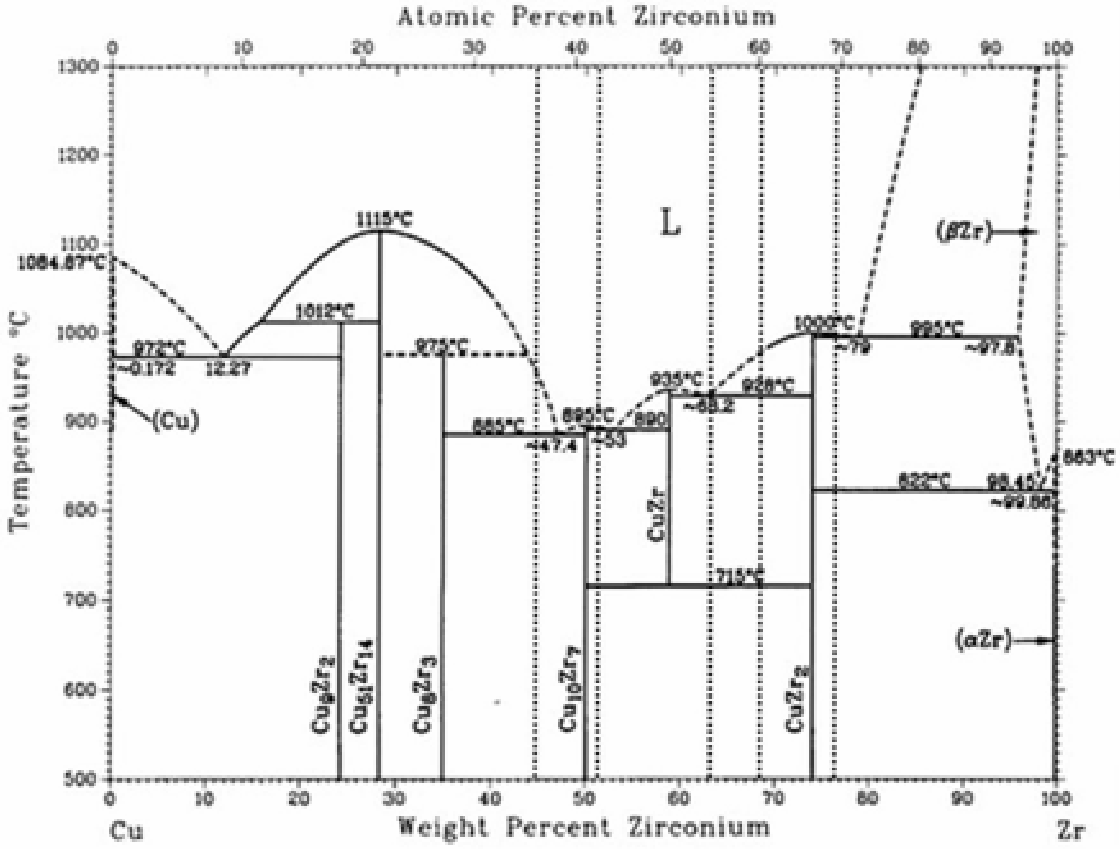

Figure 4.1 – The Cu-Zr binary phase diagram; taken from reference [22].

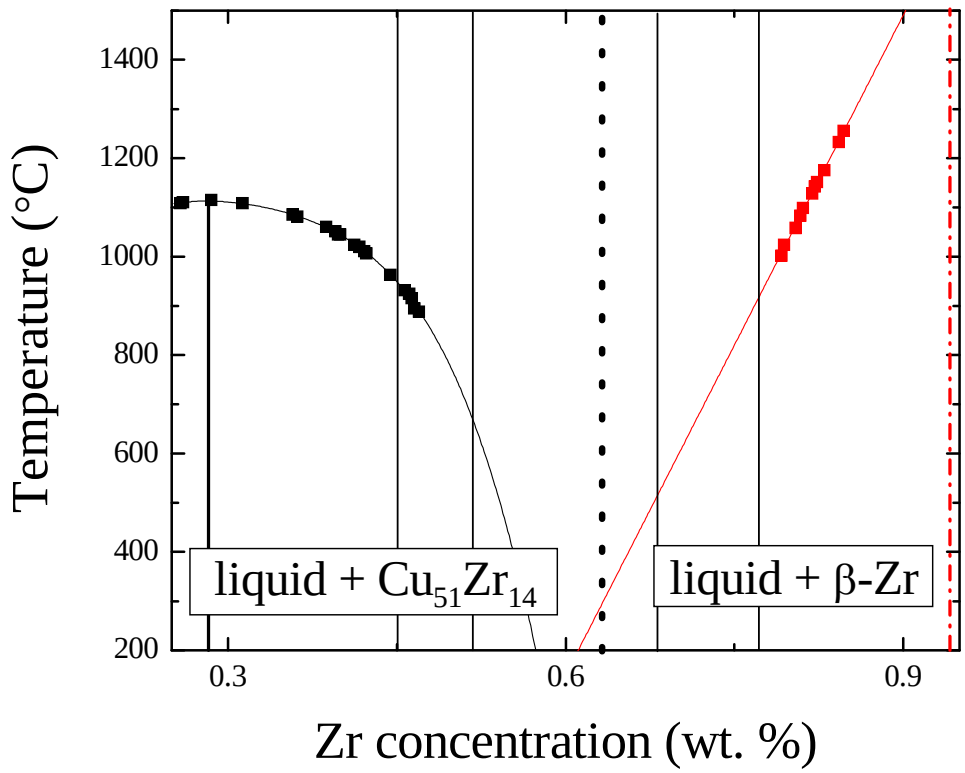

Figure 4.2 – A metastable eutectic in the binary Cu-Zr phase diagram, determined by extensions of the liquidus curves in the composition range studied; the five compositions studied in BESL are marked by the vertical lines; $Cu_{46}Zr_{54}$ is marked by the dashed vertical line.

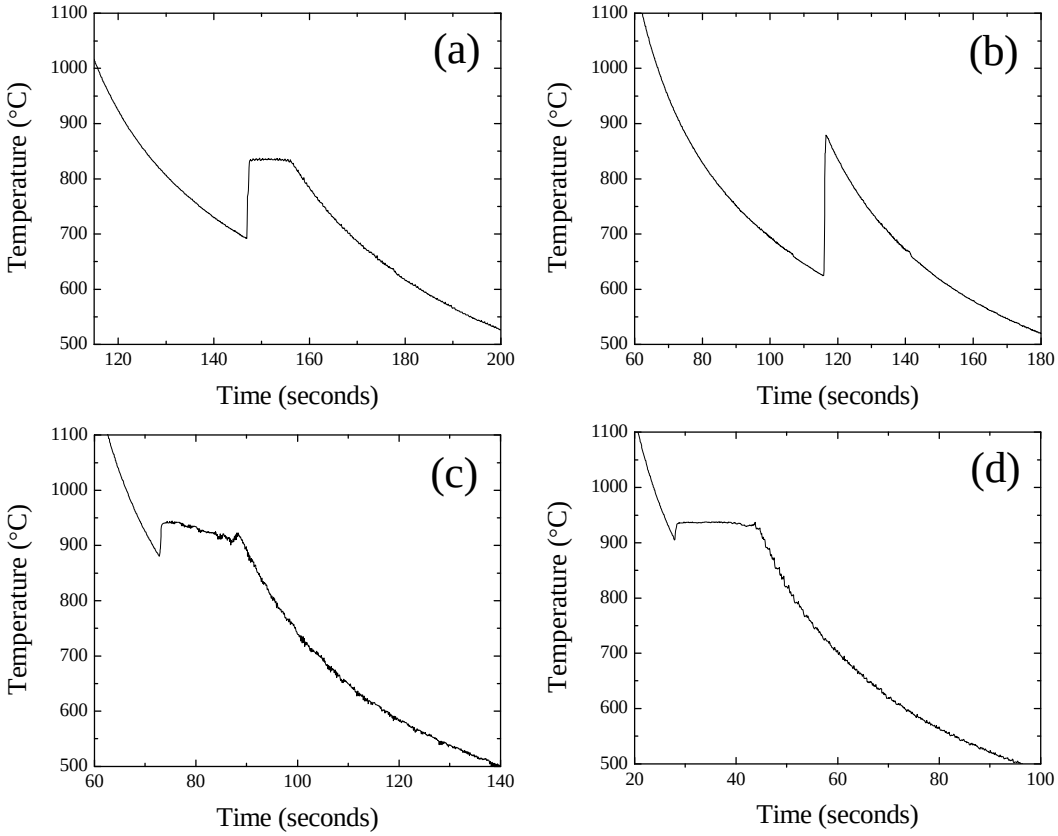

Figure 4.3 – The temperature measured as a function of time for $Cu_{(100-x)}Zr_x$ liquids during free cooling for (a) x = 36, (b) x = 54, (c) x = 60, and (d) x = 70; note the different scales on the time axis, the temperature scales are the same.

where T_l is the liquidus temperature and T_r is the recalescence temperature, is a reflection of the nucleation barrier for the primary crystallizing phase, which is a function of the driving free energy and the interfacial free energy between the liquid and crystal phases (see Chapter 1 for a discussion of nucleation theory). The reduced supercooling is thus an important parameter in the study of supercooled liquids.

Figure 4.4 shows the reduced supercooling for the $Cu_{(100-x)}Zr_x$ liquids as a function of x; the values are listed in Table 4.1. The liquidus temperatures were obtained from reference [22]. From Figure 4.4, a sharp decrease in reduced supercooling is seen with increasing Zr concentration above 54 at.% Zr. This suggests that the liquid and crystal structures are similar for Zr concentrations below 54 at.%, and less so above it, with a sudden change near that point. This is possibly due to cluster development, and could be related to an off-metastable eutectic composition. Those ideas will be discussed further in the following sections.

4.3.2. Structural studies

The structures of the liquid and solid phases in $Cu_{(100-x)}Zr_x$ were determined from x-ray diffraction, as described in §4.2. The structures of the supercooled liquid and the as-quenched glass will be compared in §4.3.2.1. An analysis of changes in $G(r)$ that suggest a transition to chemically and structurally inhomogeneous state of the supercooled liquid will be presented and briefly discussed. The crystal structure of $Cu_{46}Zr_{54}$ after recalescence of the supercooled liquid will be compared to that of the devitrified amorphous solid in §4.3.2.2, and implications to the phase diagram discussed.

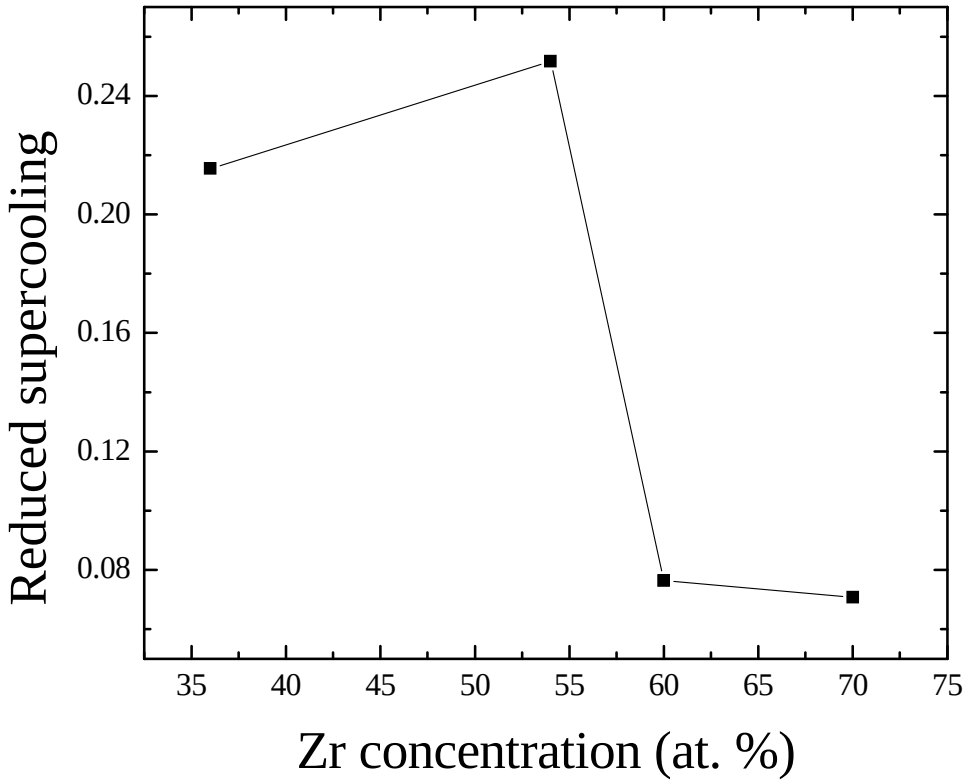

Figure 4.4 – The reduced supercooling for liquid $Cu_{(100-x)}Zr_x$ as a function of x; the sharp decrease occurs at a Zr concentration slightly higher than that of the metastable eutectic point (49 at.% Zr).

Table 4.1 – Values of the recalescence temperature, liquidus temperature, and reduced supercooling for $Cu_{(100-x)}Zr_x$ liquids.

Zr concentration, x (at. %)	**T_r (K)**	**T_l (K)**	**T_{rl}**
36	965	1230	0.215
54	898	1200	0.252
60	1154	1249	0.076
70	1178	1268	0.071

4.3.2.1. Liquid and glass structures

Figure 4.5 and Figure 4.6 show the measured $S(q)$ and the calculated $g(r)$, respectively, for liquid $Cu_{46}Zr_{54}$ at various temperatures, determined using the methods described in Chapter 2. Figure 4.7.a-d show the first peak in $G(r)$ for $Cu_{(100-x)}Zr_x$ liquids with x = 36, 43, 60, and 70, respectively. From this figure, the first peak, which corresponds to the most probable interatomic separation of first neighbor atoms, has a component at a lower value of r (2.78 Å) that is prominent in the Cu-rich compositions, and a component at a higher value of r (3.13 Å) that is prominent in the Zr-rich compositions. The difference between the two r-values is about 13%. Figure 4.8 shows the positions of the more prominent shoulder in the asymmetric first peak in $G(r)$ for the various compositions as a function of temperature. From this figure, the position of the high-r shoulder of the first peak for the liquids with greater Zr content (x = 60 and x = 70) shifts to larger values of r with supercooling. This was not observed for the lower-r shoulder that is prominent in the Cu-rich liquids. The contributions to the first peak in $G(r)$ for liquid $Cu_{46}Zr_{54}$ from the components at 2.78 and 3.13 Å are approximately equal. The first peaks for $Cu_{(100-x)}Zr_x$ liquids with x = 36, 54, and 70 are compared in Figure 4.9.

These results are not surprising, since the total $G(r)$ for $Cu_{(100-x)}Zr_x$ is composed of three partial $G(r)$ functions, one each for Cu-Cu, Cu-Zr, and Zr-Zr, each with a unique nearest neighbor separation. The complete partials can be determined by molecular dynamics (MD) simulations, but care must be taken to ensure that the potentials used are realistic and that sufficient time has been allowed to relax the systems.

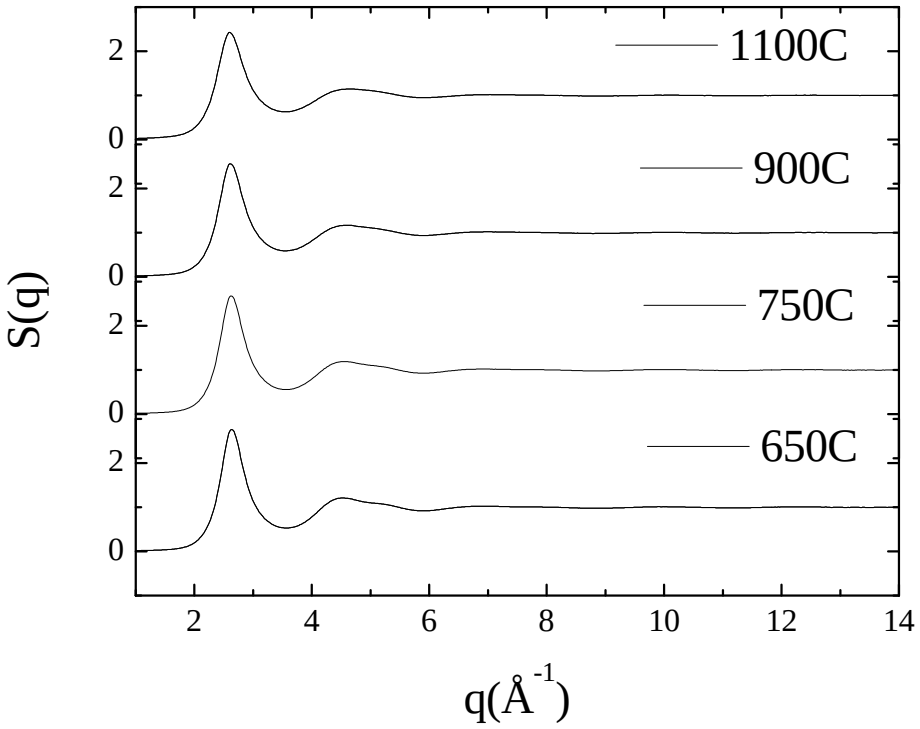

Figure 4.5 – The measured S(q) for liquid $Cu_{46}Zr_{54}$ at various temperatures.

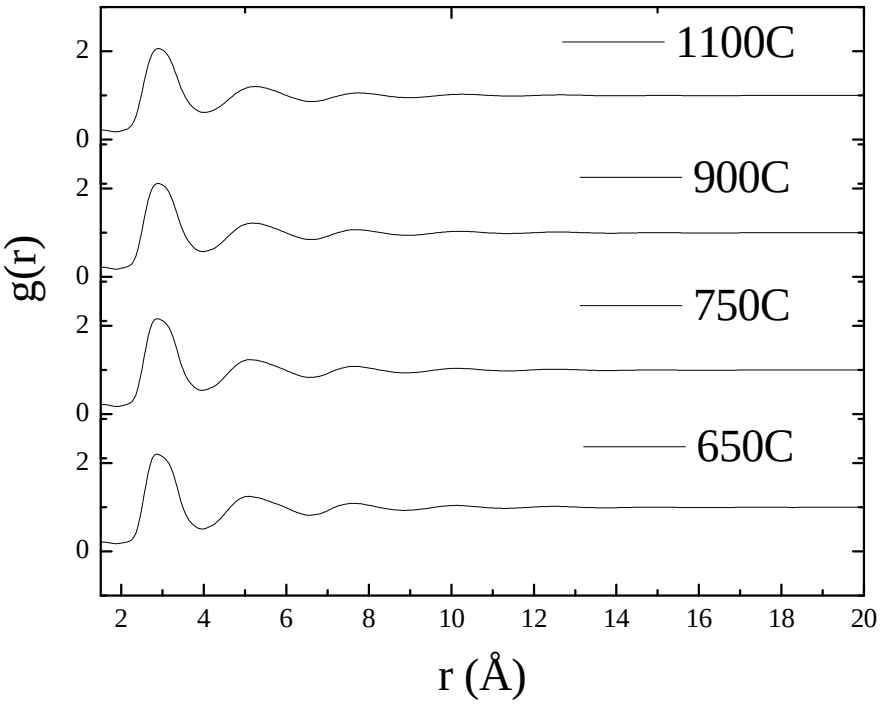

Figure 4.6 – The calculated g(r) for liquid $Cu_{46}Zr_{54}$ at various temperatures.

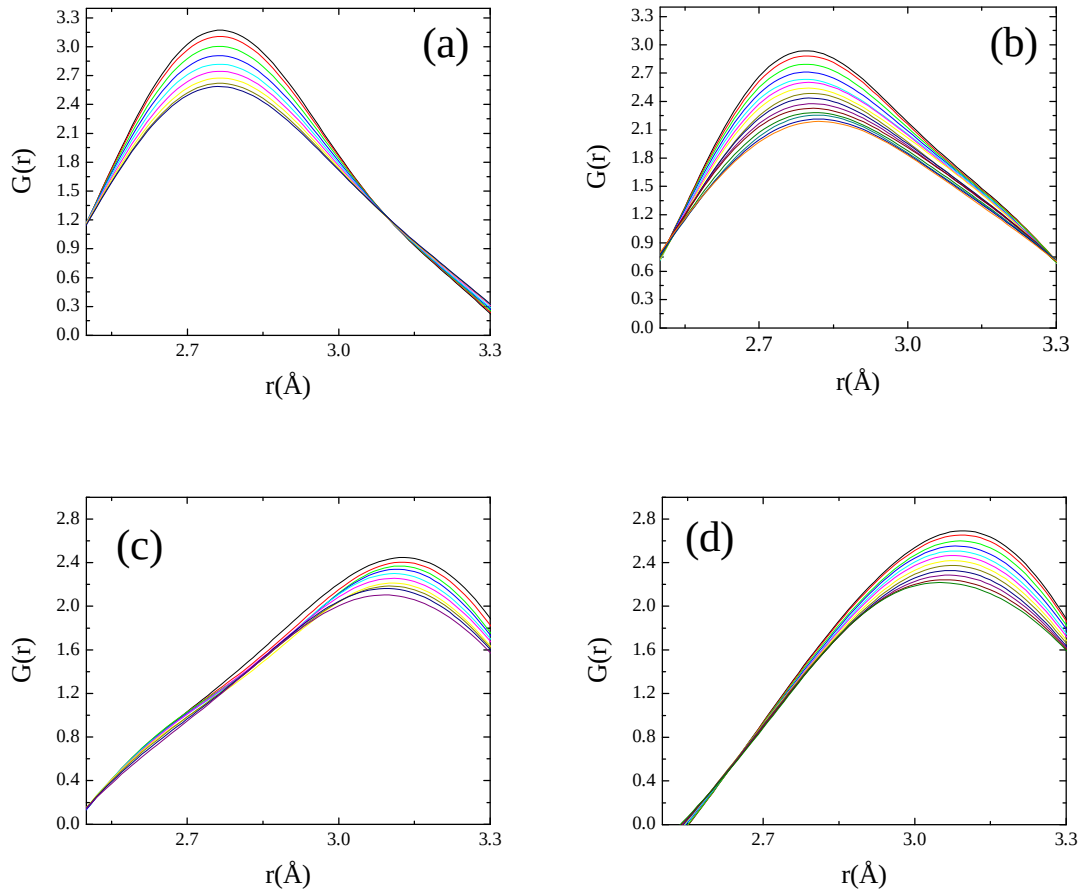

Figure 4.7 – The first peak in G(r) for $Cu_{(100-x)}Zr_x$ liquids at various temperatures for (a) x = 36, (b) x = 43, (c) x = 60, and (d) x = 70.

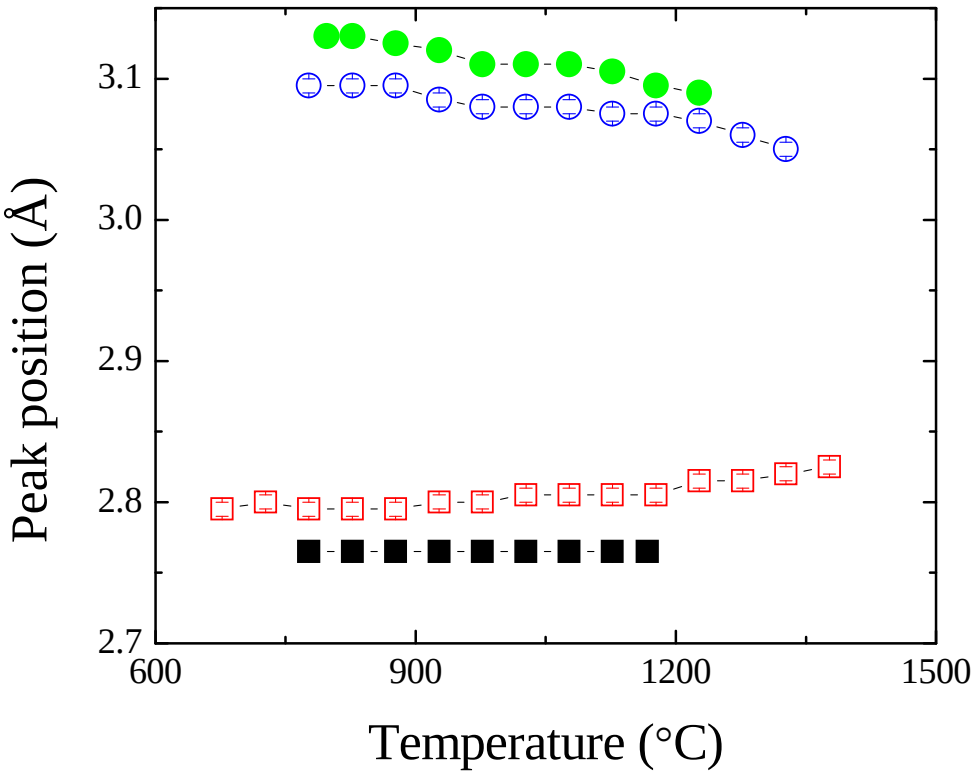

Figure 4.8 – The positions of the prominent shoulders in the first peak of G(r) for $Cu_{(100-x)}Zr_x$ liquids, as a function of temperature, for x = 36 (filled squares), x = 43 (open squares), x = 60 (filled circles), and x = 70 (open circles).

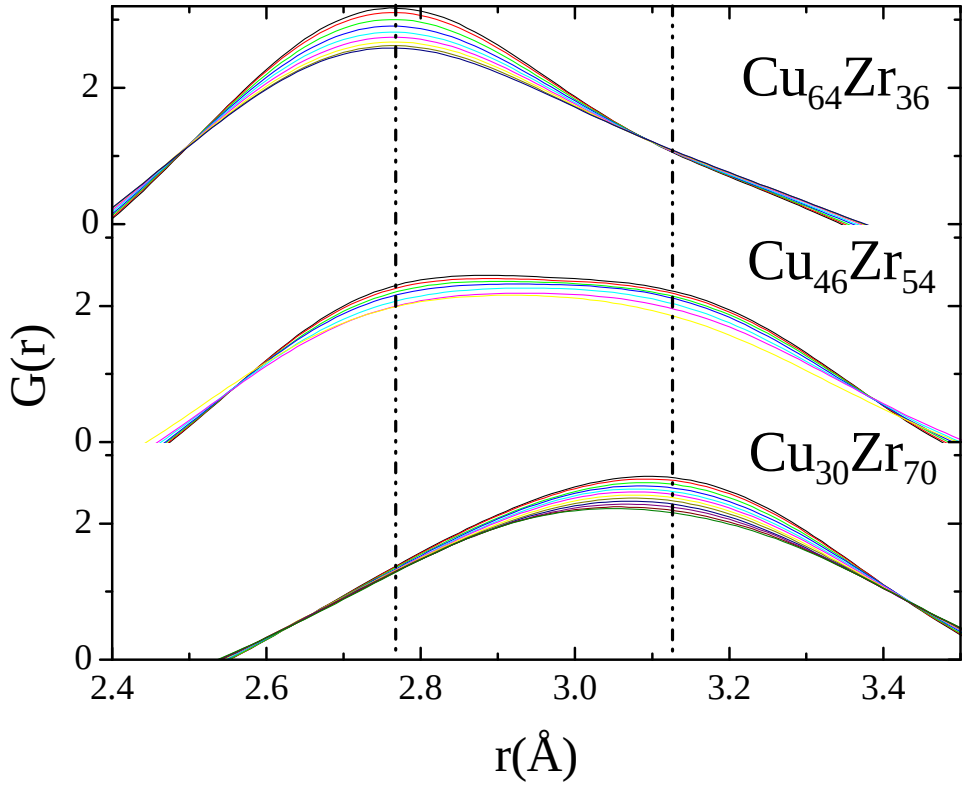

Figure 4.9 – A magnification of the first peak in G(r) for $Cu_{(100-x)}Zr_x$ liquids at various temperatures for x = 36, x = 54, and x = 70; the dashed vertical lines mark the two major components of the peaks.

An analysis of the total $G(r)$ allows the interatomic separations of the different pairs to be inferred directly from the scattering data. Extended x-ray absorption fine structure (EXAFS) results on amorphous solid $Cu_{46}Zr_{54}$ by Sadoc and others give first neighbor interatomic distances for Zr-Zr of 3.14 Å, for Cu-Cu of 2.54 Å, and for Cu-Zr of 2.72 Å [23]. Using these results, the components of the first peak in the measured $G(r)$ were identified as $r_{0,\,Cu\text{-}Zr}$ = 2.78 Å and $r_{0,\,Zr\text{-}Zr}$ = 3.13 Å, where $r_{0,\,i}$ is the position of the first peak for the ith pair (the nearest neighbor separation distance). Due to the high amount of overlap between the Cu-Cu and Cu-Zr peaks, it was not possible to infer the position of the Cu-Cu peak.

For the $Cu_{46}Zr_{54}$ liquid, the intensity of the Cu-Zr peak becomes greater than the Zr-Zr peak with increasing supercooling; this behavior begins at a temperature near 850°C (77°C supercooling) and continues with supercooling. To better quantify the evolution of the split peak with supercooling, the first peak was fit by two Gaussian functions, shown in Figure 4.10 for the $Cu_{46}Zr_{54}$ liquid at 650°C. Figure 4.11 shows the heights of the two Gaussian peaks as a function of temperature; the onset near 850°C is evident. This indicates that the number of Cu-Zr pairs, having an interatomic separation of about 2.78 Å, increases with supercooling. It should be noted that a Gaussian function is not a good approximation of the shape of peaks in $S(q)$, and that the peak is in fact composed of 3 partial functions, not 2, but this fit provides a quantitative measure of the observed changes in the measured total pair correlation function. Other data, both experimental and calculated, that point to a transition with onset near 850°C will be presented in later sections, and discussed in §4.5.

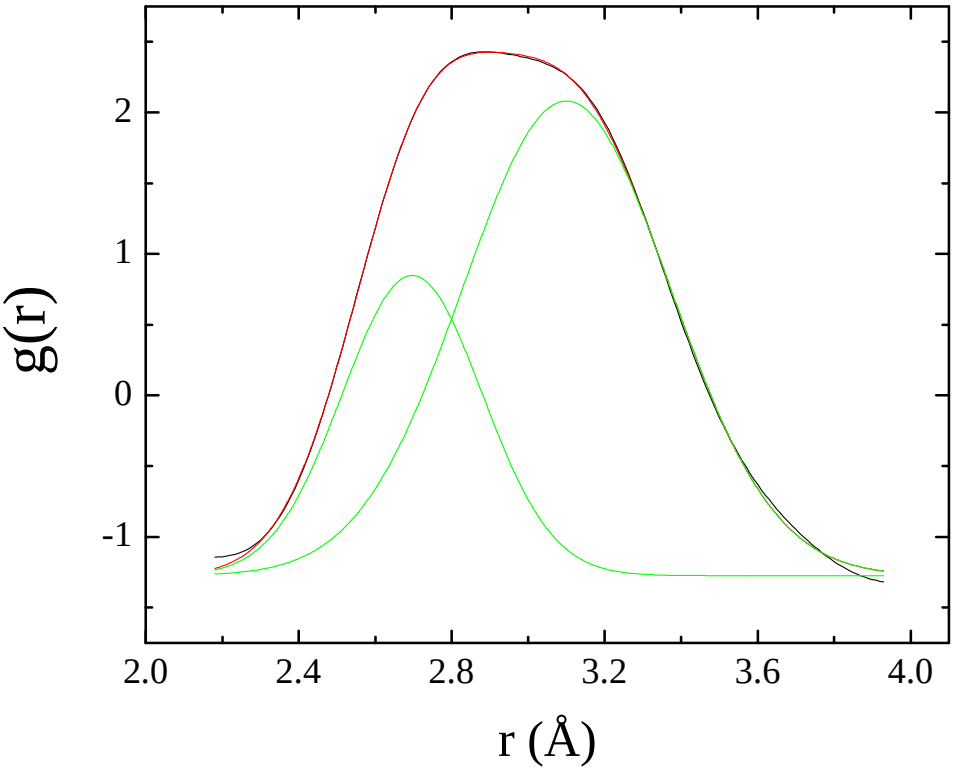

Figure 4.10 – A fit to the first peak in G(r) using two Gaussian functions for the $Cu_{46}Zr_{54}$ liquid at 650°C; the fit Gaussians are shown in green, the sum of these is shown in red and the input data in black.

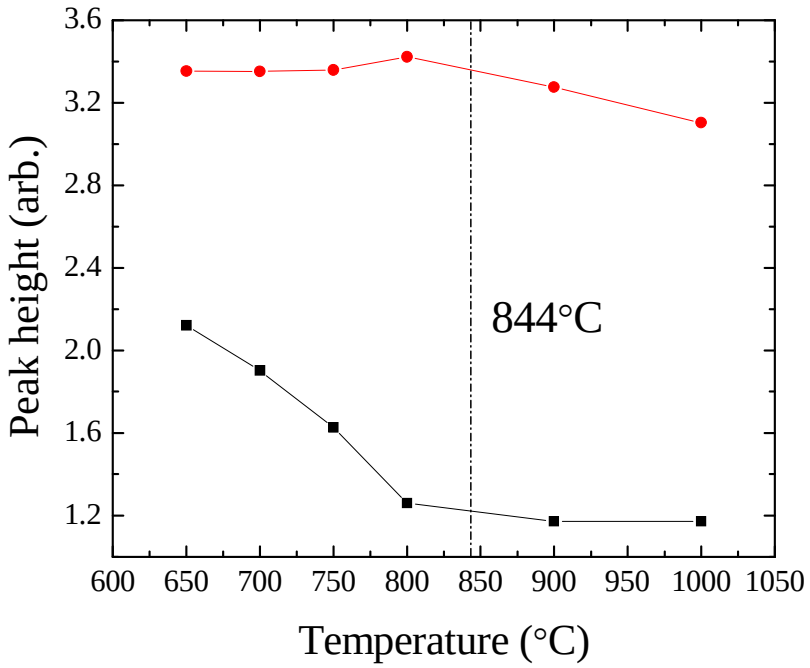

Figure 4.11 – A comparison of the heights of the two Gaussian functions used to fit the first peak in G(r) for the $Cu_{46}Zr_{54}$ liquid; the lower-r peak is shown with black squares and the higher-r peak is shown with red circles; the temperature of onset of the transition is indicated by the dashed vertical line.

X-ray diffraction measurements were also made on the as-quenched $Cu_{46}Zr_{54}$ glass; the measured $S(q)$ and calculated $g(r)$ are shown in Figure 4.12.a-b. The first peak in $G(r)$ for the $Cu_{46}Zr_{54}$ glass, shown in Figure 4.13, is composed of lower- and higher r-value component peaks ($r_{0,\ Cu\text{-}Zr}$ = 2.77 Å and $r_{0,\ Zr\text{-}Zr}$ = 3.10 Å), similar to that of the liquid (Figure 4.10).

4.3.2.2. Crystallization and devitrification structures

The structure of the crystallized $Cu_{46}Zr_{54}$ liquid after recalescence was measured using BESL. For comparison, as-quenched ribbons were devitrified *ex-situ* in a furnace, and the crystal structures were determined using the method of low energy XRD discussed in Chapter 2. The diffraction patterns for both samples are compared in Figure 4.14. It is evident that the two phases are the same, although the crystal peaks are shifted to lower values of q in the data obtained using BESL. This could be due to thermal expansion, since the temperature was higher in the BESL measurement.

The crystal structure of the sample processed in BESL was determined from the diffraction data by Rietveld refinement. The results of the fit are shown in Figure 4.15. The fit indicated a crystal phase mixture of 72 wt% $Cu_{10}Zr_7$ (orthorhombic, a = 12.632Å, b = 9.32Å, c = 9.326Å, space group C2ca) and 28 wt% Zr_2Cu (tetragonal, a = 6.456Å, c = 5.279Å, space group I4/mmm). From the phase diagram of Figure 4.1, it is expected that the $Cu_{46}Zr_{54}$ liquid should crystallize to a phase mixture of CuZr and Zr_2Cu, followed by a lower temperature transformation to $Cu_{10}Zr_7$ and Zr_2Cu.

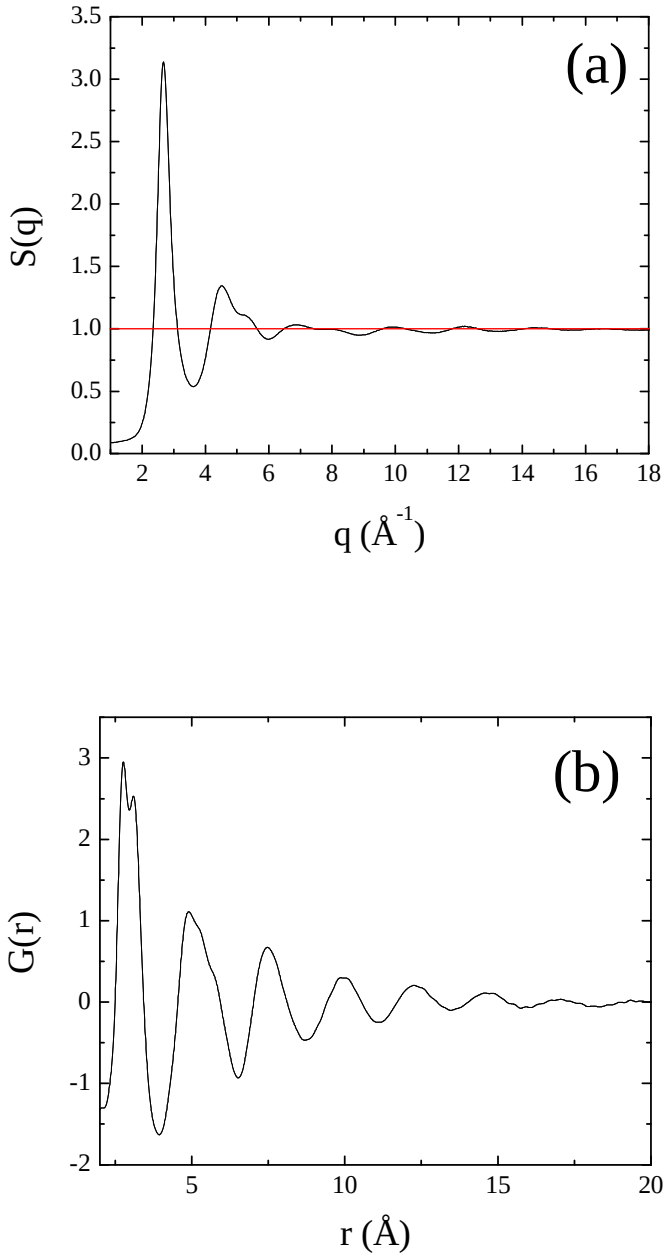

Figure 4.12 – (a) The measured *S*(*q*) and (b) calculated *G*(*r*) for the as-quenched $Cu_{46}Zr_{54}$ glass.

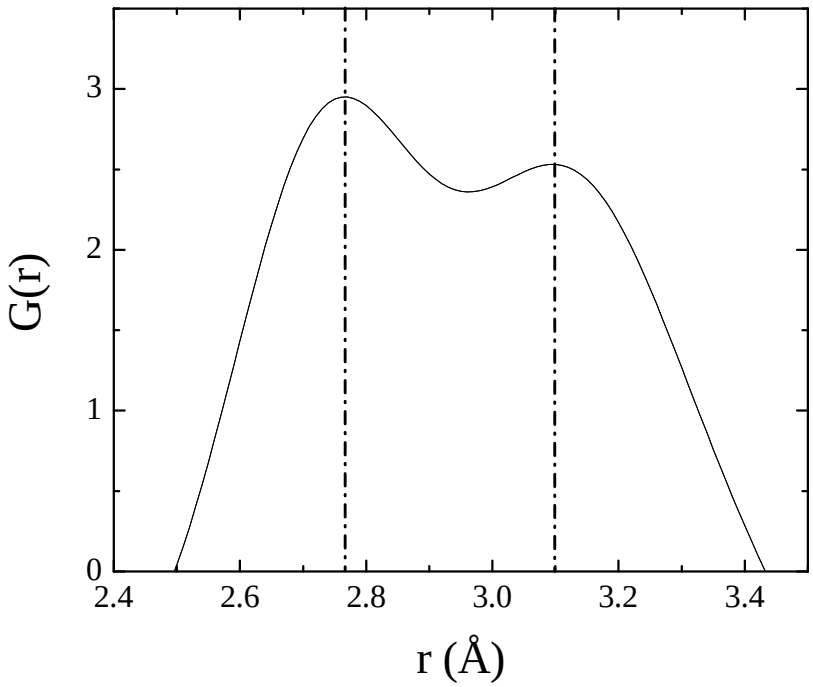

Figure 4.13 – The first peak in the calculated G(r) for the as-quenched $Cu_{46}Zr_{54}$ glass, showing the same peak splitting observed in the supercooled liquid.

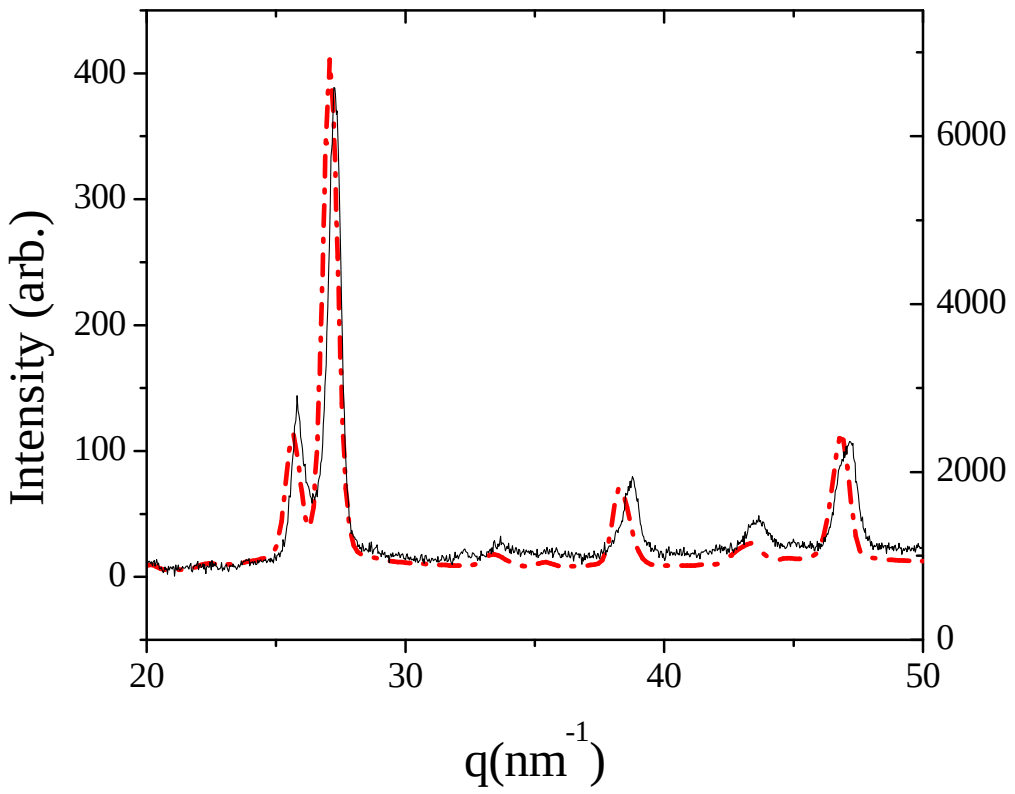

Figure 4.14 – The measured x-ray diffraction peaks for $Cu_{46}Zr_{54}$ after recalescence of the supercooled liquid in BESL (red dashed line) and from devitrification of the glass (black line), showing identical structures; the shifts in peak positions may arise from thermal expansion of the higher temperature structures measured by BESL.

However, no evidence of a two-step recalescence is observed in the time/temperaure data shown in Figure 4.3, and no evidence of the formation of the CuZr phase is found in the diffraction data collected at a nominal 10hz frame rate during recalescence. This indicates that the $Cu_{10}Zr_7$ and Zr_2Cu mixture formed directly from the liquid. Further, assuming that the formation of CuZr was kinetically inhibited, from the phase diagram, the solidifcation of $Cu_{46}Zr_{54}$ should give an equal mixture of $Cu_{10}Zr_7$ and Zr_2Cu, which is not the case. The dominant phase is $Cu_{10}Zr_7$. The $Cu_{10}Zr_7$ crystal structure contains a large amount of local icosahedral symmetry [24, 25]. These results, along with the supercooling data presented in §4.3.1, support a structural and chemical inhomogeneity of the supercooled liquid. They also suggest that the Cu-rich liquid, after formation of the inhomogeneous liquid, has more icosahedral order, due to the higher fraction of the $Cu_{10}Zr_7$ phase than expected and the lack of formation of the cubic CuZr phase.

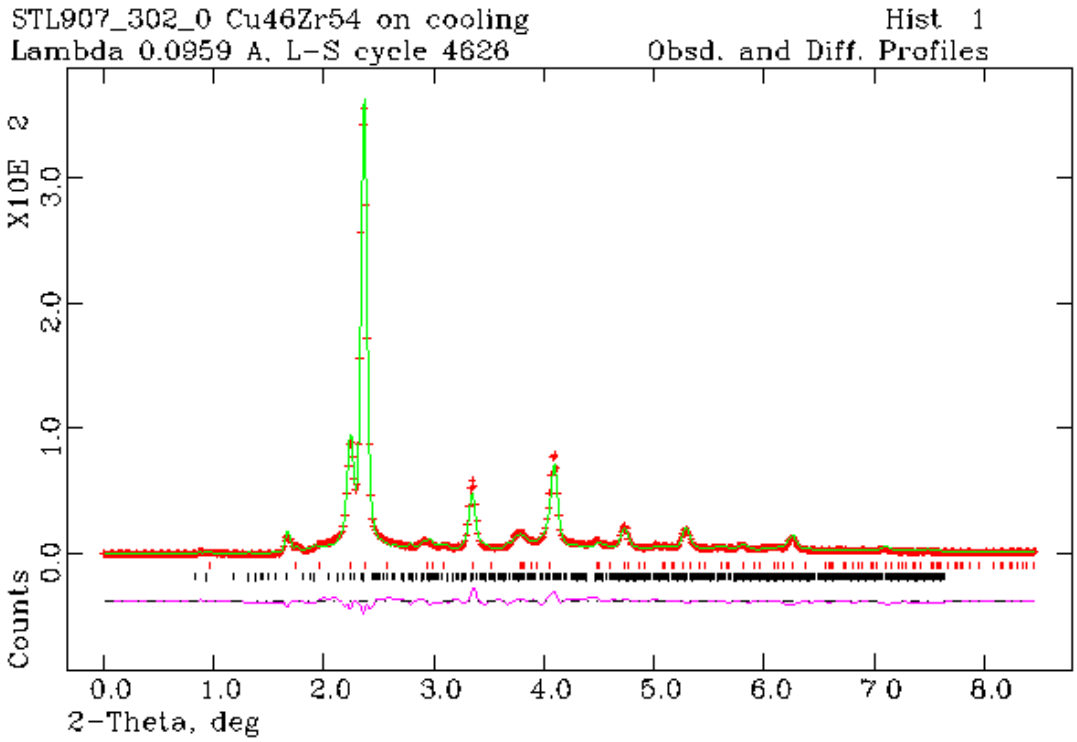

Figure 4.15 – The results of a Rietveld refinement of the diffraction data for $Cu_{46}Zr_{54}$ after liquid recalescence obtained using BESL; the fits indicate a mixture of $Cu_{10}Zr_7$ and Zr_2Cu; the input data are shown in red, the predictions from the refined structure in green, and the difference in purple; the reflection positions for $Cu_{10}Zr_7$ are marked with red dashes, for Zr_2Cu with black dashes.

4.3.3. Liquid physical properties

From the temperature data as a function of time shown in Figure 4.3, it is possible to calculate the specific heat of the liquid using a simple heat balance equation for radiation cooling, given by

$$P = \frac{dQ}{dt} = mC_p \frac{dT}{dt} \propto -\varepsilon_T \left(T^4 - T_r^4\right),$$

where P is the power, Q is the total heat evolved as a function of time, t, m is the mass, C_p the isobaric specific heat, ε_T the emissivity, T the temperature, and T_r the temperature of the surroundings. A plot of the specific heat calculated for liquid $Cu_{46}Zr_{54}$ is shown in Figure 4.16 [26]; a subtle inflection point is visible near 845°C. This inflection provides further supporting evidence for a transition in the supercooled liquid, but well above the glass transition temperature. As previously mentioned, measurements of the density were made by Hyers, including for the $Cu_{46}Zr_{54}$ liquid. An inflection was also observed in those data at 841°C, in the slope of the density as a function of temperature, which is proportional to the thermal expansion coefficient. (As shown in Figure 4.17, lines generated from separate linear fits to the high temperature and low temperature regions of the density-temperature curve cross at 841°C.) This result also supports a structural transition in the supercooled liquid.

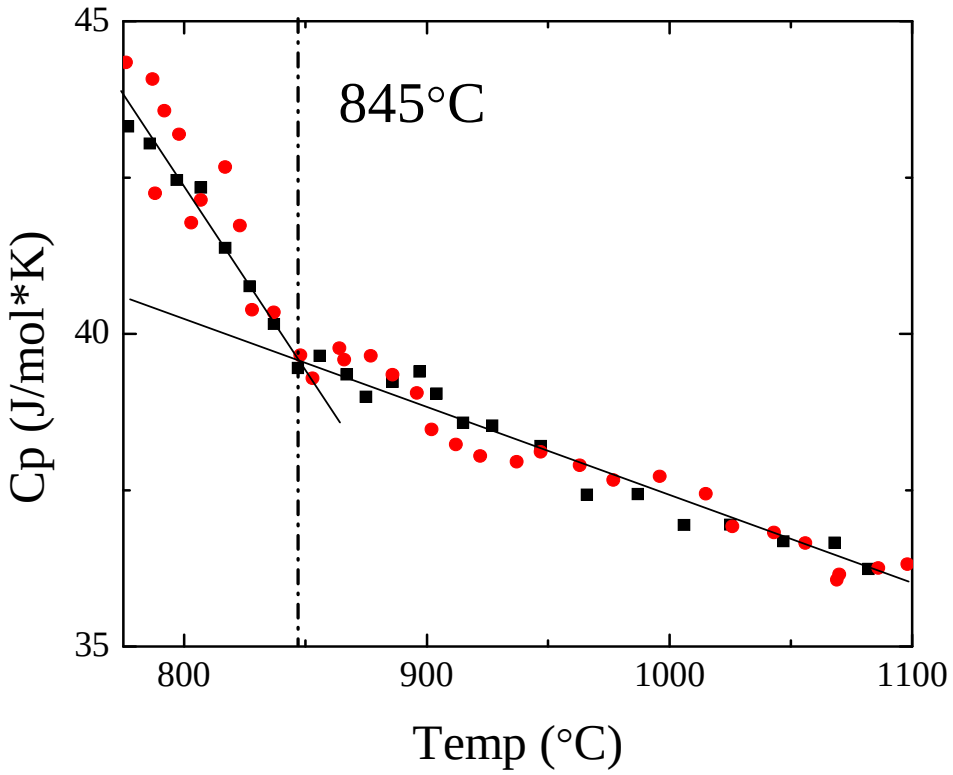

Figure 4.16 – A plot of the specific heat for liquid $Cu_{46}Zr_{54}$ as a function of temperature for two trials; the solid lines through the data are guides to the eye that indicate an inflection point around 845°C, shown by the dashed vertical line.

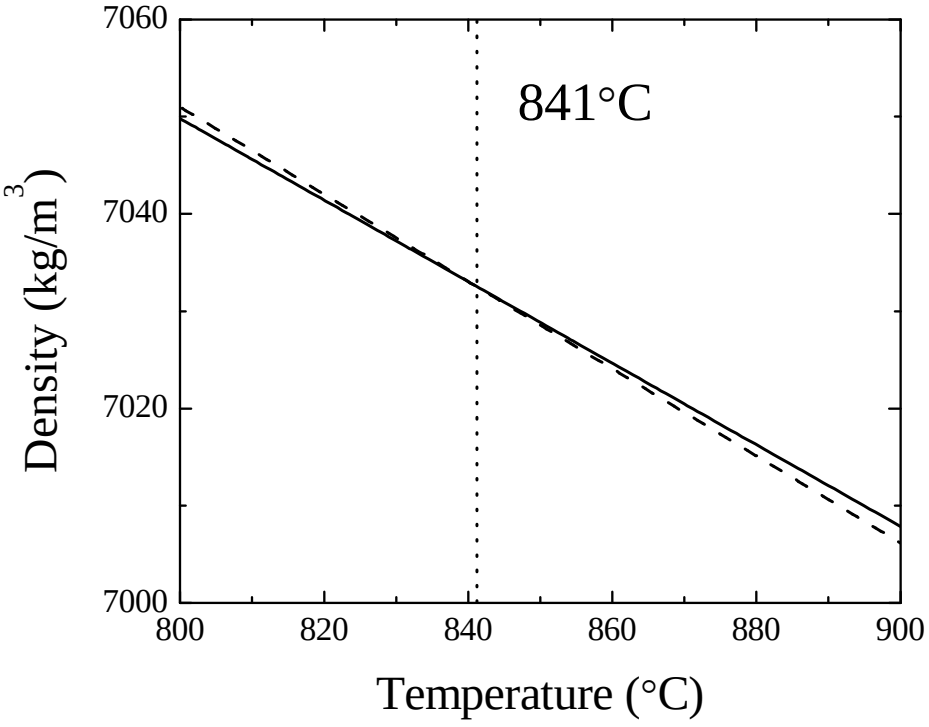

Figure 4.17 – Linear fits to the measured density of liquid $Cu_{46}Zr_{54}$, showing an inflection in the slope of the density as a function of temperature at 841°C.

4.4. Further analysis

4.4.1. Structual modeling by Reverse Monte Carlo simulation

Atomic configurations were generated for all of the $Cu_{(100-x)}Zr_x$ liquids studied using a Reverse Monte Carlo (RMC) simulation; the method described in Chapter 2 was followed to optimize the input parameters. When available, the measured densities were used. Since it was not available for the x = 43 sample, the density was taken from a MD simulation performed by Kramer. Good convergence ($\chi^2 < 10$) was achieved for all of the RMC simulations. A representative fit (x = 54 liquid at 900°C) is shown in Figure 4.18.

Further supporting evidence for the transition in the liquid near 850°C was inferred from details of the simulation. A sudden change in the shape of the exponential χ^2 convergence curve, as a function of simulation time (Monte Carlo steps), was observed between 800 and 900°C. However, the ultimate χ^2 achieved remains unchanged. This result indicates that the atomic structures from RMC can be grouped into two classes, those 800°C and below and those 900°C and above, with both configurations simulated well by the RMC method. In effect, this indicates that the RMC simulation is detecting the structural change, although no details of the arrangement can be inferred from this measure.

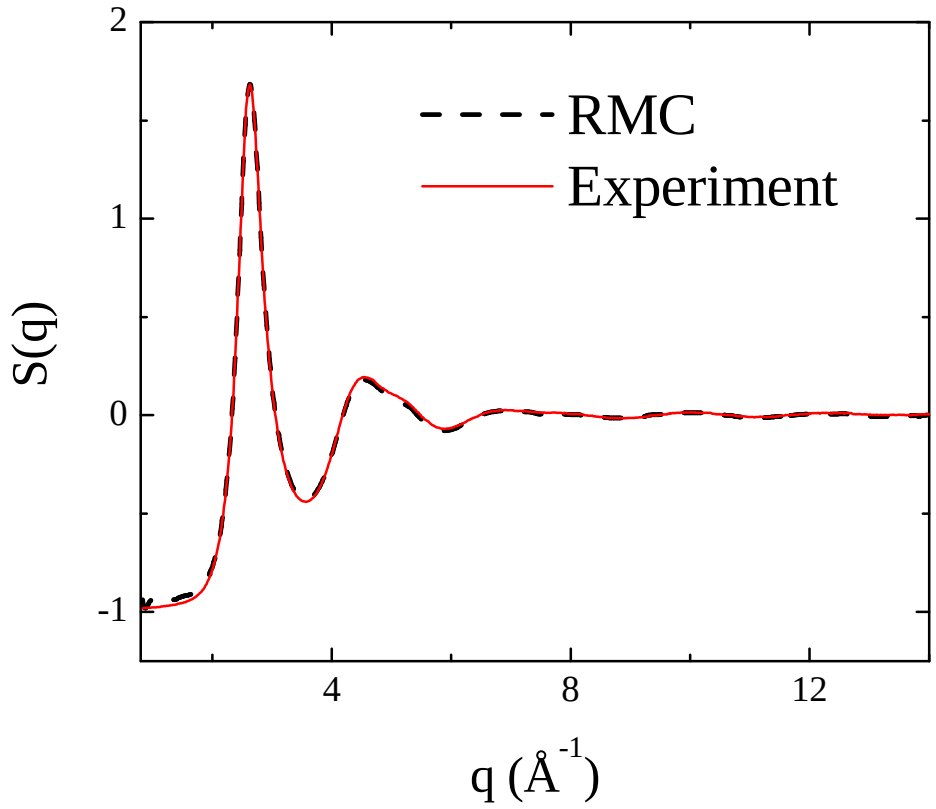

Figure 4.18 – The RMC fit (black dashed line) to the total S(q) for liquid $Cu_{46}Zr_{54}$ from experimental results (red line).

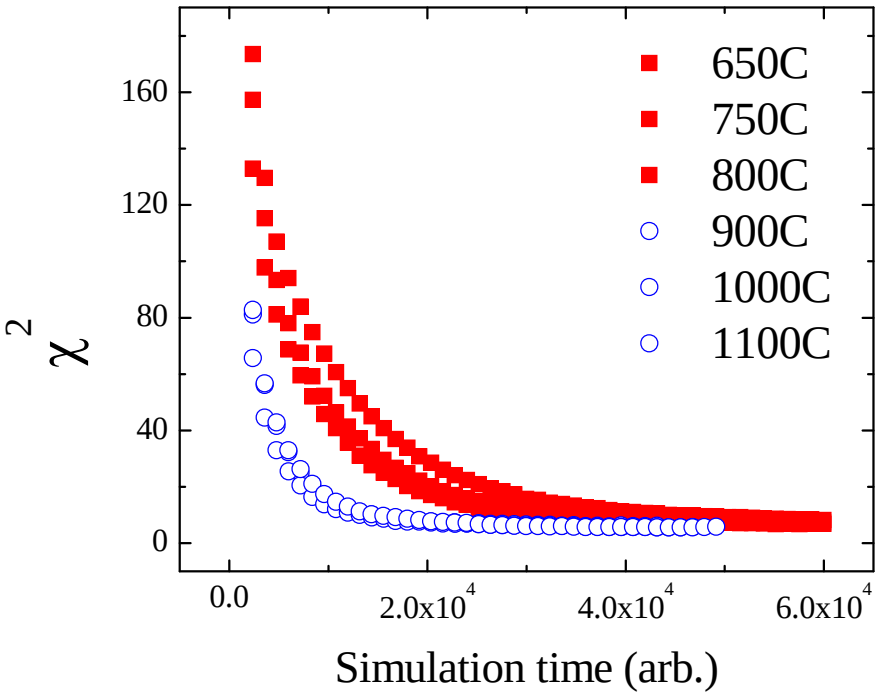

Figure 4.19 – The convergence of the RMC simulation for $Cu_{46}Zr_{54}$ liquids as a function of simulation steps; a discontinuous change in the convergence properties is observed between 900 and 800°C, consistent with the observed structural transition; the ultimate convergence value remains largely unchanged.

4.4.2. Structural characterization

Simulated structures generated from RMC for all compositions were characterized using the Honeycutt-Andersen (HA) index and Bond Orientational Order (BOO) parameter analyses, following the methods described in Chapter 2. The HA indices provide a measure of the local order around nearest neighbor pairs of atoms. Representative histograms of the frequency of HA pairs for distorted icosahedral (DICOS), icosahedral (ICOS), hexagonal close-packed/face-centered cubic (HCP/FCC), and body-centered cubic (BCC) local order for the $Cu_{46}Zr_{54}$ liquids are shown as a function of temperature in Figure 4.20. From these results it is evident that the DICOS and ICOS clusters are most prominent for all temperatures, and that the frequency of cluster fragments with ideal icosahedral order is increasing with supercooling.

The structural transition already discussed can be observed in the frequency of DICOS clusters, which is only weakly increasing on cooling to 900°C, but falls off with further supercooling, and in the frequency of ICOS clusters, which increases suddenly below 900°C. The transition can also be observed from the HA index result normalized to the total number of HA pairs, shown in Figure 4.21. Figure 4.22 shows the sum of the frequencies of DICOS and ICOS symmetries for $Cu_{(100-x)}Zr_x$ liquids in the state of deepest supercooling for various values of *x*. From this figure, the total icosahedral order in the lowest temperature liquid drops sharply at the composition above 54 at.% Zr, and correlates well with the reduced supercooling of Figure 4.4, suggesting that increasing icosahedral order in the liquid is leading to increased supercooling, consistent with the hypothesis of Frank [27], which was confirmed previously using BESL [28].

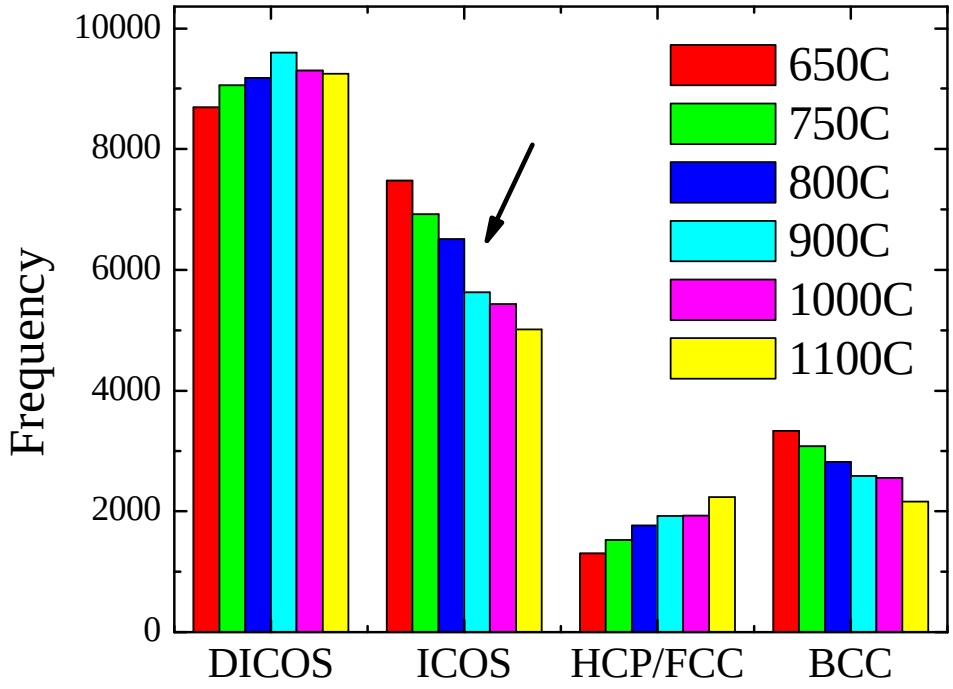

Figure 4.20 – The frequencies of HA pairs with various local symmetries for $Cu_{46}Zr_{54}$ liquids as a function of temperature; the discontinuous jump in icosahedral order between 900 and 800°C is indicated by an arrow.

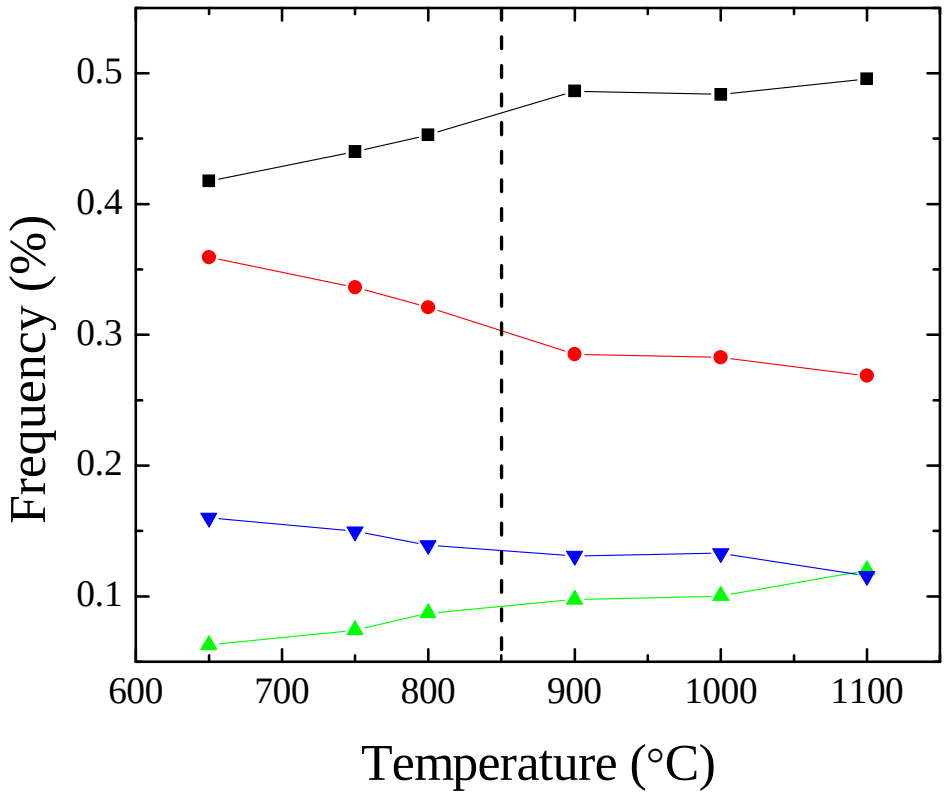

Figure 4.21 – The normalized frequency of HA pairs with various local symmetries for $Cu_{46}Zr_{54}$ liquids as a function of temperature; the DICOS (black squares) and ICOS (red circles) clusters show an inflection at the transition temperature, near 850°C (dashed line), while HCP/FCC (blue triangles, point down) and BCC (green triangles, point up) do not.

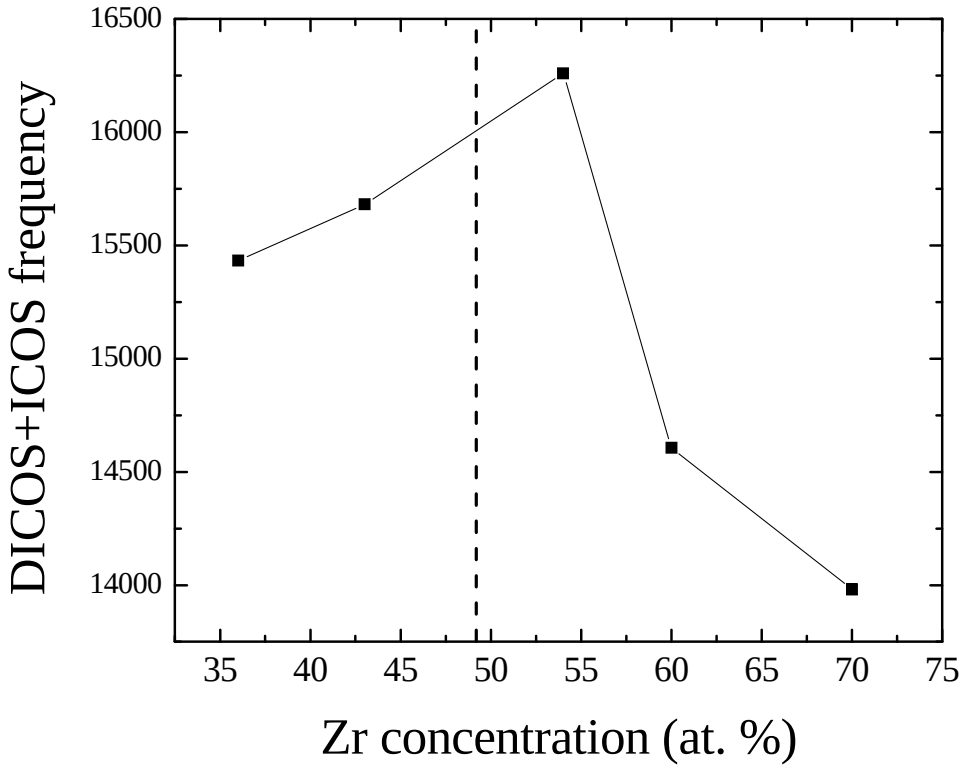

Figure 4.22 – The sum of the frequencies of DICOS and ICOS clusters for $Cu_{(100-x)}Zr_x$ liquids as a function of Zr concentration, *x*; the metastable eutectic point at $x = 49$ is indicated by the dashed line.

The results of the BOO calculations for $Cu_{46}Zr_{54}$ liquids, representative for all compositions studied, are shown in Figure 4.23. From this figure, Q_6 and Q_{10} are most prominent, consistent with a high degree of icosahedral order in the liquid. The presence of Q_4 and Q_8 indicate that other (cubic) symmetries are present, such as FCC or BCC, consistent with the HA index result. There is a slight increase of Q6 with supercooling, while the others show a weak decrease. This also supports the development of icosahedral order with supercooling.

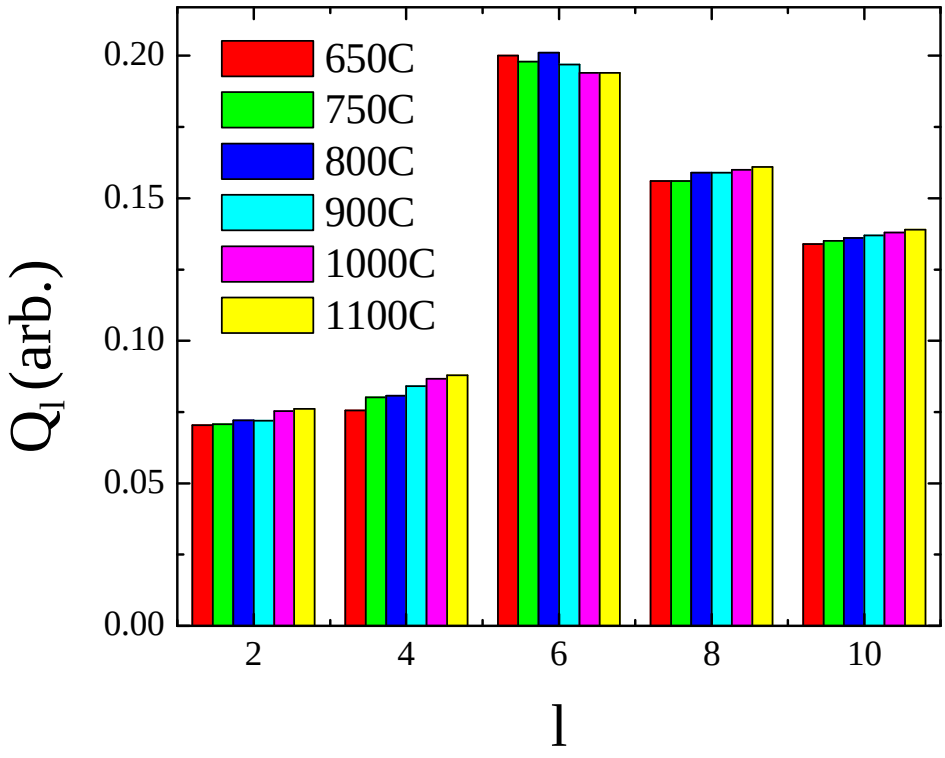

Figure 4.23 – The results of the BOO analysis for $Cu_{46}Zr_{54}$ liquids as a function of temperature; the prominence of l = 6 and l = 10 indicate icosahedral order.

4.5. Summary and discussion

In this chapter, the results of experiments and analyses using BESL, with RMC simulations, to determine the structures and physical properties of various bulk metallic glass-forming $Cu_{(100-x)}Zr_x$ liquids were presented. At a Zr concentration of 54 at.% (x = 54) an interesting structural transition in the supercooled liquid was observed from the scattering data and physical properties measurements, with an onset near 850°C. Other structural changes were observed with increased Zr relative to the same concentration.

For $Cu_{46}Zr_{54}$, the first peak in G(r), constructed from the diffraction data, began to split two overlapping peaks near 850°C, with a higher intensity of the peak at lower r. The locations of the two peaks are consistent with the Cu-Zr and Zr-Zr separations (2.78Å and 3.14 Å respectively) deduced from EXAFS data [23]. This transition is thus characterized by a sudden increase in the number of Cu-Zr near neighbors (indicated by the preferential growth of the lower-r side of the split peak), inflections in the specific heat and bulk density, and a discontinuous increase in the icosahedral order of the liquid. A transition in the same temperature range was also observed in the convergence of the RMC simulation used to generate atomic configurations from $S(q)$. The first peak in $G(r)$ for the as-quenched $Cu_{46}Zr_{54}$ glass is split in the same way as in the low temperature liquid, indicating that the changes in the liquid continue to develop through the glass transition. These results suggest that the supercooled liquid is developing significant structural and chemical inhomogeneity at this composition, with an onset near 850°C, consistent with development of icosahedral, Cu-centered clusters as predicted by MD simulations in precisely this temperature range [11, 19, 20].

In the more Zr-rich $Cu_{(100-x)}Zr_x$ liquids (x = 60 and x = 70), the high-*r* shoulder in the first peak of *G*(*r*) shifts to larger values of *r* with supercooling, indicating a lengthening of the Zr-Zr nearest-neighbor separation. No similar effect was seen in the Cu-rich compositions (x = 36 and x = 43), where the position of the lower-*r* shoulder (corresponding to the Cu-Zr nearest neighbors) remained constant with supercooling. These results support a preferential development of clusters in the liquids with Zr concentration above x = 54, where the structural transition was observed. This concentration is slightly off of a metastable eutectic point at 49 at.% Zr, which supports the improved GFA of ternary BMGs based on this composition [10]. The reduced supercooling is also much less for liquids that are more Zr-rich. The change in supercooling correlates well with of the growth of icosahedral order, determined from an RMC analysis of the data.

For $Cu_{46}Zr_{54}$ a phase mixture of $Cu_{10}Zr_7$ (72 wt %) and Zr_2Cu (28 wt %) was observed after complete liquid solidification, and following the devitrification of the as-quenched glass. From the BESL results, the $Cu_{10}Zr_7$ and Zr_2Cu phases formed directly from the liquid, with no presence of the ZrCu phase at any time during solidification, which would be expected from the equilibrium phase diagram during solidification, unless nucleation of this phase from the supercooled liquid were inhibited. From devitrification of the quenched glass, a phase mixture of $Cu_{10}Zr_7$ and Zr_2Cu is expected, as observed, although the fraction of $Cu_{10}Zr_7$ is higher than expected. The quality of powder-averaging from measurements made in BESL could be insufficient to determine phase fractions with a high degree of certainty.

These observations suggest a preference for the formation of $Cu_{10}Zr_7$, possibly because the structure of the supercooled liquid is similar to that of the crystal phase. The orthorhombic $Cu_{10}Zr_7$ phase possesses a high degree of local icosahedral symmetry, making it locally similar to the glass [24, 25]. The increasing icosahedral order in the supercooled liquids, and the fact that the $Cu_{10}Zr_7$ phase and the amorphous phase have similar local environments, support bulk glass formation, as observed when faster cooling rates than those in ESL were used.

4.6. Conclusions

These results suggest that the supercooled $Cu_{(100-x)}Zr_x$ liquids form significant structural and chemical inhomogeneities during supercooling, possibly forming Cu-rich and Zr-rich regions with unique structures. This explains the asymmetric development of the Cu-Zr pairs in $Cu_{46}Zr_{54}$, and the shift in the first peak in the Zr-Zr pairs. Only at the $Cu_{46}Zr_{54}$ concentration is the volume fraction of the two phases sufficiently similar to be able to observe the presence of both. Both the experimental data and analyses by simulation and modeling indicate that the transition to the inhomogeneous liquid begins near 845 ±5°C and develops with increased supercooling. The recalescence products support the development of different structures, with local order similar to that of the glass. The change in local chemical composition and topology in the supercooled liquid make nucleation of the high temperature phase difficult, and thus it does not form.

Recent studies using molecular dynamics simulations with *ab-initio* potentials for Cu-Zr liquids and glasses have been performed, and predict the development of unique solvent- and solute-centered clusters, including well-formed icosahedra, with an onset very close to 850°C. Thus, these results could represent the first experimental

confirmation of such cluster development. The structure of these supercooled liquids is favorable for glass formation, which is uncommon in binary alloys. This cluster development frustrates the kinetics of crystallization of the equilibrium crystal phase, enabling glass formation. These results could have implications to the empirical observation of improved GFA at off-eutectic compositions, and similarly for the metastable eutectic formalism.

Further work to determine the changes in supercooled liquid structure for more alloy compositions near the metastable eutectic would be valuable. It would help to better understand why that composition is important in relation to cluster formation, and help to determine the composition range of the observed transition. A similar study, using BESL, of the ternary Zr-Cu-Al BMG would be valuable to further confirm the theoretical results of cluster development as predicted by Chang, Ma, and Sheng.

References

1. A. Inoue, Acta Materialia, 2000. **48**(1): p. 279-306.
2. W. Johnson, JOM Journal of the Minerals, Metals and Materials Society, 2002. **54**(3): p. 40-43.
3. A. Inoue, B. L. Shen, and A. Takeuchi, Materials Transactions, 2006. **47**(5): p. 1275-1285.
4. W. Johnson, MRS Bulletin, 1999. **24**(10): p. 42-56.
5. M. Telford, Materials Today, 2004. **7**(3): p. 36-43.
6. D. Wang, Y. Li, B. B. Sun, M. L. Sui, K. Lu, and E. Ma, Applied Physics Letters, 2004. **84**(20): p. 4029-4031.
7. D. Xu, B. Lohwongwatana, G. Duan, W. L. Johnson, and C. Garland, Acta Materialia, 2004. **52**(9): p. 2621-2624.
8. G. Duan, D. Xu, Q. Zhang, G. Zhang, T. Cagin, W. L. Johnson, and W. A. Goddard, Physical Review B, 2005. **71**(22): p. 224208.
9. P. Yu, H. Y. Bai, M. B. Tang, and W. L. Wang, Journal of Non-Crystalline Solids, 2005. **351**(14-15): p. 1328-1332.
10. D. Xu, G. Duan, and W. L. Johnson, Physical Review Letters, 2004. **92**(24): p. 245504.
11. Y. Q. Cheng, E. Ma, and H. W. Sheng, Applied Physics Letters, 2008. **93**(11): p. 111913-3.
12. D. Turnbull, Contemporary Physics, 1969. **10**(5): p. 473-488.
13. H. Choi-Yim, D. Xu, and W. L. Johnson, Applied Physics Letters, 2003. **82**(7): p. 1030-1032.
14. H. Tan, Y. Zhang, D. Ma, Y. P. Feng, and Y. Li, Acta Materialia, 2003. **51**(15): p. 4551-4561.
15. W. Kurtz and D. J. Fisher, *Fundamentals of solidification*. 4th ed. 1998: Switzerland: Trans Tech.
16. L. Xia, W. H. Li, S. S. Fang, B. C. Wei, and Y. D. Dong, Journal of Applied Physics, 2006. **99**(2): p. 026103-3.
17. K. F. Yao, F. Ruan, Y. Q. Yang, and N. Chen, Applied Physics Letters, 2006. **88**(12): p. 122106-3.
18. R. J. Highmore and A. L. Greer, Nature, 1989. **339**(6223): p. 363-365.
19. N. Jakse and A. Pasturel, Physical Review B (Condensed Matter and Materials Physics), 2008. **78**(21): p. 214204-9.
20. Y. L. Sun and J. Shen, Journal of Non-Crystalline Solids, 2009. **355**(31-33): p. 1557-1560.
21. A. K. Gangopadhyay, G. W. Lee, K. F. Kelton, J. R. Rogers, A. I. Goldman, D. S. Robinson, T. J. Rathz, and R. W. Hyers, Review of Scientific Instruments, 2005. **76**(7): p. 073901.
22. *Smithell's Metals Reference Book*. 7th ed, ed. E.A. Brandes and G.B. Brook. 1992: Butterworth Heinemann.

23. A. Sadoc, Y. Calvayrac, A. Quivy, M. Harmelin, and A. M. Flank, Journal of Non-Crystalline Solids, 1984. **65**(1): p. 109-129.
24. S. Barsov, A. Getalov, V. Grebinnik, I. Gurevich, B. Kirillov, A. Klimov, S. Kruglov, L. Kuzmin, A. Lazarev, B. Mikhailov, S. Mikirtychants, B. Nikolsky, A. Pirogov, A. Ponomarev, V. Selivanov, G. Shcherbakov, S. Shilov, V. Suetin, and V. Zhukov, Hyperfine Interactions, 1986. **31**(1): p. 113-114.
25. D. V. Louzguine-Luzgin, A. R. Yavari, G. Vaughan, and A. Inoue, Intermetallics, 2009. **17**(7): p. 477-480.
26. A. K. Gangopadhyay, Private communication, 2008.
27. F. Frank, Proceedings of the Royal Society of London Series A, 1952. **215**(43).
28. K. F. Kelton, G. W. Lee, A. K. Gangopadhyay, R. W. Hyers, T. J. Rathz, J. R. Rogers, M. B. Robinson, and D. S. Robinson, Physical Review Letters, 2003. **90**(19).

Chapter 5

The Effects of Ag Addition on Glass Formation and Devitrification Mechanisms in Mg-Cu-(Ag)-Gd Metallic Glasses

This work was performed in collaboration with Dr. E. S. Park, School of Engineering and Applied Science, Harvard University, Cambridge, MA, 02138, USA

5.1. Introduction

As discussed in Chapter 1, bulk metallic glasses (BMGs) are very promising engineering materials for their desirable mechanical properties, due to their amorphous structures. One class of BMGs receiving some attention is that of lightweight glasses formed in, e.g., Al-, Ti-, and Mg-based alloys [1-4]. The Mg-based BMG's and composites are typically formed from Mg-Transition Metal-Rare Earth (Mg-TM-RE) alloys. Mg-based BMG's have been developed using the three empirical "rules" introduced by Inoue [5]: large negative heats of mixing of the constituent elements, atomic size mismatch greater than 12%, and 3 or more components. The early work was on Mg-Ni-Ce [6], Mg-Cu-Y [7] and Mg-Ni-Nd [8], and focused on characterizing their mechanical and thermal properties, and later on alloy development by pinpointing favorable off-eutectic compositions that could form the largest fully amorphous structures [9].

Men and Kim found a BMG of 8mm diameter in $Mg_{65}Cu_{25}Gd_{10}$ [10], an improvement over the previously studied $Mg_{65}Cu_{25}Y_{10}$ alloy. Park and others further

improved the glass-forming ability (GFA) with the addition of Ag, up to 10 at.%, in $Mg_{65}Cu_{(25-x)}Ag_xY_{10}$ [11] and $Mg_{65}Cu_{(25-x)}Ag_xGd_{10}$ [12]. They also found improved mechanical properties with Ag addition in $Mg_{65}Cu_{(25-x)}Ag_xGd_{10}$. Madge and Greer further examined the effects of Ag addition in $Mg_{65}Cu_{(25-x)}Ag_xY_{10}$ BMG's, and found an inverse correlation between thermal stability (this will be defined in §5.3) and the GFA, up to x = 10 [13]. They found differences in the devitrification of the alloy without Ag (x = 0) and with x = 10; with the latter showing very slow growth rates during crystallization. They argued for the presence of quenched-in nuclei in the alloy with x = 10, and against phase separation prior to glass formation. This work presents a detailed analysis of the microstructure and devitrification of $Mg_{65}Cu_{(25-x)}Ag_xGd_{10}$ alloys using thermal analysis, microscopy, and high energy x-ray diffraction techniques to follow and expand upon the analysis of Madge and Greer of Mg-Cu-(Ag)-Y.

Interestingly, many of the Mg-based BMGs just mentioned can be cast with an (apparently) amorphous structure *in an ambient air atmosphere* (the experimental method will be described in §5.2). This is a rather remarkable property since most glasses are quenched or cast in highly controlled environments to reduce the negative effects of oxygen contamination (see Chapter 2). Further, the majority component, Mg, oxidizes quite readily, so these alloys must interact during cooling with oxygen in a unique way, when compared to other glass-formers. The results of an analysis of oxygen content in the Mg-based BMGs will be presented in §5.3.

After a review of the experimental methods in §5.2, the basic characterization results, confirming the similarity to the behavior of Mg-Cu-Y, will be presented in §5.3. A detailed analysis of the microstructures and devitrification mechanisms will then be

given in §5.4. A complete summary, with a discussion of possible future directions, will be given in §5.5.

5.2. Experimental methods

All samples were prepared by Park, either while at Yonsei University, Seoul, South Korea or at Harvard University. The ribbon samples were prepared by rapid-cooling of the melt (quenching) in an inert gas atmosphere using a melt-spinning process similar to that used at Washington University. As already mentioned, bulk samples were prepared by casting in copper molds under ambient air atmosphere. To prepare the melt, alloy constituents were placed in a carbon crucible and melted by radio frequency (RF) induction heating with a constantly flowing argon purge gas. After complete melting, the melt was simply poured into the mold and allowed to cool, resulting in cooling rates on the order of 10^1 K/s.

The ribbon and bulk samples were characterized using x-ray diffraction (XRD) and differential scanning calorimetry (DSC). The characterization was performed by Park and also confirmed at Washington University. Microscopy studies were performed on as-prepared (quenched or cast) and annealed alloys using (high resolution) transmission (HRTEM) and scanning (SEM) electron microscopy. From TEM, diffraction patterns were generated by fast Fourier transform (FFT) analysis of the HR images, or collected on film from selected area diffraction (SAD) for the conventional TEM. Energy dispersive spectroscopy (EDS) was performed along with imaging in SEM. These alloys transform at temperatures as low as 100°C, so care was taken to minimize heating during preparation. Samples for TEM were prepared by ion-milling with liquid nitrogen cooling. The processing to obtain SEM specimens was minimal, i.e. bulk

samples were broken and pieces small enough to mount directly on the SEM stubs were chosen, but were not polished or etched.

High energy x-ray diffraction measurements were made, with data reduction and analysis methods, using the technique for stationary diffraction described in Chapter 2. The evacuated flight path was used, and all bulk samples were polished just prior to measurement to remove surface oxide layers. Still, some samples showed "roughness" in the diffracted intensity characteristic of scattering from small (nanoscale) crystallites. Some of the data also showed systematic error, which was difficult to correct using the standard means discussed in Chapter 2. These difficulties were often encountered in the stationary diffraction experiments; further study of experimental corrections at the point of data collection would be beneficial (see Appendices 1 and 2). Annealed samples for stationary diffraction studies were prepared using the powder method, also described in Chapter 2.

5.3. Glass formation and thermal analysis

This section presents the results of measurements made to characterize the microstructures and physical properties of the as-prepared (quenched or cast) $Mg_{65}Cu_{(25-x)}Ag_xGd_{10}$ glasses for x = 0, 5, and 10. Figure 5.1 shows the diffracted intensity measured by XRD for the as-quenched ribbons; the broad peak at low angles is characteristic of an amorphous (or nanocrystalline) structure. The diffraction patterns for pieces of the bulk samples, taken from the center of the as-cast cone, are similar to those for the ribbons. These results are used for characterization only; a more detailed analysis from high energy diffraction data will be presented in §5.4.

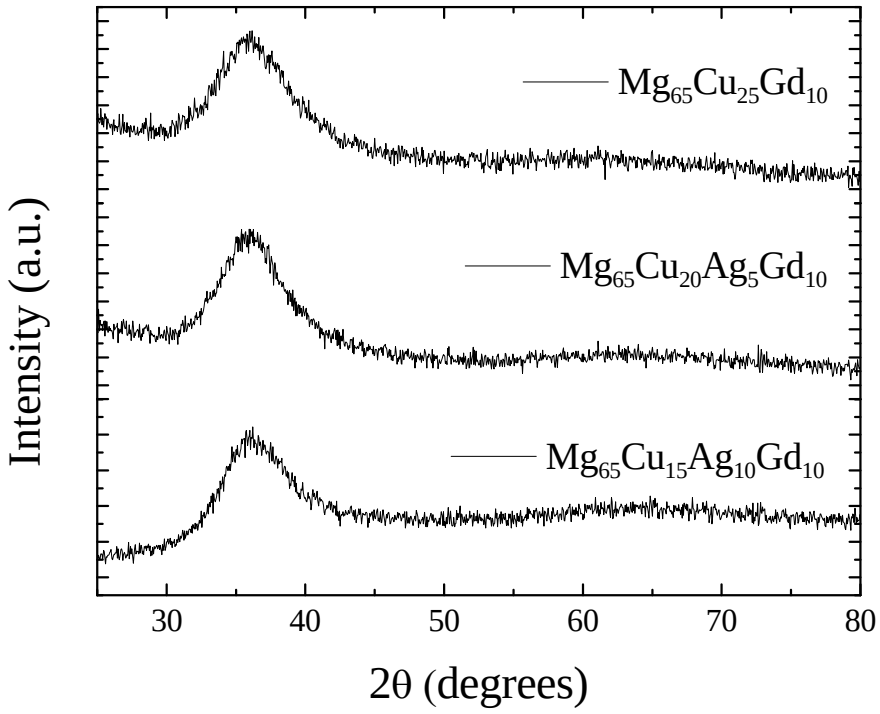

Figure 5.1 – The diffracted intensity from XRD for the $Mg_{65}Cu_{(25-x)}Ag_xGd_{10}$ alloys as-quenched, showing diffraction patterns that are characteristic of amorphous phases.

Figure 5.2.a-b show the (HR)TEM, and associated diffraction patterns, for as-quenched ribbons with x = 0 and x = 10, respectively, both of which are consistent with an amorphous structure. HRTEM was performed on as-quenched samples containing Ag, and a nanocrystal-amorphous composite structure was observed. Those results will be discussed in §5.4.2; Figure 5.2.b shows that the alloys with Ag appear amorphous from basic characterization methods.

Figure 5.3 shows the nonisothermal DSC traces for the as-quenched $Mg_{65}Cu_{(25-x)}Ag_xGd_{10}$ alloys. The presence of a substantial volume-fraction of amorphous material was confirmed by measurements of a glass transition, marked by an abrupt, but smooth, rise in the differential power with increasing temperature (see Chapter 1). The temperature range between the glass transition and the first crystallization peak, defined as the the supercooled liquid region, ΔT_x (a measure of thermal stability), decreases sharply with the addition of Ag. This suggests that the glass structure is becoming less stable against thermal fluctuations with increasing Ag concentration.

From the diffraction data, the pair distribution function, $G(r)$, was calculated by Fourier transform of the structure factor, $S(q)$, using the method described in Chapter 2. The results for the as-quenched $Mg_{65}Cu_{(25-x)}Ag_xGd_{10}$ ribbons are shown, for x = 0 and 10, in Figure 5.4. No sharp peaks can be seen, and the structures of the two glasses are qualitatively similar. There is a slight shift to higher values of r in the first peak suggesting that the average first-neighbor separation is slightly higher in the alloy with Ag. The diffraction data will be discussed further in §5.4.1.

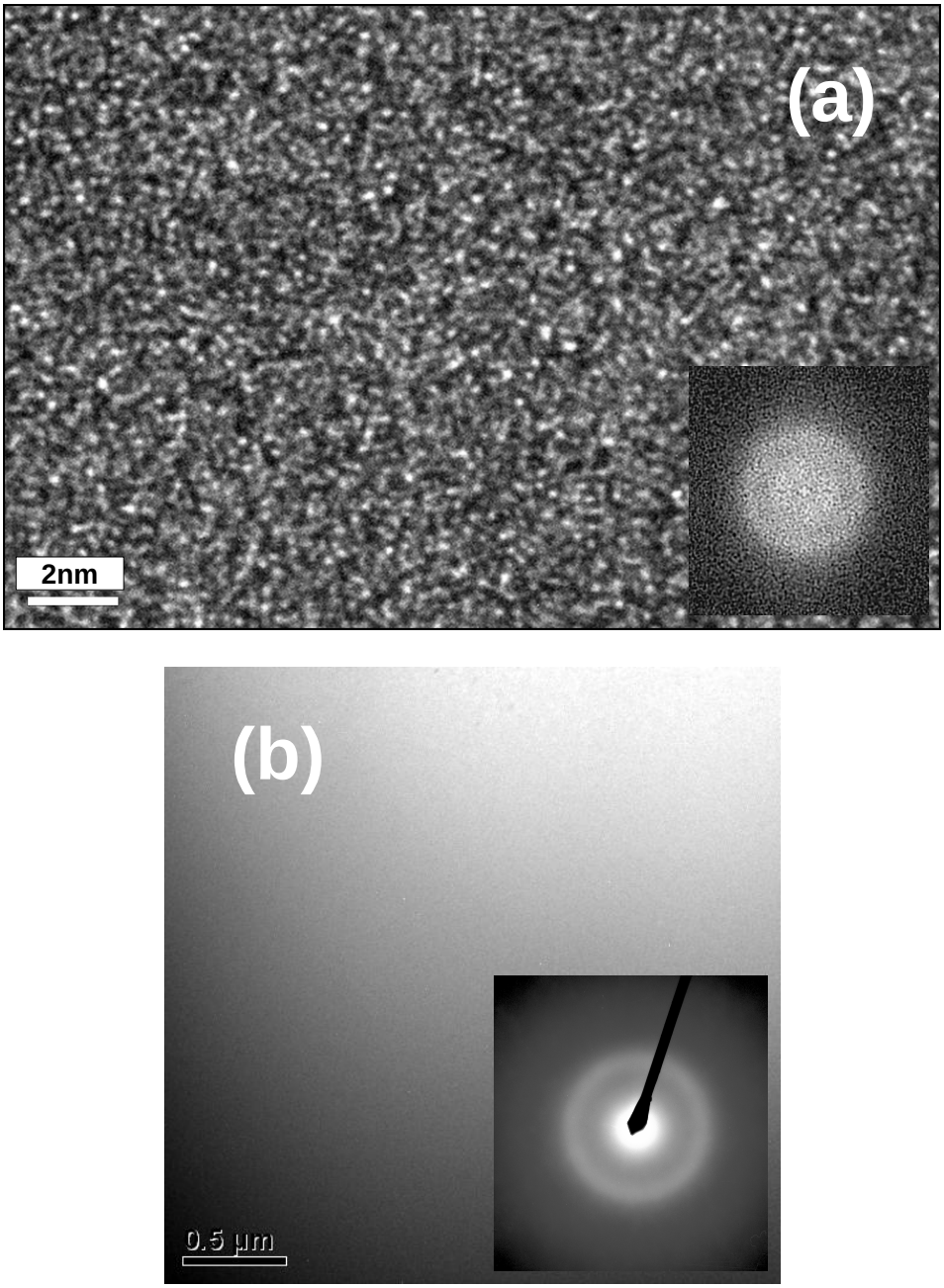

Figure 5.2 – Images from (a) HRTEM of as-quenched $Mg_{65}Cu_{25}Gd_{10}$ ribbon, and FFT diffraction pattern, consistent with an amorphous structure, and (b) TEM of as-quenched $Mg_{65}Cu_{15}Ag_{10}Gd_{10}$, and SAD pattern, showing amorphous structure.

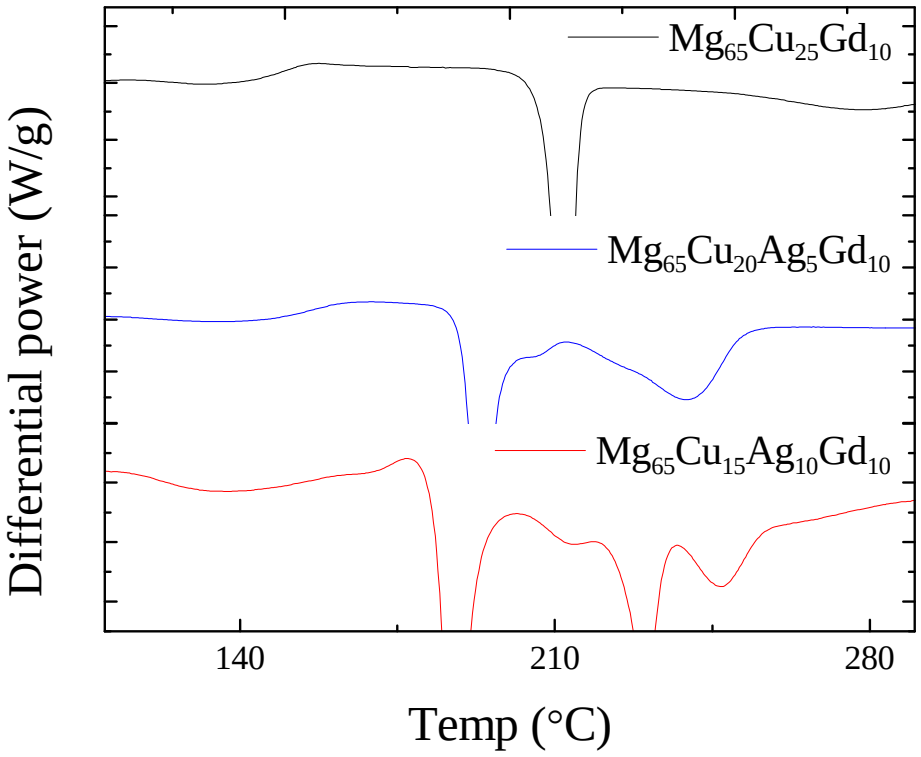

Figure 5.3 – The differential power with increasing temperature from nonisothermal DSC for as-quenched $Mg_{65}Cu_{(25-x)}Ag_xGd_{10}$ ribbons; a decrease in the supercooled liquid region and the appearance of additional phases can be seen with increasing Ag content.

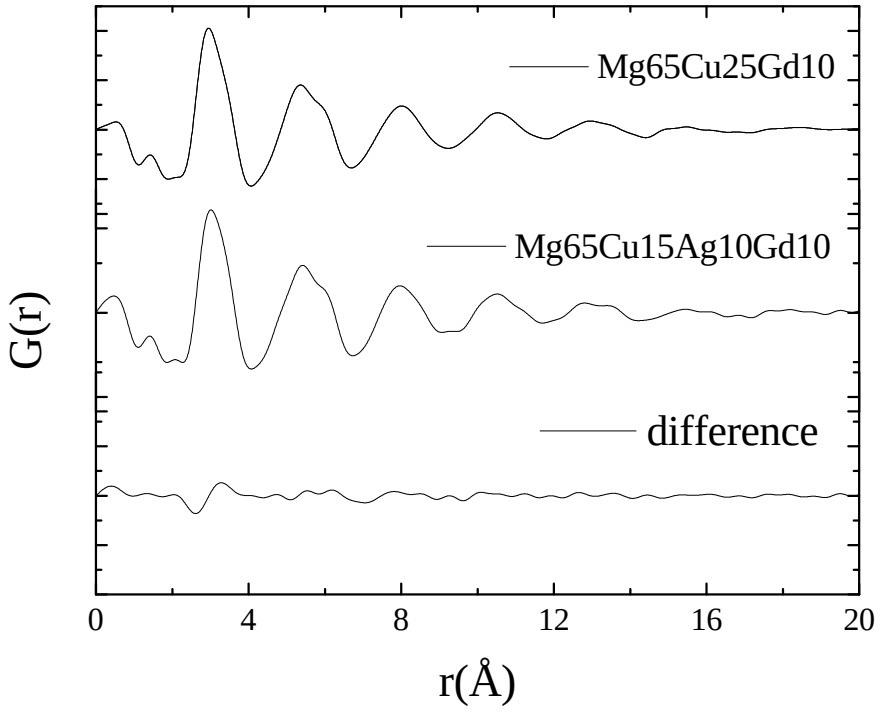

Figure 5.4 – The calculated $G(r)$ from high energy x-ray diffraction for $Mg_{65}Cu_{(25-x)}Ag_xGd_{10}$ samples, as-quenched, for x = 0 and x = 10, and the difference, showing similar structures of the two glasses.

As already mentioned, these glasses were cast in an ambient air atmosphere, so it was important to determine the role of oxygen on glass formation. The results of inert-gas fusion measurements made (by Dr. Matthew J. Kramer at Ames Laboratory, Ames, IA, 50011, USA) on pieces of the bulk samples, taken from the centers of the as-cast cones, showed very low levels of oxygen contamination. Oxygen levels of 34 ppm for the base alloy and 30 ppm for the alloy with 10 at% Ag were measured. These results indicate that the molten alloys do not getter oxygen as they solidify. This shows that the glass structure of these alloys is not stabilized by oxygen, but rather that the oxygen content remains low throughout bulk glass formation.

5.4. Devitrification of $Mg_{65}Cu_{(25-x)}Ag_xGd_{10}$

This section presents the results of annealing studies made on the $Mg_{65}Cu_{(25-x)}Ag_xGd_{10}$ glasses. As discussed in the previous section, the as-quenched (or as-cast) structures for both the base alloy (x = 0) and those with Ag additions (x = 5 and 10) appear to be amorphous. From an examination of the devitrification mechanisms (presented in §5.4.1) and the microstructures of devitrified samples (§5.4.2) it is evident that the alloys containing Ag possess a different structure than the base alloy as-quenched, and that the transformations also proceed by different mechanisms. The results will be examined to determine the role of Ag in the observed data, and its effect on other observed properties of these alloys, such as glass-forming ability and changes in mechanical strength. A complete discussion will be provided in §5.5.

5.4.1. Devitrification mechanisms

The mechanism by which the glass crystallizes (devitrifies) was studied using isothermal DSC, a method described in Chapter 2. Chen and Spaepen proposed a simple, qualitative, approach based on the appearance of the isothermal DSC signature to characterize the transition as either the nucleation and growth of crystallites from the amorphous matrix, or the coarsening of pre-existing grains [14] . (In a coarsening process large grains growing at the expense of smaller ones, with no net volume-fraction transformed). From their method, a nucleation-and-growth process is characterized by a well-defined exothermic peak in the isothermal DSC trace, and a coarsening process by a monotonic increase (endothermic). Unfortunately, as shown by Kelton [15], a process of fast nucleation and grain coarsening would also produce a monotonically increasing signal from isothermal DSC.

Figure 5.5 shows the results of isothermal DSC measurements on as-quenched $Mg_{65}Cu_{(25-x)}Ag_xGd_{10}$ ribbons for x = 0 and 10. Different transformation mechanisms may be at work for the two glasses; the trace for $Mg_{65}Cu_{25}Gd_{10}$ shows a well-defined peak after a long induction time, while the trace for $Mg_{65}Cu_{15}Ag_{10}Gd_{10}$ shows an intial rise, followed by a shallow peak, followed by a continued, slow rise. The former is consistent with the nucleation and growth of crystallites from a glass matrix, as argued by Chen and Spaepen. The latter is more complicated. The initial monotonic rise is consistent with fast nucleation and slow growth, or coarsening. The presence of a peak indicates transformation of a measurable volume-fraction. This type of trace could coincide with a 2-step process, which will be examined in more detail in the following sections.

Due to its enhanced GFA and mechanical properties, the alloy with x = 10 was chosen for a thorough analysis and comparison to the base alloy. Figure 5.6 shows isothermal DSC traces for $Mg_{65}Cu_{15}Ag_{10}Gd_{10}$ measured at various temperatures. Changes in the peak after the initial rise can be seen. In fact, only over a 10°C range of hold temperatures is the peak observed; at 160°C the trace appears to be monotonically increasing, and as well at 170°C. Using high energy x-ray diffraction, following the procedure for stationary diffraction presented in Chapter 2, the 2-step transformation process was studied in further detail. Annealed samples were prepared at different points along the transformation sequence by annealing for 3 minutes at 164°C (at the peak of the initial rise), 5 minutes at 165°C (halfway into the exothermic peak), and 10 minutes at 165°C (into the monotonic "tail").

Figure 5.7.a-b show the structure factor, $S(q)$, its peak position, and FWHM for the different annealing times. From Figure 5.7.a, $S(q)$ becomes visibly "rough," with longer annealing treatments, indicative of (nano) crystallization. Also, the first peak position and FWHM decrease, somewhat discontinuously, with the addition of Ag in the as-quenched state, and with subsequent annealing (Figure 5.7). These indicate ordering of the atomic structure, and an increasing coherence length of ordered regions (including nanocrystal grains), respectively. There is a large difference in both measures for the alloy with 10 at.% Ag, between the as-quenched and 10-minute annealing treatment, and less so between the 3-minute and 5-minute states.

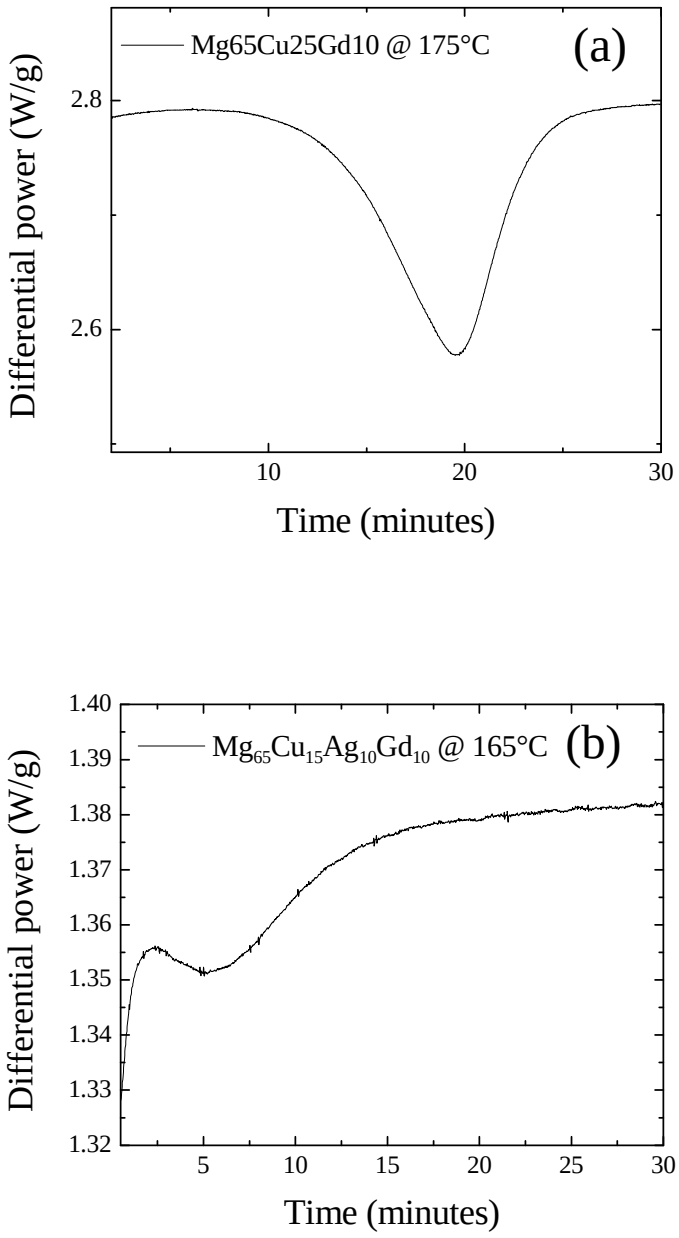

Figure 5.5 – The measured differential power during isothermal DSC for as-quenched $Mg_{65}Cu_{(25-x)}Ag_xGd_{10}$ ribbons for (a) x = 0 at 175C and (b) x = 10 at 165C, showing qualitatively different transformation mechanisms; the trace for x = 5 is similar to that of x = 10.

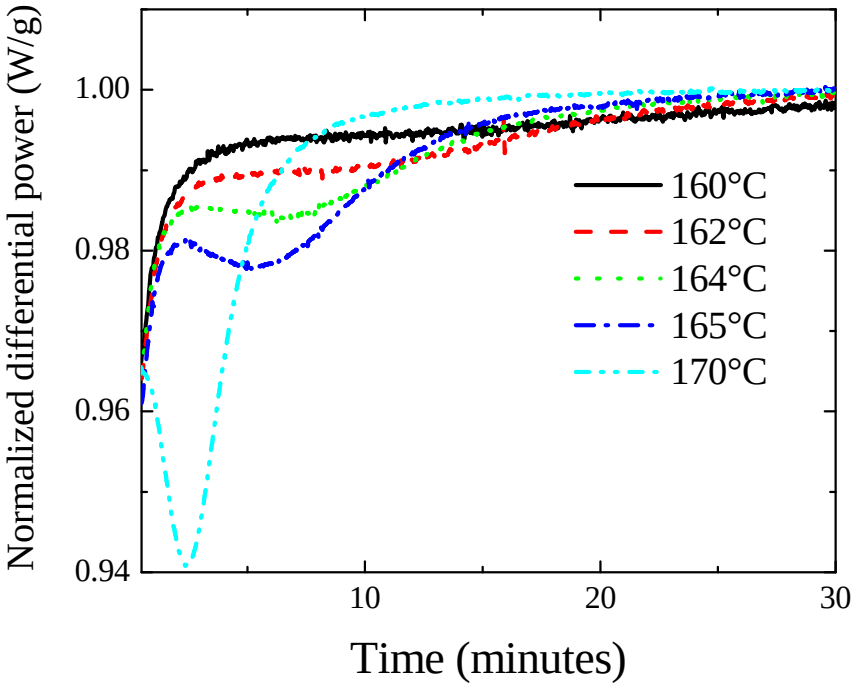

Figure 5.6 – The differential power measured from isothermal DSC $Mg_{65}Cu_{15}Ag_{10}Gd_{10}$ at various isothermal conditions.

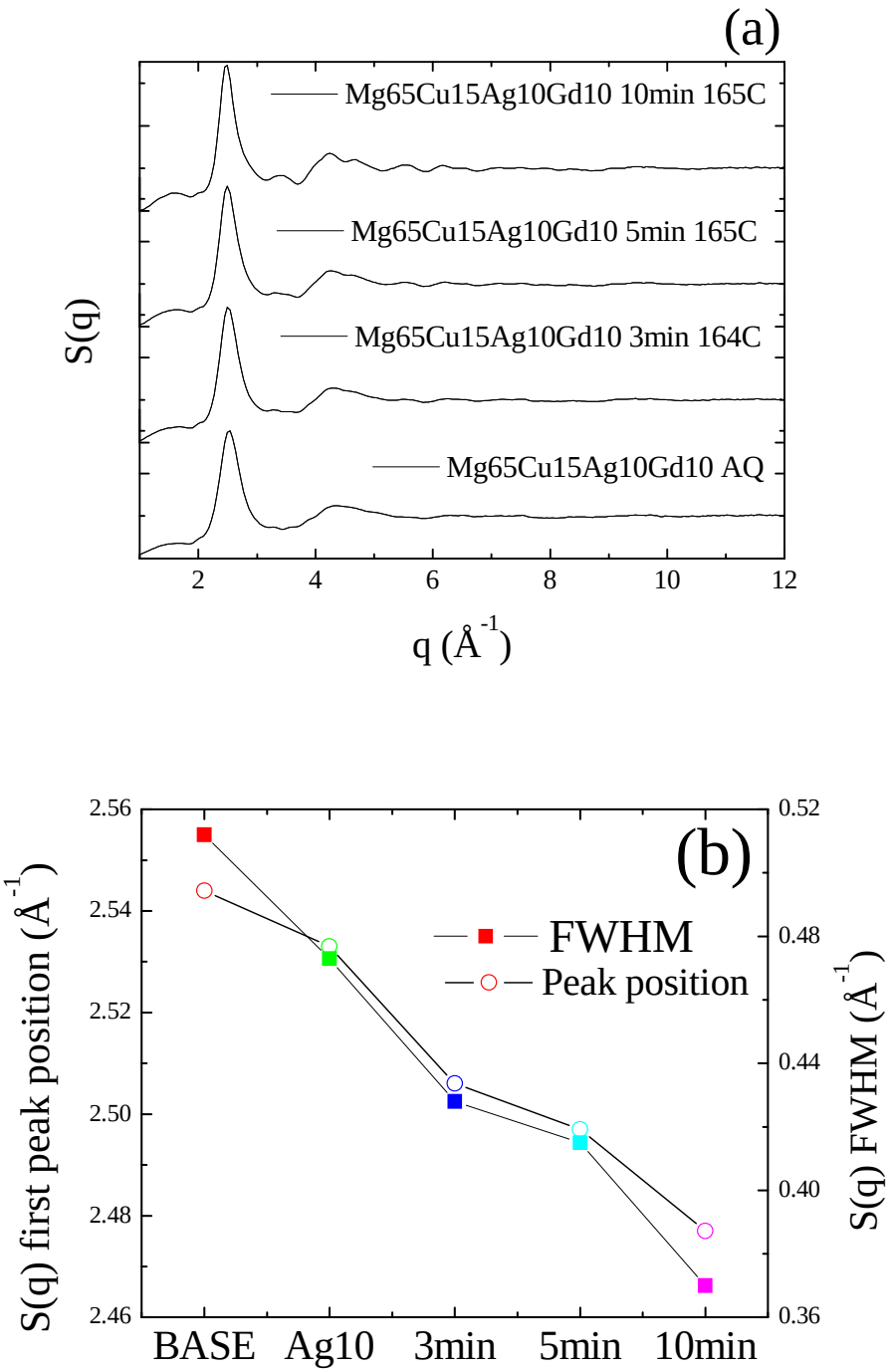

Figure 5.7 – The measured S(q) (a), the S(q) first peak position, and FWHM (b) for as-quenched and annealed $Mg_{65}Cu_{(25-x)}Ag_xGd_{10}$ ribbons.

To study the 2-step transformation, the pair distribution function after different annealing treatments, $G_i(r)$, was calculated (i indicates the annealing time) and analyzed following a procedure similar to that used by Egami and Billinge [16]. Figure 5.8.a shows a comparison of $G_3(r)$, $G_{10}(r)$, and the calculated difference. Figure 5.8.b shows $G_5(r)$, and a 1:1 linear combination of $G_3(r)$ and $G_{10}(r)$, and the calculated difference. From this analysis it is evident that, even though there is some high frequency noise in $G_i(r)$, that $G_3(r)$ and $G_{10}(r)$ are distinct outside the experimental error, and $G_5(r)$ is represented well by a 1:1 linear combination of $G_3(r)$ and $G_{10}(r)$. A comparison of $G_0(r)$ (the as-quenched state) and $G_3(r)$ confirms that the as-quenched state is distinct from the 3-minute state.

5.4.2. Devitrification microstructures

The devitrification microstructures of $Mg_{65}Cu_{(25-x)}Ag_xGd_{10}$ were also examined using SEM and (HR)TEM. Figure 5.9.a-b shows a HRTEM image of the alloy with x = 5 and a dark field TEM image of the alloy with x = 10 after the 30-minute anneal, respectively. The former shows the nanocrystal-amorphous composite character, and the latter shows crystallites of only about 10 nm in diameter, consistent with diffusion-limited coarsening or sluggish grain growth.

Park determined from XRD of cross-sections of the as-cast bulk cones that the structures were fully amorphous to diameters of 8mm, and beyond that were crystalline. This indicates that crystallization was induced by heterogeneous nucleation from the walls of the casting mold, which formed a crystal front that moved inward during casting. The microstructures of pieces taken from the edge thus provide further information about the changes in devitrification mechanisms with Ag addition.

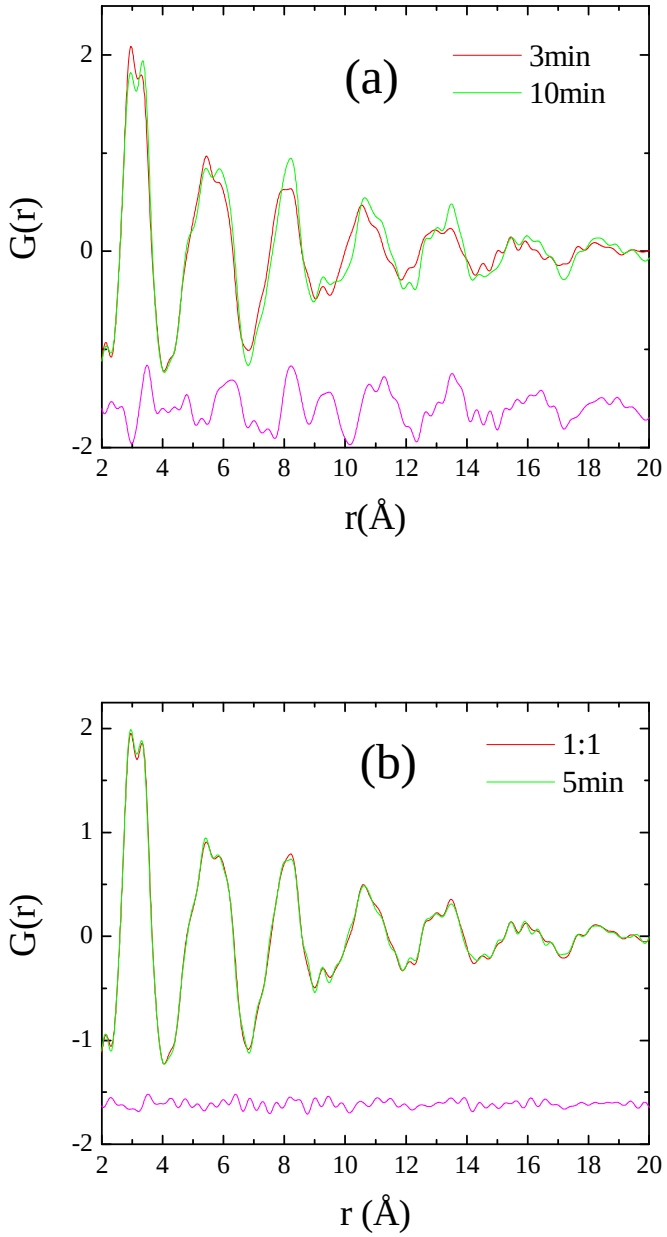

Figure 5.8 – The measured G(r) for $Mg_{65}Cu_{15}Ag_{10}Gd_{10}$ for (a) the 3 minute anneal (red line) and the 10 minute anneal (green line) and the difference, and (b) the 5 minute anneal (green line) and a 1:1 linear combination of the 3 minute and 10 minute structures, showing good agreement.

These were the structures examined in SEM. Figure 5.10 through Figure 5.12 show backscattered electron composition (BSEC) images, and the associated x-ray maps from EDS, for pieces of the bulk samples from the edges of the as-cast cones for x = 0, 5, and 10, respectively. The base alloy (x = 0) shows dendritic crystals in an amorphous matrix, consistent with a diffusion controlled nucleation-and-growth process, similar to that indicated from isothermal DSC (Figure 5.5). The results of EDS for the alloy with x = 0 showed a homogeneous distribution of all atom species, although further study may be needed to confirm that surprising result.

The alloys with x = 5 and 10 showed more complex crystallization. For x = 5, dark-colored dendritic structures rich in Cu and poor in Gd, and light-colored hexagonal structures rich in Ag and Gd, and poor in Cu, were observed. For x = 10, the dendritic regions were smaller, and the Gd-rich crystals were larger and more irregularly shaped than for x = 5. Also, for x = 10, the Ag concentration is almost equal between the amorphous matrix and the Gd-rich crystals, but still depleted for the dendrites. These results are consistent with a nucleation-limited transformation (for the Cu-poor grains) in the presence of sluggish diffusion, indicated by the slow growth and smaller dendrites with added Ag.

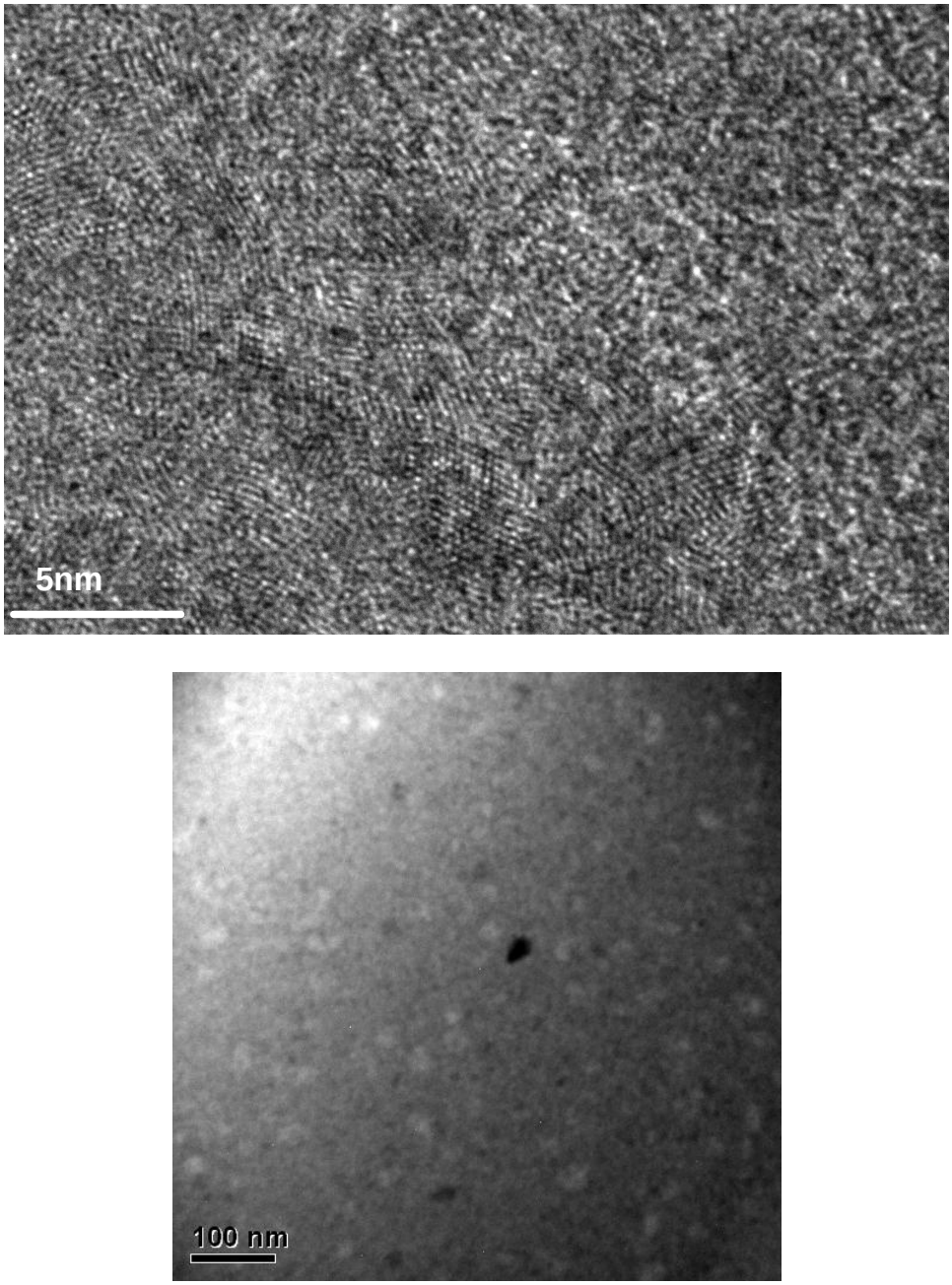

Figure 5.9 – Images of $Mg_{65}Cu_{(25-x)}Ag_xGd_{10}$ from (a) HRTEM of x = 5 as-quenched, showing a nanocrystal-amorphous composite structure and (b) TEM of x = 10 after a 30 minute anneal at 165°C (almost fully transformed); these results illustrate the slow growth of crystallites in the alloys with Ag.

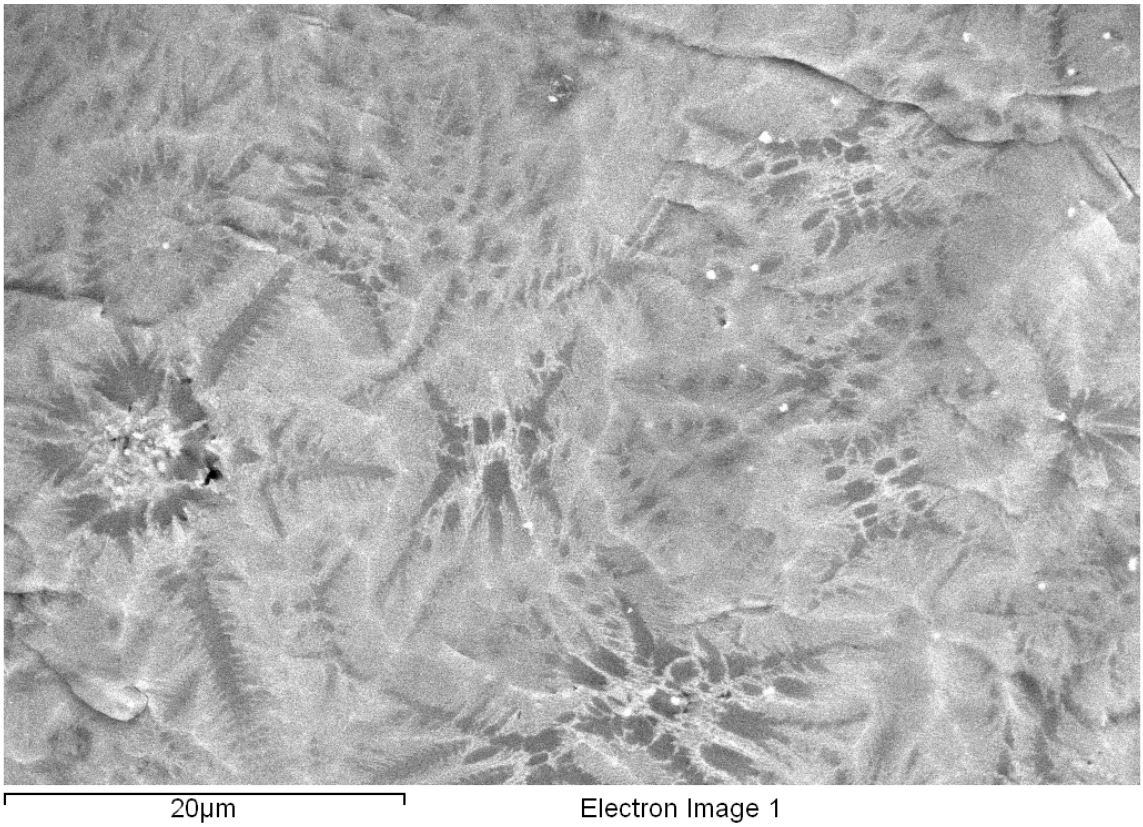

Figure 5.10 – A backscattered electron composition (BSEC) image of bulk $Mg_{65}Cu_{25}Gd_{10}$ from a region partially crystallized, showing a dendritic microstructure.

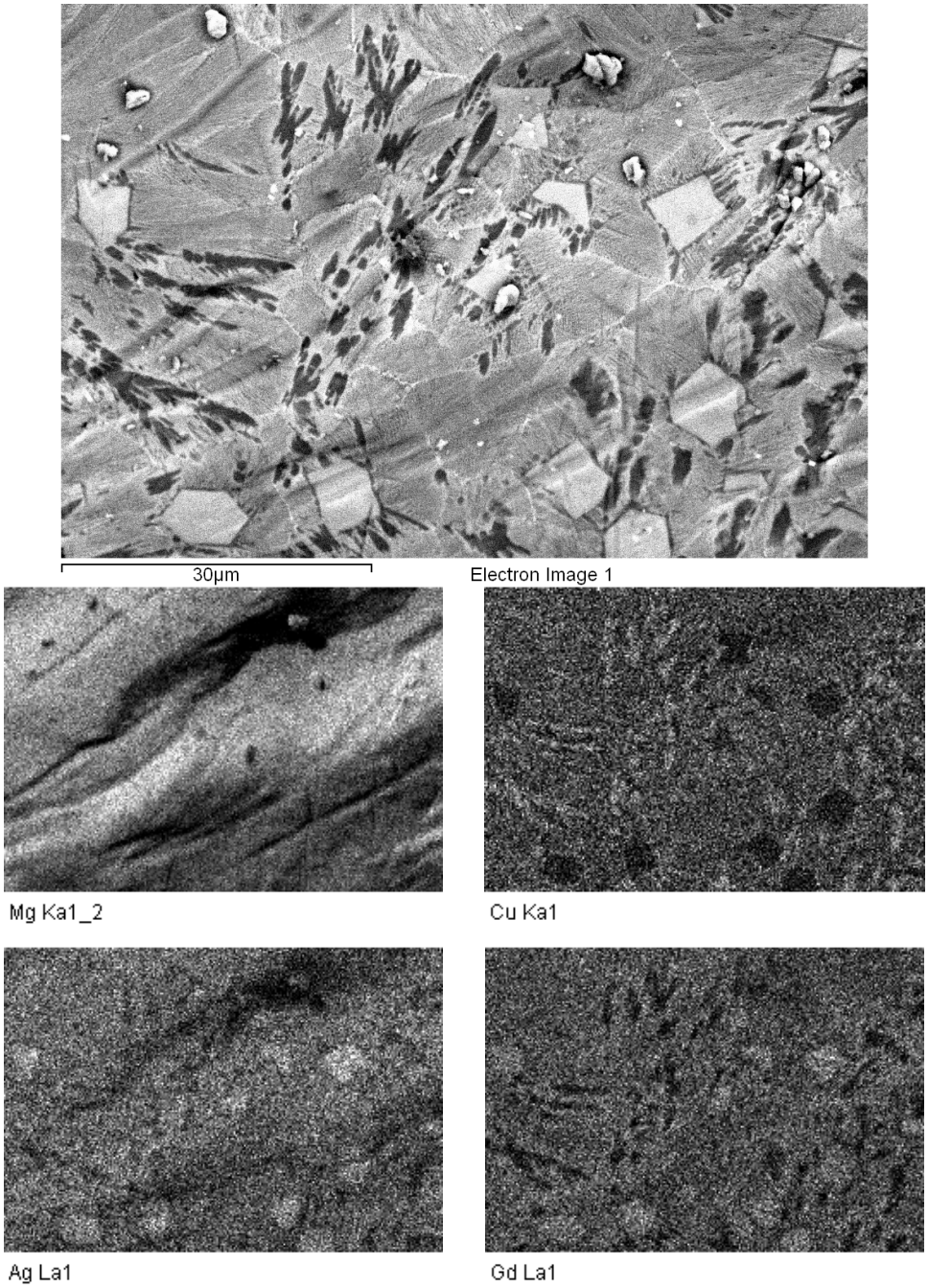

Figure 5.11 – A backscattered electron composition (BSEC) image of bulk $Mg_{65}Cu_{20}Ag_5Gd_{10}$ from a region partially crystallized, showing a composite microstructure, and the accompanying x-ray maps from EDS (where white = high concentration and black = low) for each element.

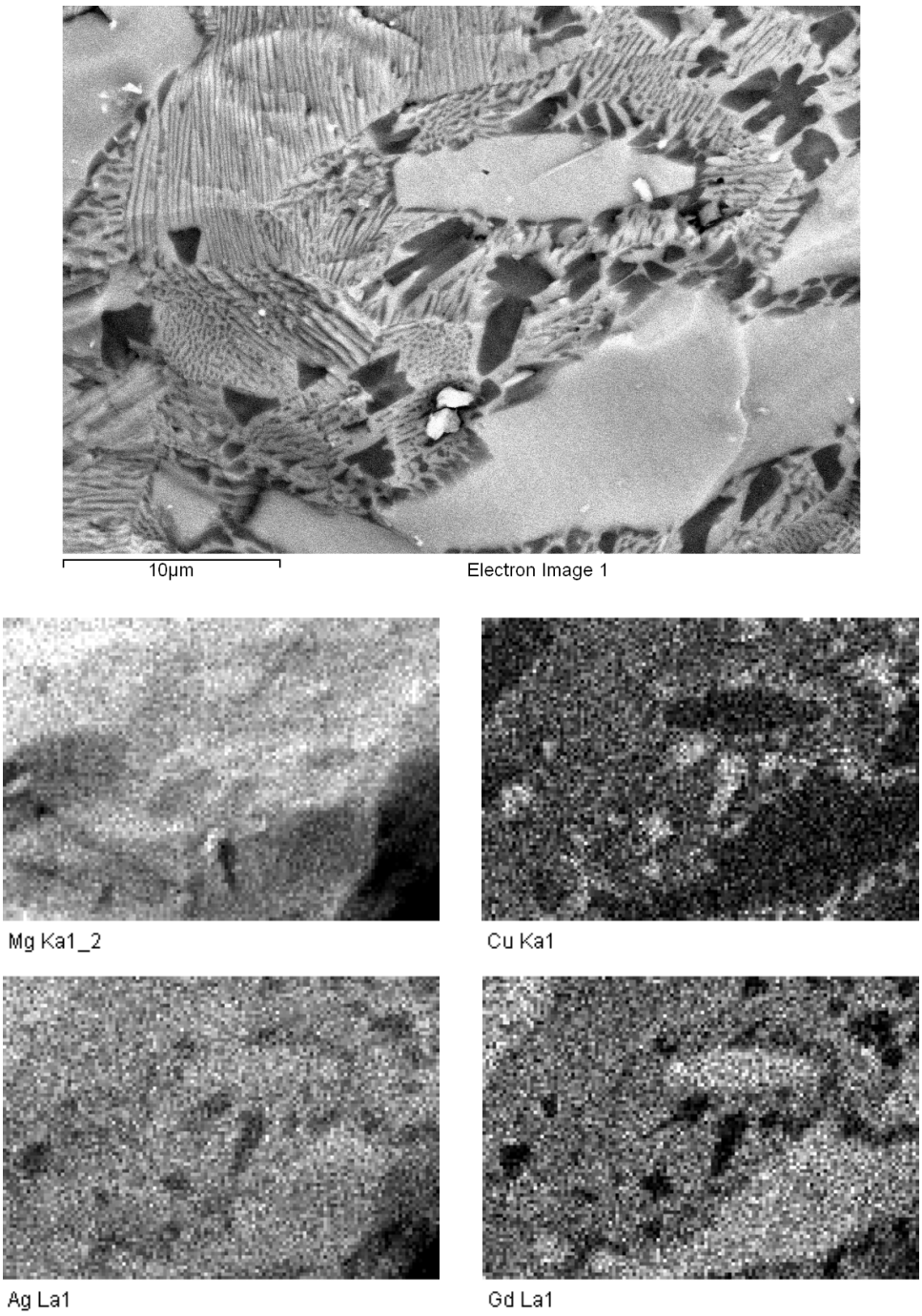

Figure 5.12 – A backscattered electron composition (BSEC) image of bulk $Mg_{65}Cu_{15}Ag_{10}Gd_{10}$ from a region partially crystallized, showing a composite microstructure, and the accompanying x-ray maps from EDS (where white = high concentration and black = low) for each element.

5.5. Summary and discussion

In this chapter, results were presented and analyzed for the as-prepared (quenched or cast) structures and the devitrification mechanisms for $Mg_{65}Cu_{(25-x)}Ag_xGd_{10}$ for x = 0, 5, and 10 from a variety of different experimental methods including high energy XRD, (HR)TEM, and DSC. From these analyses, it was evident that the addition of Ag to the base alloy changes the as-prepared nanostructure from fully amorphous to a nanocrystal-amorphous composite, and affects the growth kinetics, similar to the results of Madge and Greer for Mg-Cu-Ag-Y. Measurements of the oxygen content indicated, surprisingly, that these alloys are resistant to oxygen during casting in air, and that the glass is not stabilized by oxygen. The underlying mechanism for the resistance to oxygen is still not understood.

The base alloy devitrifies by a diffusion controlled nucleation-and-growth process, indicated by a peak in isothermal DSC after a long induction time, and supported by the devitrification microstructure, which was highly dendritic. The alloys with x = 5 and 10 transformed by a more complicated, 2-step process marked in isothermal DSC by an initial rise, followed by a peak, followed by another slow rise. The presence of a peak in isothermal DSC, for both types, rules out a coarsening process as the primary transformation mechanism. The 2-step crystallization from DSC was also observed by analysis of the pair distribution function, following the method of Egami and Billinge [16], which demonstrated that the states during the three stages of transformation observed from isothermal DSC are distinct.

The devitrification microstructures of the bulk samples for x = 5 and 10, from SEM and EDS of crystalline regions of the as-cast cones, are more complicated than that of the base alloy. A mixture of Cu-rich, Gd-poor dendrites, and more uniform, Cu-poor structures was observed. The average size of the Cu-rich dendrites decreased from 10-20μm to 1-5μm as Ag was increased from 5 to 10 at.%. The average size of the Cu-poor grains remained roughly equivalent over the same range of Ag content. For both alloys with Ag, the amorphous background (after a eutectic crystallization for x = 10) can be seen distinctly from the other crystals, with a uniform distribution of all atom species. These results support the conclusion that the Ag is slowing the crystal growth rates by inhibiting diffusion. Taken together, these results suggest the alloys with Ag may transform by initial, fast nucleation and growth of one phase, followed by a second crystallization step characterized by a larger volume-fraction transformed. Such a process could be triggered by phase separation in the glass, although this cannot be detected from the results presented here.

In conclusion, the results of this section confirmed the similarities between Mg-Cu-Ag-Gd and Mg-Cu-Ag-Y. Specifically, it was confirmed that the addition of Ag to the Mg-Cu-Gd alloy causes the as-prepared (quenched or cast) microstructure to change from fully amorphous to a nanocrystal-amorphous composite structure, including for bulk samples up to 1cm diameter. This is due to extremely slow growth rates of crystallites for the alloys with Ag, possibly due to inhibited diffusion. The composite structure of the alloys with Ag leads to improvements in the mechanical properties, and the measured decrease in thermal stability. The nature of the devitrification and crystal growth for the composite structure was explored in more detail, suggesting a 2-step process of fast

development of one phase, followed by nucleation and growth of another, with slow growth. A signature trace in isothermal DSC was associated with this transformation sequence.

Further work on these alloys to explain the resistance to oxygen would be useful for possibly extending the air-casting method to other glasses. EFTEM or atom-probe analysis would determine if the 2-step crystallization in the alloys with Ag is due to phase separation of the glass. Additional HRTEM and SEM studies, to further explore differences between quenched and cast microstructures, would be useful since, from this work, it is evident that the standard characterization techniques of XRD, TEM, and DSC can fail to detect these subtle differences.

References

1. K. S. Bondi, *Analysis of the effects of microalloying on glass formation in Al-Y-Fe alloys by fluctuation electron microscopy*. 2009, Washington University.
2. M. Telford, Materials Today, 2004. **7**(3): p. 36-43.
3. M. E. Launey, D. C. Hofmann, W. L. Johnson, and R. O. Ritchie, Proceedings of the National Academy of Sciences, 2009. **106**(13): p. 4986-4991.
4. Y.-K. Xu, H. Ma, J. Xu, and E. Ma, Acta Materialia, 2005. **53**(6): p. 1857-1866.
5. A. Inoue, Acta Materialia, 2000. **48**(1): p. 279-306.
6. A. Inoue, K. Ohtera, K. Kita, and T. Masumoto, Japanese Journal of Applied Physics. **27**(Part 2, No. 12): p. L2248.
7. S. G. Kim, A. Inoue, and T. Masumoto, Materials Transactions, JIM, Vol. No. () pp. , 1991. **32**(7): p. 609-616.
8. Y. Li, H. Y. Liu, and H. Jones, Journal of Materials Science, 1996. **31**(7): p. 1857-1863.
9. H. Ma, Q. Zheng, J. Xu, Y. Li, and E. Ma, Journal of Materials Research, 2005. **20**(9): p. 2252-2255.
10. H. Men and D. H. Kim, Journal of materials research, 2003. **18**(7): p. 1502-1504.
11. E. S. Park, H. G. Kang, W. T. Kim, and D. H. Kim, Journal of Non-Crystalline Solids, 2001. **279**(2-3): p. 154-160.
12. E. S. Park, J. Y. Lee, and D. H. Kim, Journal of Materials Research, 2005. **20**(9): p. 2379-2385.
13. S. V. Madge and A. L. Greer, Materials Science and Engineering A, 2004. **375-377**: p. 759-762.
14. L. C. Chen and F. Spaepen, Journal of Applied Physics, 1991. **69**(2): p. 679-688.
15. K. F. Kelton, Journal of Alloys and Compounds, 2007. **434-435**: p. 115-118.
16. T. Egami and S. J. L. Billinge, *Underneath the Bragg peaks*. 2003: Pergamon.

Chapter 6

Hydrogen Storage and Hydride Formation in Icosahedral Quasicrystalline $Ti_{45}Zr_{38}Ni_{17}$

As discussed in Chapter 1, one important historical contribution of materials science was to facilitate the industrial revolution. During that time, the main source of fuel for industrializing nations was coal. Almost 300 years later, coal is still the primary energy source for electricity generation, with 46.1% of US electricity generated from coal and 20.5% from natural gas [1]. Transportation fuel is derived almost exclusively from petroleum, of which large reserves remain in only a few locations across the globe that are becoming increasingly difficult and costly to access, causing a host of environmental and political problems. Even electric cars would ultimately be powered, predominantly, by coal or gas.

For those reasons, research in renewable, or "green," power generation and energy storage has received some attention in recent years. One proposed such way of storing energy is hydrogen for automobile fuel, either by generating electricity in a fuel cell, or by burning H_2 gas in an internal combustion engine. In 2003 the United States Department of Energy (USDOE) issued a "grand challenge" solicitation for basic research in hydrogen energy technology [2]. Many barriers to a hydrogen economy exist, one of which is the lack of a safe method for storing appreciable amounts of hydrogen. The DOE goal for hydrogen storage capacity of a viable transportation fuel system is 6.5 weight percent (wt%), with operating temperatures and pressures reasonable for automotive applications. A possible solution is solid storage in a metal hydrogen system

that is *reversible*, i.e. can be repeatedly loaded and unloaded with hydrogen. This chapter presents an analysis of the hydrogen storage capacity and reversibility of a quasicrystalline Ti-Zr-Ni alloy, which showed some potential for attaining the DOE target. This alloy has been well studied by this group, and the work presented here built on the existing techniques to examine preliminary results of exceptional storage.

6.1. Quasicrystals as metal-hydrogen systems

Metal hydrides are typically defined as systems in which hydrogen atoms are bonded to metal atoms. It is also possible for hydrogen to occupy interstitial sites in the atomic configuration of a metal or alloy. Thus, in this thesis, the term *metal hydrogen system* will be used broadly, with *metal hydride* referring specifically to crystalline phases that contain a metal-hydrogen bond. Hydrogen absorption by transition metal alloys is well studied, often in the context of embrittlement of structural materials due to expansion of the crystal lattice associated with absorption.

Interstitial hydrogen atoms can occupy octahedral or tetrahedral sites, and the amount of hydrogen that can be stored in the material is affected, in part, by the number of these sites [3]. Icosahedral quasicrystals, their rational approximants, and the amorphous phase (all described in detail in Chapter 1) contain tetrahedral sites, and have thus been examined for their hydrogen storage capacity [4-9]. The polytetrahedral C14 (Laves) phase, space group P63/mmc, prototype $MgZn_2$, has also been examined [10]. The i-phase $Ti_{45}Zr_{38}Ni_{17}$ alloy was of additional interest due to the affinity for hydrogen of the transition metal constituents, particularly Ti and Zr [11]. Numerous hydrogenation studies have been performed in Ti-Zr-Ni alloys by this group, using an electrochemical method [12], and by gas-loading in a furnace [5, 13]. A technique of surface etching and

deposition of a thin coating of Pd was developed to further facilitate absorption by inhibiting formation of surface oxides [6].

From those studies, icosahedral $Ti_{45}Zr_{38}Ni_{17}$ was found to absorb 1.7-1.9 hydrogen atoms per metal atom, corresponding to up to 2.9 wt%. A Sievert-type apparatus [14] for high pressure, high temperature hydrogen gas-loading of solids was built by Huett [15], and improved upon for this study (the changes are detailed in §6.2). The purpose of this study was twofold: to test preliminary results showing additional hydrogen uptake in $Ti_{45}Zr_{38}Ni_{17}$ at higher pressures than previously studied, and to examine the phase formation with increasing hydrogen (which affects the reversibility).

6.1.1. Pressure-Composition-Temperature measurements

In this thesis, hydrogen absorption and desorption data will be presented using pressure-composition-temperature (PCT) plots. Figure 6.1.a shows the pressure vs. hydrogen composition at various isothermal conditions (pressure-composition isotherms) for a $LaNi_5(H)$ metal hydride. At lower concentrations of hydrogen, the gas is dissolved in the metal as a solid solution (α phase). As the concentration of hydrogen is increased, a plateau occurs at which the hydrogen concentration increases along an isobar. This corresponds to the phase transition to the hydride (β phase). The existence of the plateau can be argued using the Gibbs phase rule, i.e.

$$\mathbf{F = C + N - P},$$

where *F* is the number of degrees of freedom, *C* is the number of components (here two, hydrogen and metal), *N* is the number of non-compositional variables (here two, pressure and temperature), and *P* is the number of phases present (here three, gas, α, and β). Thus, there is only one degree of freedom when all three phases coexist, resulting in the plateau.

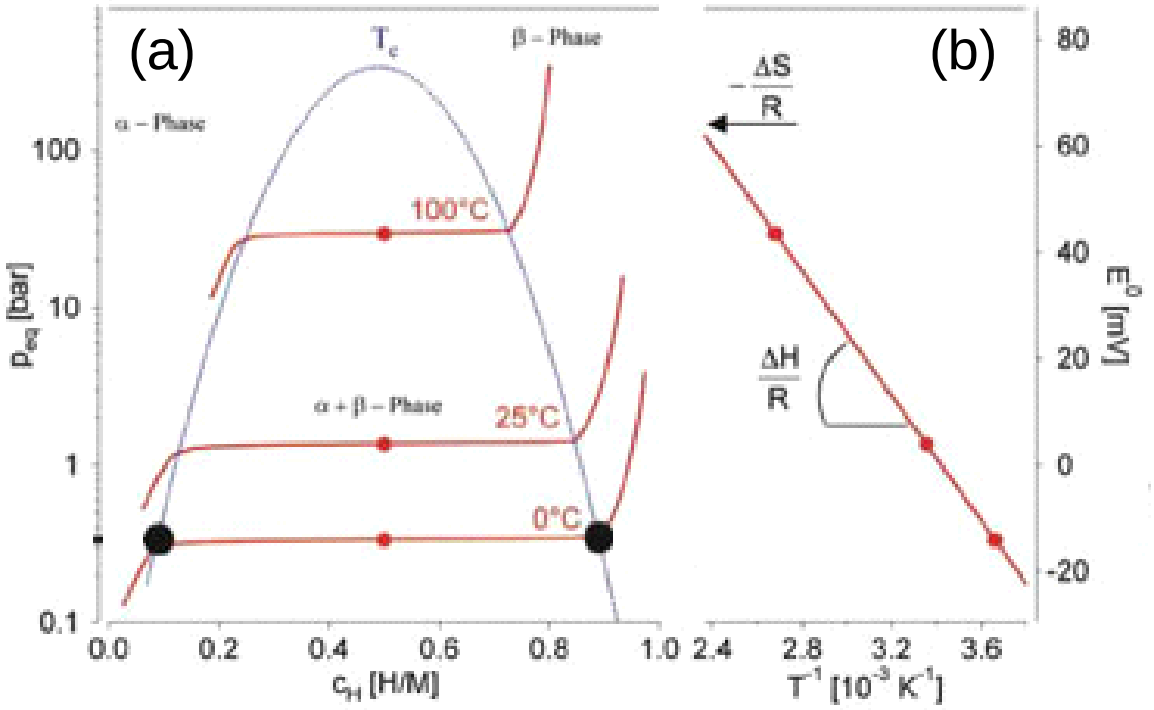

Figure 6.1 – (a) Sample PCT plots at various temperatures (red curves), with phase formation region and (b) accompanying van't Hoff plot for $LaNi_5$ metal hydride; image from [16].

Figure 6.1.b shows a van't Hoff plot, used to calculate the heat of hydride formation, ΔH_h, and the change in entropy, ΔS_h. Given

$$R\ln(P) = \frac{\Delta H_h}{T} - R\Delta S_h ,$$

where R is the gas constant, P is the equilibrium vapor pressure, and T is the temperature, the slope of the van't Hoff curve ($R\ln(P)$ vs. $1/T$) is ΔH_h and the intercept is $R\Delta S_h$.

As already discussed, in the i-phase and the glass (amorphous phase) the hydrogen atoms occupy interstitial sites, and (ideally) there is no transition to a crystal hydride. Rather, the plateau region corresponds to the filling of sites with a narrow distribution of energies. The purpose of the hydrogen loading experiments discussed here was to characterize the PCT curve at higher pressures for i-phase $Ti_{45}Zr_{38}Ni_{17}$. The possibility of a second plateau, corresponding to the filling of interstitial sites of higher energy, but with a similarly narrow distribution of site energies, was examined (results will be presented in §6.3.2). The formation of crystal hydride phases inhibits the hydrogen cycling ability of these alloys. The stable crystal phase is the hexagonal C14 Laves phase, which can store hydrogen but does not readily desorb the gas. Another goal of this work was to examine the hydride phase formation as a function of hydrogen concentration, to compare to the calculated PCT curves (those results will be presented in §6.3.3).

6.2. Experimental and analysis methods

Hydrogenation of i-phase $Ti_{45}Zr_{38}Ni_{17}$ ribbons, prepared by arc-melting and rapid quenching (both described in Chapter 2) and Pd-coating by vapor deposition [6, 15], was performed. One of the important outcomes of the work discussed here was refinement of

the high pressure apparatus of Huett to enable faster and more accurate measurements of pressure, which facilitated simpler analysis methods and a reduction of error in calculated PCT results. In §6.2.1 the apparatus will be briefly reviewed and the important modifications discussed. In §6.2.2, the analysis method will be presented, and some data reduction and smoothing techniques to reduce accumulation of error will be discussed. Appendix 3 provides text of the codes used for device control and data collection, as well as macros used for data analysis and circuit diagrams for the control electronics.

6.2.1. Experimental apparatus

Complete technical details, including CAD drawings and design specifications, of the high pressure, high temperature Sievert-type apparatus used for this work can be found elsewhere [15]. A schematic drawing is shown in Figure 6.2. The basic operation sequence is the following.

- The sample chamber volume (V_{sc}) and intermediate volume (V_{int}) were evacuated using a turbo-molecular pump.
- The hydrogen reservoir (V_{res}) was maintained at a pressure up to 500PSI, monitored by gauge P2.
- A small amount of gas was metered into V_{int} by computer control of an actuated valve (for absorption measurements), or the desorption chamber, V_{des}, was evacuated (for desorption measurements).
- The gas was released from V_{int} to V_{sc} (absorption), or from V_{sc} to V_{des} (desorption), and the pressure was monitored by gauge P0 (for low pressures), and/or gauge P3, and logged by the computer.

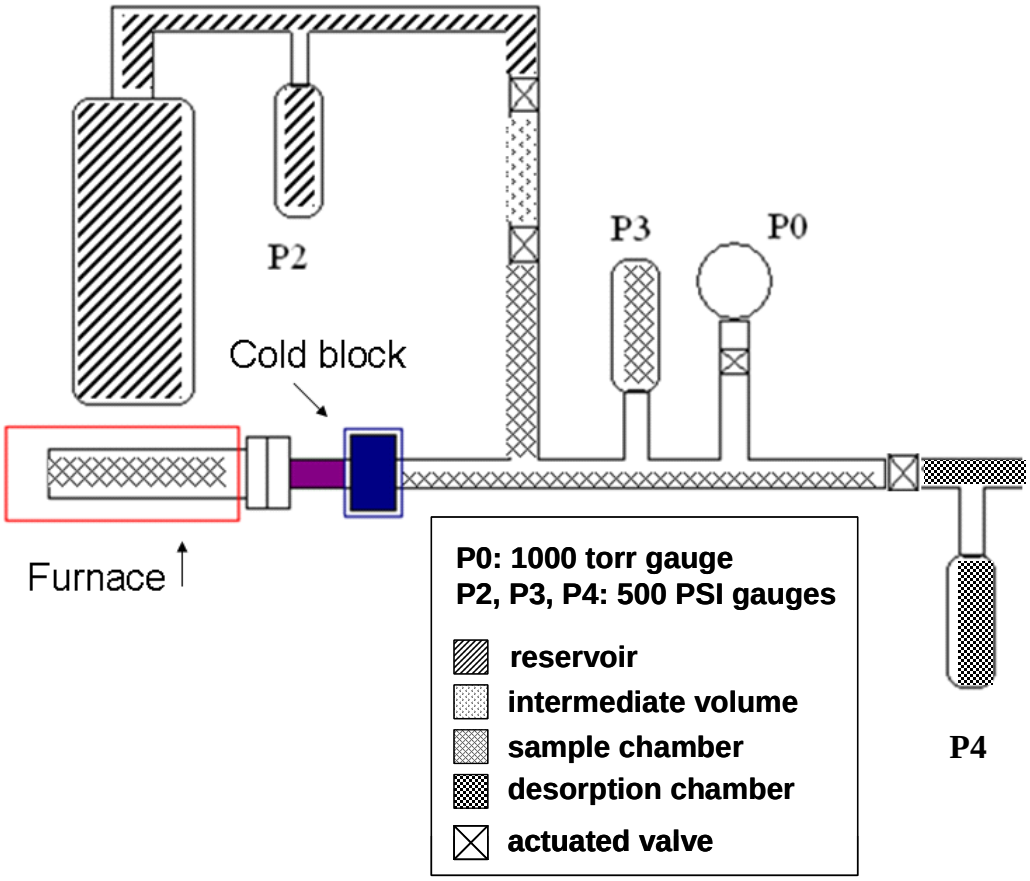

Figure 6.2 – A schematic drawing of the high pressure Sievert-type apparatus built by Huett and used for this work.

- Absorption (desorption) by the sample, residing in the portion of V_{sc} heated by the furnace, was determined by the change in gas pressure (this step will be described in detail in the following subsection).

Automation of the actuated valves and logging of readouts from the pressure gauges were realized using a Measurement Computing DAS08 analog input and digital I/0 PCI board, controlled by a simple routine in MS BASIC. The interface was similar to that used by Huett; some modifications will be discussed later, and the texts of the control routines are provided in Appendix 3.

The modifications made to improve upon the original design were the following. The original high pressure gauges (P2, P3, and P4) were upgraded to MKS Instruments Baratron 25000torr (at full-scale) pressure transducers (model# 722ARCTHA2FA), which allowed faster and more accurate sampling and communication with the data-logging computer. A schematic of the hardware configuration for device control and communication is shown in Figure 6.3. A controller was implemented between the transducers and the computer using reed-relays to isolate each output voltage during a pressure measurement. This eliminated ground loop faults and signal crossing of the output voltages from the transducers, reducing error in the pressure measurements. Circuit diagrams for the gauge controller and the valve controller are provided in Appendix 3.

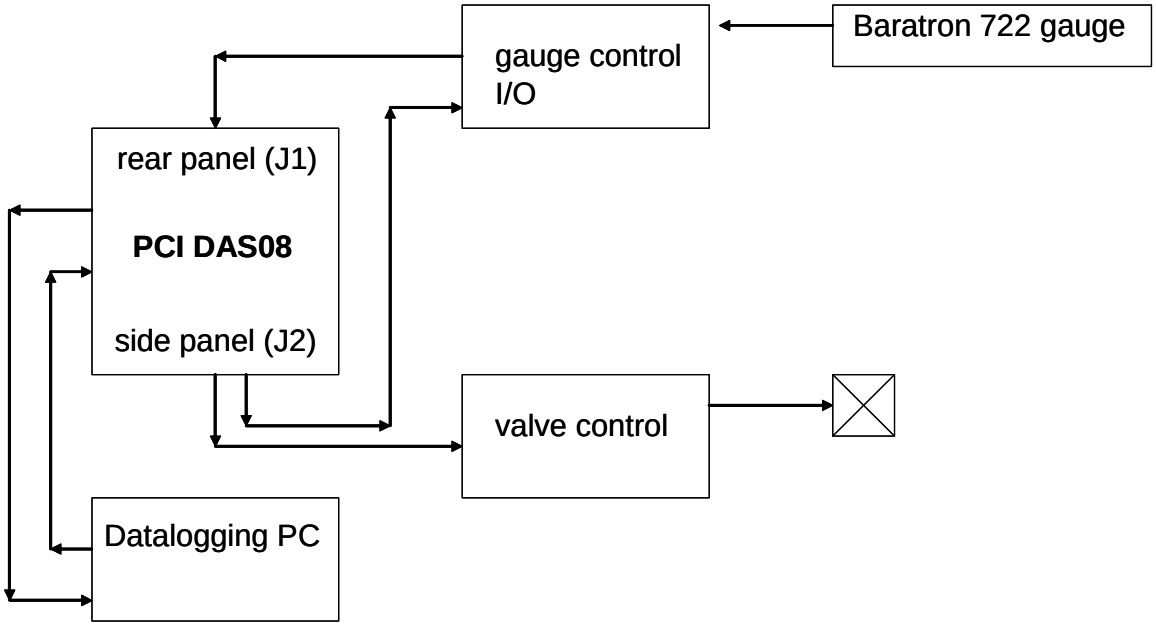

Figure 6.3 – A schematic of the device control system for the high pressure hydrogen loading apparatus.

6.2.2. Data reduction and analysis

In §6.3.2 results of the hydrogen cycling experiments for $Ti_{45}Zr_{38}Ni_{17}$ will be presented, including a discussion of preliminary results showing an ultimate [*H/M*] greater than 3. The use of a new, largely automated, analysis method, demonstrated that these preliminary result were erroneous. This method was possible due to the improved data quality and acquisition speed from the hardware modifications already discussed. For absorption, after a metered amount of hydrogen gas was introduced into V_{sc} through V_{int}, the pressure was measured by P3 or P0 and stored in the computer. From these data, the pressure difference in V_{sc} at each step, ΔP, was determined and, from the ideal gas law, was converted to a difference in the number of moles of gas, Δn, i.e.

$$\Delta n = \frac{\Delta P \times V_{SC}(T)}{RT}$$
$$\Delta P = P_{initial} - P_{final} \quad .$$

Where R is the gas constant and T is the temperature. The volume, V_{sc}, is regarded as a temperature dependent quantity to further reduce the error in Δn. The temperature profile across V_{sc}, due to the interaction of the furnace that encapsulates the sample holder and the cold block that isolates the heated volume from the rest of the sample chamber (Figure 6.2), is complicated. Thus, during calibration, the effective sample chamber volume at room temperature was determined given the various furnace temperatures.

From the measured absorption (or desorption), Δn, the hydrogen-to-metal atom ratio [*H/M*] was calculated, i.e.

$$\left[\frac{H}{M}\right]_f = \left[\frac{H}{M}\right]_i + \frac{2 g_m \sum_i \Delta n_i}{m_m}. \qquad (6.2.2.1)$$

Where g_m is the atomic weight of the alloy and m_m is the mass of the alloy. The $[H/M]_i$ term is included to accommodate desorption measurements, where Δn is less than zero; for absorption measurements $[H/M]_i$ is equal to zero.

As already mentioned, accumulation of error is a major concern when calculating PCT curves, due to the summation in Eqn. 6.2.2.1. To illustrate these effects and develop a rationale for smoothing and correction of the data, a model system was constructed and analyzed. First, idealized H_2 pressure data as a function of time was constructed with an absorption peak qualitatively similar to that measured for $Ti_{45}Zr_{38}Ni_{17}$ (Figure 6.4.a). For higher pressures, after the offset of the peak, the simulated pressure difference was fixed at zero. From the pressure difference data, the PCT curve for the simulated system was calculated (Figure 6.4.b), giving a linear rise up to about 0.25 atm at [H/M] = 0.033, a plateau from 0.3-0.6atm, and no change in [*H/M*] with further increasing pressure.

Next, spurious peaks were introduced in the pressure difference data (Figure 6.5.a), similar to what has been observed in PCT measurements of $Ti_{45}Zr_{38}Ni_{17}$ using this apparatus (further discussion of those data will be given in §6.3.2), and the data analyzed to generate a PCT curve (Figure 6.5.b). The spurious peaks were of lower magnitude than the true absorption peak, and not robust (i.e. of only a single data point). The resulting PCT curve is not smooth, and demonstrates the accumulation of error by an increasing value of [*H/M*] with increasing pressure.

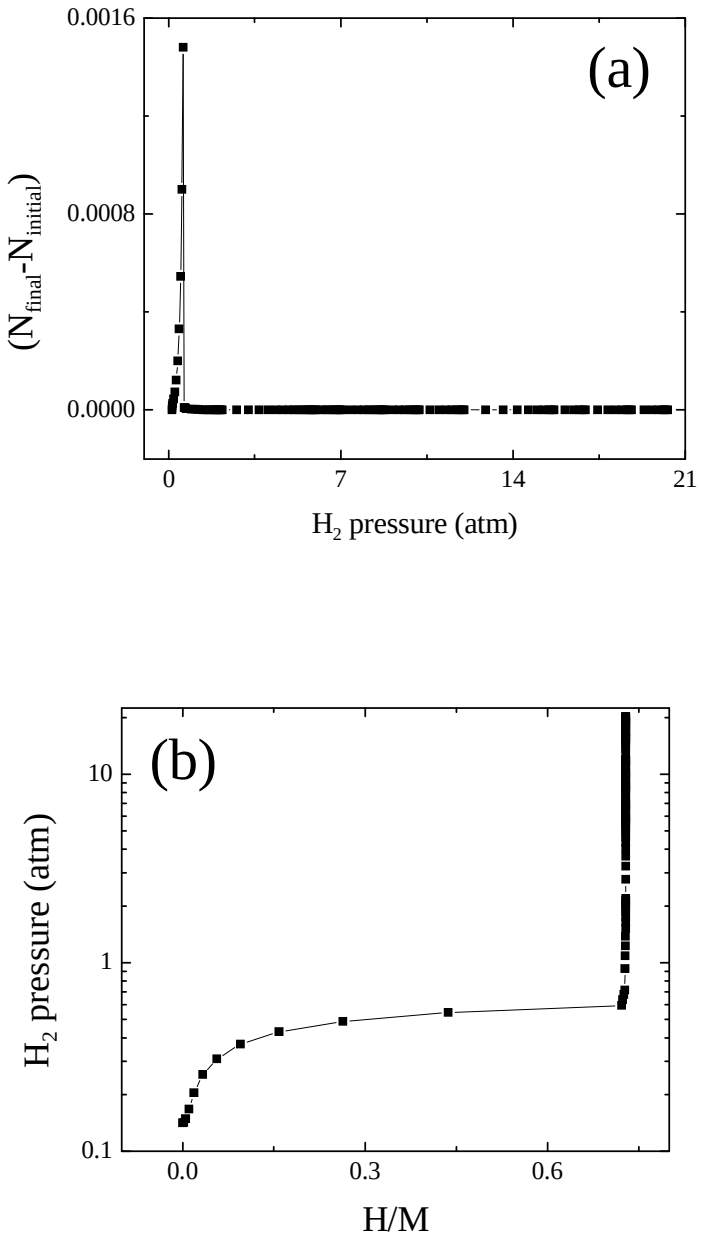

Figure 6.4 – The results of an analysis of simulated hydrogen absorption data; (a) the change in moles of hydrogen at each loading step as a function equilibrium H2 pressure; (b) the resulting PCT curve from analysis of the absorption data.

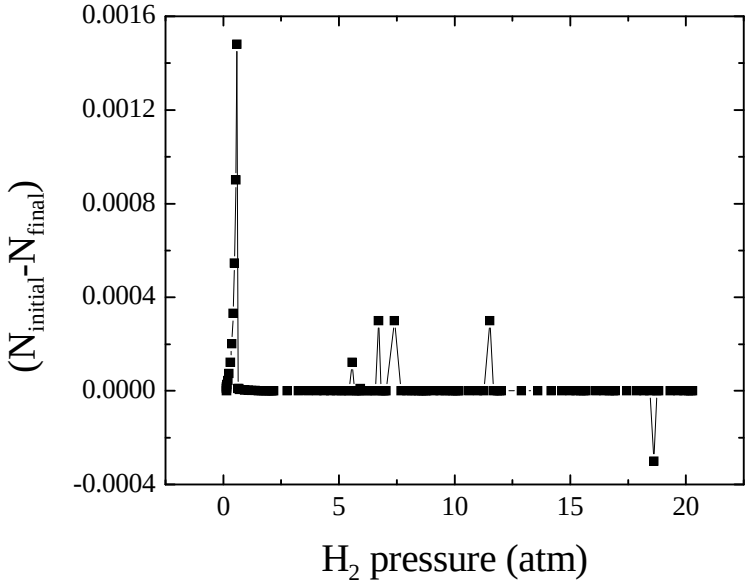

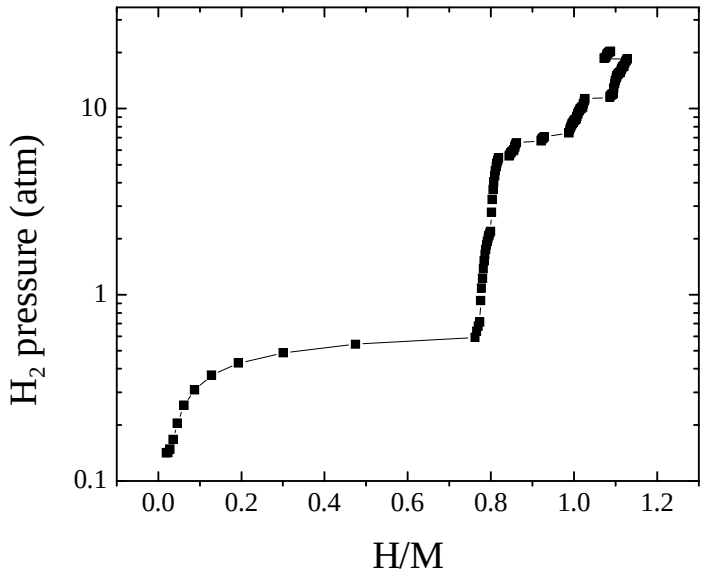

Figure 6.5 – The results of a PCT simulation with spurious peaks introduced in the absorption profile, (a), and the resulting PCT curve showing accumulated error at high pressures, (b).

Another factor is the contribution to the final [*H/M*] from an overall background in Δn. In Figure 6.6.a, a linear background was introduced in Δn with increasing pressure above the primary absorption peak. In real data a background of this type could correspond to subtle absorption arising from a different mechanism than that which creates the peak in Δn at lower pressures. The calculated PCT curve (Figure 6.6.b) at high pressures is qualitatively similar to the previously measured results for $Ti_{45}Zr_{38}Ni_{17}$. Those results will be discussed further in §6.3.2.

6.3. Results

This section presents results of the hydrogen loading studies, including hydrogen cycling of pure Pd metal, in §6.3.1, for confirmation of the efficacy of the apparatus and methods already discussed in §6.2. The results from Pd also may be used to more accurately calibrate the instrument. The hydrogen cycling behavior of $Ti_{45}Zr_{38}Ni_{17}$ is then presented in §6.3.2, showing no evidence of a second plateau in the PCT curve, up to a hydrogen pressure of about 34atm. That section also includes an examination of the PCT data in light of the data reduction techniques already discussed. Finally, §6.3.3 presents results of a study the microstructure and hydride phase formation with increasing hydrogen content in $Ti_{45}Zr_{38}Ni_{17}$ using x-ray diffraction (XRD), building on previous work from this group.

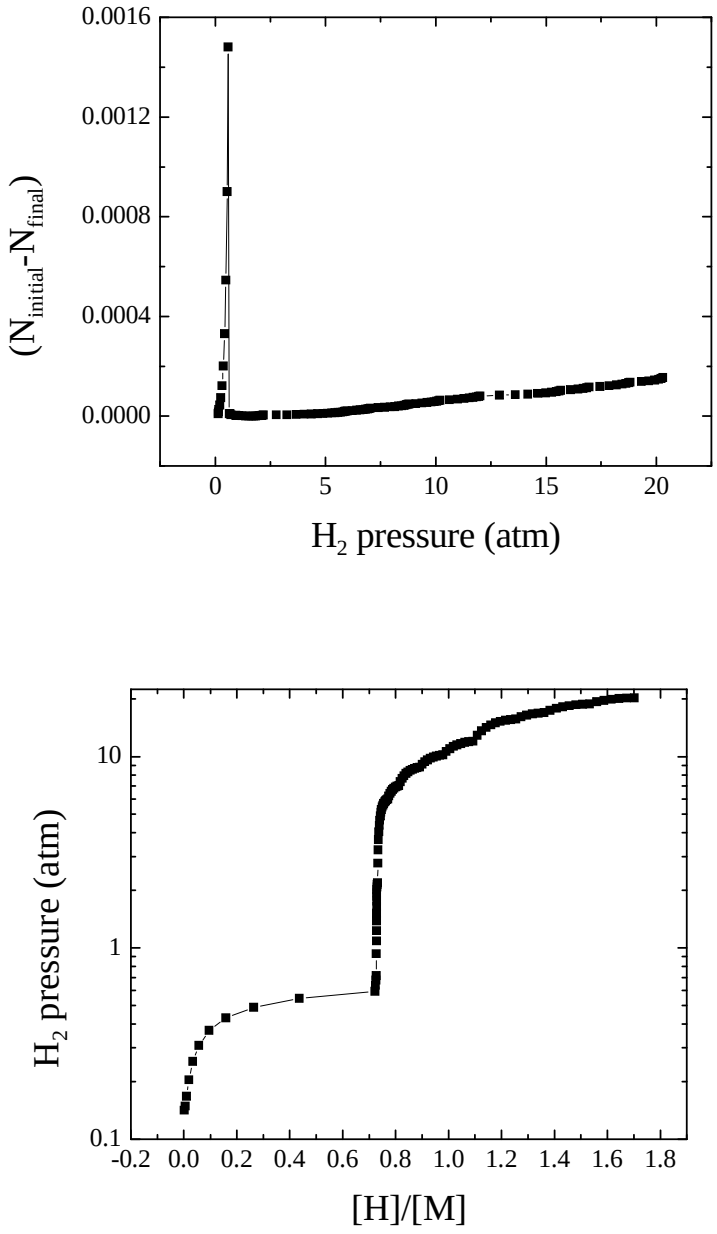

Figure 6.6 – The results of a PCT simulation with a linear background introduced in the absorption profile at high pressures, (a), and the resulting PCT curve showing accumulated error at high pressures, (b).

6.3.1. Hydrogen cycling in Pd

Pure Pd metal is a suitable standard for testing and calibration of the high pressure PCT apparatus and the modified analysis method, due to its well-known ability to store hydrogen [17, 18]. Figure 6.7.a shows the change in the number of moles of Hydrogen at each loading or unloading step for absorption and desorption, respectively, measured from the change in pressure. From Figure 6.7 it is clear that, for Pd, absorption and desorption can be easily measured directly from the change in pressure using this method. There is a slight deviation from zero in both cases, which could result in error in the calculation of the PCT curve, and may warrant further examination as part of a calibration or data correction procedure.

Figure 6.7.b shows the resulting PCT plots, which exhibit hysteresis with cycling, and a small offset at the low pressure end of the desorption curve. This offset should be noted since again, accumulation of error could arise in repeated cycling experiments. Figure 6.8 gives a comparison of PCT results for Pd, from this work and from other published results. From Figure 6.8, it appears that the measured data at nominally 200°C fall somewhere between the published data at 200 and 150°C, suggesting that further examination of the actual (or effective) temperature at the point of hydrogen loading/unloading may be required. The data shown in Figure 6.8 agree well with existing results for the Pd(H_2) system, confirming the efficacy of the measurement and analysis techniques, to within a slight temperature correction.

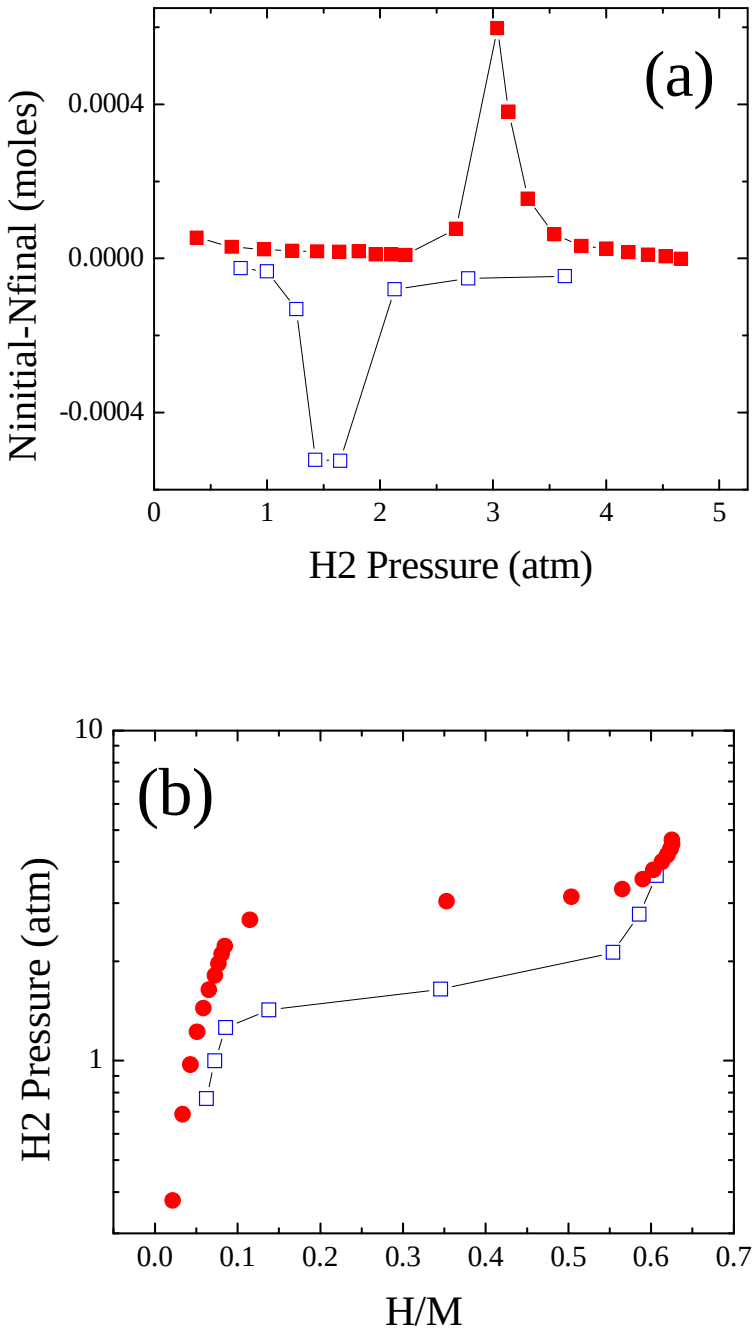

Figure 6.7 – The measured hydrogen absorption (a) and calculated PCT curves (b) for Pd at 200°C during absorption (solid red circles) and desorption (open blue squares).

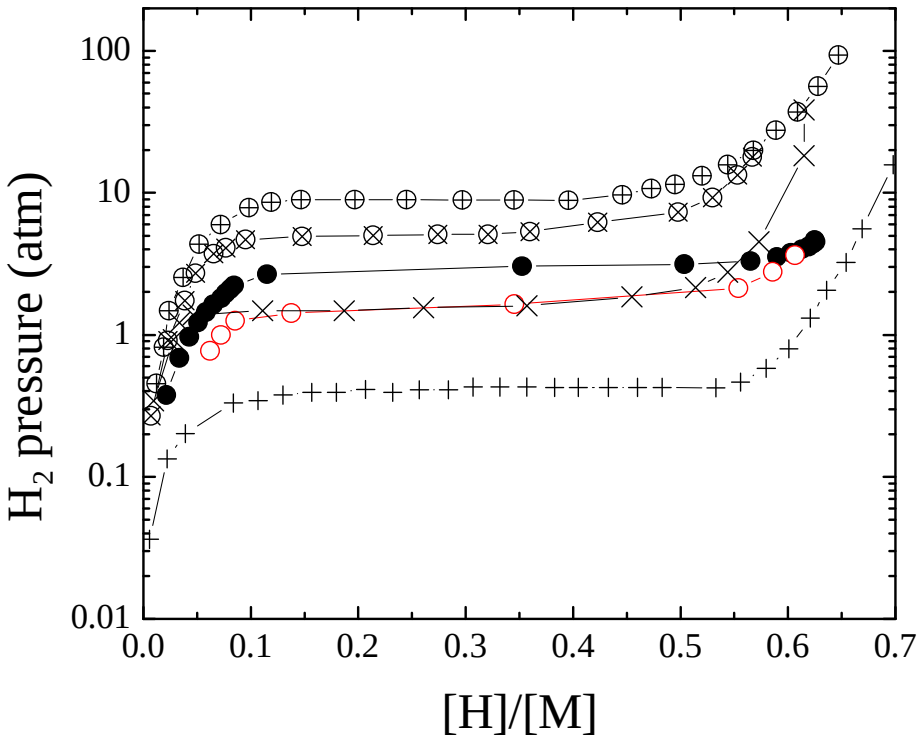

Figure 6.8 – A comparison of PCT curves for Pd: (⊕) 243°C from [17], (⊗) 200°C from [18], (●) 200°C from measured adsorption, (○) 200°C measured desorption, (×) 150°C from [18], (+) 120°C from [17].

6.3.2. Hydrogen cycling in $Ti_{45}Zr_{38}Ni_{17}$

Preliminary results from Kelton and others [19], from this laboratory, indicated the presence of a second absorption plateau at high pressures for i-phase $Ti_{45}Zr_{38}Ni_{17}$ (Figure 6.9), with an ultimate [*H/M*] value greater than 3 at equilibrium pressures of a little over 20atm. For this work, the PCT curves were calculated for i-phase $Ti_{45}Zr_{38}Ni_{17}$ for various temperatures, and **the [*H/M*] value greater than 3 was shown to be false**. This section presents the current results and some discussion of the validity of applying a background correction at high pressures.

Plots of the measured absorption for various temperatures with increasing equilibrium pressure are shown in Figure 6.10. From Figure 6.10, some spurious peaks in the absorption can be seen. These were removed, and the resulting PCT curves calculated (Figure 6.11.a). The PCT curves are qualitatively consistent with the previous results of Huett and Kim [13, 15] up to modest pressures (about 5 atm, Figure 6.12). For higher equilibrium pressures, the results from this work show a much weaker increase in [*H/M*], with little or no appearance of a second plateau. If the background correction (see §6.2.2) is included, the second plateau is completely removed (Figure 6.11.b). Again, the application of this correction is less obvious than the removal of spurious peaks, as a gradual increase in absorption could correspond to additional loading of the hydride phase (or further occupation of interstitial sites in the quasilattice). It does not, however, reflect a phase change, or occupation of a different class of interstitial sites, similar to the first plateau (cf. Figure 6.1).

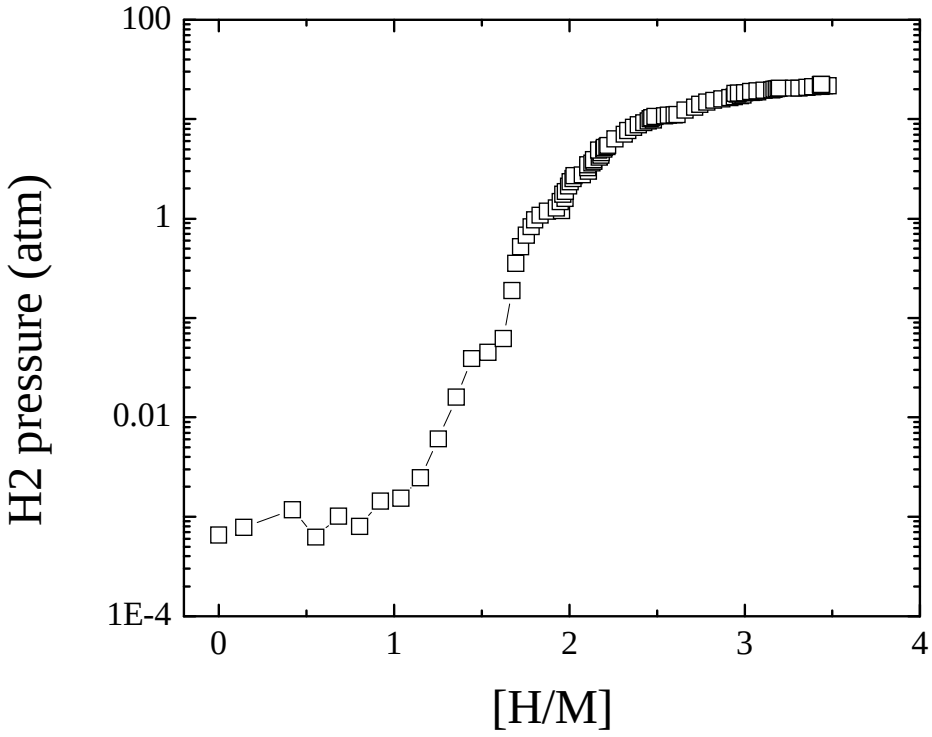

Figure 6.9 – PCT data for $Ti_{45}Zr_{38}Ni_{17}$ using the old analysis method, the apparent long second plateau is clearly seen to extend to H/M = 3.5 at 22 atm; this result is an artifact.

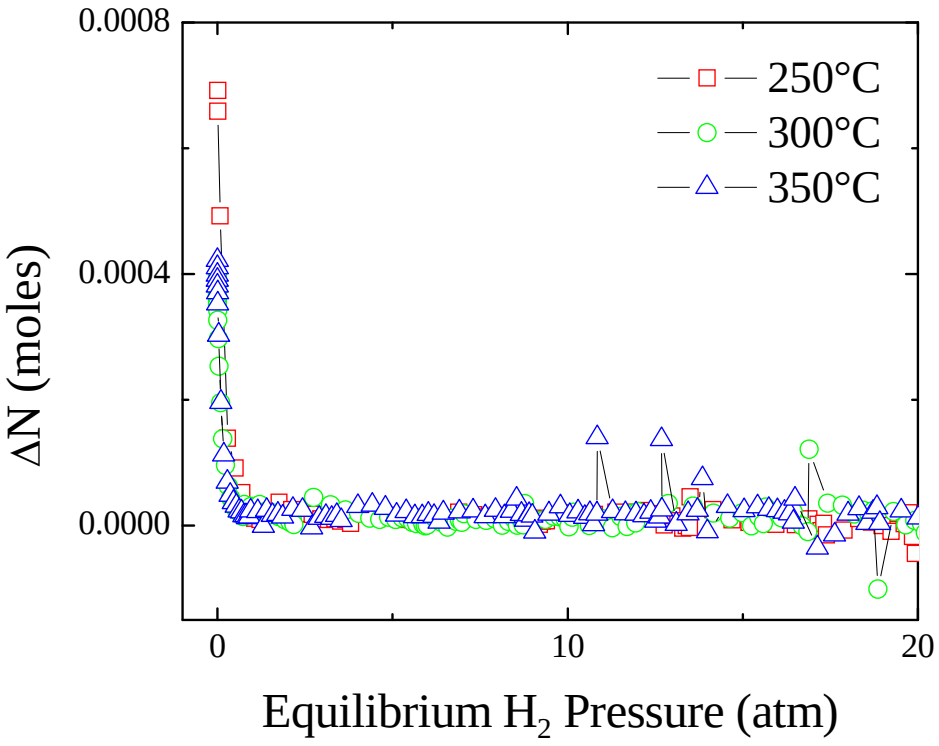

Figure 6.10 – The measured (uncorrected) absorption data for $Ti_{45}Zr_{38}Ni_{17}$ at various temperatures.

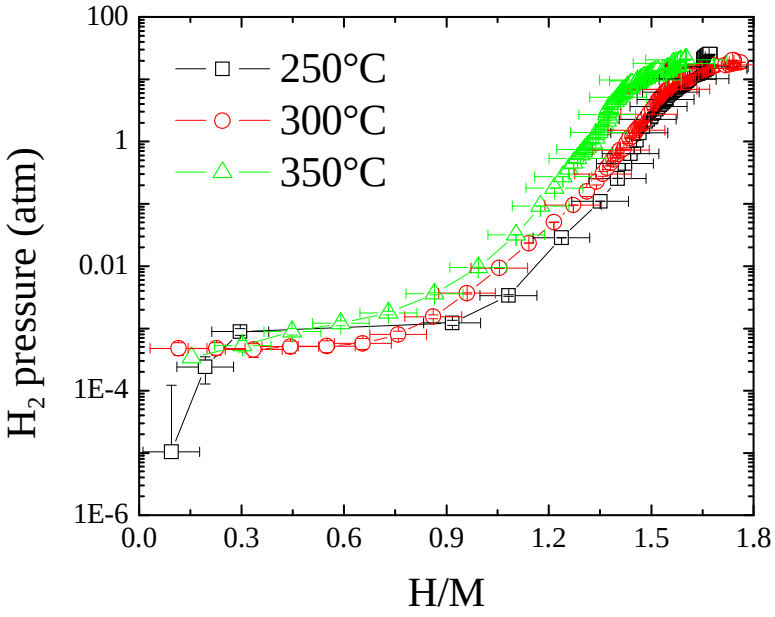

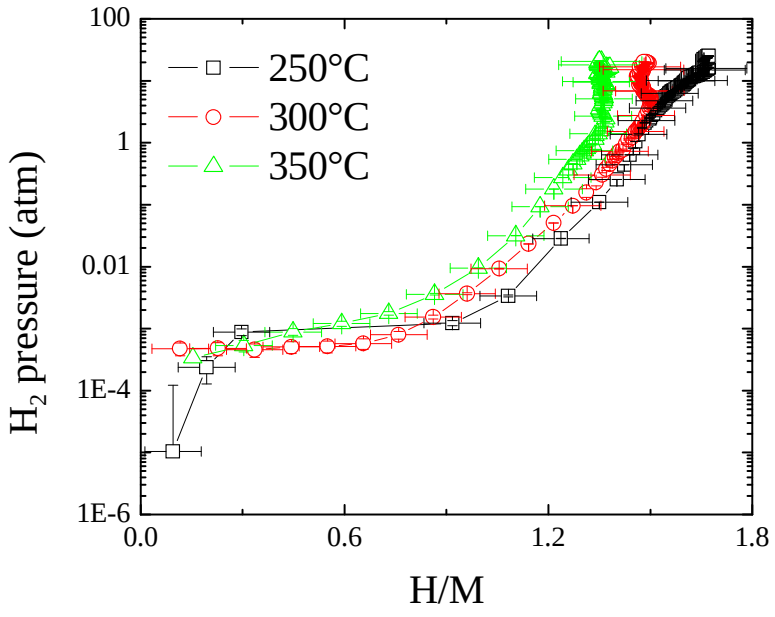

Figure 6.11 – The PCT curves for $Ti_{45}Zr_{38}Ni_{17}$, calculated from the absorption data, at various temperatures, without (a) and with (b) background subtraction.

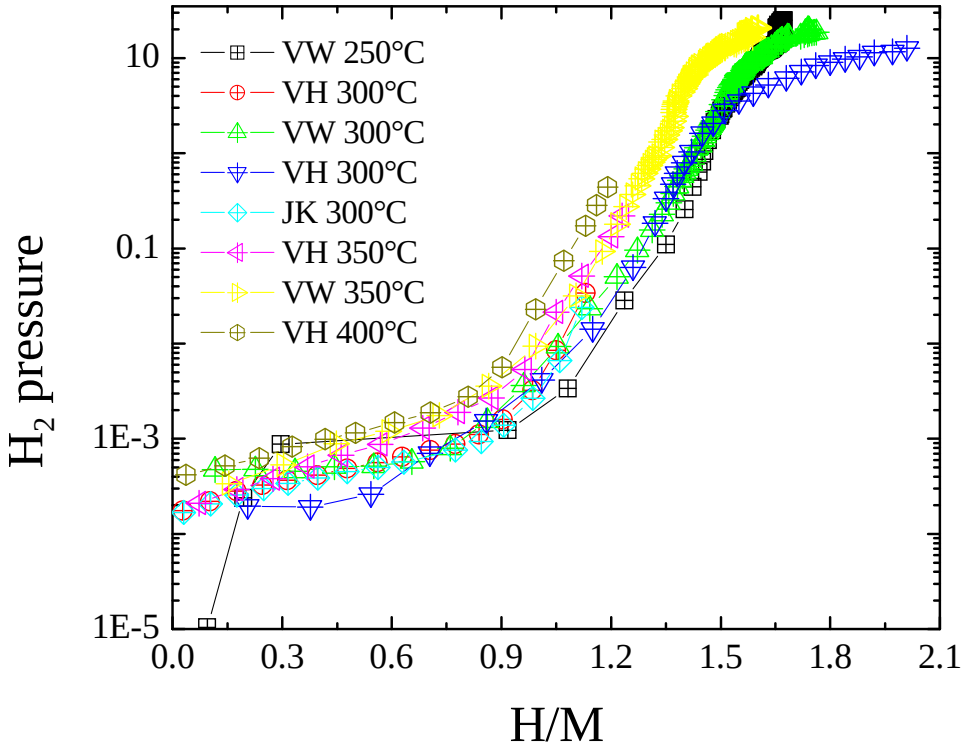

Figure 6.12 – A comparison of PCT results for $Ti_{45}Zr_{38}Ni_{17}$ from this work (*VW*, data without background subtraction are shown), reference [13] (*JK*), and reference [15] (*VH*) showing good agreement and expected temperature dependences.

6.3.3. Hydride phase formation in $Ti_{45}Zr_{38}Ni_{17}$

As mentioned here, and discussed in detail elsewhere, the formation of crystalline hydride phases during hydrogenation of i-phase alloys greatly reduces the cycling ability. The extensive work by Viano [4, 5] and Stroud [9], from this laboratory, using XRD and TEM, revealed that hydride formation can be avoided during hydrogen loading and unloading up to moderate pressures (5 atm) if the formation of surface oxides was minimized, and that complete unloading (desorption) was possible for temperatures 350°C and above. They also characterized the hydride phase as FCC (Ti-Zr)-H_2 from TEM, and found that it could be removed, and the i-phase recovered, by annealing at high temperatures (661°C). Viano found a linear dependence of the quasilattice expansion with increased hydrogen concentration, giving the expression

$$a_i^h = a_i^0 + .019742\left(\frac{H}{M}\right) \quad (6.3.3.1),$$

where a^h is the quasilattice parameter after hydrogen loading and a^0 is the quasilattice parameter before loading.

In this work, oxide formation was minimized by the Pd-coating technique and atmospheric oxygen was eliminated by evacuating the chamber, using techniques already discussed. The quasilattice constant was measured from XRD and eqn. 6.3.3.1 was verified. From the XRD results, the formation, or lack thereof, of the FCC (Ti-Zr)-H_2 phase (Figure 6.13) was determined and a phase formation diagram created (Figure 6.14). From Figure 6.14, the hydride phase appears to form at temperatures above 250°C even at moderate pressures (1atm), and only at higher pressures (> 20atm) for loading at 250°C.

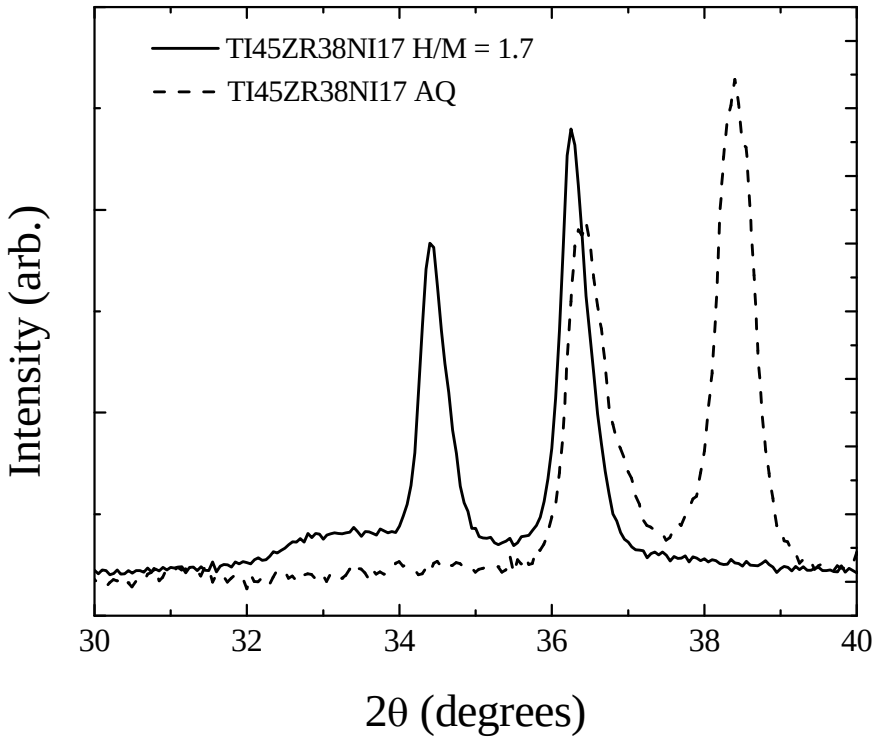

Figure 6.13 – The measured intensity from XRD for i-phase $Ti_{45}Zr_{38}Ni_{17}$ samples as-quenched (AQ, dashed line) and hydrogen-loaded to 35atm at 250°C (solid line); formation of a (Ti-Zr)-H_2 crystalline hydride can be seen from the shoulder on the first peak at low angles.

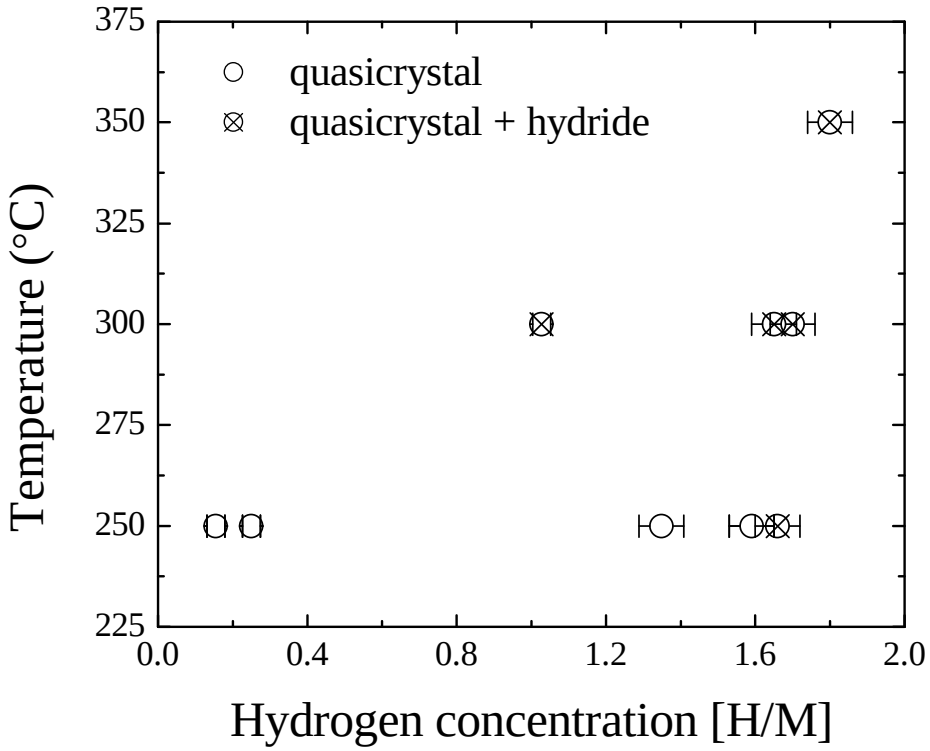

Figure 6.14 – A phase formation diagram from XRD for hydrogenated for $Ti_{45}Zr_{38}Ni_{17}$ samples, showing the range of temperatures and pressures for loading of the i-phase with or without hydride formation.

6.4. Summary

This chapter presented results and analysis of hydrogen cycling measurements for rapidly-quenched, Pd-coated, i-phase $Ti_{45}Zr_{38}Ni_{17}$. Those measurements, made using an improved Sievert-type apparatus with more accurate data reduction and analysis methods than those used in previous studies, showed no second plateau in the PCT curve up to equilibrium hydrogen pressures greater than 30atm. The maximum value of [*H/M*] attained was between 1.6-1.8, consistent with previous results. This result negates previous, preliminary results of high pressure hydrogen loading in i-phase $Ti_{45}Zr_{38}Ni_{17}$. The experimental and analysis methods were supported by measurements of the hydrogen cycling of Pd metal, not possible using the apparatus and method of the previous work, which showed good agreement with published results to within a temperature correction. The current work also agrees well with earlier studies of $Ti_{45}Zr_{38}Ni_{17}$ at lower equilibrium hydrogen pressures.

A background correction to the measured absorption data was also discussed. This type of effect was likely exaggerated in the analysis method employed by Huett and Hartzell, leading to the accumulated error and erroneous second plateau. Reduction of this background was shown to completely remove the apparent second plateau, although it was greatly reduced even without such a correction. In future work the background subtraction should be used carefully, as it may also remove subtle effects of high pressure absorption without an associated phase change, or change in site-filling in the quasilattice. Directly from the absorption data, such as in Figure 6.10, the distinction between the two

processes was measured, with a sharp peak corresponding to the plateau in the PCT curve at low pressures, and the absence of a second peak at higher pressures.

Diffraction measurements from XRD and were made to study the changes in the quasilattice and the phases formed with increasing hydrogen concentration. The previous results of Stroud and Viano were confirmed using the new technique, and a phase formation diagram was determined into the high-pressure regime. These studies showed that the FCC (Ti-Zr)-H_2 hydride phase forms readily for loading at temperatures of at least 300°C, and also for lower temperatures (250°C) at high pressures (20-30atm).

In conclusion, from these results it is evident that i-phase $Ti_{45}Zr_{38}Ni_{17}$ is not an exceptional hydrogen storage material, and the previous results showing additional hydrogen uptake at high equilibrium pressures, beyond that previously measured, were in error. This negative result is unfortunate, but many improvements to the apparatus and analysis method were made. The technique is very versatile, and could now be further refined and applied with greater confidence for hydrogenation studies for a wide variety of materials at high pressures and temperatures.

References

1. Energy Information Administration. 2009 [cited 2009 July 13]; Available from: http://www.eia.doe.gov/cneaf/electricity/epm/epm_sum.html.
2. US Department of Energy. 2003 [cited 2009 July 13]; Available from: http://www1.eere.energy.gov/hydrogenandfuelcells/2003_storage_solicitation.html.
3. K. Yvon and P. Fischer, in *Hydrogen in Intermetallic Compounds I*, L. Schlapbach, Editor. 1988, Springer-Verlag: New York.
4. A. M. Viano, R. M. Stroud, P. C. Gibbons, A. F. McDowell, M. S. Conradi, and K. F. Kelton, PHYSICAL REVIEW B, 1995. **51**(17): p. 12026.
5. A. M. Viano, E. H. Majzoub, R. M. Stroud, M. J. Kramer, S. T. Misture, P. C. Gibbons, and K. F. Kelton, Philosophical Magazine A, 1998. **78**(1): p. 131-142.
6. J. Y. Kim, P. C. Gibbons, and K. F. Kelton, Journal of Alloys and Compounds, 1998. **266**(1-2): p. 311-317.
7. H. Huang, P. Dong, C. Yin, P. Zhang, B. Bai, and C. Dong, International Journal of Hydrogen Energy, 2008. **33**(2): p. 722-727.
8. H. Wen, W. Jianli, W. Lidong, W. Yaoming, and W. Limin, Electrochemica Acta, 2009. **54**: p. 2770-2773.
9. R. M. Stroud, A. M. Viano, P. C. Gibbons, K. F. Kelton, and S. T. Misture, Applied Physics Letters, 1996. **69**(20): p. 2998-3000.
10. J. H. Harris, W. A. Curtin, and M. A. Tenhover, PHYSICAL REVIEW B, 1987. **36**(11): p. 5784.
11. W. M. Mueller, J. P. Blackledge, and G. G. Libowitz, *Metal Hydrides*. 1968, New York: Academic.
12. E. H. Majzoub, J. Y. Kim, R. G. Hennig, K. F. Kelton, P. C. Gibbons, and W. B. Yelon, Materials Science and Engineering A, 2000. **294-296**: p. 108-111.
13. J. Y. Kim, *Effects of Oxygen and Germanium on Quasicrystal Formation in Ti-Based Alloys and the Use of Hydrogen As a Structural Probe*. 1999, Washington University: St. Louis, Missouri.
14. R. Checchetto, G. Trettel, and A. Miotello, Measurement Science and Technology, 2004. **15**(1): p. 127-130.
15. V. T. Huett, *The Formation, Structure, and Hydrogen Storage Properties of Ti/Zr/Hf Based Quasicrystals and Related Phases*. 2004, Washington University: St. Louis, Missouri.
16. A. Züttel, Materials Today, 2003. **6**: p. 24-33.
17. H. Frieske and E. Wicke, Berichte der Bunsengesellschaft für Physikalische Chemie, 1973. **77**(48).
18. S. Horinouchi, Y. Yamanoi, T. Yonezawa, T. Mouri, and H. Nishihara, Langmuir, 2006. **22**(4): p. 1880-1884.
19. K. F. Kelton, J. J. Hartzell, R. G. Hennig, V. T. Huett, and A. Takasaki, Philosophical Magazine, 2006. **86**(6): p. 957-964.

Chapter 7

Summary and Conclusions

In this dissertation, the results of research in four topics were presented, all of which dealt with the phase formation and physical properties of non-crystalline alloys. The main effort was to characterize the supercooled alloy liquids and the resulting products of their solidification, using the BESL technique, for two systems of interest, presented in Chapters 3 and 4. The experimental BESL studies were complimented by computer simulation and analysis techniques, and some theoretical modeling studies were also made. In addition, properties of a lightweight, air-cast, Mg-based bulk metallic glass (BMG) were presented in Chapter 5, and an analysis of the hydrogen storage ability and phase formation in a T-based quasicrystal was presented in Chapter 6.

In Chapter 3, changes in the supercooled liquid structure of $Cu_{(100-x)}Zr_x$ were investigated as a function of composition and temperature. Binary BMGs are of great interest, both for their potential as engineering materials and because their simple compositions makes them suitable for theoretical and modeling studies, which could lead to a better understanding of metallic glass formation. Here, a transition to a chemically and structurally inhomogeneous supercooled liquid was found at x = 54 with an onset at 845 ± 5°C. It was observed from analysis of multiple experimental and simulation measures, including the pair distribution function (PDF), the bulk density, and Reverse Monte Carlo (RMC) simulation. The amount of icosahedral order and the reduced supercooling were observed to be maximal near the composition x = 54, which could explain the improved glass-forming ability of this composition at an off-metastable

eutectic composition. These results also may represent the first experimental confirmation of cluster development predicted for these liquids by molecular dynamics simulations.

In Chapter 4 research on changes in the structures and physical properties of supercooled liquid $Ti_{45}Zr_{(38-x)}Hf_xNi_{17}$ alloys, and their solidification structures, with changing Hf concentration, was presented. Previous work from this group identified a sharp phase formation boundary between the C14 Laves and cF96 structures near x = 18-21. The phase formation boundary was confirmed, and further examined, using BESL and related analysis. Scanning electron microscopy (SEM) studies revealed changes in the segregation of different atom species between the two crystal structures in the phase mixture in the samples solidified using BESL, with changing Hf concentration. The Hf was found to be homogeneously distributed, and the Zr to become more homogeneous with the addition of Hf. These changes, along with increasing icosahedral order in liquids that form the C14 structure, lead to the observed phase formation boundary. Changes in the physical properties of the supercooled liquid and the high temperature solid solution were also observed, which may help explain the segregation in the solidification structures.

In Chapter 5, a detailed examination of changes in microstructure of $Mg_{65}Cu_{(25-x)}Ag_xGd_{10}$ BMGs with changing Ag content was presented. In collaboration with E. S. Park of Harvard University it was shown that, although samples for all values of *x* appear amorphous from basic characterization with low energy x-ray diffraction (XRD) and differential scanning calorimetry (DSC) the samples with x = 5 and 10 are not truly amorphous, but rather nanocrystal-amorphous composite structures. This structure can

be maintained in the large diameter, air-cast samples due to very slow growth rates, possibly due to inhibited diffusion with added Ag, as suggested by results of SEM. Changes in the thermal properties were also observed with the addition of Ag, and the different devitrification mechanisms were explored, with a two-step crystallization signature from isothermal DSC characterized by high energy XRD.

Quasicrystals have shown promise as materials for solid storage of hydrogen for renewable energy applications. Previous research in this laboratory detailed the hydrogen absorption and cycling behavior in i-phase $Ti_{45}Zr_{38}Ni_{17}$ at modest pressures. Preliminary results from high pressure studies showed exceptional absorption. Here, in Chapter 6, those results were shown to be an artifact. As detailed there, improvements were made to the apparatus, which then allowed development of an improved analysis method, leading to the corrected results. Results of the phase formation sequence with the addition of hydrogen were also presented.

Future work using BESL on the Cu-Zr liquids to determine what, if any, is the compositional dependence of the transition observed at x = 54, and its relationship to BMG formation relative to a metastable eutectic point, would be beneficial. Neutron diffraction studies could determine the partial pair correlation functions, and the results of those experiments could provide further evidence for the cluster predictions from molecular dynamics simulations. The structures of other binary BMG-forming liquids should be examined, using similar methods, to determine if glass formation in binaries is always preceded by such cluster formation.

A study of the ternary Cu-Zr-Al system to confirm the theoretical predictions for that system would also be interesting. These results could motivate future alloy

development. Since Hf was shown in Chapter 3 to affect the chemical segregation as the liquid cools, a study of Hf substitution for Zr in Cu-Zr-Al BMGs would also provide interesting results on the interaction of these two phenomena, which could also be useful for BMG development.

Additional study of the Mg-Cu-Ag-Gd alloys, using atom probe and EFTEM could determine if there is phase separation that influences the observed changes in devitrification behavior. Further HRTEM studies could better map the crystallization sequences, and perhaps provide an improved understanding of the nature of transitions observed in isothermal DSC, to build upon the existing work of Chen and Spaepen.

Appendix 1

Scripts Used in Processing BESL Data

A1.1 Batch processing

The initial steps in the reduction of the BESL data were batch-processing and background subtraction. This was accomplished using the batch processing script *Generic_batch_kks.bat*, the text and usage of which are given below. Integration of the radial intensity was performed in the program Fit2D as already described. To streamline the process, macros were used in Fit2D. For free cooling experiments, data were analyzed frame-by-frame using the macro *Aug_8_2007-2byteInteger.mac*. For these macros, the beam center and sample-detector distance were determined from the scattering data from a Si-standard. The above topics will be presented here.

All scripts below contain a header boxed with asterisks (*) with some information about the file and its execution. This header is not necessarily a proper comment line for the language of the script, and if one wishes to recreate the program, these headers should be removed. Occasionally line breaks will appear due to long character strings. If the reader is duplicating the script from a paper copy, she may need to adjust the use of spaces/carriage returns for the script to execute properly. If working from an electronic copy, files should be able to be copied/pasted as-is. The entire contents of the folder C:\BESL, which is referenced in these scripts, is included on a compact disc included with a print copy of this dissertation.

```
**************************************************************************
FILENAME: Generic_batch_kks.bat
AUTHOR: Kisor Kumar Sahu
EXECUTION: Edit source and destination file paths as needed, on Windows PC, double click to execute
NOTES: First line points to batch processing script; second line is path for source data; third line is path to write output data (if specified folder does not exist, it will be created, if files of same name already exist, they will be overwritten without prompting); fourth line is source filename of data file; fifth line is source filename of background file, number of frames in data file, number of frames in background file
**************************************************************************

CALL C:\BESL\GE_macros\2ndset\convert2_kks_3.bat
E:\BESL07_from_on081107_21.50\STL906_Ni\Step4_Hold
E:\Vic_BESL_backup_082807\BESL_processed_VW\Ni\Step_cooling\1200C Hold_1200C_15f_1Hz_081307_17.58
empty_chamber_afterprocess_15f_1Hz_081307_18.08 15 15
```

```
**************************************************************************
FILENAME: convert2_kks_3.bat
AUTHOR: Kisor Kumar Sahu
EXECUTION: Called by Generic_batch_kks.bat on Windows PC
NOTES: Unless modifying the procedure, do not edit this file
**************************************************************************


mkdir %2
cd %2
C:\BESL\Adept\Tools\Argonne\correctPDFseq_bin_high_kks.js %1\%3 %1\%4 %5 %6
move %1\%3*.cor
move %1\%3*.avg
move %1\%3*.sum
del %1\%3_
```

```
*****************************************************************************
FILENAME: correctPDFseq_bin_high_kks.js
AUTHOR: Kisor Kumar Sahu
EXECUTION: Called as part of Generic_batch_kks.bat on Windows PC
NOTES: Unless modifying the procedure, do not edit this file
*****************************************************************************

/*****************************************************************************
*****************************
correct.js
*****************************************************************************
*****************************

MODULE DESCRIPTION:
-------------------


PROCEDURES:
-----------

          Name                        Description
------------------------------  ------------------------------------------------------------

REVISION HISTORY:
-----------------

 Rev    Date          By           SPR #           Comments
-----  ---------  ----------------  ----------  ------------------------------


/*****************************************************************************
*****************************
                        Include Files
*****************************************************************************
*****************************/

/*****************************************************************************
*****************************
                        Local Literals
*****************************************************************************
*****************************/

/*****************************************************************************
*****************************
                        Local Constants
```

```
**************************************************************************
**************************/

/**************************************************************************
**************************
                        Local Variables
**************************************************************************
**************************/

var WshShell = WScript.CreateObject("WScript.Shell");
var fso = new ActiveXObject("Scripting.FileSystemObject");
var BMFilename
="C:\\BESL\\DetectorData\\1339.6\\BIN\\1339.6N_BadPixel_d.txt.img";
var gainMapFilename =
"C:\\BESL\\DetectorData\\1339.6\\BIN\\1339.6N_GainCal_Record_High_GainMap_d_1
19_1.img";
var correctFilename = "C:\\BESL\\ADEPT\\Tools\\Argonne\\correctflwithdarkfile";
var averageFilename = "C:\\BESL\\ADEPT\\Tools\\Argonne\\avgfl";
var rows = 1024;
var BMHeader = 8192;
var objArgs = WScript.Arguments;

if(objArgs.length < 3)
{
  WScript.Echo("Please enter parameters: 1st param = x-ray filename, 2nd param = dark
filename, 3rd param = # of during images, 4th param = # before images (defaul = 5)\n");
}
else
{
  var xrayfilename = objArgs(0);
  var darkfilename = objArgs(1);
  var outputFilename1 = xrayfilename + "_";
  var outputFilename2 = xrayfilename + ".avg";
  var outputFilename3 = xrayfilename + ".sum";
  var duringFrames = objArgs(2);
  var beforeFrames;
  var totalFrames;
  var command;

  if(objArgs.length > 3)
  {
    beforeFrames = objArgs(3);
  }
  else
  {
    beforeFrames = 5;
```

```
  }
  totalFrames = parseInt(duringFrames);
  command = correctFilename + " -d 0 -e " + (beforeFrames-1) +" -x 0 ";
  command += " -z " + (totalFrames-1) + " -r " + rows + " -i " + xrayfilename;
  command += " -o " + outputFilename1 + " -b " + BMFilename +  " -h 8192 -j " +
BMHeader;
  command += " -p " + darkfilename;
  command += " -a 1";
  command += " -g " + gainMapFilename;
//  WScript.Echo(command);


  oExec = WshShell.Run(command,1,true);

//  oExec = WshShell.Exec(command);

//  while (oExec.Status == 0)
//  {
//    WScript.Sleep(100);
//  }

//  WScript.Echo("\n");
  command = averageFilename + " -i " + outputFilename1 + " -x 0 -z " + duringFrames +
" -s " + outputFilename3 + " -a " + outputFilename2 + " -r " + rows + " -h 0";
//  WScript.Echo(command);
  oExec = WshShell.Run(command,1,true);

//  oExec = WshShell.Exec(command);

//  while (oExec.Status == 0)
//  {
//    WScript.Sleep(100);
//  }
//  WScript.Echo("\n");

}
```

A2.1 Fit2D Macros

The following scripts are macros for the program Fit2D, which was used to generate average intensity from the raw detector files or from pre-processed (batch processed) files, where applicable. When studying these scripts, it is important to note what it means to be a *macro;* this file is simply automating the keystrokes which would otherwise be done by hand in the program. The numbers entered are unique to a particular experiment and some were determined from specific Si calibration measurements, as will be discussed below. If modifying these macros for a new experiment, one should take care to modify the particular values accordingly.

A2.1.1. Procedure for locating beam center and sample-detector distance

Before running a Fit2D macro, it may be necessary to check the sample-detector distance and beam center. This is accomplished by using data from a Si calibrant. Data from Si calibrants were collected at various times throughout both stationary and BESL scattering experiments, and it is important to use the calibration information which was collected as close in time to the data being analyzed, and in the same configuration of the detector and any other associated hardware, such as beam-stops or the evacuated flight path used in the stationary experiments.

This procedure assumes the user is running Fit2D in a graphics-based mode on a Windows PC. In the Fit2D graphics window

- Go to Powder Diffraction ➔ Input

- Load the desired Si-standard data; for BESL experiments this will likely be the batch-processed .sum file
- Choose file format binary
- Specify the dimensions of the image (1024 for August 2007 BESL data), the data type (Real, 4-byte IEEE for .sum file), NO to signed or unsigned, NO to swap bytes on input, 1 for byte number for start of binary data; use all defaults for the second page of inputs
- The files should be loaded and an image of Si diffraction rings appeared, choose calibrant ➔ Silicon
- Choose a reasonable sample-detector distance, specify the correct wavelength and the correct size of horizontal and vertical pixels (400 for August 2007 BESL); otherwise use defaults and confirm NO for refinement of x-ray wavelength
- Press OK, choose two-click in the lower right (the tab will display the text 'one-click' when two-click mode has been chosen), click once in the large window and again in the detail window to choose a point on the first diffraction ring and repeat for a few points around the ring. Choosing points on the center or edge of the ring is down to user preference, but all points should be either center or edge, not mixed

Press the center button to finish, results will be displayed in the command line window opened alongside the Fit2D graphics window. This information should then be checked against that contained in the macro, and if desired, a new macro created containing the appropriate calibration information.

A2.1.2. Macros for stationary diffraction studies using a MAR3450 image plate detector

Processing data from the MAR3450 detector used in stationary diffraction studies was streamlined using a Fit2D macro. For these data, there was no batch processing and no automated background subtraction was used. A representative Fit2D macro is reproduced below.

```
**************************************************************************
FILENAME: Aug08_noGEOcorr_080508_1031.mac
AUTHOR: Vic Wessels
EXECUTION: In Fit2D, choose MACROS/LOG FILE tab then RUN SEQUENCE tab
NOTES: Unless modifying the procedure, do not edit this file
**************************************************************************

%!*\ BEGINNING OF GUI MACRO FILE
%!*\
%!*\ This is a comment line
%!*\
EXIT
IMAGE PROCESSING (GENERAL)
INPUT
#IN
BINARY
X-PIXELS
3450
Y-PIXELS
3450
DATA TYPE
REAL (4-BYTE IEEE)
SIGNED
NO
BYTE SWAP
NO
STARTING BYTE
1
O.K.
EXIT
POWDER DIFFRACTION (2-D)
INTEGRATE
X-PIXEL SIZE
100
Y-PIXEL SIZE
100
DISTANCE
437.997
WAVELENGTH
0.12448
X-BEAM CENTRE
1729.742
Y-BEAM CENTRE
1722.967
TILT ROTATION
-37.034
```

ANGLE OF TILT
0.052
O.K.
%!*\START AZIMUTH
%!*\-120
%!*\END AZIMUTH
%!*\120
%!*\INNER RADIUS
%!*\0
%!*\OUTER RADIUS
%!*\480
SCAN TYPE
Q-SPACE
%!*\1 DEGREE AZ
%!*\NO
%!*\AZIMUTH BINS
%!*\1
%!*\RADIAL BINS
%!*\1000
CONSERVE INT.
NO
POLARISATION
YES
FACTOR
0.990000
GEOMETRY COR.
NO
MAX. ANGLE
45.18585
SCAN BINS
1958
MAX. D-SPACING
16.0000
O.K.
%!*\EXIT
OUTPUT
CHI
FILE NAME
#OUT
O.K.
EXIT
MACROS / LOG FILE
%!*\ END OF IO MACRO FILE

A2.1.3. Macros for BESL using GE Revolution 41-RT detector

The following two macros were used in processing the BESL data. A distinction was made between 2-byte integer and 4-byte real data sets. The 2-byte integer processing was applied to .cor files, while the 4-byte real processing was applied to .sum or .avg files. From the batch processing used for BESL data, a .cor file was produced for each frame of the scattering experiment, and a .sum and .avg file was produced as a sum and average of all frames, respectively. In typical data reduction, .cor files were analyzed for free cooling experiments, while .sum files were analyzed for step-cooling experiments.

```
**************************************************************************
FILENAME: Aug_8_2007-4byteReal.mac
AUTHOR: Matthew J Kramer
EXECUTION: In Fit2D, choose MACROS/LOG FILE tab then RUN SEQUENCE tab
NOTES: Unless modifying the procedure, do not edit this file
**************************************************************************

%!*\ BEGINNING OF GUI MACRO FILE
%!*\
%!*\ This is a comment line
%!*\
EXIT
IMAGE PROCESSING (GENERAL)
INPUT
#IN
BINARY
X-PIXELS
1024
Y-PIXELS
1024
DATA TYPE
REAL (4-BYTE IEEE)
SIGNED
NO
BYTE SWAP
NO
STARTING BYTE
1
O.K.
EXIT
POWDER DIFFRACTION (2-D)
CAKE
KEYBOARD
496.707
528.823
        1
 4.9530975E+02
 1.0751101E+01
        1
 4.9530975E+02
 1.0232599E+03
        0
        1
 1.0108168E+03
 5.3947632E+02
INTEGRATE
```

X-PIXEL SIZE
400
Y-PIXEL SIZE
400
DISTANCE
794.832
WAVELENGTH
0.09577
X-BEAM CENTRE
496.707
Y-BEAM CENTRE
528.823
TILT ROTATION
-70.012
ANGLE OF TILT
.127
O.K.
START AZIMUTH
-120
END AZIMUTH
120
INNER RADIUS
0
OUTER RADIUS
480
SCAN TYPE
Q-SPACE
1 DEGREE AZ
NO
AZIMUTH BINS
1
RADIAL BINS
1000
CONSERVE INT.
NO
POLARISATION
YES
FACTOR
0.990000
MAX. D-SPACING
16
GEOMETRY COR.
YES
O.K.
EXIT
OUTPUT

```
CHI
FILE NAME
#OUT
O.K.
EXIT
MACROS / LOG FILE
%!*\ END OF IO MACRO FILE
```

```
**************************************************************************
FILENAME: Aug_8_2007-2byteInteger.mac
AUTHOR: Matthew J Kramer
EXECUTION: In Fit2D, choose MACROS/LOG FILE tab then RUN SEQUENCE tab
NOTES: Unless modifying the procedure, do not edit this file
**************************************************************************

%!*\ BEGINNING OF GUI MACRO FILE
%!*\
%!*\ This is a comment line
%!*\
EXIT
IMAGE PROCESSING (GENERAL)
INPUT
#IN
BINARY
X-PIXELS
1024
Y-PIXELS
1024
DATA TYPE
INTEGER (2-BYTE)
UNSIGNED
NO
BYTE SWAP
NO
STARTING BYTE
1
O.K.
EXIT
POWDER DIFFRACTION (2-D)
CAKE
KEYBOARD
496.707
528.823
        1
 4.9530975E+02
 1.0751101E+01
        1
 4.9530975E+02
 1.0232599E+03
        0
        1
 1.0108168E+03
 5.3947632E+02
INTEGRATE
```

X-PIXEL SIZE
400
Y-PIXEL SIZE
400
DISTANCE
794.832
WAVELENGTH
0.09577
X-BEAM CENTRE
496.707
Y-BEAM CENTRE
528.823
TILT ROTATION
-70.012
ANGLE OF TILT
.127
O.K.
START AZIMUTH
-120
END AZIMUTH
120
INNER RADIUS
0
OUTER RADIUS
480
SCAN TYPE
Q-SPACE
1 DEGREE AZ
NO
AZIMUTH BINS
1
RADIAL BINS
1000
CONSERVE INT.
NO
POLARISATION
YES
FACTOR
0.990000
MAX. D-SPACING
16
GEOMETRY COR.
YES
O.K.
EXIT
OUTPUT

```
CHI
FILE NAME
#OUT
O.K.
EXIT
MACROS / LOG FILE
%!*\ END OF IO MACRO FILE
```

A3.1 Data processing in PDFgetX2

A3.1.1. Expt. Configuration window

The Expt. Configuration window in PDFgetX2 is shown in Figure A.1, using input values for one of the Ti-Zr-Hf-Ni samples of Chapter 4. In this window the x-ray wavelength was entered and polarization adjusted. If polarization was input in Fit2D, it was not input here to avoid a double correction. The optional information was not adjusted.

A3.1.2. Sample Information window

The Sample Information window in PDFgetX2 is shown in Figure A.2. In this window, the alloy composition was entered (in at. %), the sample geometry selected, and the mass absorption coefficient for the sample, described below, entered. As already mentioned, in BESL the diffraction of a nearly spherical liquid droplet was measured in transmission geometry. Spherical geometry is not a choice in PDFgetX2, so flat plate transmission was selected. This is a reasonable approximation given the size used for the incident beam (0.8 x 0.8 mm), but further work to develop a correction to spherical geometry would be beneficial. The mass absorption coefficient, μ, is defined relative to the loss of intensity of an incident beam of photons on a mass of thickness t, given by

$$I/I_0 = \exp\left(-\left(\mu/\rho\right)*t\right) \quad ,$$

where I_o is the incident intensity, I is the transmitted intensity, and ρ is the mass density. Values of μ/ρ have been tabulated for all elements as a function of incident beam energy, and are available from NIST [1]. The attenuation coefficient $\mu*t$, one of the PDFgetX2

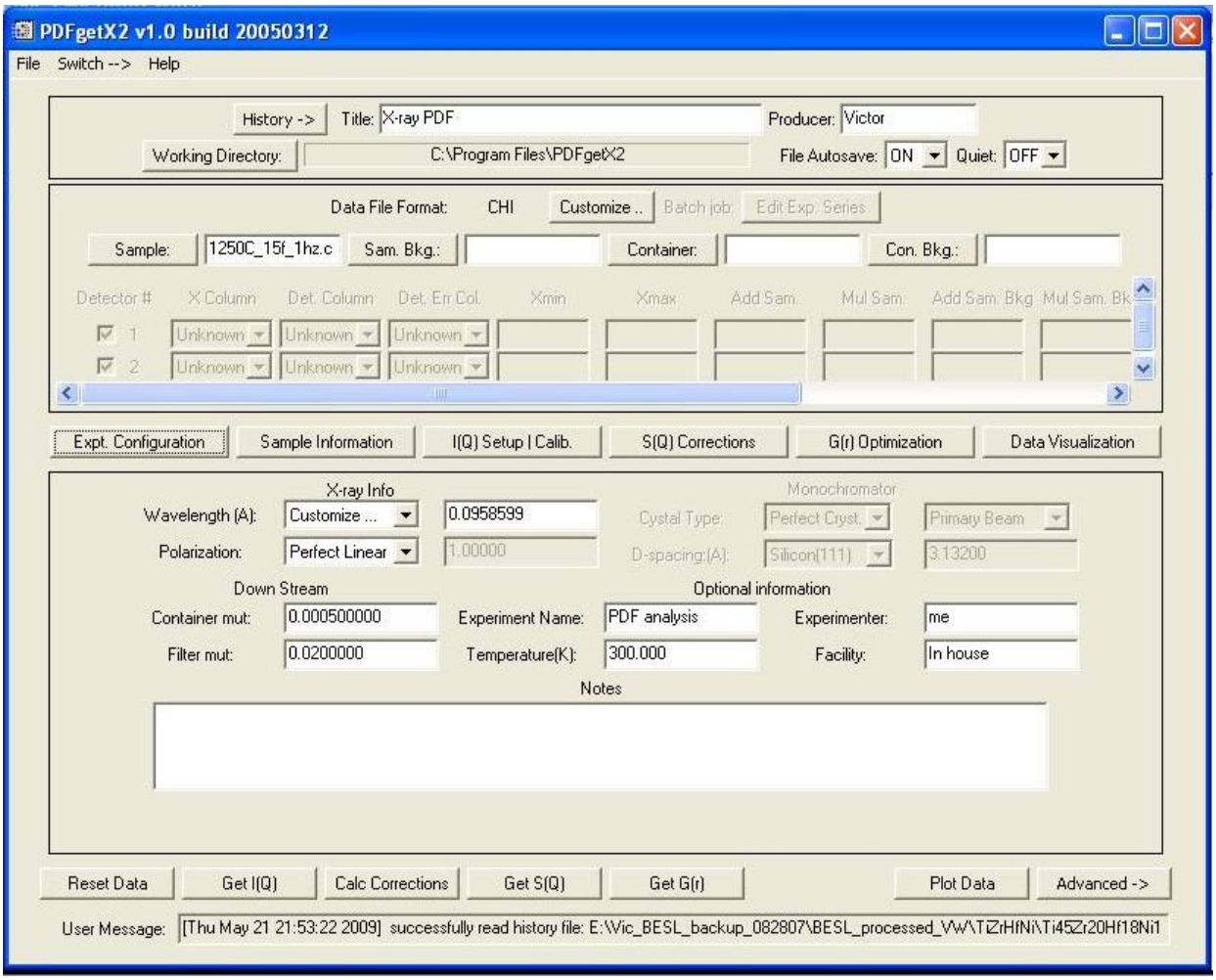

Figure A.1 – The Expt. Configuration window in PDFgetX2.

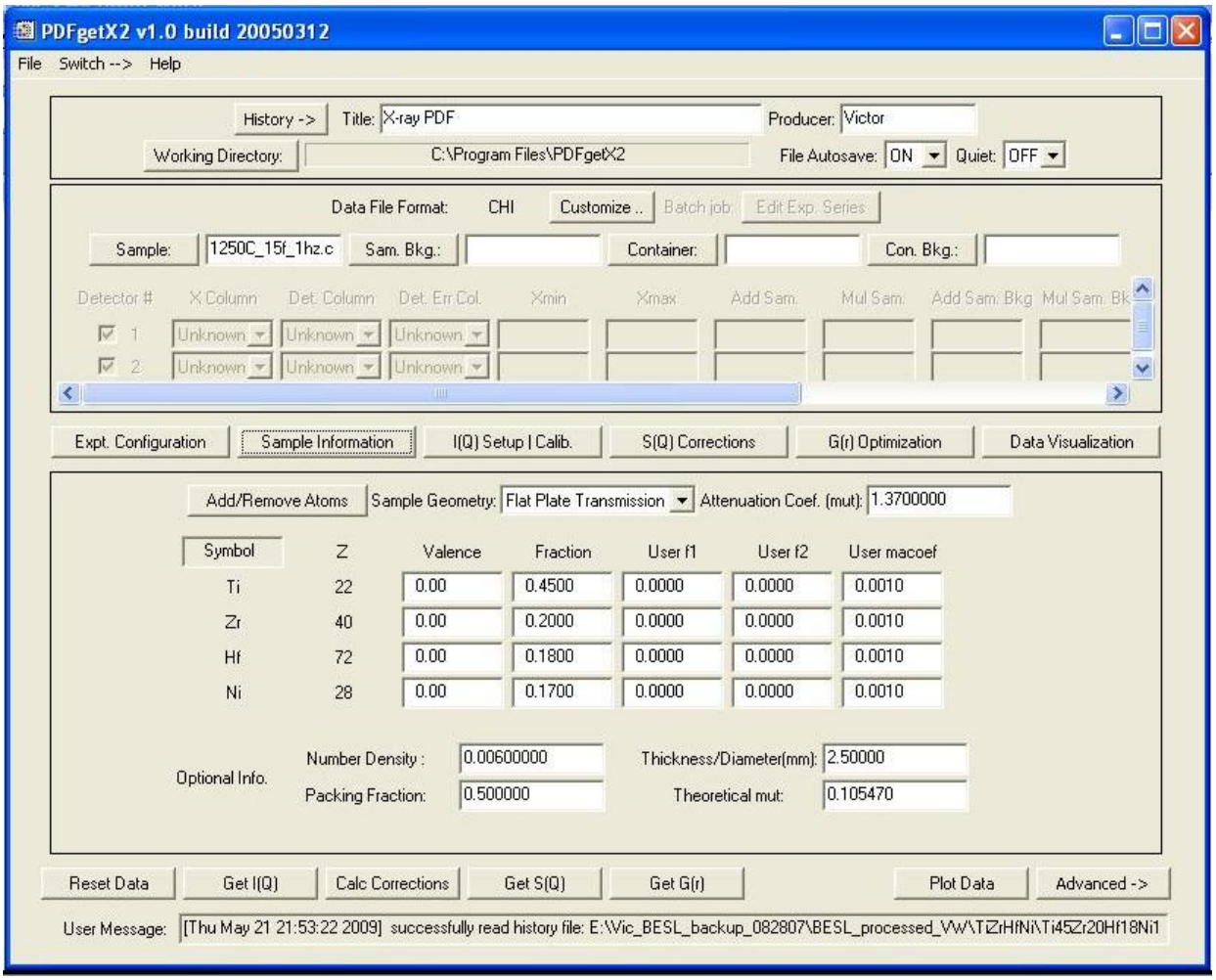

Figure A.2 – The Sample Information window in PDFgetX2.

inputs, was calculated for all samples as a weighted average (by weight percent, not atomic percent) of the values of μ/ρ, which was then multiplied by the density and thickness. The density used was the density at the specified temperature, measured using the technique discussed in Chapter 2. The thickness could be measured or estimated; for these experiments it was estimated as 2.5mm.

A3.1.3. I(Q) Setup/Calib. window

In this window (Figure A.3) the x-column format was selected, and filter and container parameters may be input. For the experiments discussed here, q(nm^{-1}) was the x-column format and the filter and container parameters were not used, since no filter was in place for this work, and container background was removed by a background subtraction, as described in Appendix A.

A3.1.4. S(Q) Corrections window

In this window (Figure A.4) there are many parameters to adjust, which have a major impact on the determination of $S(q)$ from $I(q)$. Sample self-absorption and multiple scattering were used for all samples studied. A fluorescence correction was used for the Ti-Zr-Hf-Ni samples that will be discussed in Chapter 4. It is needed if a constituent of the alloy has an absorption edge near the energy of the incident beam. A more complete description of the fluorescence correction for Ti-Zr-Hf-Ni is given in Chapter 4. The oblique incidence correction was not applied, as this correction is redundant with the geometrical correction in Fit2D, as already described**; it is important to make this correction in only one of these programs, not both.** Similarly to the oblique incidence correction, x-ray polarization is applied only if it was not applied in

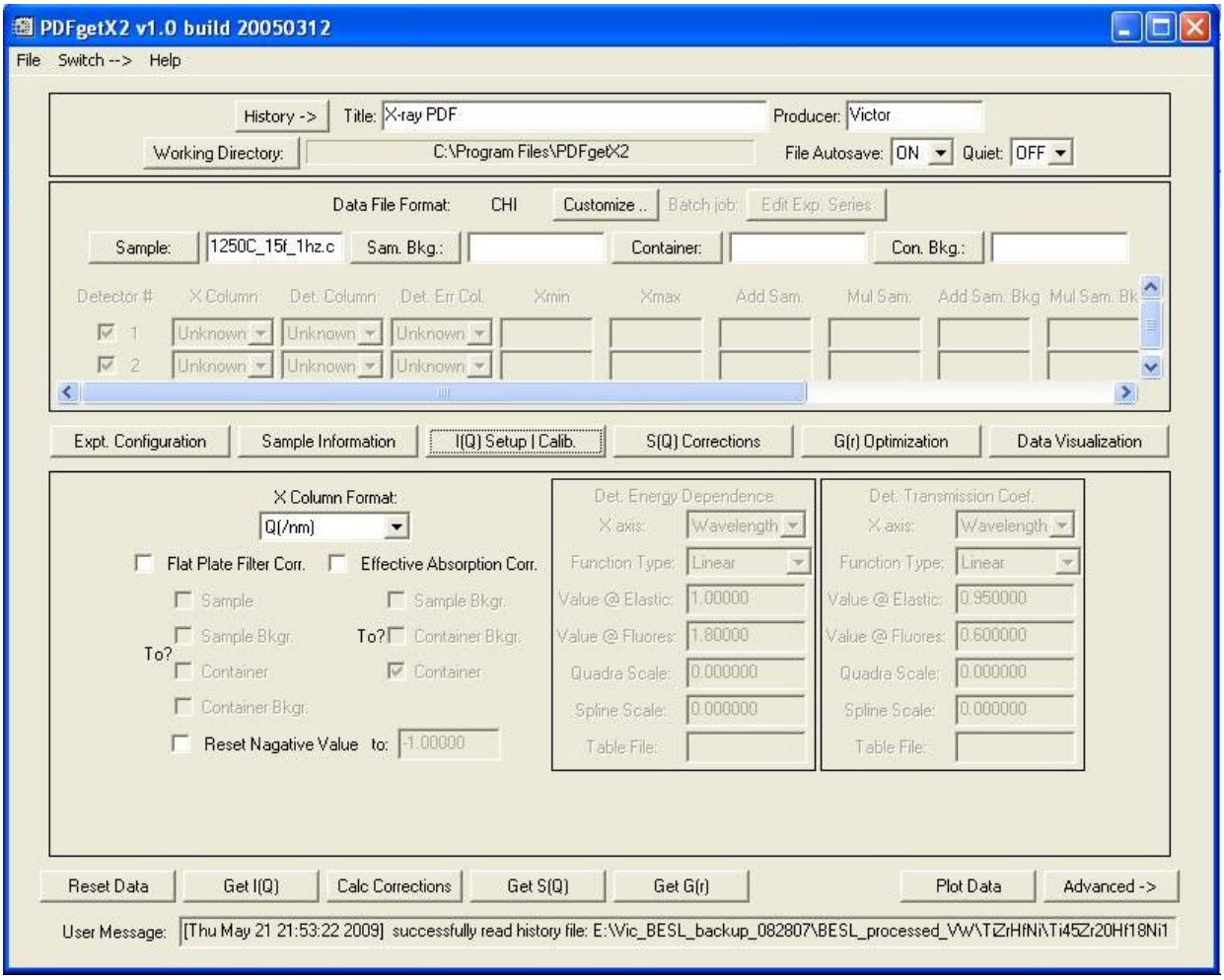

Figure A.3 – The I(Q) Setup/Calib. window in PDFgetX2.

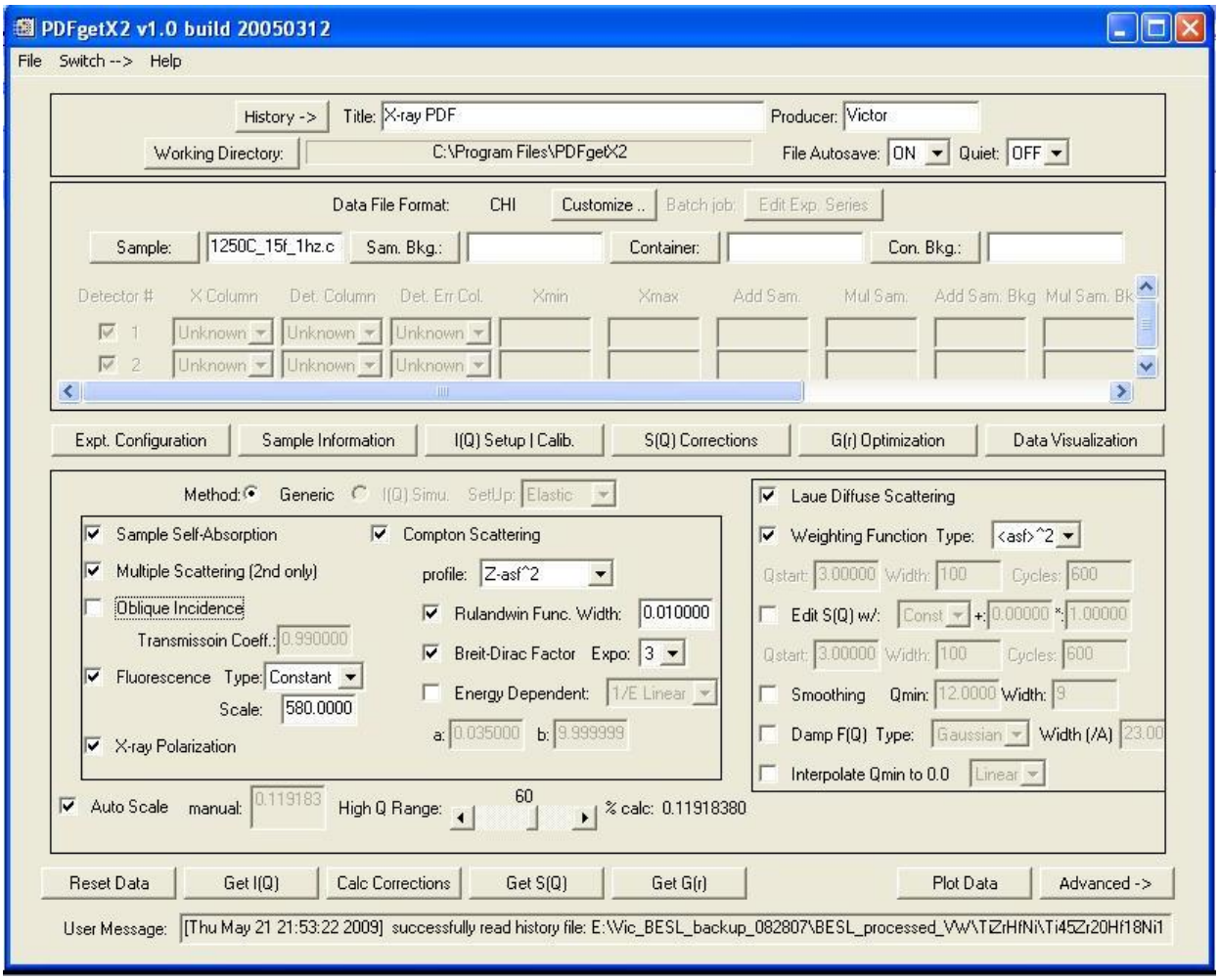

Figure A.4 – The S(Q) Corrections window in PDFgetX2**.**

prior processing with Fit2D. The Compton scattering correction was applied using the profile $Z\text{-}asf^2$, where Z is the atomic number and *asf* is the atomic scattering factor. The value of the Ruland function width used was 0.01 and the Breit-Dirac factor exponent used was 3. The Laue diffuse scattering correction was applied, and the weighting function type used was $\langle asf \rangle^2$. Auto scale was used for all samples. The high-q range adjustment refers to the preference given to high-q values for calculating corrections such as Compton scattering, and can be adjusted empirically to improve the resultant $S(q)$. For most samples a value of 60 (the default value) was used.

A3.1.5. G(r) Optimization window

The parameters adjusted in this window (Figure A.5) do not affect the data correction, but adjust the Fourier transform from $S(q)$ to $G(r)$, and can control ripples in $G(r)$ introduced from a truncation of $S(q)$. The refinement flags may be checked or unchecked to provide the smoothest G(r), as determined by the user. The most important parameter adjusted was *S(q) to use*. It is important to choose a large enough q-value to capture as much structural information as possible, but ripples are introduced into $G(r)$ if the high-q values of $S(q)$ are inaccurate, or if a sharp cutoff is included.

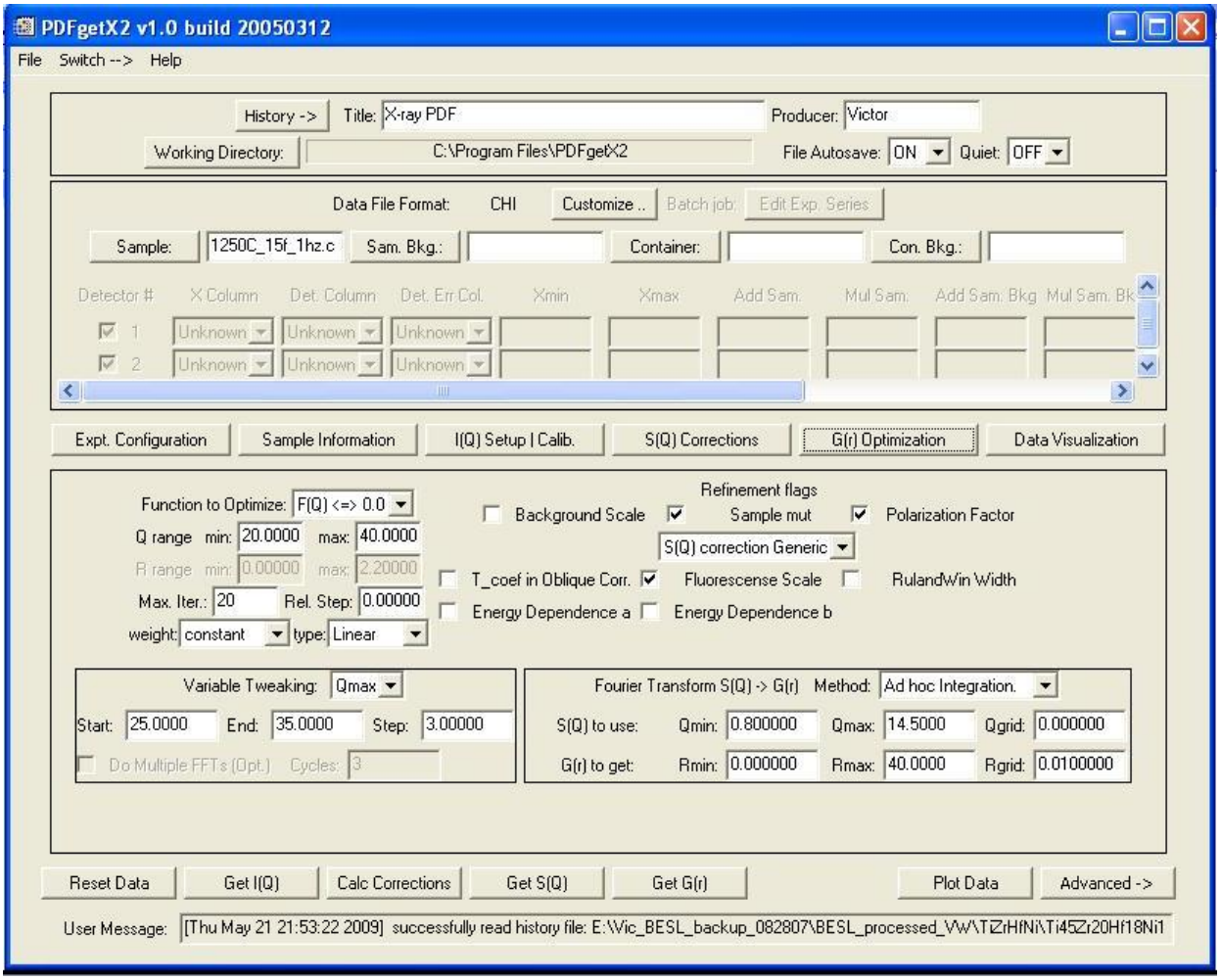

Figure A.5 – The G(r) Optimization window in PDFgetX2.

References

1. http://physics.nist.gov/PhysRefData/XrayMassCoef/cover.html.

Appendix 2

The Effects of Al Fluorescence Filters on Stationary Diffraction Data

Filtering of the scattered x-ray beam with Aluminum shielding was tested to determine its effect on background correction and improved signal to noise ratio. Al has no absorption edge near the energy of x-rays used in this experiment (100keV), so filtering in this manner could absorb low energy radiation from fluorescence while allowing the diffraction cone from the sample to pass through almost unaffected. A sequence of increasingly thick Al sheets was placed between the end of the flight path and the detector. The figure below shows the intensity profile of a quenched Al-Y-Fe metallic glass with increasing thickness of Al filters. It is evident that the Al is reducing the measured intensity and is not introducing coherent scattering.

The effect of shielding on the structure factor, $S(q)$, is more ambiguous. The intensity values shown in Figure B.1 were processed in PDFgetX2 as described in chapter 2, and the resulting values of the structure factor are shown in Figure B.2 through Figure B.5. For all amounts of shielding, there was a drift in the measured signal at high-q. A fluorescence correction was applied in PDFgetX2 which corrects for this, with mixed results for the various intensities. Good oscillation of $S(q)$ about unity out to 18 $Å^{-1}$ was achieved for no shielding and for 1.5mm shielding, for the others a curvature, which could not be corrected, was observed. It is unclear if this is a direct result of the shielding experiment, or if it simply represents variability in the data. Such variability has been

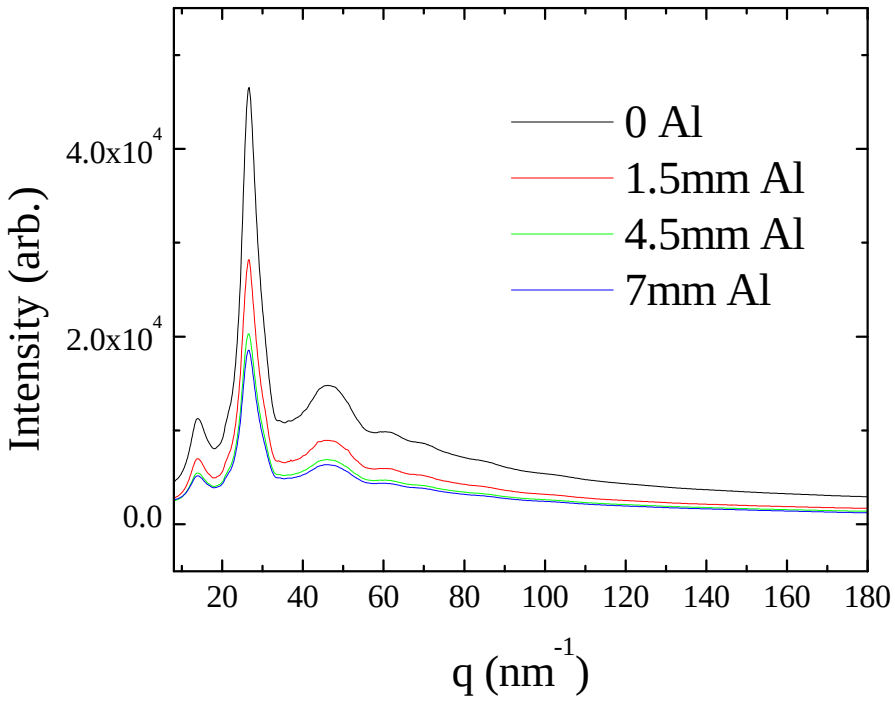

Figure B.1 – The diffracted intensity from an Al-Y-Fe ribbon with various thicknesses of Al sheets for fluorescence filtration.

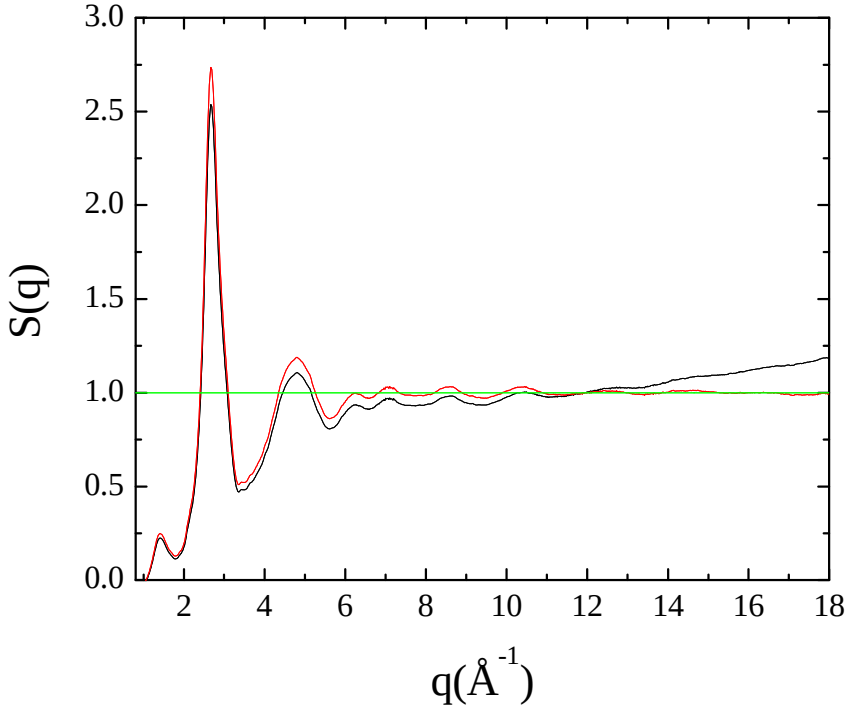

Figure B.2 – The total structure factor S(q) for an Al-Y-Fe glass with no Al shielding, and no applied fluorescence correction (black line), and the same data with a fluorescence correction of 350 applied (red line). Unity is shown in green as a baseline.

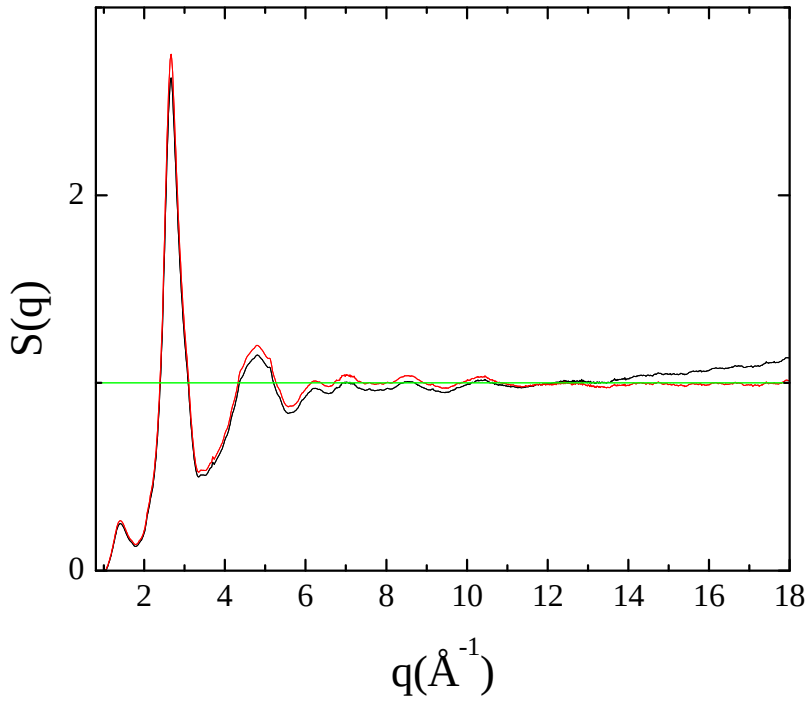

Figure B.3 – The total structure factor S(q) for an Al-Y-Fe glass with 1.5mm Al shielding, and no applied fluorescence correction (black line), and the same data with a fluorescence correction of 130 applied (red line). Unity is shown in green as a baseline.

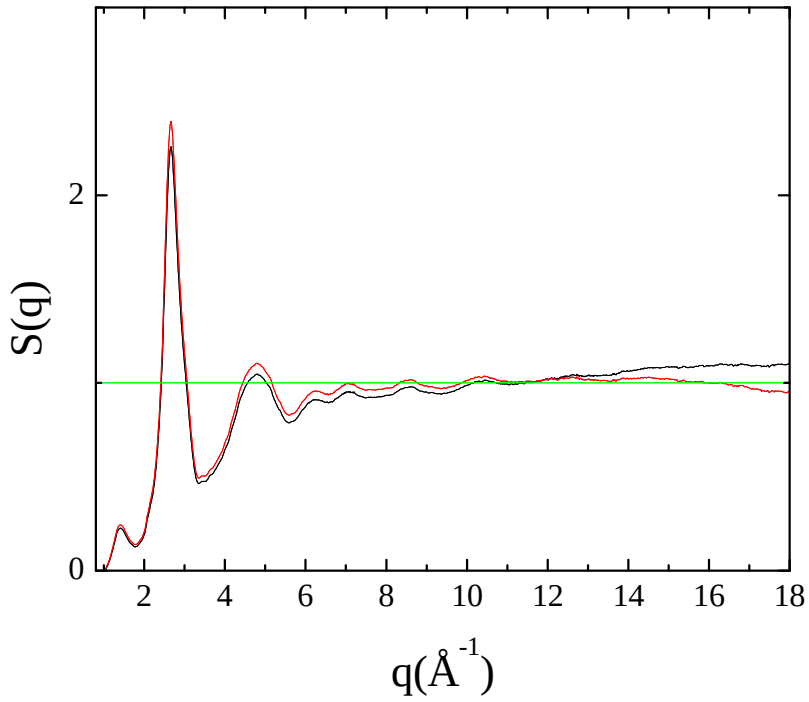

Figure B.4 – The total structure factor S(q) for the Al-Y-Fe glass with 4.5mm Al shielding, and no applied fluorescence correction (black line), and the same data with a fluorescence correction of 130 applied (red line). Unity is shown in green as a baseline.

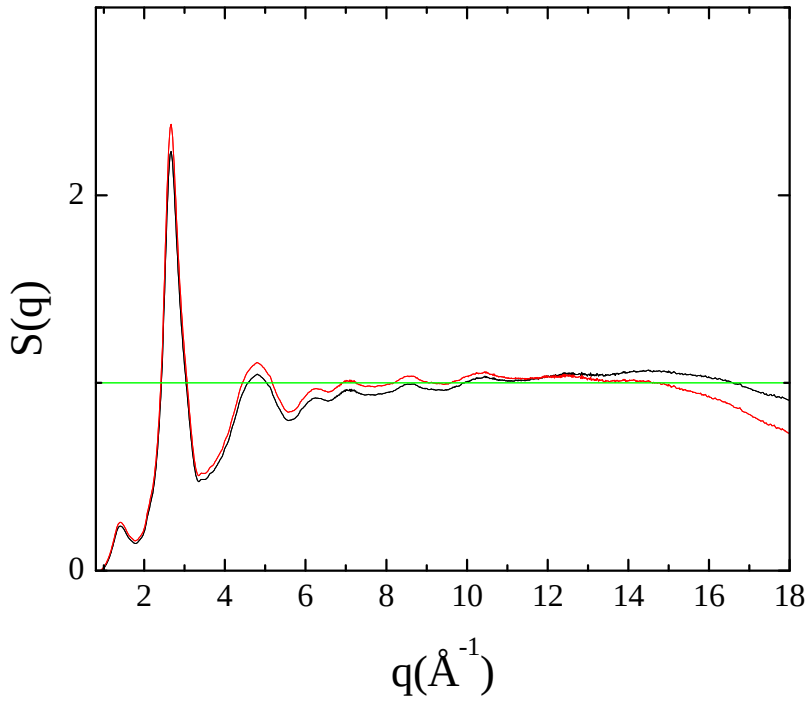

Figure B.5 – The total structure factor S(q) for the Al-Y-Fe glass with 7mm Al shielding, and no applied fluorescence correction (black line), and the same data with a fluorescence correction of 130 applied (red line). Unity is shown in green as a baseline.

observed throughout these experiments, and has been difficult to control. It is possible that the shielding is reducing the intensity at high-q to a point where it affects the calculation of the Compton scattering correction or the weighting function in PDFgetX2. This could provide clues to future data correction and background reduction methods.

Appendix 3

Circuit Diagrams and Device Control/Analysis Code for the Sievert-Type Apparatus for Hydrogen Loading Studies

This appendix provides information on the modifications to the high pressure-high temperature Sievert-type apparatus, used for the hydrogen loading studies discussed in Chapter 6, in three parts: circuit diagrams for the control electronics, texts of the device control codes in MS BASIC, and texts of the VBA macros used for data analysis in MS Excel. Electronic copies of the code are also provided on the disc accompanying the thesis.

A3.1. Circuit diagrams

As mentioned in Chapter 6, the MKS 722 pressure transducers were electronically isolated from one another during measurement using a Reed relay circuit. This circuit is shown in Figure A3.1, and was repeated 4 times for the 4 gauges. The basic operating principle was to trigger the Reed relay to close at the desired time of measurement by sending a low (digital ground) signal from pin *n* on panel J2, energizing the relay and routing the output signal to panel J1, which was then processed and logged by the computer (see the code in §3.1.2). The output lines of all gauges were routed to the same pinouts on panel J1 to eliminate signal cross-talk across the card. Figure A3.2 shows a diagram for the valve control circuit, using solid state relays to switch the 110VAC of the actuated valves from pins 30-37 of panel J2.

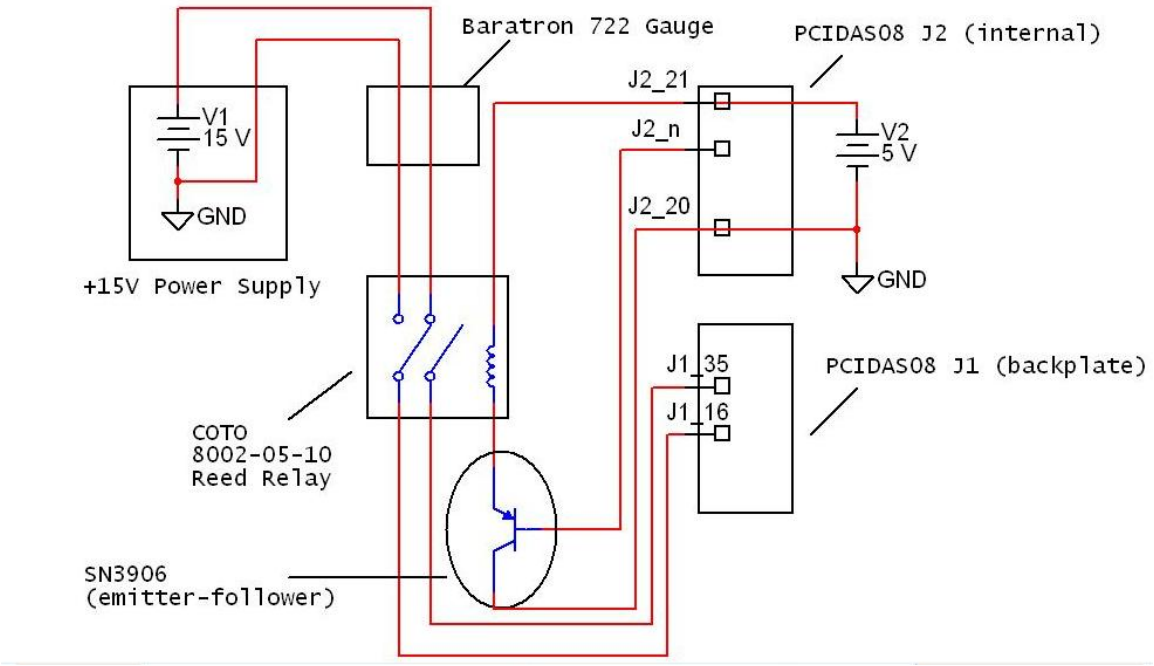

Figure A3.1 – A circuit diagram for the gauge controller; the circuit is repeated for all *n* gauges.

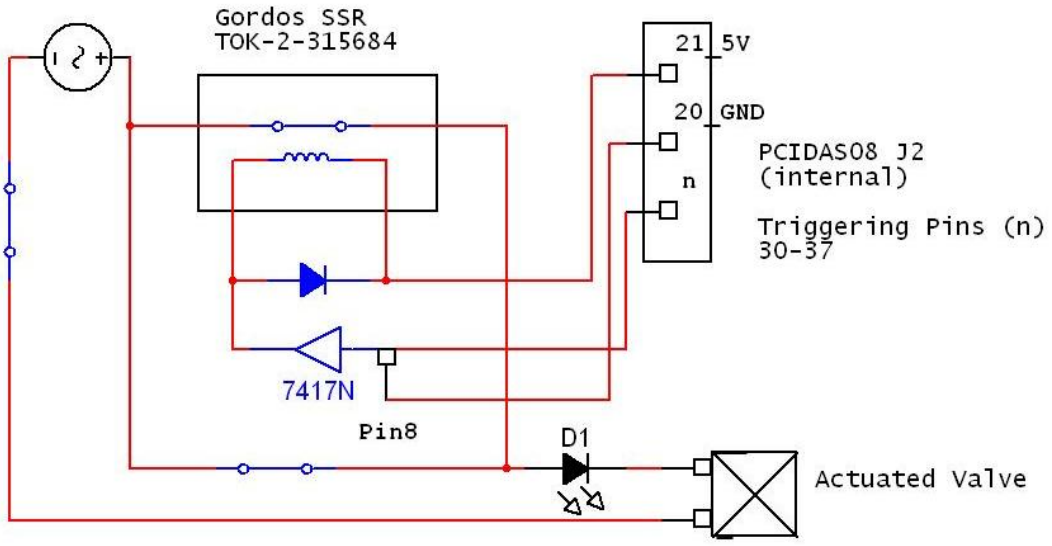

Figure A3.2 – A circuit diagram for the valve controller (the switches are shown closed); the circuit is repeated for all n valves.

A3.2. Device control code in MS BASIC

The output signals to the control electronics described in the previous section, from panels J1 and J2, and logging of the gauge readouts were automated by code in MS BASIC. Two routines were written, one to control a gas loading (absorption) setup and one for a gas un-loading (desorption) setup. The texts of the two codes are provided on the ensuing pages. One important note is the pointer printed for later use in the data analysis. The software includes a pointer to the line in the data corresponding to a cycling of the actuated valves (either an addition or removal of gas, depending on the setup) as a string of 8's. This string is referenced in the VBA macro used for automation of the analysis, presented in the following section.

A3.3. Analysis macros in MS VBA

To expedite data analysis, and also to minimize the contribution of human error through subjective analysis, a macro was developed in MS VBA for data processing using MS Excel. The routine queries the data file for the row of 8's used as a pointer for an addition or removal of gas, and calculates the relevant quantities (see Chapter 6) to determine the number of moles of gas absorbed or desorbed by the material. The routines can also be used in calibration, to determine the absorption/desorption profile of the empty chamber, and for volume calibration. The macros run in 2 parts, the first step (PCT1) simply refines the raw data, the second (PCT2) performs the calculations. Final input parameters, such as the mass of the sample and the temperature, were input by hand. These macros are incorporated into the Excel sheet PCT01.xls, included on the disc provided with this document.

```
/************BEGIN CODE ABSORB.BAS************/

'
'This code uses the optimized time delays and suports very large number
'averages along with reed relay control for independent multiplexing
'Written by Vic Wessels 6/2006
'
'Modified to include temperature measurements from a type K thermocouple
'read through the HP34401A digital voltmeter (DVM).
'
'
'Last update 6/13/2007
'


DECLARE SUB cnvrt (m%, N%, volt!)       ""initialization
basadr% = &H300
OUT basadr% + 11, 128                   ""this initializes the A/D board

OUT basadr% + 8, 255                ""close all relays and valves
OUT basadr% + 9, 31

CLS
PRINT
PRINT "This program outputs data used in volume calibration of the high"
PRINT "pressure PCT apparatus"
PRINT " "
PRINT "To quit at any time, press <Shift+q>.   "
PRINT " "
PRINT "Type <Enter> when ready to begin."
INPUT a$

PRINT "Are you continuing an experiment? (y/n)";
INPUT chknew$
PRINT " "

PRINT "Please name the output file (not including '.dat')";
INPUT nm$
nm$ = nm$ + ".dat"
PRINT " "

IF chknew$ = "y" THEN
        OPEN nm$ FOR APPEND AS #2
END IF

IF chknew$ = "n" THEN
        OPEN nm$ FOR OUTPUT AS #2
```

```
END IF

PRINT "Please enter the degree of accuracy for the high pressure gauges";
INPUT H%
PRINT " "

PRINT "Please enter the degree of accuracy for the low pressure gauges";
INPUT L%
PRINT " "

PRINT "Set time delay between gas additions (in hours)";
INPUT delay1
delay1 = delay1 * 3600
PRINT " "

PRINT "Set time delay between readings (in seconds not less than 5)";
INPUT delay2
PRINT " "

WHILE chkval$ <> "y"
PRINT "Are all manual valve controls off (y/n)?";
INPUT chkval$
PRINT " "
WEND

CLS
LOCATE 1, 1
DIM cmd$(100), resp$(1000)
REM Set up serial port for 9600 baud, even parity, 7 bits;
REM Ignore Request to Send and Carrier Detect; Send line feed,
REM enable parity check, reserve 1000 bytes for input buffer
REM
OPEN "com1:9600,e,7,2,rs,cd,lf,pe" FOR RANDOM AS #1 LEN = 1000
REM
REM Put the multimeter into the remote operation mode
PRINT #1, ":SYST:REM"
REM
REM Query the multimeter's id string
REM
PRINT #1, "*IDN?"
LINE INPUT #1, resp$
PRINT "*IDN? returned: ", resp$
REM
REM Ask what revision of SCPI the multimeter conforms to
PRINT #1, ":SYST:VERS?"
LINE INPUT #1, resp$
```

```
PRINT ":SYST:VERS? returned: ", resp$
REM
REM Send a message to the multimeter's display, and generate a beep
PRINT #1, ":SYST:BEEP;:DISP:TEXT 'HP 34401A'"
REM
REM Configure the multimeter for dc voltage readings,
REM 1 V range, 0.000001 V resolution, 1 readings
PRINT #1, ":CONF:VOLT:DC 2,0.000001;:SAMP:COUN 1"

CLS

"""""""this piece of code is the startup pressure monitor"""""""

WHILE (INKEY$ <> "Q")

PRINT "The approximate reservoir pressure (PSIA) is"

cnvrt 1, L%, V2
Press2 = 48.342 * V2
IF Press2 < 0 THEN Press2 = 0

PRINT USING "###.##"; Press2
PRINT "  "

PRINT "The approximate sample chamber pressure (PSIA) is"

cnvrt 3, L%, V3
Press3 = 48.342 * V3
IF Press3 < 0 THEN Press3 = 0

PRINT USING "###.##"; Press3
PRINT "  "

PRINT "The approximate desorption reservoir pressure (PSIA) is"

cnvrt 7, L%, V4
Press4 = 48.342 * V4
IF Press4 < 0 THEN Press4 = 0

PRINT USING "###.##"; Press4
PRINT "  "

PRINT "The approximate temperature (degrees C) at P3 is"

REM Trigger the readings, and fetch the results
PRINT #1, ":READ?"
```

```
INPUT #1, VT
'LINE INPUT #1, resp$
'PRINT ":READ? returned: ", resp$
'PRINT resp$

temp = .226584602# + 24152.109# * VT + 67233.42479999999# * (VT) ^ 2 +
2210340.682# *

(VT) ^ 3

PRINT USING "##.##"; temp
PRINT "  "

PRINT "Press <shift>+q at any time to exit this pressure monitor"
PRINT " "

tstart# = TIMER
tnow# = TIMER + 86400
WHILE ((tnow# - tstart#) MOD 86400 < 5)
tnow# = TIMER + 86400
WEND

CLS

WEND
""""""""""""this ends the startup pressure monitor""""""""""

""""""""""""this piece of code is the main body""""""""""""
tag = 0
tstart = TIMER
day = 0
elapsed = 0
tadd = TIMER
tnew = 0
tagP3 = 1

'PRINT "*** ALL VALUES ARE GIVEN IN P.S.I.A ***"

WHILE (INKEY$ <> "Q")

cnvrt 1, H%, V2  ""call subroutine to read voltages and take averages
cnvrt 3, H%, V3
cnvrt 7, L%, V4

IF tagP3 = 1 THEN
```

```
        IF Press3 < 15 THEN
                OUT basadr% + 8, 223    """Low pressure condition to open valve V3 to

Barocel
        ELSE
                OUT basadr% + 8, 255
        END IF

tagP3 = 0

END IF

cnvrt 0, L%, V0  ""read P0

REM Trigger the readings, and fetch the results         ""read TC voltage from HP DVM
PRINT #1, ":READ?"
INPUT #1, VT
'LINE INPUT #1, resp$
'PRINT ":READ? returned: ", resp$
'PRINT resp$

tnow = TIMER
IF tnow < delay2 THEN     """this tells the computer what to do at midnight (time=0)
day = day + 1
END IF

time = ((tnow - tstart) / 3600 + (86400 * day) / 3600)  ""record time since start

Press0 = (105.7306 * V0 - 57.306) * .01934
IF Press0 < 0 THEN Press0 = 0

Press2 = 48.342 * V2
IF Press2 < 0 THEN Press2 = 0

Press3 = 48.342 * V3
IF Press3 < 0 THEN Press3 = 0

Press4 = 48.342 * V4
IF Press4 < 0 THEN Press4 = 0

temp = .226584602# + 24152.109# * VT + 67233.42479999999# * (VT) ^ 2 +
2210340.682# *

(VT) ^ 3

IF tag = 0 THEN
```

```
PRINT "P2     P0     P3     P4     V2     V0     V3     V4    temp   time"
END IF

PRINT USING "###.##"; Press2;
PRINT "  ";
PRINT USING "##.###"; Press0;
PRINT "  ";
PRINT USING "###.##"; Press3;
PRINT "  ";
PRINT USING "###.##"; Press4;
PRINT "  ";
PRINT USING "#.###"; V2;
PRINT "  ";
PRINT USING "#.###"; V0;
PRINT "  ";
PRINT USING "#.###"; V3;
PRINT "  ";
PRINT USING "#.###"; V4;
PRINT "  ";
PRINT USING "##.##"; temp
PRINT "  ";
PRINT USING "##.##"; time

PRINT #2, time, Press0, Press2, Press3, Press4, V0, V2, V3, V4, temp

tag = tag + 1

IF tag = 10 THEN
tag = 0
PRINT ""

'PRINT "elapsed time = ";
'PRINT elapsed
'PRINT ""

END IF

"""""""this code finishes up and quits if P2-P3 < 8PSI"""""""""""""

IF ABS(Press2 - Press3) < 8 THEN

FOR i = 1 TO 10

tstart# = TIMER
tnow# = TIMER + 86400
WHILE ((tnow# - tstart#) MOD 86400 < delay2)   'set delay between succesive readings
```

```
tnow# = TIMER + 86400
WEND

cnvrt 0, L%, V0
cnvrt 1, H%, V2
cnvrt 3, H%, V3
cnvrt 7, L%, V4

REM Trigger the readings, and fetch the results         ""read TC voltage from HP DVM
PRINT #1, ":READ?"
INPUT #1, VT
'LINE INPUT #1, resp$
'PRINT ":READ? returned: ", resp$
'PRINT resp$

tnow = TIMER
IF tnow < delay2 THEN     ""this tells the computer what to do at midnight (time=0)
day = day + 1
END IF

time = ((tnow - tstart) / 3600 + (86400 * day) / 3600)  ""record time since start

temp = .226584602# + 24152.109# * VT + 67233.42479999999# * (VT) ^ 2 +
2210340.682# *

(VT) ^ 3

Press0 = (105.7306 * V0 - 57.306) * .01934
IF Press0 < 0 THEN Press0 = 0

Press2 = 48.342 * V2
IF Press2 < 0 THEN Press2 = 0

Press3 = 48.342 * V3
IF Press3 < 0 THEN Press3 = 0

Press4 = 48.342 * V4
IF Press4 < 0 THEN Press4 = 0

CLS
endtime = delay2 * (11 - i)
endminute = endtime / 60

PRINT "Preparing to quit in less than";
PRINT endminute;
PRINT "minutes"
```

```
PRINT #2, time, Press0, Press2, Press3, Press4, V0, V2, V3, V4, temp

NEXT i

CLOSE #1
CLOSE #2
OUT basadr% + 8, 255

END

END IF

"""""""""""""""end quitting condition"""""""""""""""""""

tstart# = TIMER
tnow# = TIMER + 86400
WHILE ((tnow# - tstart#) MOD 86400 < delay2)   'set delay between succesive readings
tnow# = TIMER + 86400
WEND

tnew = TIMER + 86400
elapsed = ((tnew - tadd) MOD 86400)

IF elapsed > delay1 THEN

PRINT " "
PRINT "Now I will make an addition!"
PRINT " "
'PRINT "elapsed time = ";
'PRINT elapsed;
'PRINT " "

tstart# = TIMER
tnow# = TIMER + 86400
WHILE ((tnow# - tstart#) MOD 86400 < 1)
tnow# = TIMER + 86400
WEND

                OUT basadr% + 8, 255
                tstart# = TIMER
                tnow# = TIMER + 86400
                WHILE ((tnow# - tstart#) MOD 86400 < 1)
                        tnow# = TIMER + 86400
                WEND
```

```
                OUT basadr% + 8, 127
                tstart# = TIMER
                tnow# = TIMER + 86400
                WHILE ((tnow# - tstart#) MOD 86400 < 2)
                        tnow# = TIMER + 86400
                WEND

                OUT basadr% + 8, 255
                tstart# = TIMER
                tnow# = TIMER + 86400
                WHILE ((tnow# - tstart#) MOD 86400 < 1)
                        tnow# = TIMER + 86400
                WEND

                OUT basadr% + 8, 191
                tstart# = TIMER
                tnow# = TIMER + 86400
                WHILE ((tnow# - tstart#) MOD 86400 < 1)
                        tnow# = TIMER + 86400
                WEND

                OUT basadr% + 8, 255
                tstart# = TIMER
                tnow# = TIMER + 86400
                WHILE ((tnow# - tstart#) MOD 86400 < 1)
                        tnow# = TIMER + 86400
                WEND

                PRINT #2, 888888, 888888, 888888, 888888, 888888, 888888, 888888,

888888, 888888

'tstart# = TIMER
'tnow# = TIMER + 86400
'WHILE ((tnow# - tstart#) MOD 86400 < 1)
'tnow# = TIMER + 86400
'WEND

tag = 0
tadd = TIMER
tagP3 = 1

END IF

WEND
```

```
OUT basadr% + 8, 255

CLOSE #1
CLOSE #2

END

'''''''''''''''end of main body code''''''''''''''''''

SUB cnvrt (m%, N%, volt) STATIC

basadr% = &H300
nn% = 2 AND 7

sumvolt = 0

OUT basadr% + 9, (30 - m%)
tstart# = TIMER
tnow# = TIMER + 86400
WHILE ((tnow# - tstart#) MOD 86400 < .25)
        tnow# = TIMER + 86400
WEND

FOR i = 1 TO N%

OUT basadr% + 2, nn%
OUT basadr% + 1, nn%
WHILE (INP(basadr% + 2) AND &H80) <> 0
WEND
lo% = INP(basadr%)
hi% = INP(basadr% + 1)
dt% = &H10 * hi% + lo% \ &H10
volt = dt% * 10! / 4096

sumvolt = sumvolt + volt

NEXT i

volt = sumvolt / N%

OUT basadr% + 9, 31
END SUB


/**********END CODE ABSORB.BAS**********/
```

```
/************BEGIN CODE DESORB.BAS************/
''''''''''''''''''''''''''''''''''''''''''''''''''''''''''''''''''''''''''''''''''''


'
'This program runs a simple procedure for desorption measurements on the high pressure
'PCT apparatus located in Compton 56.
'
'This code assumes the use of reed relays for independent multiplexing through
'BASADR%+9 and valve control through BASADR%+8
'
'Gauge calibration for MKS Baratron model 722 25000 Torr capacitance manometers
'
'Temperature measurement using type K thermocouple with cold junction compensation
'read through HP34401A digital voltmeter (DVM)
'
'Written by Vic Wessels 1/07
'Last update 1/8/07 VW
''''''''''''''''''''''''''''''''''''''''''''''''''''''''''''''''''''''''''''''''''''


'



DECLARE SUB cnvrt (m%, N%, volt!)       ''initialization
basadr% = &H300
OUT basadr% + 11, 128                   ''this initializes the A/D board

OUT basadr% + 8, 255                ''close all relays and valves
OUT basadr% + 9, 31

                                    '''the following code initializes the HP34401A DVM
CLS
LOCATE 1, 1
DIM cmd$(100), resp$(1000)
REM Set up serial port for 9600 baud, even parity, 7 bits;
REM Ignore Request to Send and Carrier Detect; Send line feed,
REM enable parity check, reserve 1000 bytes for input buffer
REM
OPEN "com1:9600,e,7,2,rs,cd,lf,pe" FOR RANDOM AS #1 LEN = 1000
REM
REM Put the multimeter into the remote operation mode
PRINT #1, ":SYST:REM"
REM
REM Query the multimeter's id string
REM
PRINT #1, "*IDN?"
LINE INPUT #1, resp$
```

```
PRINT "*IDN? returned: ", resp$
REM
REM Ask what revision of SCPI the multimeter conforms to
PRINT #1, ":SYST:VERS?"
LINE INPUT #1, resp$
PRINT ":SYST:VERS? returned: ", resp$
REM
REM Send a message to the multimeter's display, and generate a beep
PRINT #1, ":SYST:BEEP;:DISP:TEXT 'HP 34401A'"
REM
REM Configure the multimeter for dc voltage readings,
REM 1 V range, 0.001 mV resolution, 1 readings
PRINT #1, ":CONF:VOLT:DC 1,0.000001;:SAMP:COUN 1"


delay3 = 3600

CLS
PRINT
PRINT "This program runs a simple desorption procedure and outputs the data to a file."
PRINT "The (rough) pumping time is set to"; (delay3 / 3600); "hours."
PRINT " "
PRINT "To quit at any time, press <Shift+q>.   "
PRINT " "
PRINT "Press <Enter> when ready to begin."
INPUT a$

PRINT "Please name the output file(not including '.dat')";
INPUT nm$
nm$ = nm$ + ".dat"
PRINT " "

PRINT "Please enter the degree of accuracy for all gauges";
INPUT H%
PRINT " "

PRINT "Set equilibration time delay (in hours)";
INPUT delay1
delay1 = delay1 * 3600
PRINT " "

PRINT "Set time delay between readings (in seconds not less than 5)";
INPUT delay2
PRINT " "

OPEN nm$ FOR OUTPUT AS #2       ""open output file
```

```
CLS

"""""""this piece of code is the startup pressure monitor"""""""

WHILE (INKEY$ <> "Q")

PRINT "The reservoir pressure (PSIA) is"

cnvrt 1, H%, V2
Press2 = 50 * V2
IF Press2 < 0 THEN Press2 = 0

PRINT USING "###.##"; Press2
PRINT "  "

PRINT "The sample chamber pressure (PSIA) is"

cnvrt 3, H%, V3
Press3 = 50 * V3
IF Press3 < 0 THEN Press3 = 0

PRINT USING "###.##"; Press3
PRINT "  "

PRINT "The desorption reservoir pressure (PSIA) is"

cnvrt 7, H%, V4
Press4 = 50 * V4
IF Press4 < 0 THEN Press4 = 0

PRINT USING "###.##"; Press4
PRINT "  "

PRINT "The approximate temperature (degrees C) at P3 is"

GOSUB TEMPOUT
PRINT USING "##.##"; Temp
PRINT ""

PRINT "Press <shift>+q at any time to exit this pressure monitor"
PRINT " "

tstart# = TIMER
tnow# = TIMER + 86400
```

```
WHILE ((tnow# - tstart#) MOD 86400 < 5)
tnow# = TIMER + 86400
WEND

CLS

WEND


"""""""""""""this ends the startup pressure monitor""""""""""


"""""""""""""this piece of code is the main body"""""""""""""

tag = 0
tstart = TIMER
day = 0
elapsed4 = 0
elapsed5 = 0
tadd4 = TIMER
tadd5 = TIMER
tnew = 0

WHILE (INKEY$ <> "Q")

GOSUB GETPRESS
GOSUB TEMPOUT
GOSUB GETTIME

IF tag = 0 THEN
PRINT "P2     P0     P3     P4     V2     V0     V3     V4     time"
END IF

PRINT USING "##.###"; time
PRINT "  ";
PRINT USING "###.##"; Press2;
PRINT "  ";
PRINT USING "##.###"; Press0;
PRINT "  ";
PRINT USING "###.##"; Press3;
PRINT "  ";
PRINT USING "###.##"; Press4;
PRINT "  ";
PRINT USING "#.###"; V2;
PRINT "  ";
PRINT USING "#.###"; V0;
```

```
PRINT "  ";
PRINT USING "#.###"; V3;
PRINT "  ";
PRINT USING "#.###"; V4;
PRINT "  ";
PRINT USING "##.##"; Temp

PRINT #2, time, Press0, Press2, Press3, Press4, V0, V2, V3, V4, Temp

tag = tag + 1

IF tag = 10 THEN
tag = 0
PRINT ""
END IF


"""""""this code finishes up and quits if P0 < .01 PSI"""""""""""""

IF ABS(Press0) < .01 THEN

FOR i = 1 TO 10

tstart# = TIMER
tnow# = TIMER + 86400
WHILE ((tnow# - tstart#) MOD 86400 < delay2)   'set delay between succesive readings
tnow# = TIMER + 86400
WEND

GOSUB GETPRESS
GOSUB TEMPOUT
GOSUB GETTIME

CLS
endtime = delay2 * (11 - i)
endminute = endtime / 60

PRINT "Preparing to quit in less than";
PRINT endminute;
PRINT "minutes"

PRINT #2, time, Press0, Press2, Press3, Press4, V0, V2, V3, V4, Temp

NEXT i

END
```

```
END IF

"""""""""""""""end quitting condition"""""""""""""""""""

tstart# = TIMER
tnow# = TIMER + 86400
WHILE ((tnow# - tstart#) MOD 86400 < delay2)   'set delay between succesive readings
tnow# = TIMER + 86400
WEND

tnew = TIMER + 86400

elapsed4 = ((tnew - tadd4) MOD 86400)
elapsed5 = ((tnew - tadd5) MOD 86400)

IF elapsed4 > delay1 THEN

PRINT " "
PRINT "Now I will open desorption chamber at V4!"
PRINT " "
'PRINT "elapsed time = ";
'PRINT elapsed4;
'PRINT " "

tstart# = TIMER
tnow# = TIMER + 86400
WHILE ((tnow# - tstart#) MOD 86400 < 5)
tnow# = TIMER + 86400
WEND

                OUT basadr% + 8, 255
                tstart# = TIMER
                tnow# = TIMER + 86400
                WHILE ((tnow# - tstart#) MOD 86400 < 2)
                        tnow# = TIMER + 86400
                WEND

                OUT basadr% + 8, 183
                tstart# = TIMER
                tnow# = TIMER + 86400
                WHILE ((tnow# - tstart#) MOD 86400 < 2)
                        tnow# = TIMER + 86400
                WEND

                OUT basadr% + 8, 255
```

```
                tstart# = TIMER
                tnow# = TIMER + 86400
                WHILE ((tnow# - tstart#) MOD 86400 < 2)
                        tnow# = TIMER + 86400
                WEND

                PRINT #1, 888888, 888888, 888888, 888888, 888888, 888888, 888888,
888888

tstart# = TIMER
tnow# = TIMER + 86400
WHILE ((tnow# - tstart#) MOD 86400 < 5)
tnow# = TIMER + 86400
WEND

tag = 0
tadd4 = TIMER

END IF

IF elapsed5 > delay3 THEN

PRINT " "
PRINT "Now I will open V5 to evacuate!"
PRINT " "
'PRINT "elapsed time = ";
'PRINT elapsed;
'PRINT " "

tstart# = TIMER
tnow# = TIMER + 86400
WHILE ((tnow# - tstart#) MOD 86400 < 5)
tnow# = TIMER + 86400
WEND

                OUT basadr% + 8, 255
                tstart# = TIMER
                tnow# = TIMER + 86400
                WHILE ((tnow# - tstart#) MOD 86400 < 2)
                        tnow# = TIMER + 86400
                WEND

                OUT basadr% + 8, 179
                tstart# = TIMER
                tnow# = TIMER + 86400
                WHILE ((tnow# - tstart#) MOD 86400 < 2)
```

```
                tnow# = TIMER + 86400
        WEND

        OUT basadr% + 8, 255
        tstart# = TIMER
        tnow# = TIMER + 86400
        WHILE ((tnow# - tstart#) MOD 86400 < 2)
                tnow# = TIMER + 86400
        WEND

        PRINT #1, 999999, 999999, 999999, 999999, 999999, 999999, 999999,
999999

tstart# = TIMER
tnow# = TIMER + 86400
WHILE ((tnow# - tstart#) MOD 86400 < 5)
tnow# = TIMER + 86400
WEND

tag = 0
tadd5 = TIMER

END IF


"""""""""check for safe opening of barocel valve V3"""""""""""""""""""

cnvrt 3, H%, V3
Press3 = 48.342 * V3
IF Press3 < 0 THEN Press3 = 0

        IF Press3 < 17 THEN

                OUT basadr% + 8, 223    """Low pressure condition to open valve V3 to

Barocel
        ELSE
                OUT basadr% + 8, 255
        END IF


WEND

OUT basadr% + 8, 255

CLOSE #1
```

```
CLOSE #2

END

'''''''''''''''end of main body code''''''''''''''''''

GETPRESS:

cnvrt 0, H%, V0         ""call subroutine to read voltages and take averages
cnvrt 1, H%, V2
cnvrt 3, H%, V3
cnvrt 7, H%, V4

Press0 = 1.9995 * V0 - 1.1936
IF Press0 < 0 THEN Press0 = 0

Press2 = 48.342 * V2
IF Press2 < 0 THEN Press2 = 0

Press3 = 48.342 * V3
IF Press3 < 0 THEN Press3 = 0

Press4 = 48.342 * V4
IF Press4 < 0 THEN Press4 = 0

RETURN

TEMPOUT:

REM Trigger the readings, and fetch the results
PRINT #1, ":READ?"
LINE INPUT #1, resp$

VT$ = resp$

Temp = .226584602# + 24152.109# * VT + 67233.42479999999# * (VT) ^ 2 +
2210340.682# *

(VT) ^ 3

RETURN

GETTIME:

tnow = TIMER
IF tnow < delay2 THEN     """this tells the computer what to do at midnight (time=0)
```

```
day = day + 1
END IF

time = ((tnow - tstart) / 3600 + (86400 * day) / 3600)  ""record time since start

RETURN

SUB cnvrt (m%, N%, volt) STATIC

basadr% = &H300
nn% = 2 AND 7

sumvolt = 0

OUT basadr% + 9, (30 - m%)
tstart# = TIMER
tnow# = TIMER + 86400
WHILE ((tnow# - tstart#) MOD 86400 < .25)
        tnow# = TIMER + 86400
WEND

FOR i = 1 TO N%

OUT basadr% + 2, nn%
OUT basadr% + 1, nn%
WHILE (INP(basadr% + 2) AND &H80) <> 0
WEND
lo% = INP(basadr%)
hi% = INP(basadr% + 1)
dt% = &H10 * hi% + lo% \ &H10
volt = dt% * 10! / 4096

sumvolt = sumvolt + volt

NEXT i

volt = sumvolt / N%

OUT basadr% + 9, 31
END SUB
/************END CODE DESORB.BAS************/
```

```
/************BEGIN CODE OF MACRO PCT1************/

Sub PCT1()
'This program simply refines raw PCT voltage data
'VW 1/09/07

'Application.ScreenUpdating = False

Sheet1.Select

   Range("H1").Select

   PreV2 = 0
   PostV2 = 0
   PreV3 = 0
   PostV3 = 0
   PreV0 = 0
   PostV0 = 0

   i = 0
   ii = 0
   jj = 0

   Do Until Selection.Value = ""

      If Selection.Value = "888888" Then

         PreV2 = Selection.Offset(-1, 0).Value
         PostV2 = Selection.Offset(1, 0).Value

         For i = 0 To 9
         PreV3 = PreV3 + Selection.Offset(-10 + i, 1).Value
         Next i

         For i = 0 To 9
         PreV0 = PreV0 + Selection.Offset(-10 + i, -1).Value
         'PreV0 = Selection.Offset(-2, -1).Value
         Next i

         'For I = 0 To 9
         'PostV3 = PostV3 + Selection.Offset(2 + I, 1).Value
         PostV3 = Selection.Offset(1, 1).Value
         'Next I

         'For i = 0 To 9
         'PostV0 = PostV0 + Selection.Offset(1 + i, -1).Value
```

```
    PostV0 = Selection.Offset(1, -1).Value
    'Next i

    Temper = Selection.Offset(-1, 3).Value

    Range("L1").Select
    Selection.Offset(jj, 0).Value = PreV2

    Range("M1").Select
    Selection.Offset(jj, 0).Value = PostV2

    Range("N1").Select
    Selection.Offset(jj, 0).Value = PreV3 / 10

    Range("O1").Select
    Selection.Offset(jj, 0).Value = PreV0 / 10

    Range("P1").Select
    Selection.Offset(jj, 0).Value = PostV3

    Range("Q1").Select
    Selection.Offset(jj, 0).Value = PostV0

    Range("R1").Select
    Selection.Offset(jj, 0).Value = Temper

    Range("H1").Select
    Selection.Offset(ii + 1, 0).Select

    jj = jj + 1

    PreV2 = 0
    PostV2 = 0
    PreV3 = 0
    PreV0 = 0
    PostV3 = 0
    PostV0 = 0

Else
    Range("H1").Select
    Selection.Offset(ii + 1, 0).Select
    ii = ii + 1
End If

Loop
```

```
    Range("A1").Select

'Application.ScreenUpdating = True

End Sub
/************END CODE OF MACRO PCT1***********/

/************BEGIN CODE OF MACRO PCT2***********/

Sub PCT2()

'This program refines voltage data generated by module PCT1.
'It is intended to run in Sheet2 of a workbook with PCT1 data in sheet 1,
'and provided neccessary calibration data and constants.
'VW 1/09/07

Sheet2.Select

Range("B5").Select

M0 = Selection.Offset(0, 0).Value
B0 = Selection.Offset(0, 2).Value

M2 = Selection.Offset(1, 0).Value
B2 = Selection.Offset(1, 2).Value

M3 = Selection.Offset(2, 0).Value
B3 = Selection.Offset(2, 2).Value

M4 = Selection.Offset(3, 0).Value
B4 = Selection.Offset(3, 2).Value

Range("B12").Select

Thot = Selection.Offset(0, 8).Value
Vsh = Selection.Offset(2, 8).Value
rho = Selection.Offset(0, 12).Value
m = Selection.Offset(0, 16).Value
R = 1205.91

Sheet1.Select

Range("L1").Select

i = 0
ii = 0
```

```
jj = 0

SumP2 = 0

Do Until Selection.Value = ""

    PreP2 = M2 * Selection.Offset(0, 0).Value + B2
    PostP2 = M2 * Selection.Offset(0, 1).Value + B2
    DeltaP2 = PreP2 - PostP2
    SumP2 = SumP2 + DeltaP2

    PreP3 = M3 * Selection.Offset(0, 2).Value + B3
    PostP3 = M3 * Selection.Offset(0, 4).Value + B3

    PreP0 = M0 * Selection.Offset(0, 3).Value + B0
    PostP0 = M0 * Selection.Offset(0, 5).Value + B0

    Troom = Selection.Offset(0, 6).Value

    Sheet2.Select

    Range("H2").Select
    Selection.Offset(jj, 0).Value = PreP2

    Selection.Offset(jj, 1).Value = PostP2

    Selection.Offset(jj, 2).Value = DeltaP2

    Selection.Offset(jj, 3).Value = SumP2

    Selection.Offset(jj, 4).Value = PreP3

    Selection.Offset(jj, 5).Value = PreP0

    Selection.Offset(jj, 6).Value = PostP3

    Selection.Offset(jj, 7).Value = PostP0

    Selection.Offset(jj, 8).Value = Troom

    Sheet1.Select
    Range("L1").Select
    Selection.Offset(ii + 1, 0).Select

    ii = ii + 1
    jj = jj + 1
```

```
Loop

Sheet2.Select

Range("H1").Select
   Selection.Offset(0, 0).Value = "PreP2"

   Selection.Offset(0, 1).Value = "PostP2"

   Selection.Offset(0, 2).Value = "DeltaP2"

   Selection.Offset(0, 3).Value = "SumP2"

   Selection.Offset(0, 4).Value = "PreP3"

   Selection.Offset(0, 5).Value = "PreP0"

   Selection.Offset(0, 6).Value = "PostP3"

   Selection.Offset(0, 7).Value = "PostP0"

   Selection.Offset(0, 8).Value = "Troom"

Range("A1").Select

'Application.ScreenUpdating = True

End Sub
/************END CODE OF MACRO PCT2************/
```